University of Southampton

Faculty of Natural and Environmental Sciences

Ocean and Earth Science

Tectonics of Fold-Thrust Belts Driven by Plate Convergence and Gravitational Instability

by

Xiaodong Yang

Thesis for the Degree of Doctor of Philosophy

November 2018

UNIVERSITY OF SOUTHAMPTON

ABSTRACT

FALCULTY OF NATURAL AND ENVIRONMENTAL SCIENCES

Ocean and Earth Science

Doctor of Philosophy

TECTONICS OF FOLD-THRUST BELTS DRIVEN BY PLATE CONVERGENCE AND GRAVITATIONAL INSTABILITY

by Xiaodong Yang

Fold-thrust belts (FTBs) related to plate convergence are found in active margins and in the foreland of orogenic belts, while those related to gravitational failure are typically found on passive margins. Seismic imaging of the subsurface structure, combined with decades of study and analysis, have resulted in a good first-pass understanding of their tectonics and mechanics, but there are still many significant unresolved issues.

Numerical models were used to investigate aspects of thrust belt growth: the interplay between the overall wedge taper, width and height, deformation front, internal movement, and fault position, activity, displacement and dip. After a new thrust initiates at the wedge front, the entire wedge shortens and thickens to re- attain critical taper, with significant frontal thrust activity and minor activity on older thrusts. Models show that thrust belts grow cyclically, with periods of accretion (rapid thrust-front advance, high displacement and strain rate), and periods of adjustment (slow wedge deformation, low displacement and strain rate). Detailed observation of the zone in front of the thrust front indicates that deformation in that region is a critical component of system advance. New area balancing methods, involving evaluation of the role of the regional slope, have been developed to improve the accuracy of structural restoration and shortening quantification. Application to analogue models and natural fold-thrust belts highlights the importance of regional slope in area balancing restoration: a higher regional dip results in reduced shortening while a lower regional dip leads to increased shortening. Accuracy of the shortening estimate requires independent constraint of parameters, particularly the initial regional slope. The tectonics of the Northwest Borneo Fold-Thrust Belt (NBFB), offshore Brunei, are investigated using 3D seismic data. The NBFB contains three fold types: fault-propagation folds (dominant); detachment folds (minor); and fault-bend folds (rare). For each fold, structural style varies along strike, in response to changes in the magnitude of folding, basal décollement strength, and inherited structure and basement topography. Fault spacing responds to basement topography and topography also blocks forward propagation of the fold-thrust belt. Fault dip increases as the fault and fold matures. The low taper angle (mostly <6°) implies a high basal fluid pressure (>0.7 of lithostatic pressure). Evidence of two distinct stages of fault (fold) activity, wide distribution of active contractional deformation across the entire belt (rather than just at the toe), and present-day extensional inactivity, suggest that the NBFB results from a combination of primary gravitational tectonics and secondary plate convergence. Fold-thrust belts caused by plate convergence are compared with gravity-driven systems. The energy source in gravity-driven systems is the release of gravitational potential energy within the sediment pile, producing upslope extension and downslope contraction. This is resupplied by sedimentation. Episodic sediment input leads to fluctuations in deformation rate. In contrast, the energy source of convergence driven systems is movement of a stressed lithosphere-scale boundary. Plate movement is continuous, so thrust belt deformation is less episodic. Back-thrusts and fault back rotation are more common in convergence-driven systems and landward-vergent thrusts can be present. The rate of shortening across convergence-driven systems is high and generally continuous on a long time scale. Whereas rates are lower across the contractional domain of a gravity-driven system and more variable through time. A plate-driven system is limited by plate motion rate, i.e. the rate at which the plate is fed into the FTB, whereas a gravity driven system is resisted by the strength of the sediments and detachment.

Table of Contents

Table of Tables

Table of Tables

Table of Figures

Research Thesis: Declaration of Authorship

Print name:	Xiaodong Yang

Title of thesis:	Tectonics of Fold-Thrust Belts Driven by Plate Convergence and Gravitational Instability

I declare that this thesis and the work presented in it are my own and has been generated by me as the result of my own original research.

I confirm that:

1. This work was done wholly or mainly while in candidature for a research degree at this University;
2. Where any part of this thesis has previously been submitted for a degree or any other qualification at this University or any other institution, this has been clearly stated;
3. Where I have consulted the published work of others, this is always clearly attributed;
4. Where I have quoted from the work of others, the source is always given. With the exception of such quotations, this thesis is entirely my own work;
5. I have acknowledged all main sources of help;
6. Where the thesis is based on work done by myself jointly with others, I have made clear exactly what was done by others and what I have contributed myself;
7. Parts of this work have been published as:

Yang, X., Peel, F.J., Sanderson, D.J., and McNeill, L.C., 2017, Episodic growth of fold-thrust belts: Insights from Finite Element Modelling; Journal of Structural Geology, 102, 113-129, doi.org/10.1016/j.jsg.2017.07.012.

Signature:	Xiaodong Yang	Date:	8/11/2018

Acknowledgements

Many people, in different countries, have made numerous and invaluable contributions to my PhD research, without which I don't think I should have reached this stage of thesis completion.

First of all, I would like to express my most sincere gratitude to my supervisors Frank Peel, Lisa McNeill and David Sanderson who offered me the opportunity of doing a PhD with them in Britain. During my PhD research, they have been incredibly helpful and strongly supportive with numerous and beneficial discussions, instructions, draft edits, language improvement, research planning, which I am extremely grateful. Their professions, dedications and contributions to my study have been the most important things for me to learn for many years ahead.

I greatly appreciate Susan Ellis, Susanne Buiter, John Suppe for the beneficial discussions and constructive comments and feedbacks to my study, which directly led to the publication of my first paper. Mark Behn is sincerely acknowledged for hosting me as a visiting student at Woods Hole Oceanographic Institute, and instructing me to learn and practice the mathematical theories of numerical modelling. Jonas Ruh is very much appreciated for being very kind to teach me the finite difference modelling. Through these external studies and communications, I have gained abundant and essential knowledge of structural geology, geomechanics, Matlab coding and numerical modelling.

Apart from the intensive PhD research, I have also been very fortunate to experience and understand many British cultures and traditional games, including pub socials, dancing, Winchester Bonfire, visit to parliament, English food, BBC documentary, Rugby, Cricket, Snooker, etc. These are all done with enormous helps from my friends Age, Gavin, Jamie, Jonny, Steven, David, Melanie, James, Matt, Matthias, Oli, Amaya, Lin, Nathanial, to whom I own huge debts.

"A Huge Thank You" goes to the UK that I have made home for four years. The UK provides me a wealth of culture, history, landscape, "incredible weather" and dynamic

politics from which I am greatly benefited.

University of Southampton, National Oceanography Centre Southampton and NERC CDT in Oil and Gas funded my research in the UK, which is very much appreciated. I am confident that these financial supports will be demonstrated worthwhile by my future success in various subjects, e.g., scientific achievement, high education and public service.

I really appreciate my parents for being strongly supportive to me through every stage of my education, I couldn't have entered university without their constant supports and encouragements.

Last, but not least, thanks to my country, China, which makes me always proud.

Chapter 1 Introduction

1.1 Fold-thrust belts

Fold-thrust belts (FTBs) are common geological features of the Earth's upper crust (e.g., Dahlen, 1990). They occur in three main tectonic settings: (1) submarine accretionary wedges associated with subduction zones (*Figure 1.1a*), (2) the subaerial foreland of orogenic zones associated with continent-continent collision or intracontinental shortening, and (3) the contractional toes of gravity-driven linked systems of extension and contraction, most commonly but not exclusively developed on passive continental margins where the sediment sequence lies above a weak décollement (salt, overpressured mud or shale) (*Figure 1.1b*). For review see Boyer and Elliot (1982), Dahlen (1990), Poblet and Lisle (2011), Rowan et al. (2004), Morley et al. (2011), Buiter (2012), King and Morley (2017).

The presence of deformed basement rocks within FTBs determines whether an FTB is thin-skinned, mainly involving sediments at only shallow levels of crust, or thick-skinned where thrusts and folds incorporate basement or affect the entire upper crust and possibly lower crust (Rodgers, 1949; Coward, 1983; Pfiffner, 2006; Buiter, 2012). If the thrusts cut into the upper part of crystalline basement, levelling off the basement/cover interface, deformation can be defined as basement-involved thin-skinned (Kley, 1996; Miller, 2003; Pfiffner, 2006; Ruh, 2013)

The early understanding of the geometry and processes of fold-thrust belts began with the study of onshore fold belts that were driven by continent-continent collision, such as the Scottish Moine Thrust Belt (Peach et al., 1907; Elliott and Johnson, 1980), the Appalachians (Rich, 1934; Rodgers, 1949; Rodgers, 1963; Hatcher Jr, 1972), the Canadian Rockies (e.g., Bally et al., 1966; Dahlstrom, 1969; Dahlstrom, 1970; Price and Mountjoy, 1970; Price, 1981), the Alps (Trümpy, 1960) and the Idaho-Wyoming Thrust Belt (Armstrong and Oriel, 1965). This tectonic setting dominated the paradigm of FTBs for some time (Boyer and Elliott, 1982).

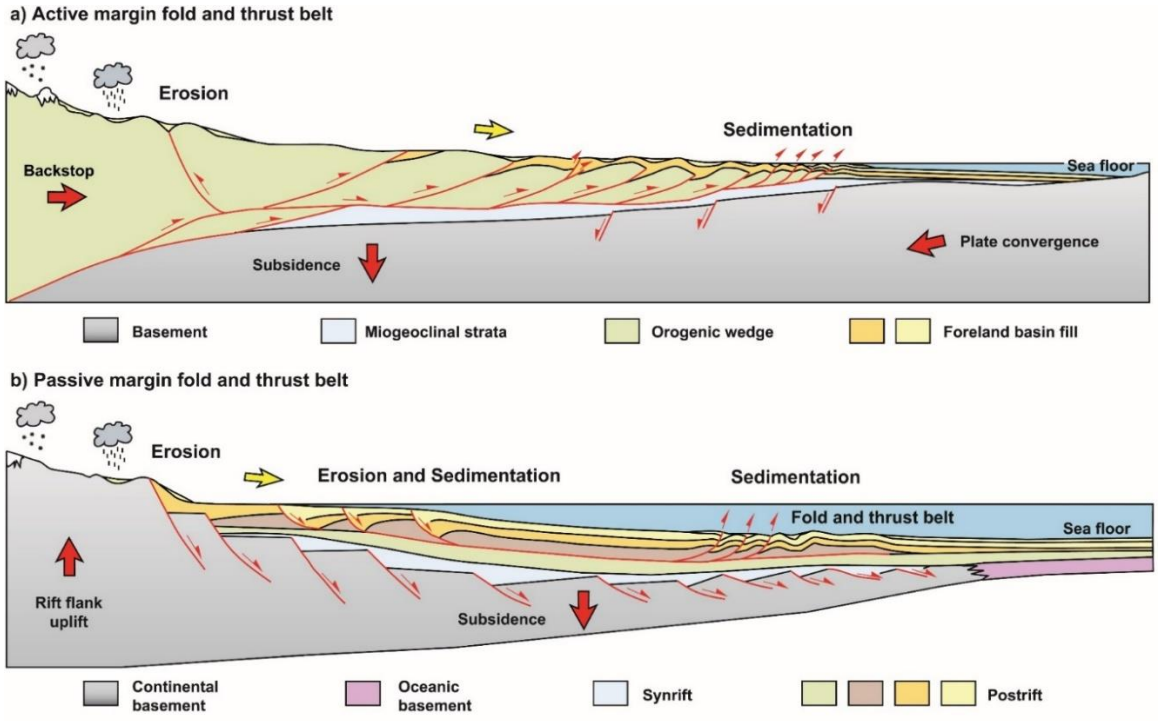

Figure 1.1 Conceptual cartoon showing the interaction of synkinematic sedimentation and synkinematic erosion within fold-thrust belts induced by (a) plate convergence at an active margin and (b) gravitational failure at a passive margin, after Wu and McClay (2011).

From the 1970s onwards, largely through the use of marine 2D reflection data, information on accretionary wedges in subduction zones emerged, revealing that these consist of thrust systems with close relation to onshore FTBs (e.g., Davis et al., 1983; Dahlen et al., 1984). Continuing study of accretionary wedge systems, such as Nankai, the Lesser Antilles, Barbados, Sumatra and Makran (e.g., Westbrook et al., 1982; White, 1982; White and Louden, 1982; Platt et al., 1985; Moore and Silver, 1987; Westbrook et al., 1988; Moore et al., 1990; Morgan and Karig, 1995; Moore et al., 2001; Moore and Saffer, 2001; Bangs et al., 2004; Smith et al., 2012; Smith et al., 2013) was motivated in part by the need to predict geohazards including earthquakes, tsunamis and landslides. This confirmed that accretionary systems form a continuum with FTBs in continental collision settings.

Information on a different class of FTB began to emerge in the 1990s, spurred on by petroleum exploration into progressively deeper water on passive continental margins. These passive margin deepwater thrust belts in the toes of gravity-driven linked systems were initially identified on 2D reflection seismic data, later supported by 3D seismic data and exploration drilling. The first published examples came from the US Gulf of Mexico

(e.g., Wu et al., 1990; Weimer and Buffler, 1992; Diegel et al., 1995; Peel et al., 1995; Trudgill et al., 1995; Trudgill et al., 1999; Rowan et al., 2000). Examples from other basins have subsequently been published, e.g. Angola, Niger Delta, Orange Basin, Amazon Fan, Para-Maranhao Basin, Congo Basin, offshore Brazil (Broucke et al., 2004; Cobbold et al., 2004; Rowan et al., 2004; Bilotti and Shaw, 2005; Corredor et al., 2005; Zalan et al., 2005; Granado et al., 2009; Butler and Paton, 2010; de Vera et al., 2010; Morley et al., 2011; Cruciani and Barchi, 2016; Scarselli et al., 2016; Cruciani et al., 2017). As new data emerged, it appeared that gravity-driven FTB systems may develop on every passive margin where a major source of clastic sediments feeds onto a margin that contains an effective décollement.

We note that FTBs may not be limited to a single driving mechanism, instead, they may have components of both plate convergence and gravitational deformation, creating hybrid systems, such as the Makran accretionary prism (Grando and McClay, 2007), and the NW Borneo FTBs (Ingram et al., 2004; Hesse et al., 2009; King et al., 2010a). The recognition of features that can distinguish these processes in geological examples is a basic aim of this thesis (see Section 1.3).

Fold-thrust belts (FTBs) occur worldwide and have long been the focus of research and exploration by generations of structural geologists who have devised a variety of techniques to image, characterize, quantify and model their structural features (Cooper, 2007; Nemcok et al., 2009; Poblet and Lisle, 2011). For instance: (a) Busk and dip domain methods (Busk, 1929); (b) balanced cross-sections (e.g., Chamberlin, 1910; Dahlstrom, 1969; Mitra and Namson, 1989); (c) the Area-depth-strain (ADS) method (Epard and Groshong, 1993; Groshong et al., 2012; Groshong, 2015), and (d) theoretical models of the quantitative relationships between faults and their related fold structures and geometric rules to constrain the subsurface structures using the outcrop data (Suppe, 1983; Jamison, 1987; Mitra, 1990; Suppe and Medwedeff, 1990; Erslev, 1991; Suppe et al., 2004; Shaw et al., 2005) have all advanced our understanding. These techniques have allowed construction, quantification, and validation of admissible and retrodeformable geological sections across individual structures, structural sequences and entire FTBs (see also Poblet and Lisle (2011)).

In addition to this, scaled physical analogue models and numerical models have been built to investigate the brittle/plastic thin-skinned fold-thrust belts, focussing on the effect of

internal, basal and lateral strength, detachment dip, surface slope and topography, and surface processes (erosion and deposition) on the overall thrust belt dynamics and development history. One important group of models involves critical taper theory (see next section). The basic model has been extended to consider the effect of gravitational load leading to foreland flexure, the influence of layer rheology within the deforming wedge, and the effect of variable shapes of the backstop. The theoretical models have been compared with analogue and numerical models and real-world examples (Liu et al., 1992; Byrne et al., 1993; Storti and McClay, 1995b; Strayer et al., 2001; Marques and Cobbold, 2002; Koyi and Vendeville, 2003; Lohrmann et al., 2003; Smit et al., 2003; Ellis et al., 2004; McClay et al., 2004; Buiter et al., 2006; Marques and Cobbold, 2006; Schreurs et al., 2006; Simpson, 2006; Selzer et al., 2007; Stockmal, 2007; Selzer et al., 2008; Simpson, 2009; Braun and Yamato, 2010; Cruz et al., 2010; Simpson, 2010b; Simpson, 2011; Wu and McClay, 2011; Yamato et al., 2011; Fillon et al., 2012; Nilfouroushan et al., 2012; Ruh et al., 2012; Nilfouroushan et al., 2013; Ruh et al., 2013; Buiter et al., 2016; Schreurs et al., 2016; Zhou et al., 2016; Yang et al., 2017). For reviews of these types of studies see Buiter (2012) and Graveleau et al. (2012).

1.2 **Critical taper theory**

The Critical taper theory was developed for subaerial collisional fold-thrust belts and accretionary wedges (e.g., Davis et al., 1983; Dahlen et al., 1984), and was a major step forward in the understanding of the kinematics and dynamics of FTBs. It considers the mechanics of thin-skinned FTBs analogous to a wedge of snow, sand or soil in front of a moving bulldozer at the verge of compressional failure throughout (Davis et al., 1983; Dahlen, 1984; Dahlen et al., 1984; Dahlen, 1990). The material within the wedge deforms until a critical taper is attained, after that, it will grow self similarly, maintaining its critical taper as additional material is accreted to the toe.

The wedge taper, defined as the sum of surface slope α and basal dip β (*Figure 1.2b*), is a function of the relative strength of the wedge interior and the basal décollement, the weaker the basal décollement and/or the stronger the wedge material, the narrower the wedge taper. The wedge strength is defined by coefficients of friction and fluid-pressure ratios for both the internally deforming wedge and its basal décollement. Davis et al. (1983) derived the equation for calculating the critical taper angle from force equilibrium

on a wedge. An enhancement of the critical-taper equation, with cohesion incorporated, was derived by Dahlen (1990) and is given as

$$\alpha + \beta \approx \frac{(1 - \rho_w/\rho)\beta + \mu_b(1 - \lambda_b) - \frac{S_b}{\rho g H}}{(1 - \rho_w/\rho) + 2(1 - \lambda)\left(\frac{\sin\varphi}{1} - \sin\varphi\right) - \frac{S}{\rho g H}} \quad (1\text{-}1)$$

where ρ is the bulk density of the wedge material; ρ_w is the density of seawater (in a submarine wedge case); λ and λ_b are the fluid-pressure ratio (Hubbert and Rubey, 1959) for the wedge and the basal detachment; S_b and C are the cohesive strengths of the basal detachment and the wedge material, respectively; g is the gravitational acceleration constant; H is the wedge thickness; and μ_b is the coefficient of basal sliding friction.

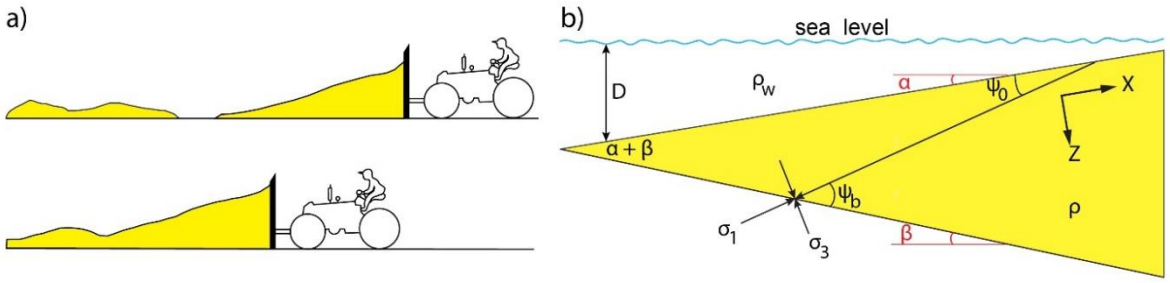

Figure 1.2 Cross-section through a wedge with a *critical taper angle* α+β. ψ_b *is the angle between the maximum compressive stress* σ_1 *and the base of the wedge,* ψ_0 *the angle between* σ_1 *and the top of the wedge,* θ_f *the dip angle of forward thrusts with the base of the wedge,* θ_b *the dip angle of backward thrusts with the base of the wedge, ρ wedge density,* ρ_w *water density, and* D *local water depth. After Dahlen (1984).*

This solution is a small-angle approximation, $\alpha \ll 1, \beta \ll 1, \sin\alpha \approx \alpha, \sin\beta \approx \beta$. It is largely valid for all thin-skinned wedges of geological interest (Dahlen, 1990).

A more extensively applicable non-cohesive Coulomb wedge solution was established by Dahlen (1984). The equations to calculate critical taper value are derived from stress equilibrium, the Coulomb criterion, and the boundary conditions of a shear free top and a prescribed friction on the base:

$$\alpha + \beta = \psi_b - \psi_0 \quad (1\text{-}2)$$

where ψ_b and ψ_0 are denoted as the angles between the maximum principal compressive stress and base and top of the wedge, respectively (*Figure 1.2*). Based on a simple analysis

of triangle geometry, Equation 1-2 is obviously a precise critical taper equation for non-cohesive Coulomb wedge with homogeneous material.

$$\psi_b = \frac{1}{2}\arcsin\left(\frac{\sin\varphi'_b}{\sin\varphi}\right) - \frac{1}{2}\Phi'_b \tag{1-3}$$

$$\psi_0 = \frac{1}{2}\arcsin\left(\frac{\sin\alpha'}{\sin\Phi}\right) - \frac{1}{2}\alpha' \tag{1-4}$$

φ'_b is the effective basal friction angle defined by

$$\varphi'_b = \arctan\left[\mu_b\left(\frac{1-\lambda_b}{1-\lambda}\right)\right] \tag{1-5}$$

The quantity α' is a modified surface slope angle given by

$$\alpha' = \arctan\left[\left(\frac{1-\rho_w/\rho}{1-\lambda}\right)\tan\alpha\right] \tag{1-6}$$

The generalized pore fluid factor with hydrostatic pressure incorporated for submarine cases are as follow:

$$\lambda = \frac{P - \rho_w g D}{\sigma_z - \rho_w g D} \tag{1-7}$$

$$\lambda_b = \frac{P_b - \rho_w g D}{\sigma_z - \rho_w g D} \tag{1-8}$$

P is pressure, P_b pore fluid pressure at the basal detachment, D the local water depth for submarine wedges.

The exact solution provides the minimum and maximum taper angles for a given range of rock properties (Dahlen, 1984).The area enclosed by the maximum and minimum critical tapers is the stable area (*Figure 1.3*). If a wedge with a given basal slope exhibits a surface angle below the minimum critical taper value, then the wedge is subcritical. It has to deform internally to attain the minimal critical taper, usually through thrusting (including out-of-sequence thrusting), to steepen the wedge surface slope. A wedge within the stable area will slide stably along the basal décollement and incorporate new material at its front as long as the basal friction is unchanged, leading to a reduction of the surface slope. If a wedge with a fixed basal dip has a surface angle above the maximum critical angle, it is supercritical; it fails by normal faulting to flatten the wedge until it reaches the stable area (*Figure 1.3*).

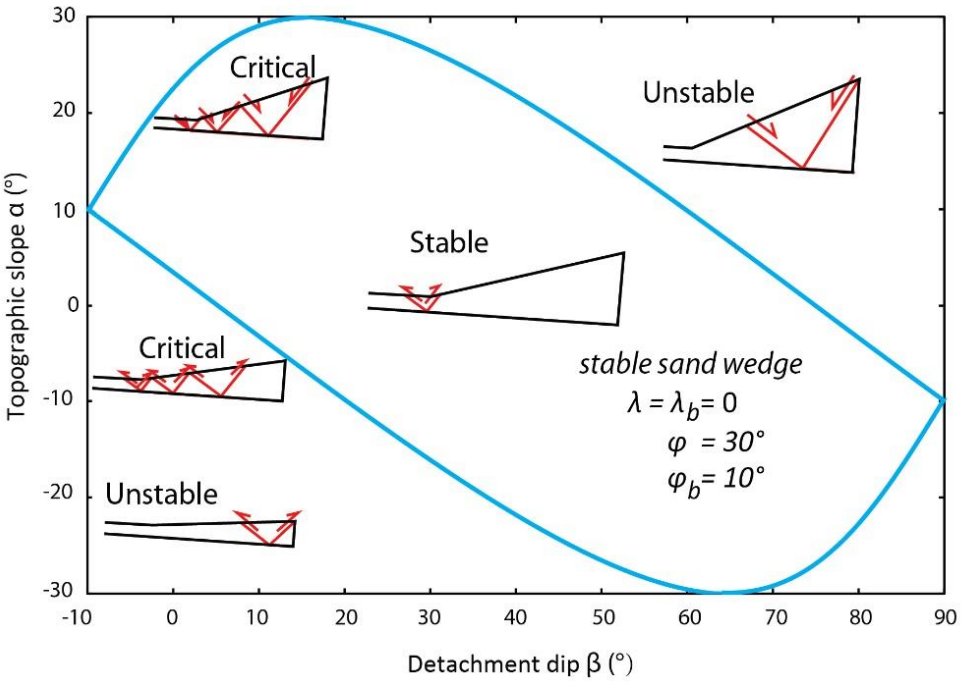

Figure 1.3 The mechanical states of a thrust wedge defined by the critical taper theory (Davis et al., 1983; Dahlen, 1984), after Cubas et al. (2016).

The critical taper theory for a Coulomb wedge has been very successful in explaining the first-order geometry of convergent margin thin-skinned fold-thrust belts (Davis et al., 1983; Dahlen, 1984; Dahlen et al., 1984; Platt, 1986; Zhao et al., 1986; Lallemand and Le Pichon, 1987; Woodward, 1987; Dahlen, 1990; Bombolakis, 1994; Braathen et al., 1999; Mouthereau et al., 2006; Suppe, 2007; Fagereng, 2011; von Hagke et al., 2014) and gravity-driven fold thrust belts mostly on passive margins (Bilotti and Shaw, 2005; Mourgues et al., 2014).

1.3 Questions and aims of the thesis

Although fold-thrust belts are well understood and have been extensively investigated (Dahlen, 1990; Rowan et al., 2004; Morley et al., 2011; Poblet and Lisle, 2011; Buiter, 2012; Graveleau et al., 2012), there are still many significant aspects that have not been examined in detail.

1) The specific interactions between the various structural elements during the kinematic growth of a fold-thrust belt, such as the overall taper angle, wedge width and height, fault position, deformation front position, fault dip, and wedge movement. These are of critical importance to understanding how the fold-thrust belt

system self-organizes internally in response to frontal accretion and tectonic shortening.

2) The activity and interaction of individual thrust faults in an evolving fold-thrust belt, such as the temporal variation in fault slip rate (e.g., Cowie et al., 2012; Gunderson et al., 2013; Bergen et al., 2017), fault displacement (e.g., Koyi et al., 2000; Sun et al., 2016) and fault dip (e.g., Buiter et al., 2006; Selzer et al., 2007; Buiter et al., 2016), and their relationships. The changes in slip rate with time and interaction between faults are also important for the general understanding of fault system development and for hazard assessment.
3) The accuracy and precision of the conventional balancing methods for calculation of shortening. Specifically, the role of regional slope in the area balancing method. The conventional area balancing method uses a single regional slope, usually parallel to the basal detachment, to restore a deformed section to an initial rectangular shape (Chamberlin, 1910; Dahlstrom, 1969; Hossack, 1979; Mitra and Namson, 1989). However, most fold-thrust belts exhibit a wedge or trapezium shape in cross-section, thinning towards the foreland. This violates the assumptions in many existing restorations, and a new alternative solution is needed to better estimate shortening with the effect of regional slope included.
4) Whether the driving mechanism for formation of a fold-thrust belt ultimately controls its structure and development, i.e., are gravity-driven fold-thrust belts basically the same as the FTBs driven by plate convergence or are there fundamental differences? This has to be examined in the form of both detailed studies of individual fold-thrust belts (here we examine the structural properties, structural development and tectonic history of the Northwest Borneo fold-thrust belt system, a potential hybrid system, in order to determine its tectonic origin) and by compilation and comparison of multiple examples.

To address these questions, the following objectives were set for the research within this thesis: (1) construct 2D finite element models (FEM) with Abaqus 6.14 to investigate the dynamic growth of a simple fold-thrust belt that includes internal deformation, overall growth and frontal accretion (Chapters 2 and 3), (2) develop a robust tool to perform more accurate area balancing restoration of fold-thrust belts with various regional slopes (Chapter 4), (3) interpret the geometry, structures and tectonic history of the NW Borneo fold-thrust belt system, and resolve the debate on its driving mechanism (Chapter 5), (4)

explore the similarities and differences between fold-thrust belts induced by plate convergence, gravitational failure or a combination of the two (Chapter 6).

1.4 Study areas

Within this thesis, multiple examples of fold-thrust belt are used to address the questions

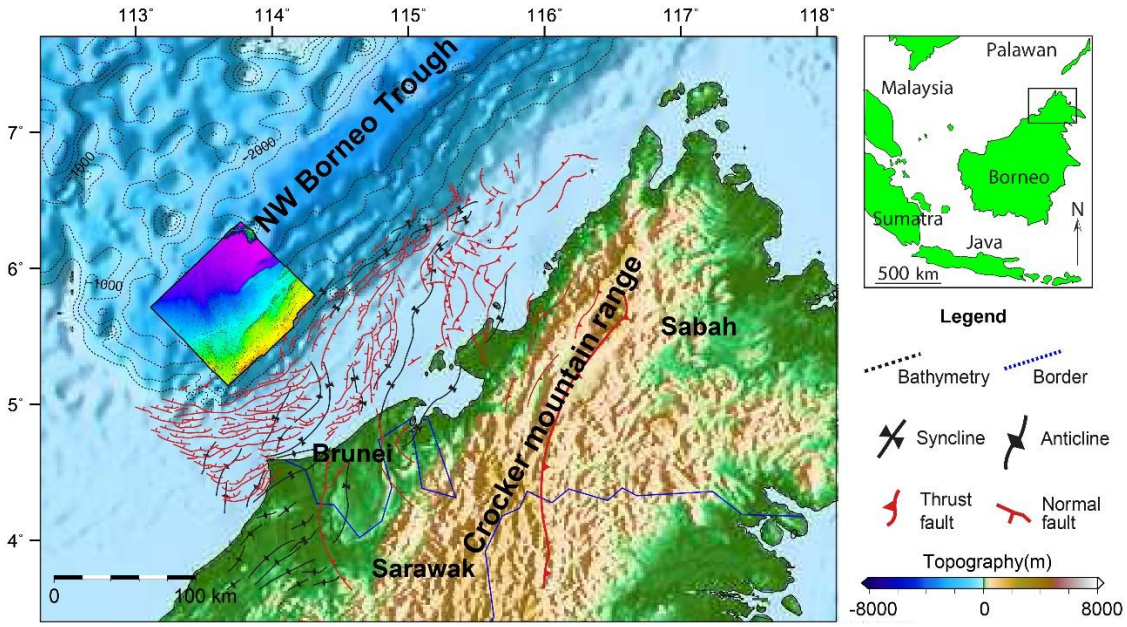

Figure 1.4 Regional map of NW Borneo and the NW Borneo margin and trough, showing the key tectonic elements of the study area, bathymetry and topography, and location of the 3D seismic data, after Morley (2009). Bathymetric contours are 500 m intervals. Inset shows regional setting. The colored box of the 3D data area is a seafloor map colored with depth in two way travel time (TWT), with purple indicating deep depths to yellow indicating shallow depths.

posed above. However, the continental shelf and slope area of NW Borneo, lying offshore Brunei and the Sabah and Sarawak provinces of Malaysia (*Figure 1.4a*) (James, 1984; Levell, 1987; Hinz et al., 1989; Sandal, 1996; Ingram et al., 2004; Morley et al., 2008; Hesse et al., 2009; Morley, 2009a; Hesse et al., 2010b; Morley et al., 2014) is used as a primary study area. This example has unresolved tectonic origin, with possible contributions from both gravity and plate convergence to its FTB development, and good quality seismic reflection data and borehole constraints are available. For the wider compilation of FTBs to explore the differences and similarities between gravity and plate convergence drivers, the following example margins are used: the Orange basin and

passive margin, Namibia; the Para-Maranhao basin and passive margin, Brazil; the Amazon fan and passive margin, Brazil; the Niger delta and passive margin, Nigeria; the Nankai prism and subduction margin, Japan; the Hikurangi prism and subduction margin, New Zealand; the western Makran outer prism and subduction zone, Iran; and the NW Borneo margin, Brunei. This set provides a number of end member examples with clear gravity-driven control (Orange, Para-Maranhao, Amazon, Niger), two end member plate convergence/subduction zone examples (Nankai, Hikurangi), and two examples with possible contributions from both gravity and convergence, each with one likely to be dominant but potentially changing through time (NW Borneo, Makran). In addition, the results are compared with other FTB examples from the published literature.

A more complete tectonic and stratigraphic background of the NW Borneo margin is given in Chapter 5, but a brief summary is provided here. The shelf and slope consist of marine clastic sediments of Middle Miocene to Holocene age, which locally attain thicknesses in excess of 10 km (Morley, 2007b; Morley, 2009b; Morley, 2009a) (Hess et al., 2009). The shelf sequence is deformed with both extensional and compressional structures, including kilometre-scale, syn-sedimentary normal faults (growth faults), shale diapirs, thrusts and inversion-related anticlines (Sandal, 1996; Morley et al., 2003; Van Rensbergen and Morley, 2003; Morley et al., 2008; King et al., 2009).The slope is affected by thin-skinned folding and thrusting (James, 1984; Levell, 1987; Sandal, 1996; Ingram et al., 2004; Franke et al., 2008; Hesse et al., 2009; Morley, 2009b; Morley, 2009a; Hesse et al., 2010b; Morley et al., 2014). We herein refer to this general domain as the NBFB (Northwest Borneo Fold-Thrust Belt). The NBFB extends the length of Sabah and Brunei and terminates offshore Sarawak (*Figure 1.4a*). Previous work based on 2D and 3D seismic data has given a general characterisation of the internal structure of the NBFB (James, 1984; Hinz and Schluter, 1985; Hinz et al., 1989; Sandal, 1996; Schlüter et al., 1996; Morley, 2009a). The imbricate thrusts of the NBFB sole out at depth into one or two décollements (Ingram et al., 2004; Morley, 2007b; Franke et al., 2008; Hesse et al., 2009, 2010b).

Whether there is collision, regional compression or subduction in the present day on the NW Borneo margin has been long debated (Sapin et al., 2013). Therefore possible mechanisms for generating the Miocene to Recent fold-thrust belt are as follows: (1) active subduction, possibly driven by far-field stresses from the Australia–Indonesia

collision zone, deformation around Sulawesi, or from collisional events in the Phillippines (e.g., Hinz et al., 1989; Simons et al., 2007; Franke et al., 2008; Cullen, 2010; Sapin et al., 2013) (2) gravity-driven deformation (e.g., Hazebroek and Tan, 1993; Hall and Morley, 2004; Hall et al., 2008; Hall, 2013); or (3) a combination of 1 and 2 (e.g., Ingram et al., 2004; Morley, 2007b; Hesse et al., 2009; King et al., 2010a).To resolve this debate, detailed examination of fault and fold activity in relation to its potential driving mechanism is required.

1.5 Techniques used

As the main body of this thesis consists of published and planned papers, I provide here a brief discussion of the range of techniques used in these papers/chapters.

1.5.1 Mechanical analysis

Critical taper theory explains the first-order geometry of a fold-thrust belt as a function of the relative strength within the wedge interior and along the basal décollement (Davis et al., 1983; Dahlen et al., 1984). Here the mechanical analysis is performed using the Critical taper theory to predict the fluid pressure ratio for the internal material and basal décollement (λ and λ_b) of the fold-thrust belts from numerical modelling and real-world regions. The results are then compared with other published data (e.g., Davis et al., 1983; Dahlen, 1984; Bilotti and Shaw, 2005; Morley, 2007b; Suppe, 2007, 2014).

1.5.2 Numerical modelling

Numerical modelling is a robust technique to investigate the long-term structural development and dynamic evolution of thin-skinned fold-thrust belts (Yamada et al., 2006; Buiter, 2012). A main characteristic of fold-thrust belts is the occurrence of faults, which represent brittle failure of the deforming rocks (Ruh, 2013). As most numerical codes model continuous deformation, the methods used must be able to localise deformation to develop shear bands depending on a predefined failure criterion in order to model brittle wedges (Mohr-Coulomb failure criterion in this research). The numerical solution used in this study to simulate the fold-thrust belts is the Finite Element Method that provides solutions of various problems by approximating an overall equation by separating it into many simple element equations (Zienkiewicz and Taylor, 1991; Ruh,

2013). To simulate deformation in fold-and-thrust belts, models are based on the continuum equations. The FEM is the most applied technique for modelling intermediate to large, lithospheric-scale structural deformation induced by plate convergence or gravitational failure (e.g., Beaumont et al., 1992; Willett et al., 1993; Ellis et al., 2004; Selzer et al., 2008; Ruh et al., 2012; Tuitt et al., 2012; Yang et al., 2017). Details of the model set-up used are described in Chapter 2.

1.5.3 2D/3D Seismic interpretation

The observations of FTBs in this thesis are made from the interpretation of 2D and 3D seismic reflection surveys. To link the reflection data (in TWTT) to geometry, it is necessary to convert the images to depth if reliable velocity data are available.

Ten thousand square kilometres of 3D seismic datasets acquired and processed by Petroleum Geo-Services (PGS) in 2000 and 2001 across the deepwater margin of Brunei were used as a primary dataset (*Figure 1.4a*). This is the same dataset used by (Morley, 2009b; Morley, 2009a). Seismic interpretation including sedimentary horizons, unconformities, faults, folds and associated surface mapping were conducted using Petrel 2014. For quantitative structural analysis, we measured fault displacement, dip, and spacing, and strain across the fold-thrust belt using Midland Valley 2D Move software.

Depth conversion

The V_0-K method (Marsden, 1992) was used to depth convert the seismic data as explained below

$$V_i = V_0 + K*Z \quad (1\text{-}9)$$

$$V_i = dz/dt \quad (1\text{-}10)$$

The first formula states that the instantaneous velocity V_i increases linearly with depth Z; V_0, is a constant and K is the rate of velocity increase compaction factor (Marsden, 1992). The second equation states that the instantaneous velocity is the rate of change of depth with time. Details of velocity data used are provided in Chapter 5.

Structural restoration

Bed length measurement, sequential restoration, and conventional area balancing methods are used to perform structural restoration in order to quantify deformation

across the FTBs from the Northwest Borneo margin (primary study area) and other example FTBs. In addition, two new, simple, quantitative area balancing solutions are developed to test the role of regional slope in shortening estimates and associated uncertainties, such as bed length changes. In this research, structural restoration is performed primarily using 2D Move.

1.5.4 Deformation measurements

Deformation for fault structures is measured as the fault displacement that is actual fault slip in depth-converted seismic sections or fault heave in time sections. For anticlinal structures, strain is determined as the difference between the deformed and restored bed length, which is mainly achieved using structural restoration techniques described in section 1.5.31.5.3 and in relevant Chapters. In a purely or partly gravity-driven system, strain is quantified for the extension in the upslope region and contraction in the downslope region (see also Butler and Paton (2010)) to distinguish the contribution of different driving mechanisms.

1.5.5 Deformation timing and history

To evaluate the deformation history (relative timing and location) within a fold-thrust belt and relative to associated extensional zones, we (1) map the stratigraphic units in each cross-section; (2) identify the deformation-related sedimentary successions, i.e., basement, pre-kinematic, syn-kinematic/growth and post-kinematic, based on the relationship between the structures (thrusts, folds, normal faults, uplift/subsidence) and sedimentary sequences (i.e., presence or absence of growth strata, displacement/deformation of sequences); (3) group the different types of fault, i.e., normal fault, basinward-vergent thrust fault and landward-vergent thrust fault, detachment/décollement fault; (4) analyse the timing of folding and faulting of individual structures in a system; (6) quantify the amount of contraction, extension or both as a proxy for strain distribution and partitioning in cross sections with well-imaged stratigraphy; and (7) evaluate deformation initiation and propagation, timing and patterns.

1.6 Outline of the thesis

This PhD thesis presents results obtained from numerical modelling, 2D/3D seismic interpretation, tectono-stratigraphic mapping, structural restoration, strain measurement, deformation quantification and mechanical analysis. Numerical models help to understand the kinematic growth of fold-thrust belts and the tempo-spatial interactions between multiple structural features and parameters, i.e. taper angle, width and height of an FTB, fault position, slip rate and dip, and deformation front position. Seismic interpretation and structural analysis help to investigate the geometry, structures, strain distribution and deformation history of real-world fold-thrust belts, including the similarities and differences between FTBs induced by plate convergence, gravitational failure or a combination of two.

Chapter 1 introduces the research background, questions and aims of this thesis. The key theory and some methods are explained, such as Critical taper theory, 2D/3D seismic interpretation, depth conversion, structural restoration, strain measurement, and deformation quantification. Further methodology details are provided in each subsequent chapter.

Chapter 2 investigates the dynamic growth of a simple fold-thrust belt that includes internal deformation and frontal accretion at the wedge toe by using a visco-elasto-plastic Finite Element numerical model. Results are compared to the Critical wedge theory, analogue sandbox models of brittle wedges and natural examples. The episodic growth characteristics of fold-thrust belts and the active interaction between various structural parameters are highlighted and discussed. *This chapter is published as: Yang, X., Peel, F.J., Sanderson, D.J., and McNeill, L.C., 2017, Episodic growth of fold-thrust belts: Insights from Finite Element Modelling; Journal of Structural Geology, 102, 113-129, doi.org/10.1016/j.jsg.2017.07.012.*

Chapter 3 presents new insights on the timing of fault activity and interactions in an evolving fold-thrust belt inferred from numerical modelling. The fault displacement, strain rate and fault dips are tracked and examined to understand the role of individual faults (activity, growth, propagation) and the interplay between multiple faults during the fold-thrust belt development. This chapter was submitted to Geophysical Journal

International, but was rejected and is being modified for resubmission, with some additional models and discussion of results.

Chapter 4 analysed the principles, assumptions and deficiencies of conventional structural restoration techniques, i.e., the area balancing method and bed length measurement (Chamberlin, 1910; Dahlstrom, 1969; Mitra and Namson, 1989). We develop new, simple, quantitative solutions using area balancing that restores a thrust wedge to a trapezium. The trapezium has two vertical, parallel sides representing the extent of the deformed zone, with the lower edge representing the dip of the detachment and the upper edge representing the regional slope of a sediment wedge. Thus, the methods are more appropriate for accretionary wedges and other FTBs. The results are tested against sandbox models of well constrained dimensions and natural examples of fold-thrust belts (the Hikurangi accretionary wedge and NW Borneo margin FTB) using a range of input parameters to evaluate the role of regional slope and associated uncertainties in shortening estimates.

Chapter 5 investigates the nature, structural development and tectonic history of the Northwest Borneo fold-thrust belt (NBFB). This examines the along-strike variation in structural styles and its controlling factors, the behaviour of faults and folds (growth and propagation), history of fault activity, strain partitioning between folds and thrusts, and the décollement geometry and properties. This was conducted by 2D/3D seismic interpretation of a 3D seismic volume from offshore Brunei, structural style classification, structural reconstruction, strain measurement, and mechanical analysis.

Chapter 6 compares natural examples of FTBs from gravity-driven and plate-convergence –driven systems and those driven by a combination, to document similarities and differences between them. It investigates whether the difference in tectonic setting and hence driving mechanism (and resulting different boundary conditions) may give rise to differences in structure, behaviour and evolution by examining the fold and thrust geometries, studying the interaction between structures involved in the system, i.e. folds, faults and basal detachment, evaluating the timing of deformation, quantifying the strain distribution in the system, and exploring the tectonic and mechanical control on these structural elements.

Chapter 7 summarises the results of Chapters 2-6, addressing the questions posed in the Introduction (Chapter 1, section 1.3), and discusses potential future work.

Chapter 2 Episodic growth of fold-thrust belts: insights from Finite Element Modelling

This chapter is a reproduction of an article published in the Journal of Structural Geology in 2017 - *Yang, X., Peel, F.J., Sanderson, D.J., and McNeill, L.C., 2017, Episodic growth of fold-thrust belts: Insights from Finite Element Modelling; Journal of Structural Geology, 102, 113-129, doi.org/10.1016/j.jsg.2017.07.012.*

Modelled developed, data collected, analysed and written-up by Xiaodong Yang with feedback, discussion and editorial assistance from Frank Peel, David Sanderson, Lisa McNeill.

Episodic growth of fold-thrust belts: insights from Finite Element Modelling

Xiaodong YANG [a,*], Frank J. PEEL [b,c], David J. SANDERSON [a,d], Lisa C. MCNEILL [a]

[a] Ocean and Earth Science, National Oceanography Centre, Southampton, University of Southampton, Southampton, SO14 3ZH, UK.

[b] *Department* of *Earth Science* and Engineering, Imperial College London, London, SW7 2BP, UK.

[c] Bureau of Economic Geology, The University of Texas at Austin, Austin, TX, USA.

[d] Engineering and Environment, University of Southampton, Southampton, SO17 1BJ, UK.

Abstract

The sequential development of a fold-thrust belt was investigated using 2D Finite Element Modelling (FEM). The new model results show that a thrust system is typically composed of three distinct regions: the thrust wedge, pre-wedge, and undeformed region. The thrust wedge involves growth that repeats episodically and cyclically. A cycle of wedge building starts as frontal accretion occurs, which is accompanied by a rapid increase in wedge width reducing the taper angle below critical. In response to this, the wedge interior (tracked here by the 50 m displacement position) rapidly propagates forwards into a region of incipient folding. The taper angle progressively increases until it obtains a constant apparent critical value (~10°). During this period, the wedge experiences significant shortening after a new thrust initiates at the failure front, leading to a decrease in wedge width. Successive widening of the wedge and subsequent shortening and thrusting maintain a reasonably constant taper angle. The fold-thrust belt evolves cyclically, through a combination of rapid advancement of the wedge and subsequent gradual, slow wedge growth. The new model results also highlights that there is clear, although minor, deformation (0-10 m horizontal displacement) in front of the thrust wedge.

2.1 Introduction

The Coulomb Wedge Model (CWM) has been very successful in describing the mechanics of orogenic and subduction-related thin-skinned fold-thrust belts from around the world (Davis et al., 1983; Dahlen, 1984; Dahlen et al., 1984; Platt, 1986; Zhao et al., 1986; Lallemand and Le Pichon, 1987; Woodward, 1987; Dahlen, 1990; Braathen et al., 1999; Mouthereau et al., 2006; Suppe, 2007; Fagereng, 2011; von Hagke et al., 2014; Sun et al., 2016). According to the model, the thrust belt is analogous to a wedge of soil or snow in front of a moving bulldozer, and the material within the wedge deforms until it develops a critical taper, and basal shear and wedge translation can occur (internal and basal shear stresses are balanced in critical state), after which it grows self-similarly as additional material is accreted at the toe (Davis et al., 1983; Dahlen, 1984; Dahlen et al., 1984; Dahlen, 1990). The theory can be used to understand the effects of internal and basal strength (Mulugeta, 1988; Willett, 1992; Burbidge and Braun, 2002; Lohrmann et al., 2003; Simpson, 2009), dip of detachment (Davis et al., 1983; Koyi and Vendeville, 2003; Smit et al., 2003), surface slope and topography (Marques and Cobbold, 2002, 2006; Sun et al., 2016), lateral friction (Zhou et al., 2016), surface processes, i.e., erosion and sedimentation (Storti and McClay, 1995a; Hoth et al., 2006; Simpson, 2006; Stockmal, 2007; Cruz et al., 2010; Simpson, 2010a; Wu and McClay, 2011; Fillon et al., 2012), and the rheology of single and multiple detachments (Ruh et al., 2012) on the growth of fold-thrust belts. For a review see Buiter (2012) and Graveleau et al. (2012).

Coulomb Wedge Model only provides a static view of the thrust wedge, assuming constant conditions with the wedge maintained at Coulomb failure throughout (Chapple, 1978; Davis et al., 1983). A simple Coulomb Wedge retains a constant taper as it moves without addition of material being encountered (*Figure 2.1a*, see Supplementary Material). In reality, as a wedge grows, new material is added, most commonly at the toe (*Figure 2.1b*), with the thrust wedge accreting in a piggyback style during its forward advance (Mulugeta and Koyi, 1992). Accommodated by nucleation of new thrusts in front of the wedge, accretion of sediments thickens the wedge and raises the surface topography (Platt, 1986; Mulugeta and Koyi, 1992; Gutscher et al., 1996; Burbidge and Braun, 2002; McClay et al., 2004; Bigi et al., 2010), rendering the wedge unstable. A stable geometry can be regained by internal deformation, most commonly involving shortening, imbricating and folding (*Figure 2.1c*),(Davis et al., 1983; Lallemand and Le Pichon, 1987;

Burbidge and Braun, 2002) As real world thrust wedges develop, they do so by the addition of discrete, often large, thrust sheets (*Figure 2.1d*). Evolution of the wedge taper angle occurs by progressive internal deformation and accretion of new units to the wedge front (*Figure 2.1c*). The initiation of discrete faults or zones of deformation produces an episodic development (*Figure 2.1d*), with a change in shape and taper angle as the wedge grows. Accretion of new material into the wedge may not occur at the same time as deformation within the wedge. This behaviour is seen in physical analogues, with the wedge geometry changing as the accretion of imbricate slices builds the wedge forward, thereby lowering the taper to subcritical (Gutscher et al., 1996; Lohrmann et al., 2003). The assumption that thrust wedges constantly exist in a state of critical taper is therefore not sufficient to describe the dynamic evolution of a real thrust wedge.

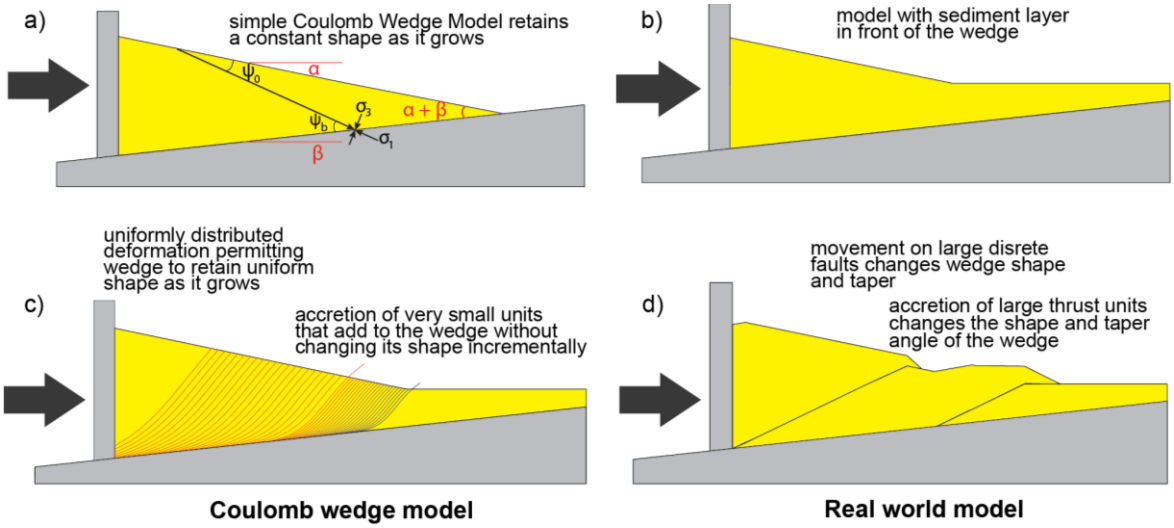

Figure 2.1 Conceptual cartoon illustrating the difference between the theoretical Coulomb wedge model and a real world example. (a) Simple Coulomb Wedge Model (CWM), which retains a constant shape as it moves, α and β are topographic slope and detachment dip, respectively, ψ_b and ψ_0 are the angles between the maximum principal compressive stress σ_1 and base and top of the wedge; (b) Model with sediment layer in front of wedge; (c) Simple Coulomb Model without advance of wedge front; (d) Accretion by imbrication on large discrete thrusts that will change the wedge shape and taper with time.

In natural systems, a number of studies of the growth of fold-thrust belts have been undertaken. Fitz-Diaz et al. (2014) used illite Ar/Ar dating to obtain absolute ages of folds and shear zones, suggesting episodic progression of deformation from west to east in Mexican Fold-Thrust Belt. Through detailed chronostratigraphic study of syn-tectonic sediments, the episodic uplift of mountain ranges (Ji et al., 2008; Lease et al., 2012) and

growth of an individual anticline(Masaferro et al., 1999) have been reported. Studies of the deep-sea turbidites and silicic plutonic sequences revealed the episodic growth of the south-west Alaska convergent margin (Byrne and Fisher, 1987). Though these field-based studies reveal the overall growth pattern of mountain belt and accretionary prism, the quantitative spatial and temporal variations in associated geometric parameters are still poorly resolved. For example, what is the behaviour of wedge material when transported forwards? Is deformation constant or episodic? What are the effects of thrust initiation and frontal accretion on wedge geometry? What happens in front of the wedge when developing a critical taper? How do these different elements correlate with each other during the wedge-building process?

Numerical modelling and scaled analogue experiments with digital image correlation technique can provide insights into the dynamic evolution of deforming wedges because these enable us to simulate the development of a realistic thrust system, and to measure the geometry, stress, and strain at every stage in its growth, which cannot be done for natural examples (Beaumont et al., 1992; Ellis et al., 2004; Adam et al., 2005; Buiter et al., 2006; Simpson, 2006; Yamada et al., 2006; Selzer et al., 2007; Stockmal, 2007; Selzer et al., 2008; Simpson, 2009; Cruz et al., 2010; Simpson, 2010b; Buiter, 2012; Fillon et al., 2012; Ruh et al., 2012; Adam et al., 2013; Ruh et al., 2013; Buiter et al., 2016; Dotare et al., 2016).

This study aims to produce a 2D finite element model (FEM), built with Abaqus 6.14, to investigate the dynamic growth of a simple fold-thrust belt that includes frontal accretion at the wedge toe. This model is used to understand:

(1) How the system propagates at the wedge toe and quantify what happens in front of the thrust wedge.
(2) How the critical taper is achieved in response to wedge accretion, testing this against the theoretical predictions from the CWM (Dahlen, 1984). How the spatial and temporal evolution of different variables can be resolved during the critical-subcritical transition period.
(3) How the thrust system evolves over many cycles of wedge building in terms of internal wedge movement, propagation of displacement front and failure front, and variations in wedge height and width.

2.2 Methods

2.2.1 Brittle rheology and material properties

The wedge is modelled as a mass of homogeneous, cohesive material whose behaviour is visco-elasto-plastic resembling that of dry quartz sand (*Table 2-1*). The material deforms elastically until plastic or viscous yield is reached, after which deformation continues on yield (Buiter et al., 2006). It is therefore equivalent to physical analogue (sandbox) models that themselves constitute scaled models of natural systems. The mechanical parameters assigned to the model are density, Young's modulus, Poisson's ratio, internal friction angle and basal friction angle, Poisson's ratio, gravity, angle of dilation, cohesion and viscosity, with values taken from previous studies(Ellis et al., 2004; Buiter et al., 2006) (see *Table 2-1).* The wedge material deforms elastically at the early stage after loading and shortening, followed by strain hardening prior to failure at peak strength (Lohrmann et al., 2003). Further strain leads to softening until the stable dynamic strength is reached (Lohrmann et al., 2003; Panien et al., 2006). The Drucker-Prager failure criterion is employed as a smooth version of the angular Mohr-Coulomb failure criterion to model the wedge deformation (Buiter, 2012; Tuitt et al., 2012). Localised failure in the form of shear bands occurs close to the peak strength at maximum dilation rates, whereas the dynamic stable state is associated with decreased dilation rates (Buiter et al., 2016). The dynamic stable state is a stage characterised by a dynamically constant shear load and steadily increasing shear strain. Strain softening is simulated by a linear decrease from a peak internal friction angle to a stable frictional angle over a finite strain interval of 0.5-1.0 (finite strain is total accumulated effective strain as measured by the square root of the second invariant of the strain tensor) (Buiter et al., 2006). A frictional contact is implemented between the wedge and wall and base. Gravity is applied as a distributed load on the wedge material. Since the code models frictional behaviour using a Coulomb yield criterion with non-associated flow law, frictional volumetric changes (or dilation) are not included in the model.

Discrete faulting (movement on a fault surface) cannot be modelled as the solution does not support the development of discontinuities in the mesh. The FE solution, together with the strain-softening rheology, results in the development of narrow shear zones which effectively behave as discrete faults at a macroscopic scale. The computational

mesh grids are sufficiently fine to model movement on these zones, with elements up to a maximum aspect ratio of ~15. Re-meshing was tried, but did not significantly improve the modelling of these shear bands.

Table 2-1 Material properties used in the wedge models

Material	D (kg m^{-3})	φ_{peak} (°)	φ_{stable} (°)	E (MPa)	ν	G ($m*s^{-2}$)	ψ (°)	C （Pa）	η (Pa s)	μ_b	μ_s
Wedge	1560	36	31	5e10	0.25	10	0.1	10	5e4	0.3	0.075
Basement and two walls	2800			5e12	0.25		0.1				

D=Density, φ_{peak}=Angle of internal friction at peak strength, φ_{stable}=Angle of internal friction at stable strength, E=Young's modulus, v=Poisson's ratio, G=Gravitational acceleration, ψ=Angle of dilation, C=Cohesion, η=Viscosity, μ_b=coefficient of basal friction, μ_s=coefficient of side friction.

2.2.2 Thrust Belt Model

The main model was set up 1) to allow building of a critically tapered wedge from the horizontal layers and then 2) to investigate how the subsequent thrust wedge develops and accretes material. The spatial positions within the wedge and associated deformation parameters are specified in relation to a 2D coordinate system which has a fixed zero position at the initial base of the vertical wall (*Figure 2.2a*). Key geometrical parameters of the thrust system are systematically measured and analysed in order to investigate the quantitative growth of the fold-thrust belt (*Figure 2.2b&c*). These are:

a) *Displacement front* - the point of zero displacement along the detachment which shows how far shortening is transmitted across the deforming wedge along its base, the parameter positions tracked for analysis are all horizontal displacements;

b) *50 m displacement position*–we constantly tracked the point at which a fixed and relatively small displacement (50 m) is reached along the basal detachment. This is used to track the development of displacement behind the displacement front (i.e., in front of the main thrust wedge). The selection of a 50 m-offset threshold is somewhat arbitrary, but it (1) lies within the range of displacements accumulated

during a cycle; (2) the point of 50 m displacement is consistently ahead of the new frontal thrust, but it sufficiently far from the displacement front to illustrate the cyclic changes; and (3) ends up within the strain gradient that localises into the next frontal thrust. Following the position of a fixed amount of displacement provides a useful insight into the cyclic evolution of the thrust system and a valuable and instructive marker of minor deformation;

c) *Failure front* – the point at which the current frontal thrust fault roots into the detachment. This is of particular importance for understanding the initiation and forward advancement of a new thrust fault (*Figure 2.2b*);

d) *Surface deformation front* – the point of zero displacement at the surface;

e) *Inboard corner of the wedge* - used to examine how a critical taper is developed and reached (*Figure 2.2b*);

f) *Taper angle* - determined by the slope of the straight line from the deformation front d to the inboard corner of the wedge e;

g) *Surface slope* - determined as the best fitting line enveloping the thrust wedge (i.e., Bigi et al., 2010; Schreurs et al., 2016; see also *Figure 2.2c*);

h) *Wedge height* - the highest elevation of the top of thrust wedge (*Figure 2.2c*);

i) *Wedge width* - measured as the horizontal distance from the deformation front d to the moving left-hand wall.

The locations of the measured parameters are shown graphically by their x-coordinates, measured from the initial left hand side of the model (*Figure 2.2*).

2.2.3 Model set-up

Our model is a two-dimensional representation of a propagating thrust system. As a simple test of the model and its parameters, we reproduced a simple experiment of Buiter et al. (2016), in which a wedge of material is moved over a horizontal base with no frontal accretion (i.e., *Figure 2.2a*). The model results are described in the Supplementary Material and demonstrate that Abaqus can model a simple thrust wedge, maintaining its initial taper angle (20°) after 1500 m of translation, in accordance with the CWM (Davis et al., 1983) .

Other model tests (see Appendix A) were used to explore the solution sensitivity to changes in the following parameter values: strain-softening thresholds, material strength, initial wedge thickness and mesh resolution (cell size). The results mainly indicate the strain-softening exerts a first order control on strain localisation, the mesh size determines the width of shear zone while the thickness of the initial model governs the fault spacing.

In this study, we accept the observations describing general thrust system development, and its sensitivity to controlling parameters. These have been established by previous publications, and we take these as a starting point. The model presented in the main body of this paper does not include a full parameter study of the whole system. We focused on a model with parameters similar to Buiter et al. (2006). Our FEM does not include re-meshing, so we present results from the model that remained numerically stable to the largest increment of shortening. We use this to investigate in detail the important aspects of thrust development that are revealed by systematic fine-scale analysis. Our focus was particularly directed at the spatial and temporal variation in the earliest stages of thrust fault propagation, which are revealed by examining the first increments of displacement and strain, particularly in the frontal regions of the developing thrust wedge.

We constructed the main model (*Figure 2.2a*) as a wedge with an initial horizontal surface (i.e. with a subcritical taper). It consists of a mobile left-hand wall, a fixed right-hand wall and base, containing a body of homogenous, isotropic sediment length 10000 m and initial thickness 600 m (*Figure 2.2a*), with passive, initially horizontal marker layers. The size of the FE cell is 25m X 25m, with a total of 9600 cells set up to model the thrust deformation, providing adequate detail/resolution to examine the wedge dynamics. The model thickness of 600 m is chosen to be more realistic for the toe of a real wedge. Abaqus can only handle small-scale deformation: we tested a number of models with various size, and the one with dimension 10000 m x 600 m gives the most geological reasonable results, and allows computation of largest horizontal displacement (3268m). Shortening is modelled by moving the mobile wall from left to right whilst the right wall and base remain fixed. The moving wall is in direct contact with the base, therefore a sharp velocity discontinuity is formed at the left corner (Buiter et al., 2016), which affects the initial development of the thrust wedge. The coefficient of effective friction between the walls and the horizontal layers is 0.075, and the coefficient of friction between the

horizontal layers and base is 0.3. The basal friction should not exceed the internal friction for the existence of Coulomb Wedge, and an even smaller side friction allows the wedge material to move freely along the walls.

We selected this model (including the side friction 0.75 and basal friction 0.3) based on the following requirements:

(1) To generate the geologically reasonable results (looks like the natural examples and experimental models);

(2) To use parameter values based on those used in previous studies (and often remain the same), permitting direct comparison between our results and other studies;

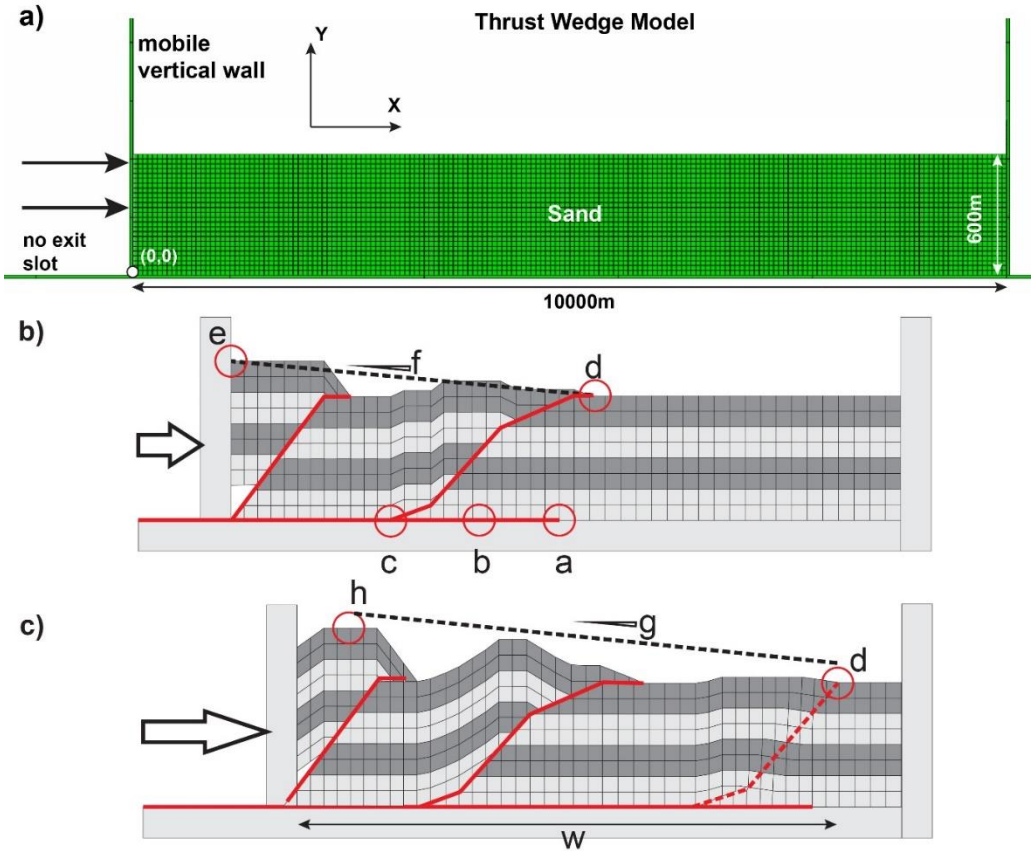

Figure 2.2 Setup of the thrust wedge experiments and illustration of wedge parameters at different shortening periods. (a) Setup of thrust wedge model, a horizontal sand layer with width of 10000 m and thickness of 600 m is shortened by a mobile wall running from left to right, while the base and right wall remain fixed. (b) Schematic illustration of the approach followed for measurements of wedge parameters. a = displacement front, defined as position of 0 m displacement along the detachment, b = 50 m displacement position along the detachment, c = failure front where the frontal thrust roots into the

detachment, d = deformation front (in this case, the frontal thrust tip), e = inboard corner of the wedge, f = overall taper angle determined by the slope of straight line from e to d. (c) Schematic showing the measurements of additional wedge parameters. As further shortening is added, a new fold is formed in front of the existing thrust. A new thrust is about to initiate to break the new fold with its fault tip reaching the wedge surface at the deformation front d. g = surface slope determined as the best fitting line enveloping the thrust wedge (Schreurs et al., 2006), h = height of the thrust wedge, w= wedge width determined by the distance from deformation front d to the moving left hand wall.

(3) To enable computation of the largest displacement, allowing us to derive the maximum value from the simulation.

The system is described by a fixed 2D coordinate system in which the origin (x=0, y=0) is defined as the position at the bottom left corner at the start of model (*Figure 2.2a*).

2.2.4 The role of basal dip

Here we describe and define the initial model setting for the basal fault (basal dip) in order to compare with previous scaled sandbox and numerical experiments (e.g., Ellis et al., 2004; Cruz et al., 2010; Miyakawa et al., 2010; Simpson et al., 2011; Ruh et al., 2012, 2013; Wu and McClay, 2012). The effect of basal dip on the overall wedge shape, as shown by one of the early wedge mechanics papers (Davis et al., 1983), is that an increase in basal dip angle is accompanied by a decrease in surface dip angle and an increase in taper angle. This is true for low values of surface and basal slope, i.e. the minimum critical taper angle is represented by the lower envelope of the two critical taper branches (see also Figure 1.3). Smit et al. (2003) reported a change in deformation style for brittle sand wedges that build above basal dips between 0.75° and 3.0°. A shallow dipping base created a wide wedge with mainly forward thrusts while a slightly steeper base led to a narrower wedge dominated by forward and backward thrusts (Buiter et al., 2012). It appears that the basal dip plays a role in determining the overall wedge taper, structural style and wedge width, but plays a limited role in the sequential development of the fold-thrust belt, though few studies have systematically investigated the thrust behaviour above a varying basal dip (Buiter, 2012).

In this study, the defined horizontal basal dip is therefore thought to have minimal effect

on the examination of thrust wedge growth behaviour.

2.3 Results

After experimentation with a range of input parameters, we ran a number of models, which show very similar features but with some differences observed (see Supplementary Material). Here we describe results for a single model that provided the longest "well-behaved" numerical simulation with no computational problems and fits the requirements described in Section 2.2 above for most feasible parameter values (*Figure 2.3*). The total shortening of the model is 3268 m, with all geometric parameters measured at every 17-67 m of shortening, the exact value being determined by the stepped nature of the numerical solution.

At the final stage of the simulation, six major thrust faults developed (F1 – F6), dividing the model into six imbricate fault blocks (*I*1 to *I*6) and a less deformed footwall block with minor folding (*Figure 2.4*). The first group of faults F1-F3 are located close to the moving left hand wall: they initially develop from the detachment, they are subsequently squeezed and rotated by both the mobile wall and velocity discontinuity at the left corner (Buiter et al., 2016). These form an initial wedge with shortening resulting in 3 closely-spaced thrusts (~200 m apart, see Stage 1 in *Figure 2.3*). In contrast, in the second stage of wedge development, faults F4 to F6 develop and propagate forward away from the model boundary with a wider fault spacing of 940 -1400 m (see Stage 2 in *Figure 2.3*). Two short-cut faults (red dotted lines, *Figure 2.4*) are created within the imbricate blocks *I*4 and *I*6, which lead to connection between F3 and F4, and F5 and F6 (*Figure 2.3*, *Figure 2.4*).

Details of the shear zone grid are shown in *Figure 2.3*. The cell is significantly deformed and elongated along the shear zone and tilted towards the foreland. The geometry of deformed numerical cell is similar to that observed from numerical models and scaled analogue experiments (Ellis et al., 2004; Adam et al., 2005). In contrast, the cells at the region away from the shear zones show little deformation, in accordance with the implemented Mohr-Coulomb failure criterion.

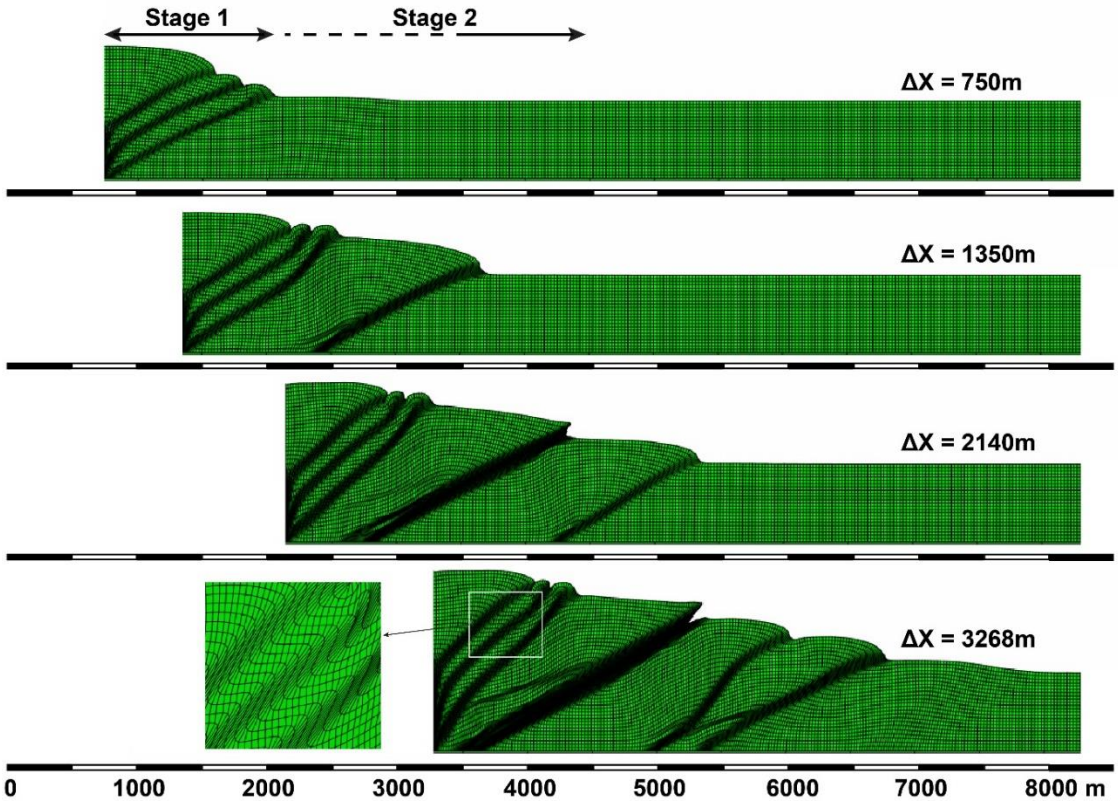

Figure 2.3 Sequential development of the thrust belt model. ΔX indicates the amount of shortening. The enlarged region shows the cells along the shear zone is significantly deformed, elongated and tilted towards the foreland.

The fold-thrust system can be divided into three regions (*Figure 2.4*):

i. The thrust wedge, which consists of the material above and behind the frontal imbricate thrust;

ii. The pre-wedge, ahead of the frontal imbricate thrust, in which strain builds up as a gentle fold and some lateral translation due to movement on the basal detachment. This region is similar (but not equivalent) to the previously recognised "proto-thrust" region in sub-marine accretionary prisms (Karig and Lundberg, 1990; Tsuji et al., 2005; Ku and Hsu, 2009; Lin et al., 2009; Barnes et al., 2010; Ghisetti et al., 2016) as both regions deform the present-day seafloor and tend to be incorporated into the main deforming wedge as deformation proceeds. However the proto-thrust region described by these authors commonly contains sets of moderately to steeply dipping reverse faults, and has been identified as the region both ahead (MacKay, 1995; Moore et al., 2001; Gulick et al., 2004; Ku and Hsu, 2009; Barnes et al., 2010; Ghisetti et al., 2016) and behind (Adam et al., 2004; Ku and Hsu, 2009; Lin et al., 2009) the deformation front. However, the pre-wedge in our model is characterised by gentle

detachment folding without major established faults, and is situated between the frontal thrust and deformation front (*Figure 2.4*). The proto-thrust described by Karig and Lundberg (1990) and others is a qualitative definition. In contrast, we can define the pre-wedge region by the quantified wedge features, i.e., displacement front, deformation front and failure front (*Figure 2.4*);

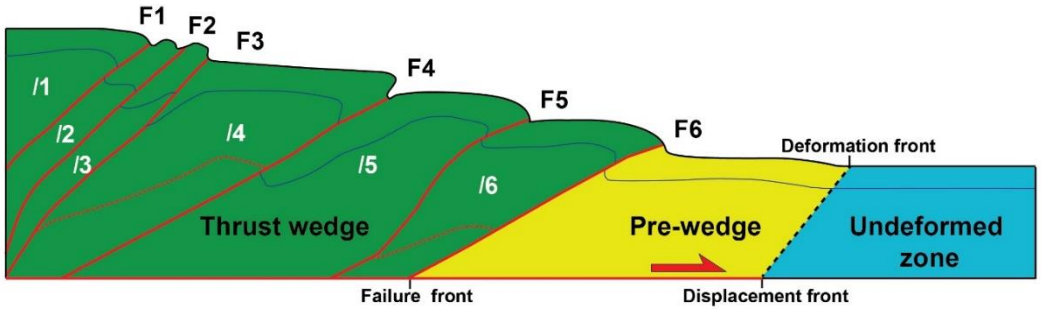

Figure 2.4 Thrust model after 3268 m of shortening, showing the principal structural elements discussed in the text. I1 to I6 are the major imbricate fault blocks. F1-F6 are the major thrust faults. Dotted thin red lines in fault blocks I4 and I6 are significant short- cut faults. Blue line is an originally continuous stratigraphic marker. The thrust system can be divided into a thrust wedge, pre-wedge, and undeformed region.

iii. The undeformed region, ahead of the displacement front, with the boundary between the pre-wedge region and undeformed zone being diffuse, as displayed by the dotted line in *Figure 2.4*.

2.3.1 Surface slope and taper angle

One of the primary applications of the CWM is to predict the critical taper angle of a thrust belt by combining the known or estimated rock strength and stress equilibrium conditions within the wedge interior and along the basal detachment (Davis et al., 1983; Dahlen, 1984, 1990). Here we can test whether the taper angle of the modelled thrust wedge is consistent with these theoretical predictions.

As shortening is applied to the moving wall, the surface slope starts to grow rapidly until it reaches an angle of 24.8°, at ~413 m shortening (*Figure 2.5*). It then increases slowly to a peak value of 25.4°, at ~750 m shortening, at which, the slope angle then rapidly decreases to 13.0°. Similar to the surface slope, the taper angle exhibits an initial increase to a peak value of 16.4° (*Figure 2.5*). Within this first fast growth phase, there are two brief periods where the taper angle is relatively stable; from 165 m to 228 m of

shortening, and 367 m to 413 m of shortening. These two episodes represent the rapid transitional process from critical to sub-critical state of the thrust wedge. Following ~700 m shortening, the taper angle decreases from 16.5° to 10.4° (as the surface slope decreases from 25.4° to 13.0°).

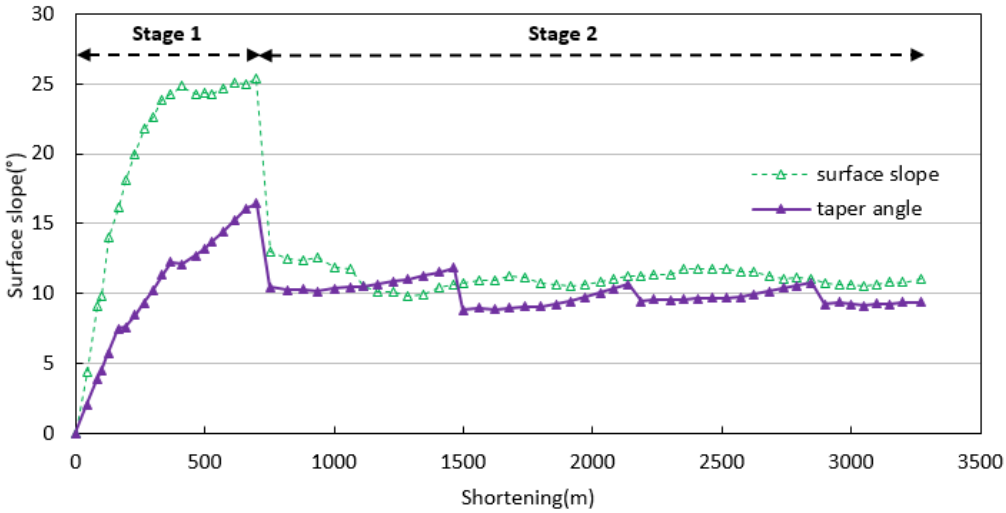

Figure 2.5 Plot of surface slope (green) and taper angle (purple) against shortening. Stage 1 is the initial wedge building phase which is largely controlled by boundary conditions and velocity discontinuity, while Stage 2 (beyond 700 m shortening) is a steady state phase of thrust wedge development which is thought to be highly relevant to natural thrust systems.

These results indicate that the model can be divided into two time stages:

1) Stage 1: A period (from 0 – 700 m shortening) in which a wedge is built adjacent to the moving wall. At this stage the failure front is fixed at the origin and the wedge gains height and topography through the development of fault blocks *I*1, *I*2 and *I*3 (*Figure 2.4&Figure 2.5*). Up to this point there is little deformation ahead of the wedge, with the 50 m shortening extending to ~700 m (*Figure 2.3*). During this stage, the geometry of the model is largely controlled by the boundary conditions, particularly of the moving wall and velocity discontinuity at the left corner and may not be indicative of natural thrust belts. This stage does not represent the critical taper relationship and is not used in our detailed analysis.
2) Stage 2: Beyond 700 m shortening, the system transitions rapidly into a dynamic equilibrium state. During this stage there is oscillation between critical and sub-critical taper, with both surface slope and taper angle having a constant apparent critical value of ~10°. This stage is characterized by an approximately steady state

development of thrust wedges *I*4, *I*5 and *I*6, and will be discussed in detail in the rest of the paper as it is thought to be highly relevant to natural thrust systems.

Figure 2.5 shows that the surface slope is consistently larger than the simplified taper angle in the early period of establishing the thrust wedge (before shortening of 1110 m). With the exception of differences in values at the initial wedge development stage, the evolution patterns of surface slope and taper angle are very similar to each other. As the bulk strength is controlled by the weakest component of material friction strength (Lohrmann et al., 2003) which in this case is 31° (*Table 2-1*) , the minimum and maximum critical taper are computed as 5.8° and 31° using the solution of Dahlen (1984) (*Figure 2.1*a, Equations (2-(1-5)). The wedge fails by thrusting at the minimum critical taper while failing by normal faulting at the maximum critical taper. All measured surface slope and taper angles remain in the stable field of the Coulomb Wedge (Dahlen, 1984), similar to that observed from previous studies (Buiter et al., 2006; Schreurs et al., 2006; Cruz et al., 2010; Buiter et al., 2016), demonstrating the model results are effective. In this case, the thrust wedge is established through folding and thrusting as the modelled constant apparent critical value of surface slope and taper angle, both ~ 10°, is approaching the minimum critical taper angle 5.8° predicted by CMW (Dahlen, 1984).

$$\psi_b = \frac{1}{2}\arcsin\left(\frac{\sin\varphi_b'}{\sin\varphi}\right) - \frac{1}{2}\varphi_b' \tag{2-1}$$

$$\psi_0 = \frac{1}{2}\arcsin\left(\frac{\sin\alpha'}{\sin\varphi}\right) - \frac{1}{2}\alpha' \tag{2-2}$$

$$\varphi_b' = \arctan\left[\mu_b\left(\frac{1-\lambda_b}{1-\lambda}\right)\right] \tag{2-3}$$

$$\alpha' = \arctan\left[\left(\frac{1-\rho_w/\rho}{1-\lambda}\right)\tan\alpha\right] \tag{2-4}$$

$$\alpha_{max} = \arctan\left[\frac{\mu(1-\lambda)}{1-\rho_w/\rho}\right] \tag{2-5}$$

ψ_b and ψ_0 are the angles between the maximum principal compressive stress and base and top of the wedge, φ angle of internal friction (μ=tan φ), φ_b angle of basal friction (μ_b=tan φ_b), λ the pore fluid factor in wedge, λ_b basal pore fluid factor, ρ density of wedge material, ρ_w density of fluid.

The analytical CWM has been developed as a description of a static wedge in a condition of stress equilibrium and it does not incorporate the effects of discrete thrust and related

folding on wedge growth. Real world thrust systems and modelled wedges evolve dynamically with imbricated thrusts and folds that affect the overall geometry of thrust wedge, which probably results in the inconsistency between theoretical and measured taper angles (pers. comm., J. Suppe, 2016). In addition, the definition of a single value for the "taper angle" in real-world systems is non-trivial, because they commonly exhibit complex topography, and rarely consist of simple uniform-tapering wedges.

In this study, we define "taper angle" simply as the slope of the straight line from the deformation front to inboard corner of the wedge (*Figure 2.2b*), which ignores any variation in topography of the top surface of the modelled thrust belt. *Figure 2.5* shows how the overall taper angle of the model continuously changes as the model develops, with a tendency for it to self-adjust in such a way as to approach the minimum critical taper. This behaviour was also observed in physical analogue experiments by Wang and Davis (1986) and Lohrmann et al. (2003). In our numerical models, the constant critical taper angle appears to be approximately 10°. Taper angles below this value are subcritical, because they cannot be stably maintained. The frontal ramp (pre-wedge in *Figure 2.4*), side friction, imposed boundary conditions, velocity discontinuity at the left corner (*Figure 2.2*) and material cohesion all affect the modelled taper angle.

2.3.2 Wedge width and height

Wedge height and width are plotted against shortening (*Figure 2.6a*), and separately as growth rate of wedge height (*Figure 2.6b*). Wedge height is defined as the highest elevation of the top of thrust wedge, with the initial value of height being the original thickness of the pre-deformation thrust wedge (600 m; *Figure 2.6b*). Its growth rate is the slope of wedge height calculated from two successive values of shortening. Wedge width is measured between the mobile wall and the deformation front (see Cotton and Koyi, 2000; Schreurs et al., 2006; *Figure 2.2b*).

In our model, there are 6 distinct episodes of rapid increase in wedge width (*Figure 2.6a*). In each episode, displacement steps forward along the basal décollement and a new incipient fold develops. The rapid jumps in wedge width are followed by a slow increase and then decrease in wedge width prior to the next phase of wedge accretion. The second ‘steady state’ stage (Stage 2: shortening >700 m) follows a significant increase in wedge width (~900 m). An overall wedge width of 4650 m is gained over shortening of

3268 m. Such a phased accretion in the thrust wedge has also been reported by previous authors (Mulugeta and Koyi, 1992; Cotton and Koyi, 2000; Bigi et al., 2010; Cruz et al., 2010; Wu and McClay, 2011; Ruh et al., 2012).

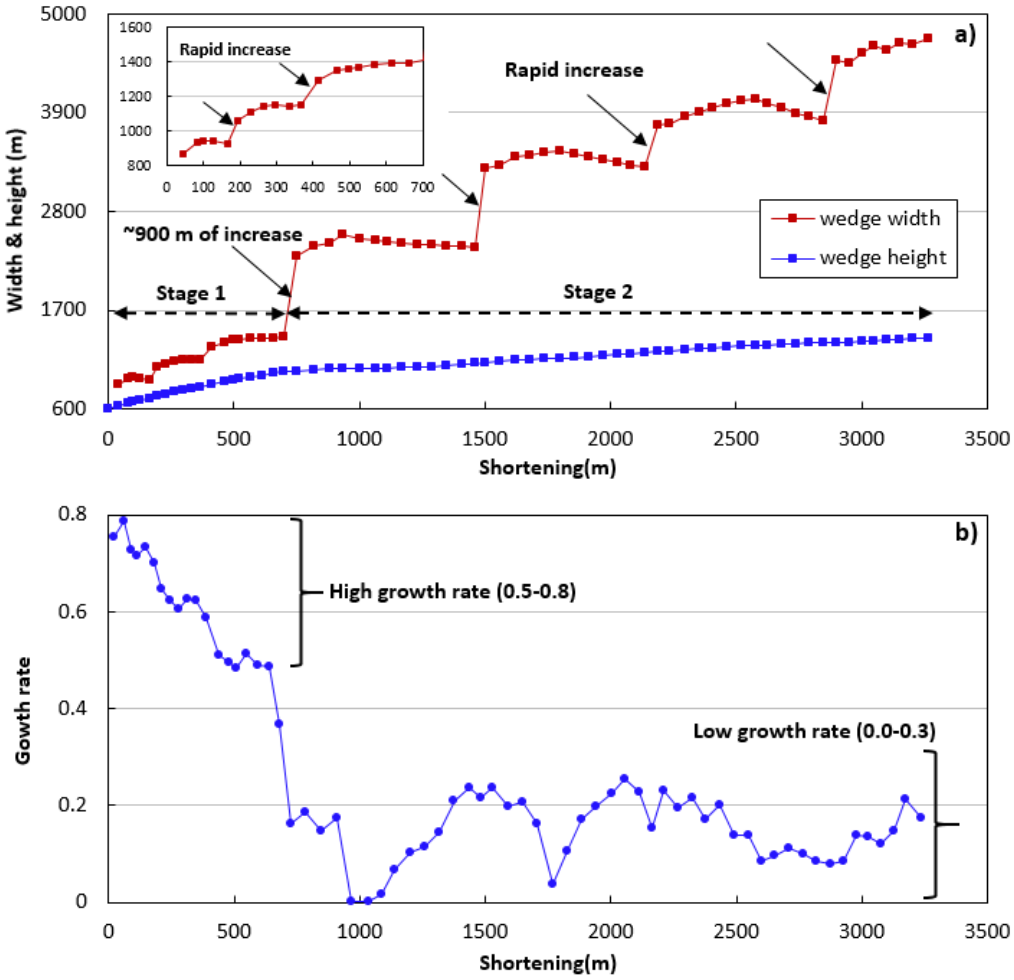

Figure 2.6 (a) Wedge width and height against shortening with an inserted figure enlarging the initial phase of wedge width growth over 0-700 m of shortening. With Stage 2, 4 wedge accretions can be recognised where the wedge width rapidly increases. b) Growth rate of wedge height versus shortening. The growth rate at Stage 1 is typically higher than that in Stage 2.

In contrast, the wedge height continuously grows to 1025 m, at shortening of ~700 m (*Figure 2.6a*), with growth rates of 0.5-0.8 (*Figure 2.6b*), and then increases more slowly until it reaches 1396 m at 3268 m of shortening (Fig. 6a), with a growth rate range of 0.0-0.3 (*Figure 2.6b*). The episodes of rapid increase are less obvious, but there is some indication of cyclicity, in parallel with wedge accretion. Similar results have been observed in physical analogue models through direct measurement of wedge height (Koyi, 1995; Burbidge and Braun, 2002; Bose et al., 2009). Bose et al. (2009) reported that early rapid

increasing wedge height is followed by a long-term stable wedge growth. Our results show wedge height continues to grow with alternating high and low rates throughout the entire process. Potentially our model allows more detail to be resolved in this "stable" phase (Stage 2 in *Figure 2.6*).

2.3.3 Propagation of the displacement front, 50 m displacement position and failure front

In the process of developing a thrust wedge, the material within the wedge is deformed by folding and faulting as the thrust wedge progressively advances into the undeformed frontal area (Wu and McClay, 2011). This episodic and cyclic growth pattern has been seen in sand box models (Mulugeta and Koyi, 1992; Willett, 1992; Gutscher et al., 1996; Wang and Davis, 1996; Gutscher et al., 1998; Sherkati et al., 2006; Selzer et al., 2008). In this study, three parameters are used to show how a thrust belt evolves in response to continuous convergence: the displacement front; the 50 m displacement position; and the failure front (*Figure 2.2a* & *Figure 2.2b*).

The distribution of total, horizontal and vertical displacement for the model scaled to 0-2390 m, 0-2300 m and 0-665 m are displayed in *Figure 2.7a*, *2.7b* & 2.7c, respectively. The total and horizontal displacement present similar patterns of distribution, indicating that the horizontal/forward movement dominates the growth of the thrust belt. However, the fully scaled models cannot resolve minor deformation (less than ~230 m) or the displacement front (position of 0 m displacement) due to limited resolution. Therefore, we also plot at a different scale (0-50 m) to highlight small scale displacement and to constrain incipient deformation in the wedge front (*Figure 2.7d*, *2.7e* & 2.7*f*). Because the system is dominated by forward advancement, the horizontal positions of the displacement front, the 50 m displacement and the failure front along the detachment are defined to examine the advancing behaviour of the wedge front *Figure 2.7*.

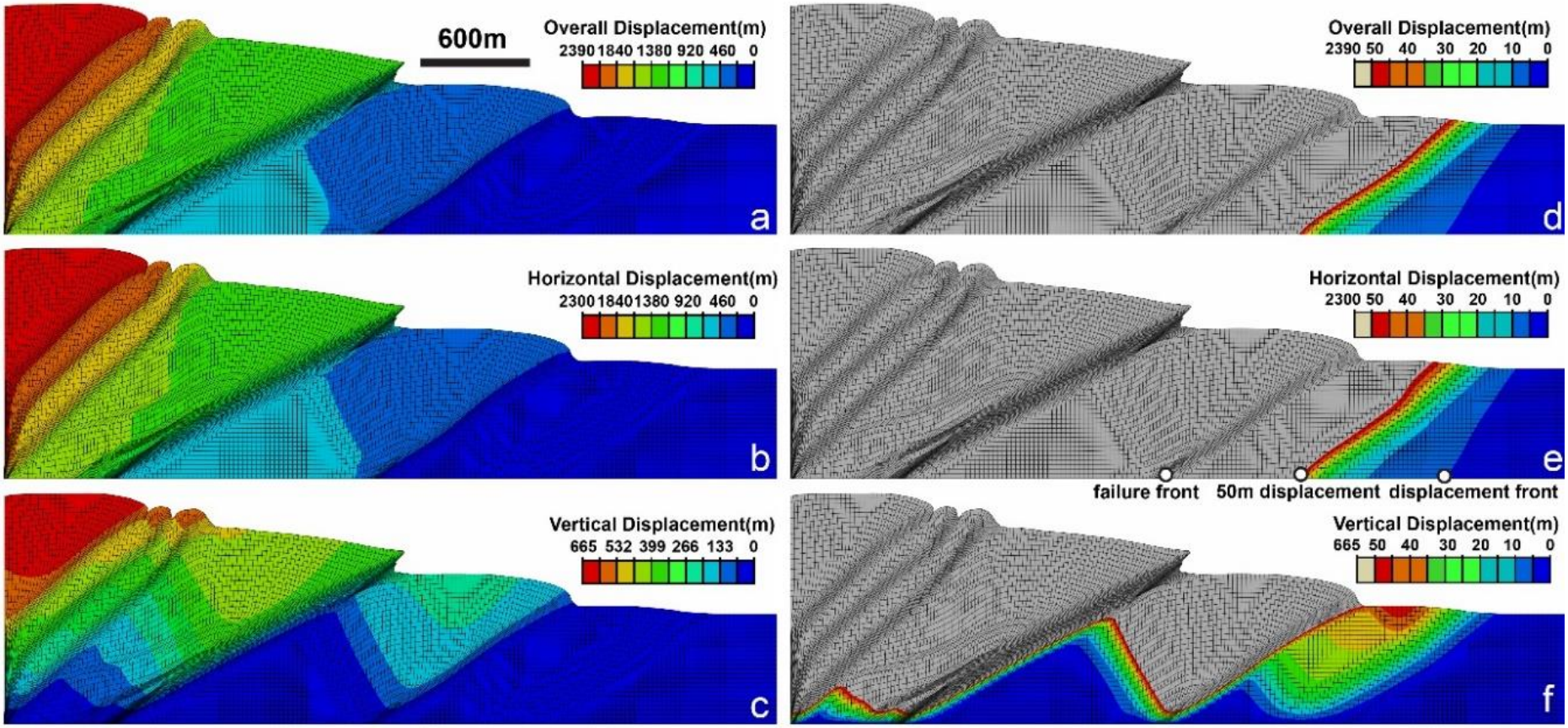

Figure 2.7 A model example of a fold-thrust belt with total shortening of 2300 m. (a),(b) and (c) show the fully scaled distribution of the total, horizontal and vertical displacement in the wedge; (d),(f) and (e) present the total, horizontal and vertical displacement scaled to 0-50 m in the wedge front showing the displacement front and the 0-50 m displacement contours with focus on small scale deformation. The failure front is where the frontal thrust roots into the detachment.

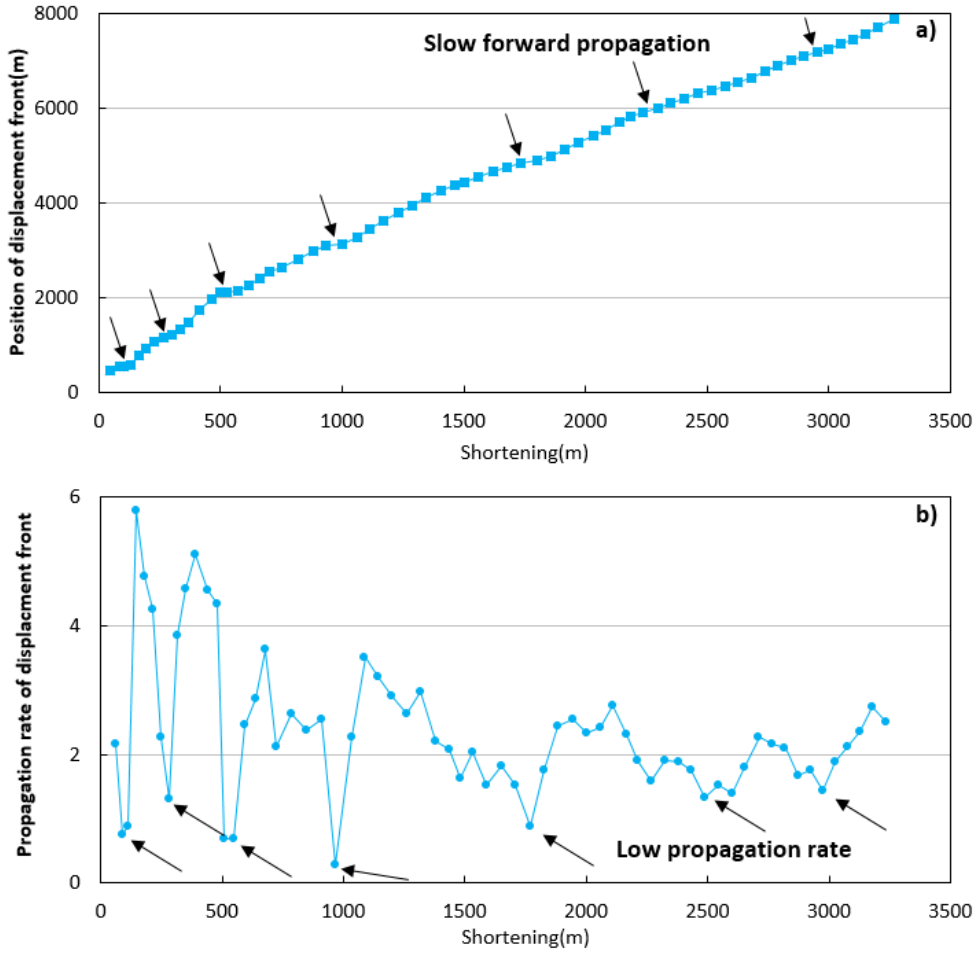

Figure 2.8 Evolution of horizontal displacement (X coordinate value) front vs. shortening. (a) Position of displacement front against shortening. (b) Rate of propagation of the displacement front against shortening (same method as calculated growth rate of wedge height Figure 2.6b), black arrows indicate the low propagation rate phases within each cyclic period.

In order to reveal the details of these displacement parameters, in each case the propagation rate of the parameter is calculated using the same method as that for the growth rate of wedge height (see above). The displacement front propagates forward at variable rates from a position of 540 m to 7880 m during the two stages of wedge building (Figure 2.8). The propagation rate plot of this parameter (Figure 2.8b) indicates cyclicity, with alternating high and low propagation rates with the latter relating directly to the cyclic changes in the wedge height (Figure 2.6b).

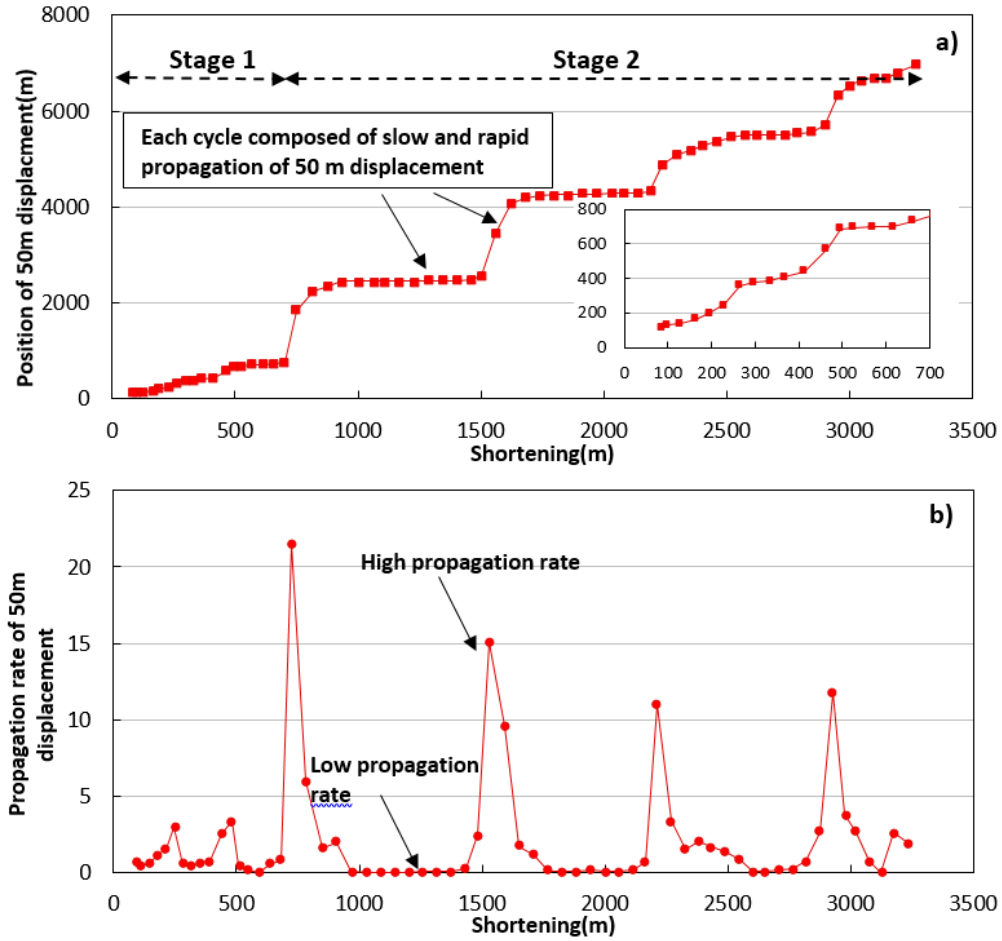

Figure 2.9 Position of 50 m displacement (X coordinate value) vs. shortening. (a) Plot of 50 m displacement position against shortening with inset enlarging the initial 0-700m of shortening. (b) Propagation rate of the 50 m displacement position against shortening.

The 50 m displacement position starts at a position of 119 m at shortening 84 m (*Figure 2.9a*). The position advances over 6 cycles each composed of a relatively long period of slow forward propagation followed by a short episode of rapid propagation. The first three of these cycles are developed within Stage 1 and represent relatively small advancements of position and low propagation rates. These are followed by 3 further cycles within Stage 2 that include phases of high propagation rate and greater jumps forward in the position of the 50 m displacement within Stage 2.

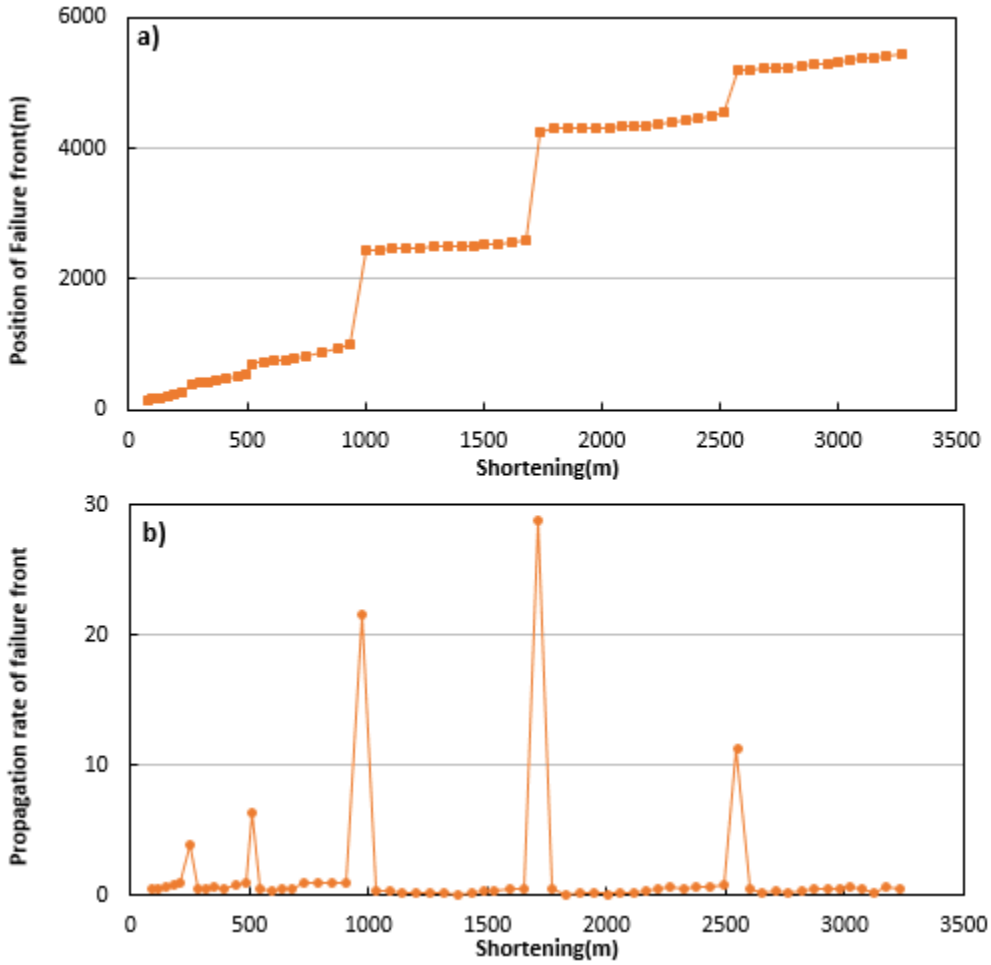

Figure 2.10 (a) Position of failure front (X coordinate value) against shortening, inset enlarging the initial 0-800 m of shortening. (b) Propagation rate of the failure front against shortening.

The failure front initiates at a position of 154 m at shortening 84 m (Figure 2.10). As with the 50 m displacement position, six cycles can be identified where relatively long periods of slow propagation are followed by rapid advancement. Rapid propagation of the failure front typically occurs as an old thrust is abandoned and a new thrust is about to initiate at the failure front. As soon as this happens, the newly formed thrust (and hence the failure front) then tends to advance very slowly (Figure 2.10).

2.3.4 The spatial and temporal relationship between the displacement front, 50 m displacement and failure front

To investigate how the different deformation parameters are related, they are plotted together against shortening as a proxy for time (*Figure 2.11*). In contrast to the episodic propagation of the 50 m displacement position and failure front, the displacement front

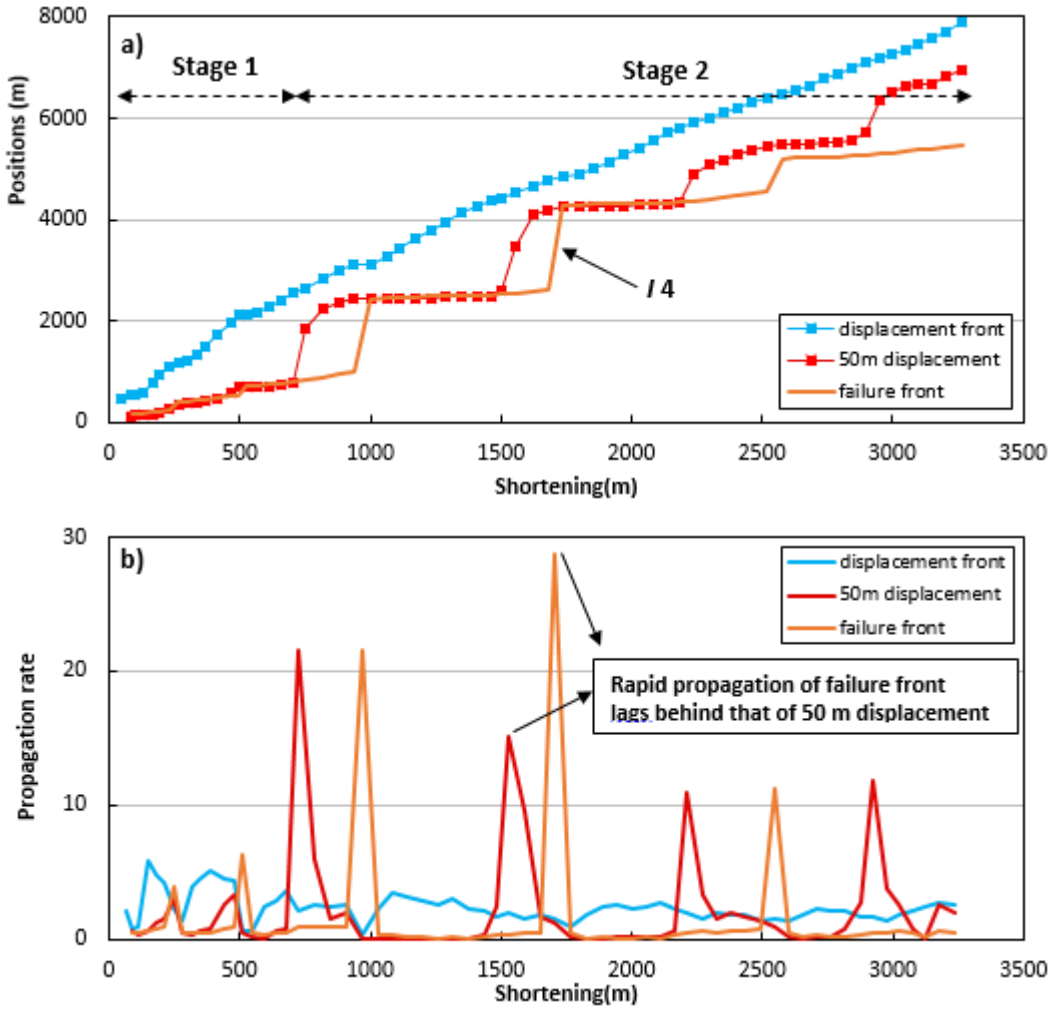

Figure 2.11 Evolution of associated parameters with thrust wedge advancement vs. shortening. (a) Position of displacement front, 50 m displacement position and failure front against shortening. (b) Propagation rate of displacement front, 50 m displacement and failure front against shortening.

shows a relatively constant advance (*Figure 2.11*a), suggesting that this parameter is less affected by the wedge building process. The rapid propagation of the 50 m displacement position and failure front are not coincident in time, with the 50 m displacement position advancing before the failure front (*Figure 2.11*). As displayed in *Figure 2.11b*, the rapid propagation of failure front (shown by orange line) lags behind that of the 50 m displacement position (shown by red line). The 50 m displacement position moves progressively forward before reaching a stable position, prior to the establishment of a new failure front. The deformation sweeps forward, and then stabilizes, with new failure front then localising in the resulting displacement gradient. For example, in the development of wedge I4, the 50 m displacement position propagates to a new position

with progressive shortening and then the failure front jumps to this position as a new discrete fault forms (*Figure 2.11a*).

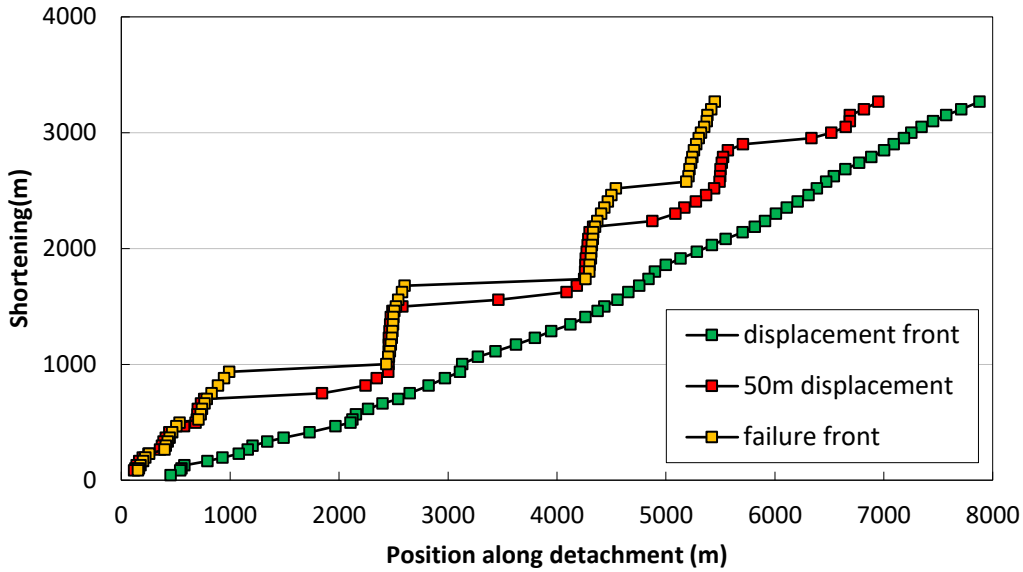

Figure 2.12 A synthetic diagram showing the evolution of shortening vs. the displacement front, 50 m displacement and failure front.

Figure 2.12 presents the data redisplayed in order to emphasize the spatial relationships. The graph tracks the position of three features: the displacement front, the 50 m displacement and the failure front. The separation of the 50 m displacement position from the displacement front provides a measure of the displacement gradient at the tip and following the position of this marker provides a useful insight into the cyclic evolution of the thrust system. Throughout the process of wedge building, the displacement front is leading the system in advance of both the 50 m displacement position and failure front (*Figure 2.12*).

The key stages in the growth of a thrust wedge can be visualized from the modelling results (*Figure 2.13*). Here, two sets of model images of horizontal displacement and distributed strain are used to illustrate the cyclic evolution of imbricate block I6 in Stage 2 as an example of the typical cycle of wedge growth. The strain used is principal strain derived from the FE modelling, which is indicative of the magnitude and distribution of deformation in a simulated thrust belt. Four stages are depicted, as follows:

1) ~2278 m (shortening), wedge accretion (start of a cycle). This phase is characterised by the rapid advancement of the 50 m displacement position towards the zone of incipient folding (*Figure 2.13a*) while the frontal thrust is slowly advancing. A zone of

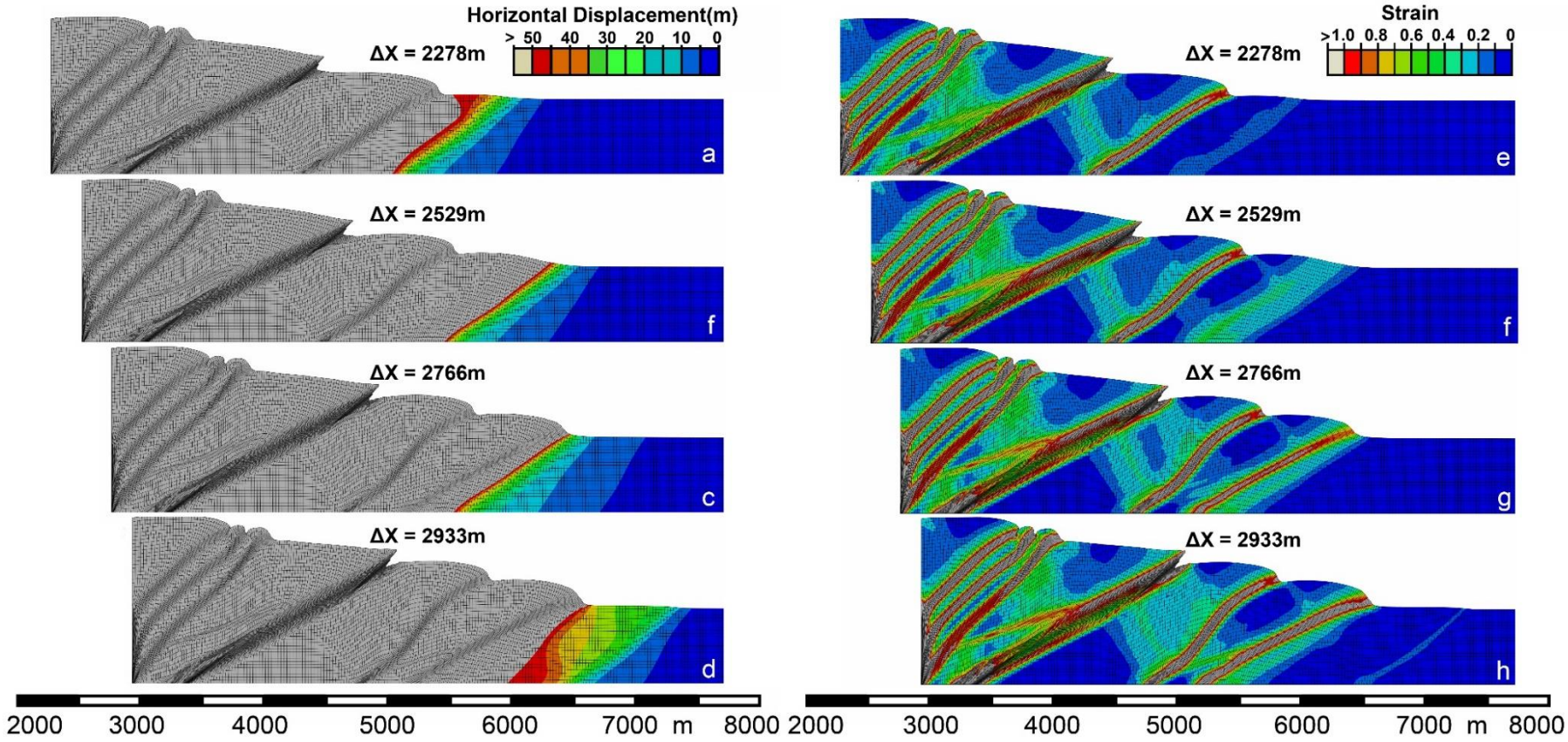

Figure 2.13 Model results of horizontal displacement and principal strain showing cyclic evolution of imbricate thrust block I6 through a cycle of thrust wedge development. ΔX indicates the amount of shortening. (a) Wedge accretion after 2278 m of shortening. (b) Diffused deformation over the incipient folding. (c) Strain localisation and initiation of new thrust at the failure front after 2766m of shortening. (d) The completion of a cycle. (e) – (h) show the corresponding strain distribution at the same 4 stages as (a)-(d).

minor strain occurs (*Figure 2.13e*) highlighting the initial minor deformation corresponding to the observed minor displacement in the pre-wedge region.

2) ~2529 m, diffused deformation. With additional bulk shortening, the 50 m displacement position completes its rapid forward propagation as indicated by the narrow zone of large displacement (red band in *Figure 2.13b*). This is accompanied by the expansion of diffused deformation across the outermost area of folding (*Figure 2.13f*), similar to the observed "diffuse shear strain" of Adam et al. (2005). These features are also compatible with the previously reported activity of numerous short-lived weak shear bands prior to the initiation of a new thrust in scaled analogue models (Dotare et al., 2016). At this point, the incipient fold is above a broad strain zone not a discrete thrust, and is therefore identified as a pre-thrust anticline.

3) ~2766 m, strain localisation and initiation of a new thrust. As soon as new thrust F6 forms in the pre-wedge region, the 50 m displacement position and the failure front both shift to new, but coincident positions (*Figure 2.13c* & *Figure 2.13g*). Both the 50 m displacement position and failure front stabilise without significant forward propagation. During this period, the entire system is subject to shortening and thickening in order to establish a critical tapered wedge (Bigi et al., 2010; Wu and McClay, 2011). The strain map (*Figure 2.13g*) shows the formation of a strain localised shear zone which resembles a discrete thrust in natural examples. This stage corresponds to the "after failure and stable sliding phase" of shear tests in granular materials (Lohrmann et al., 2003). During this stage, the strain is primarily released by the new frontal thrust(Dotare et al., 2016).

4) ~2933 m, completion of a cycle (equivalent to ~ 2278 m of shortening). The cycle of I6 evolution ends with the development of a new pre-thrust anticline in front of the wedge (*Figure 2.13d* & *Figure 2.13h*), which is accompanied by a significant increase of the wedge width and decrease of the taper angle. This phase also marks the start of a new cycle of imbricate block development as a new strain zone forms in the wedge front (*Figure 2.13h*).

2.4 Discussion

Many previous models have been created and run to test the effects of material rheology on overall thrust belt development, and we have not tried to replicate these approaches. Instead, we have examined the results from a complete model in great detail, which reveals many previously undescribed aspects of thrust wedge growth.

2.4.1 The episodic growth of the fold-thrust belt

The episodic growth of a thrust belt has been described in many previous studies using a variety of methods including numerical modelling, physical analogue experiments, and field-based structural studies (Mulugeta and Koyi, 1992; Gutscher et al., 1996, 1998; Davis et al., 2006; Del Castello and Cooke, 2007; Ji et al., 2008; Bigi et al., 2010; Cruz et al., 2010; Fitz-Diaz et al., 2014). Although these studies demonstrate the episodic behaviour of thrust wedge growth, a comprehensive quantitative analysis has not yet been reported.

In this study, the taper angle throughout Stage 2 is directly related to the position of the deformation front, which is defined by a zero displacement at surface and migrates as a function of wedge growth (*Figure 2.2b*&*Figure 2.2c*). This definition of taper angle is less subjective compared to the previously used taper angles incorporating the "enveloping wedge slope" (Liu et al., 1992; Gutscher et al., 1996; Schreurs et al., 2006; Wu and McClay, 2011; Sun et al., 2016). The taper angle is then used to determine the critical state of the thrust wedge.

The synthetic diagram of *Figure 2.14* illustrates the clear temporal relationships between the different wedge parameters. The horizontal axis indicates the amount of shortening, a proxy for time, green bars (labelled A3-A6 from left to right) denote phases of wedge accretion, and pink bars (named F4-F6 from left to right) denote periods of new fault initiation. Comparing *Figure 2.14 a* of the taper angle with *Figure 2.14 b* & *Figure 2.14 c*, there are six typical periods of thrust wedge accretion (green bars) which follow gradual evolution of wedge width, and these periods correlate directly with distinct changes of other variable (i.e., position of 50 m displacement). For example, in the cycle of development of imbricate block *I*4 when the wedge is obtaining a constant apparent critical value ~10° (period between A3 and A4, *Figure 2.14a*), wedge interior, here tracked by the 50 m displacement position, accelerates forward (A3 in *Figure 2.14c*) until a new

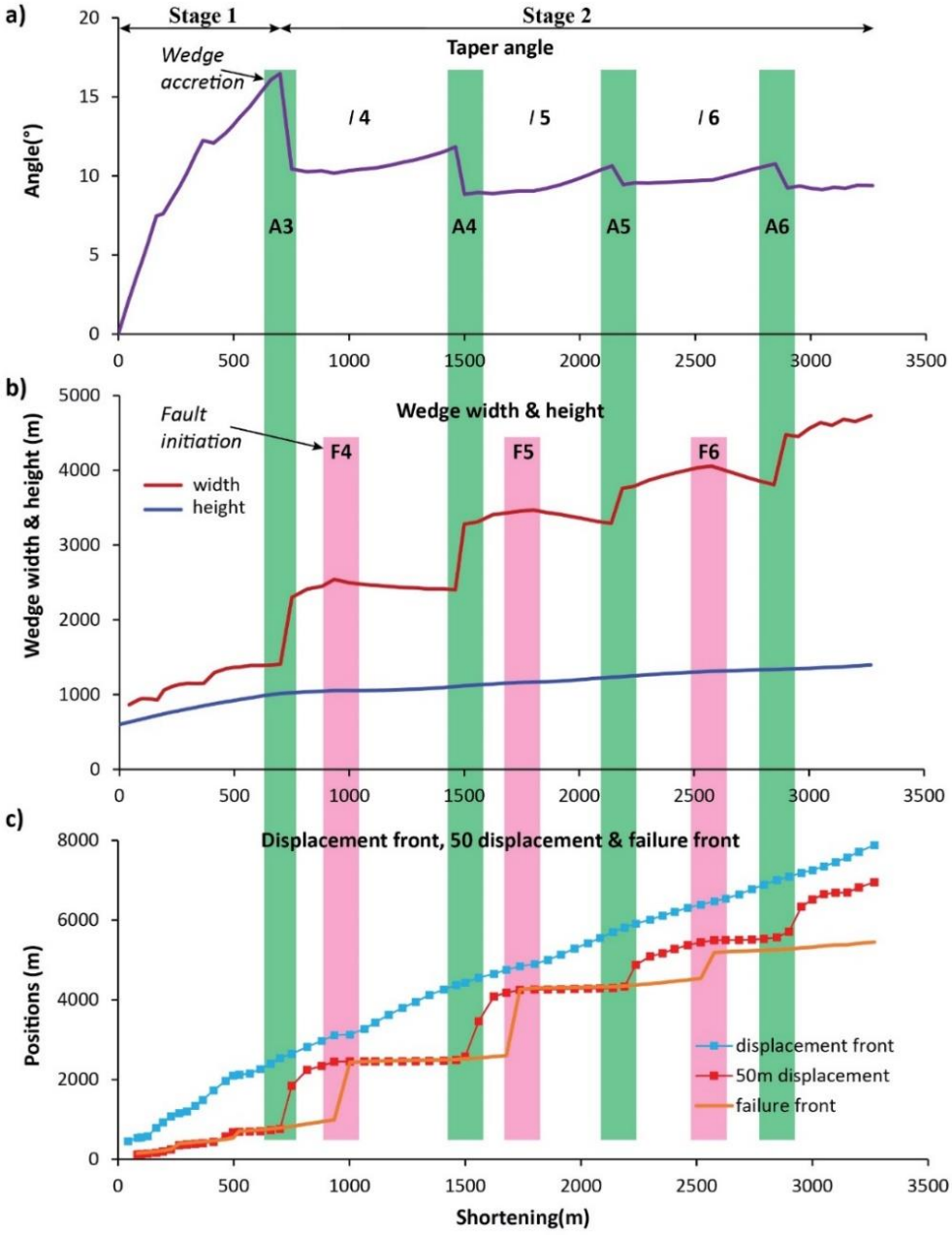

Figure 2.14 Relationship of different wedge parameters. Horizontal axis for plots is shortening, a proxy for time. Green bars (named A3-A6 from left to right) denote wedge accretion phases in which the taper angle drops immediately after obtaining a critical taper; pink bars (named F4-F6 from left to right) donate periods of new fault initiation. I4, I5 and I6 represent the periods of development of imbricate blocks between wedge accretion phases. (a) Plot of taper angle against the amount of shortening. (b) Plot of wedge width and height against the amount of shortening. (c) Plot of the displacement front, 50 m displacement and failure front versus the amount of shortening. Both green because wedge accretion in previous studies is determined as the formation of the new and red bands show the correlation between different deformation parameters throughout the process.

thrust initiates at the failure front (F4 in *Figure 2.14c*). The wedge then progressively advances until the next wedge accretion phase occurs (F4 to A4 in *Figure 2.14c*). Throughout the process of *I*4 block development, the wedge width gradually increases until a peak value shown by pink bar F4 (*Figure 2.14b*), then followed by a slow decrease before the next wedge accretion phase (A4, *Figure 2.14b*). The peak wedge width coincides with the initiation of a new thrust, occurring at the same time as the failure front rapidly advances forward (F4 in *Figure 2.14b* & *Figure 2.14c*).

The rapid increase in wedge width corresponds to wedge accretion. The evolution of the wedge width in this study is slightly different from that of previous studies, which show that wedge width progressively decreases after thrust formation (Koyi and Vendeville, 2003; Cruz et al., 2010; Wu and McClay, 2011; Ruh et al., 2013; Sun et al., 2016). This is frontal thrust (Mulugeta and Koyi, 1992; Wu and McClay, 2011), whereas in this study it is determined by incipient folding prior to thrusting. According to our observations (*Figure 2.3*, *Figure 2.7* & *Figure 2.13*), this incipient folding develops in advance of establishment of the new thrust fault throughout the wedge growth process. As soon as a new thrust develops at the failure front, by the fault tip breaking through the fold to the surface, the wedge experiences significant shortening. This leads to a slight decrease in wedge width (*Figure 2.14b*) as the entire thrust wedge is subjected to shortening and thickening (Gutscher et al., 1996). At this stage, the wedge is slowly moving forward as demonstrated by movement of the 50 m displacement position from F4 to A4 in *Figure 2.14c*.

Each episode of rapid decrease in taper angle represents a short transition from critical to subcritical taper and coincides with wedge accretion (green bars in *Figure 2.14a* & *Figure 2.14b*). The accretion of frontal material builds the wedge forward, thereby increasing wedge width and reducing surface topography (Mulugeta and Koyi, 1992; Gutscher et al., 1996, 1998; Cotton and Koyi, 2000; Koyi and Vendeville, 2003; Bigi et al., 2010; Wu and McClay, 2011; Graveleau et al., 2012). The transition from critical to subcritical taper is rapid with respect to the time period when the thrust wedge is attaining its critical taper (A3 to A4 in *Figure 2.14a*). Similar results have been observed in physical analogues (Gutscher et al., 1996; Wang and Davis, 1996; Dotare et al., 2016; Schreurs et al., 2016; Sun et al., 2016) and numerical experiments (Buiter et al., 2006; Cruz et al., 2010; Buiter

et al., 2016) but the interaction between different wedge parameters during this transitional period had not previously been analysed in detail.

The rapid propagation of the failure front, as a new fault initiates (pink bars in *Figure 2.14c*), lags behind the propagation of the 50 m displacement position (green bars in *Figure 2.14c*). But the failure front completes its rapid propagation within one shortening period, effectively "jumping" to a new position with the formation of a discrete fault, whereas the 50 m displacement position propagates over several shortening periods (*Figure 2.14c*). Both the failure front and 50 m displacement position complete their advancement phases simultaneously, despite differing in initiation time (*Figure 2.14c*). A total of 6 short episodes are observed when the thrust wedge is transferring from critical to subcritical taper as a result of wedge accretion (represented by green bars), dividing the overall process of wedge building into 7 periods. Therefore, a typical cycle of creating a thrust wedge (one period) involves growth through a combination of rapid advancement of the thrust belt and slow building of the wedge (see examples of I6 in *Figure 2.13* & *Figure 2.14*).

In the case of high basal friction (80%-90% of the internal friction), cyclic behaviour has been observed in analogue models, alternating between frontal accretion of imbricate thrust slices and basal accretion of underthrusting of long, undeformed sheets (Gutscher et al., 1996). In this study, where the basal friction (μ_b=0.3) is half of the internal friction (μ=0.6), i.e., relatively low, the episodic and cyclic growth of the thrust wedge is still observed, but dominantly through frontal accretion. Therefore, the ratio of basal friction to internal friction is not a precondition for cyclical growth of a fold-thrust belt as long as the basal detachment is not stronger than the wedge material for the existence of a critical Coulomb Wedge (Dahlen, 1984; Bilotti and Shaw, 2005; Fagereng, 2011). But the ratio of basal friction over internal friction exerts a first order control on the growth mechanism of thrust wedge i.e., frontal accretion, basal accretion or mixture of both. As such, the resultant structures in an accretionary prism appear to be indicative of the basal strength; development of the imbricate thrust slices suggest low basal friction (i.e., 50% of the internal friction) while the under-thrusting implies high basal friction (i.e., 80%-90% of the internal friction).

To reveal in detail the internal deformation of the pre-wedge region and the forward propagation of the thrust wedge, we tracked the 0-50 m displacement contours and

analysed the strain distribution in our models (*Figure 2.13*, *Figure 2.14*). Our results show that there is clear, although minor, deformation (0-10 m displacement) in front of the thrust wedge, which distinguishes the failure front from the displacement front throughout fold-thrust belt development (*Figure 2.13*). This indicates that frontal accretion starts with small scale displacement of material and minor strain accumulation characterised by pre-thrust folding, which is followed by subsequent thrusting after additional convergence. This spatial and temporal relationship has been recognized from natural examples in the form of proto-thrust zones (Wang et al., 1994; Adam et al., 2004; Gulick et al., 2004; Lin et al., 2009) and some modelling/experimental studies (Yamada et al., 2006; Dotare et al., 2016), however, through examining the process of initiation of a thrust fault, we have been able to quantify and determine the timing and significance of this small amount of deformation (*Figure 2.13*). The integrated analysis suggests that the evolution of minor deformation in the pre-wedge region is episodic, with each phase resulting in the establishment of a new imbricate block (*Figure 2.13*) as a new cycle of wedge building starts. Without this minor deformation, the thrust belt is unable to propagate forwards.

2.4.2 The thrust wedge development process

Figure 2.15 illustrates the sequence of events during a typical cycle of fold-thrust belt growth, the pink and green background colour corresponds to the pink and green bars in *Figure 2.14* and the size of the black arrows represents the relative displacements. In order to achieve a critical taper, the wedge has to deform internally which effectively results in movement along a pre-existing thrust (*Figure 2.15a*) as the deformation front propagates forward. As soon as wedge accretion occurs, the material within the wedge advances rapidly toward the locus of new folding at the deformation front (beyond the region of thrust faulting), leading to a significant increase in wedge width (*Figure 2.15a*).

Wedge material rapidly moves towards the newly formed fold where the strain is localised (*Figure 2.15c*). As additional strain builds up in the folding area, a new thrust starts to form and propagates upwards to break the existing fold with its fault tip reaching the wedge surface (*Figure 2.15d*). It is worth noting that, in the FE model, thrusts are represented and modelled as strain localised shear zones which differ from discrete thrusts that break through folds in natural examples. Major displacement (see *Figure 2.13b* & *Figure 2.13c*) then takes places within the new thrust zone and the wedge

interior deforms to re-establish its critical taper (*Figure 2.15e*), resulting in decreased wedge width (see pink bars in *Figure 2.14*). Similar to the phase in *Figure 2.15a*, pre-formed thrusts reactivate so as to build up the taper angle to critical while the internal movement of the wedge slows, marking the start of another cycle (*Figure 2.15e*).

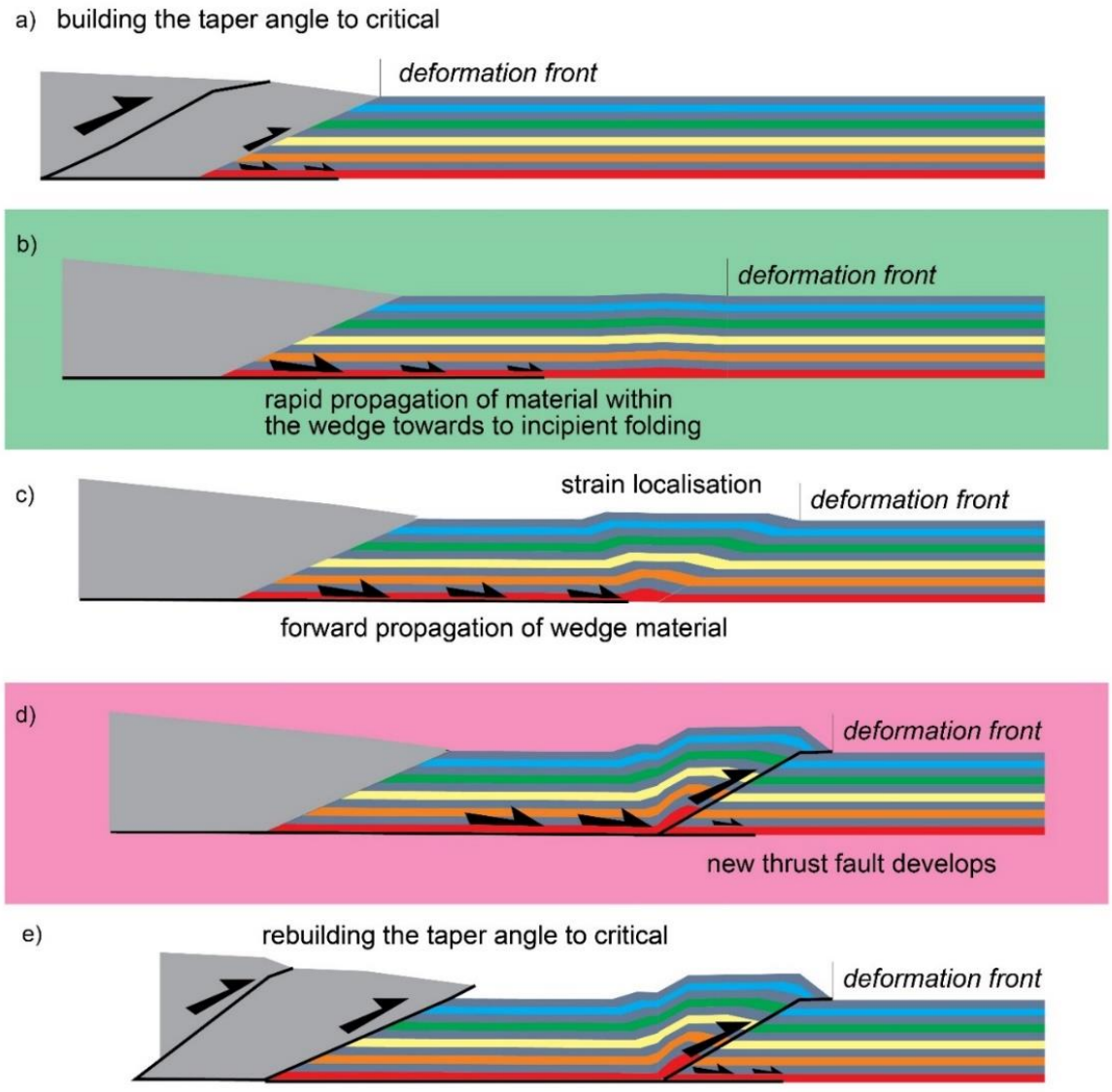

Figure 2.15 Schematic sections showing how the observed cyclic behaviour in the numerical model relates to the cyclicity of tectonic processes in the thrust wedge. Pink (new fault initiation) and green background (wedge accretion) corresponds to the pink and green bars in Figure 14. The size of black arrow represents the scale of displacement in the process of wedge growth.

2.5 Conclusions

By monitoring multiple wedge parameters, this study provides new insights into deformation during cycles of thrust accretion as a fold-thrust belt or wedge develops. Integration of these parameters into a synthetic diagram (*Figure 2.14*) and comparison of the rates of change of these parameters show how they interact and how the wedge uplifts and propagates in response to continuous shortening and frontal accretion. The results clearly indicate that the development of a fold-thrust belt occurs through growth stages that repeat cyclically and episodically as the system undergoes continuous shortening. The key findings are:

1) A fold-thrust system can be broken down into three primary deformation components – the thrust wedge, pre-wedge and undeformed region (*Figure 2.4*), which are characterised by distinct deformation processes and phases of deformation and can be recognised throughout the wedge development process.

2) In the early stage (Stage 1 in this study), a composite thrust wedge is built adjacent to the mobile wall and this builds a critical taper. The wedge then propagates forward by the sequential development of new imbricate thrust blocks (*I*4, *I*5 & *I*6).

3) As soon as thrust accretion occurs, the wedge width increases significantly reducing the taper angle below critical whilst the wedge interior (tracked by the 50 m displacement position) rapidly propagates forward (green bars *Figure 2.14*).

4) During attainment of a critical taper, the wedge experiences significant shortening after a new thrust initiates, leading to a decrease in wedge width (pinks bars *Figure 2.14*). Successive widening of the wedge and subsequent shortening and thrusting maintain a reasonably constant taper angle.

5) The rapid propagation of the failure front as a new fault initiates (pink bars) lags behind that of the 50 m displacement position (green bars, *Figure 2.14*). Both parameters complete their advancement phases simultaneously.

6) The fold-thrust belt evolves cyclically, through a combination of rapid advancement of the fold-thrust belt and gradual, slow building of the wedge (example *I*4 in *Figure 2.13* & *Figure 2.14*).

7) Minor deformation at the front of the thrust wedge is quantified. The results clearly indicate minor deformation (0-10 m displacement) in front of the thrust wedge. This zone of deformation separates the failure front from the displacement front and without this minor deformation, the wedge is unable to move forward.

Acknowledgements

We acknowledge funding to X. Yang from the Natural Environment Research Council (NERC) Centre for Doctoral Training (CDT) in Oil and Gas and the University of Southampton. We thank S. Ellis for sharing her model and her suggestions to modify the model settings, and we are grateful to S. Buiter and J. Suppe for helpful discussions. We thank the two reviewers, J. Adam and S. Ellis, for extremely helpful and constructive reviews that improved the manuscript.

Chapter 3 Fault Activity and Interaction in a Finite Element Model of a Developing Fold-Thrust Belt

Abstract

The fault activity and interaction in an evolving fold-thrust belt are investigated using 2D finite element models to track the evolution of fault displacement, strain rate and fault dip. The results show that an individual thrust experiences two distinct stages of evolution: 1) rapid growth with significantly increased displacement and high strain rate after initiation, 2) subsequent slow but continued growth with slowly accumulated displacement and low strain rate. When a thrust wedge advances, existing thrusts are reactivated to facilitate this process. As a new thrust initiates at the wedge front, the entire wedge is subjected to shortening and thickening to obtain a critical taper, accompanied by significant activity of the frontal thrust and minor or negligible activity of the early formed thrusts. Short-cut faults can develop between two imbricate thrusts with a shallow dip (~11°), slip on a short-cut fault accommodates a component of shortening, changing the displacement pattern along an individual fault. A main thrust, with total displacement ~3-4 times that of other imbricate thrusts, plays a key role in accommodating strain. Fault dip evolves through three stages: 1) initial decrease to Mohr-Coulomb angle due to rotation of maximum compressional stress σ_1, (2) subsequent increase to Roscoe angle as thrust steepens, (3) final stabilization as distance from the deformation front increases with time.

3.1 Introduction

The internal deformation of a fold-thrust belt and submarine accretionary prism, in both nature and experiment, is characterized by imbricate thrusts with usually a forward advancing sequence of thrust development (piggyback mode), where the younger thrusts form in front of older, less active thrusts (Boyer and Elliott, 1982). According to the Coulomb Wedge Model, a thrust fault grows and propagates until a critical taper is built, then subsequent deformation involves transport of the whole wedge along the basal detachment (Davis et al., 1983; Koyi et al., 2000). End member models of deformation within a fold-thrust belt may involve either: 1) an essentially in-sequence model, with

early formed thrusts being rotated to high dips and becoming inactive (Mulugeta and Koyi, 1987; Koyi, 1995; Lohrmann et al., 2003; Wu and McClay, 2011; Dotare et al., 2016) as younger thrusts develop in front of them accommodating the majority of strain (Koyi, 1995; Koyi et al., 2000), or 2) a model that incorporates significant out-of-sequence thrusting (OOST), in which early formed faults in the hinterland of the fold-thrust belt continue to accumulate displacement as deformation proceeds (Dixon and Liu, 1992; Adam et al., 2005; Yamada et al., 2006). However, lack of real-time-monitoring of fault activity and growth has prevented resolving the role of these two deformation styles in modern, active systems.

Slip rate is often derived from displacement and age of the ground surface and sub-surface horizons, but such rates are commonly averaged over relatively long timescales. This, together with uncertainties in horizon ages, tends to mask spatial and temporal variations during growth of an individual fault or whole fold-thrust system. Understanding changes in slip rate with time and interaction between faults are important for the general understanding of fault system development, but also for hazard assessment.

Numerical modelling provides insights into the dynamic growth of fold-thrust belts (Ellis et al., 2004; Stockmal, 2007; Simpson, 2011; Ruh et al., 2012; Buiter et al., 2016), allowing the measurement of geometrical and mechanical parameters of the wedge and individual faults at every stage of the model simulation. Using 2D Finite Element Modelling (FEM), Yang et al. (2017) investigated the kinematic growth of fold-thrust belt and its relationship with the temporal-spatial variations in multiply wedge parameters including wedge taper, height, width, displacement front, failure front and 50 m displacement. The results suggest that a fold-thrust belt develops episodically through a combination of rapid advancement of the wedge and subsequent gradual, slow wedge growth. In this study, we examine the role of individual faults and the interaction of multiple faults to elucidate: (1) how an individual thrust fault grows and how fault displacement, strain rate and fault dip evolve; (2) the timing of individual and relative fault activity; (3) the tectonic controls on fault activity in a growing thrust system; (4) which fault accommodates the majority of strain across a thrust wedge.

3.2 Modelling methods

3.2.1 Model set-up

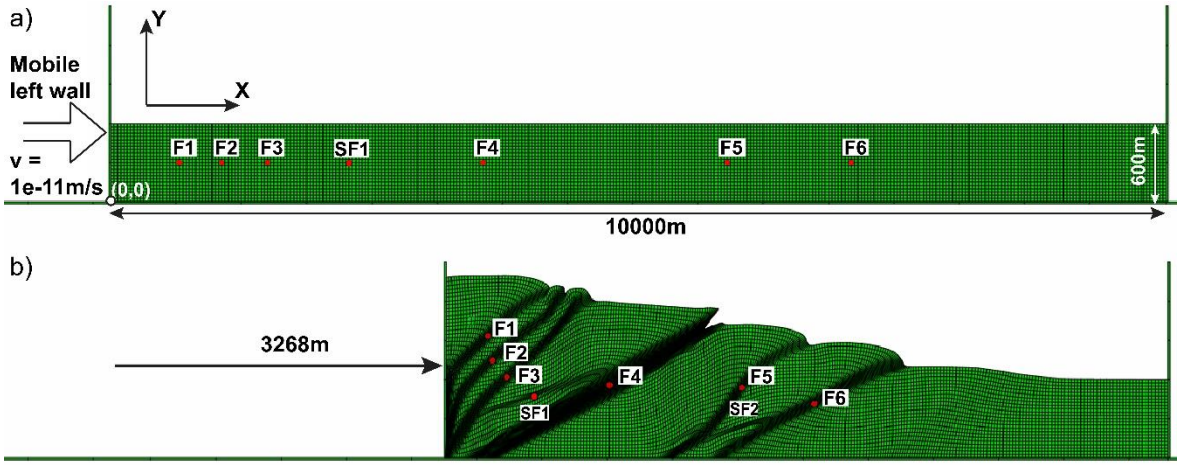

Figure 3.1 Setup of the thrust wedge model. (a) A body of homogenous, isotropic sand length 10000 m and thickness 600 m with initially horizontal layers is shortened by a mobile wall running from left to right with a constant velocity 1e-11 m/s (~0.3 mm/yr) while the right-hand wall and basement are fixed. The highlighted red dots along the central layer (300 m height above the detachment) are used to track the strain rate of imbricate thrust faults and short-cut fault through time. (b) Model result after 3268 m of shortening. The resulting thrust wedge contains 6 discrete faults (F1- F6) and two short-cut faults (SF1-SF2) verging to the foreland, post-deformation positions of the selected nodes are shown along the thrust zone.

The model consists of a mobile left-hand wall, a fixed right-hand wall and base, a wedge of homogeneous, isotropic sediment of length 10,000 m and initial thickness 600 m with passive, initially horizontal layers. The size of the FE cell is 25 x 25 m, with a total of 9600 cells in the model, providing adequate resolution with which to examine the fault dynamics. Shortening is modelled by inward movement of the mobile wall over the horizontal base with a constant velocity of 1 x 10^{-11} m/s (~0.3 mm/yr, *Figure 3.1a*). In this model, the Mohr-Coulomb failure criterion is employed for the deforming material, which is independent of the overall convergence rate, i.e., the inward movement velocity of the mobile wall. The 0.3 mm/yr of velocity used in the model is used to resemble the generally constant shortening rate across a convergence system at plate-lithosphere scale, and does not represent a specific example. Under these conditions, the resulting

fault slip rate in the model is a relative value, but allows the examination of fault activity and growth at the same deformational scale. The highlighted red dots along the marker horizon (300 m above detachment) are nodes at the centre of each developed thrust, at which the strain rate was monitored (*Figure 3.1a*). Figure 1b shows the model after 3268 m of shortening, with a thrust wedge containing 6 discrete thrusts (F1-F6) and 2 short-cut faults (SF1 and SF2) verging forward, and the post-deformation positions of the nodes along the resulting thrust system. The nodes are labelled according to the thrusts in which they occur.

3.2.2 Brittle rheology and material properties

The wedge is modelled as a mass of homogeneous, cohesive material whose behaviour is visco-elasto-plastic, resembling that of dry quartz sand (Yang et al., 2017). The mechanical parameters assigned to the model are density, Young's modulus, Poisson's ratio, internal friction angle and basal friction angle, gravity, angle of dilation, cohesion and viscosity, with values taken from previous studies (Ellis et al., 2004; Buiter et al., 2006) (see *Table 2-1*). The wedge material deforms elastically at the early stage, followed by strain hardening prior to failure at peak strength (Lohrmann et al., 2003). Further strain leads to softening until the stable dynamic strength is reached (Lohrmann et al., 2003; Panien et al., 2006). The Drucker-Prager failure criterion is employed as a smooth version of the angular Mohr-Coulomb failure criterion to model the thrust development (Buiter, 2012; Tuitt et al., 2012; Yang et al., 2017).

The material deformation is governed by the rheology implemented by the model, which is independent of the rate of model shortening. The material deforms elastically until plastic or viscous yield is reached, after which deformation continues on yield (Buiter et al., 2006). Localised failure in the form of shear bands occurs close to the peak strength at maximum dilation rates, whereas the dynamic stable state is associated with decreased dilation rates (Buiter et al., 2016). Strain softening is simulated by a linear decrease from a peak internal friction angle to a stable frictional angle over a finite strain interval of 0.5-1.0 (finite strain is total accumulated effective strain as measured by the square root of the second invariant of the strain tensor) (Buiter et al., 2006). All these deformation is controlled by the implemented rock properties, failure criterion and strain softening, which are independent of the rate of inward movement of the mobile wall.

3.2.3 Fault parameters

To investigate the fault activity and interaction, we monitored the fault displacement, slip rate, strain rate and fault dip throughout the growth and forward propagation of a fold-thrust belt.

1) Fault displacement was measured as the offset of a marker horizon (initially 300 m above detachment) along the shear zone at every ~16-67 m of shortening, over a total of 3268 m of shortening, which provides adequate details to investigate the evolution of a thrust fault during the wedge building process. The total displacement of a thrust fault is used to quantify the strain distribution across the resultant thrust belt.

2) Slip rate is calculated by the changes of measured fault displacement over time which can be obtained from the model given the constant shortening rate of $1x10^{-11}$ m/s. It is representative of the level of velocity of fault movement, i.e. rapid, or slow.

3) Different from indirectly obtained slip rate, strain rate was monitored at the selected nodes along the thrust zones by the model (*Figure 3.1*). It is determined by the changes of principal strain with time in finite element model. It indicates the precise timing of fault activity and is an equivalent parameter to the generally used slip rate in natural examples.

4) Fault dip is determined by the steepest angle of a thrust zone at the same shortening interval as the displacement, it is used to examine the temporal variation of a thrust angle in a growing fold-thrust belt.

3.3 Model results

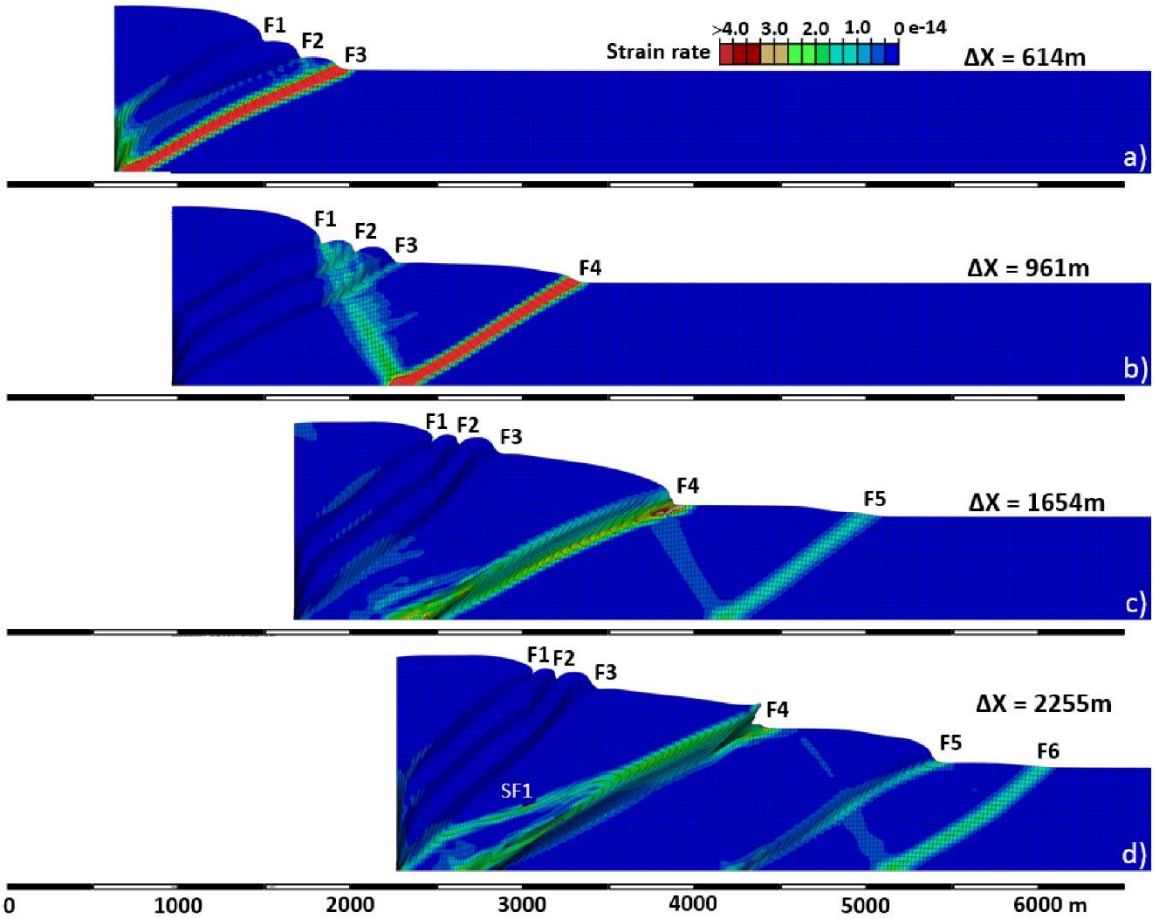

Figure 3.2 Model results showing the distribution of strain rate across the thrust wedge for 4 shortening periods, ΔX indicates the amount of shortening.

After experimentation with a range of input parameters, the model creates a fold-thrust belt which resembles the structures seen from seismic profiles and natural examples (*Figure 3.1* & *Figure 3.2*).

3.3.1 Thrust wedge

The model results are displayed as strain rate at different modelling stages: shortening of 614 m, 961 m, 1654 m and 2255 m (*Figure 3.2*). Here, we choose to display the strain rate ranging between 0 and 4 x 10^{-14} s^{-1} in order to highlight the region with low strain rate and minor deformation in the thrust wedge, the region with strain rate exceeding 4 x 10^{-14} s^{-1} is shown by red grid. Six discrete thrusts (F1-F6) develop sequentially from the hinterland to foreland in piggyback mode, forming a leading imbricate system (Boyer and Elliott, 1982; McClay, 1992). In *Figure 3.2a* & *Figure 3.2b*, as soon as a new (frontal) thrust (F3

and F4) initiates, it attains a high strain rate, with the existing thrusts (F1, F2 and F3) having very low or negligible strain rate. *Figure 3.2c & Figure 3.2d* show that the early formed thrusts (F1-F4) are reactivated during the formation of new frontal thrusts (F5 and F6) as indicated by the high strain rate along the thrust zone. The model also highlights some minor activity along axial surface of fold (*Figure 3.2*), suggesting a component of shortening is accommodated by the active fold axial surface. To reveal the detailed temporal variation of fault activity, the precise strain rate through time needs to be resolved.

In addition to imbricate thrusts, a short-cut fault SF1 with a shallow dip of 19° is developed connecting F3 and F4 (*Figure 3.2d*). SF1 continues to evolve through the rest of simulation, its role in the growth of the connected thrusts (i.e., F4) can be revealed through examining the variations in associated strain rate.

3.3.2 Fault displacement, slip rate and strain rate

The fault displacement, combined with slip rate and strain rate, are used to examine the activity and growth history of the individual faults. For example, the displacement and strain rate of fault F2 is plotted against the amount of shortening (*Figure 3.3*). Since a constant velocity is applied to the mobile wall in the model (*Figure 3.1a*), the shortening is a proxy for time. In *Figure 3.3a*, as soon as the thrust F2 initiates, fault displacement rapidly increases to a stable value 137 m at shortening 660 m with a high slip rate of 0.10 mm/yr. It then continues slowly at a much lower overall slip rate of 0-0.01 mm/yr throughout the rest of deformation. Similar to fault displacement, the strain rate of F2 rapidly increases until it reaches a peak value of 1.1×10^{-13} s^{-1}, at shortening 660 m. This is followed by a significant drop to 3.9×10^{-17} s^{-1}. It then shows temporal variation between 3.9×10^{-17} s^{-1} and 3.5×10^{-14} s^{-1}.

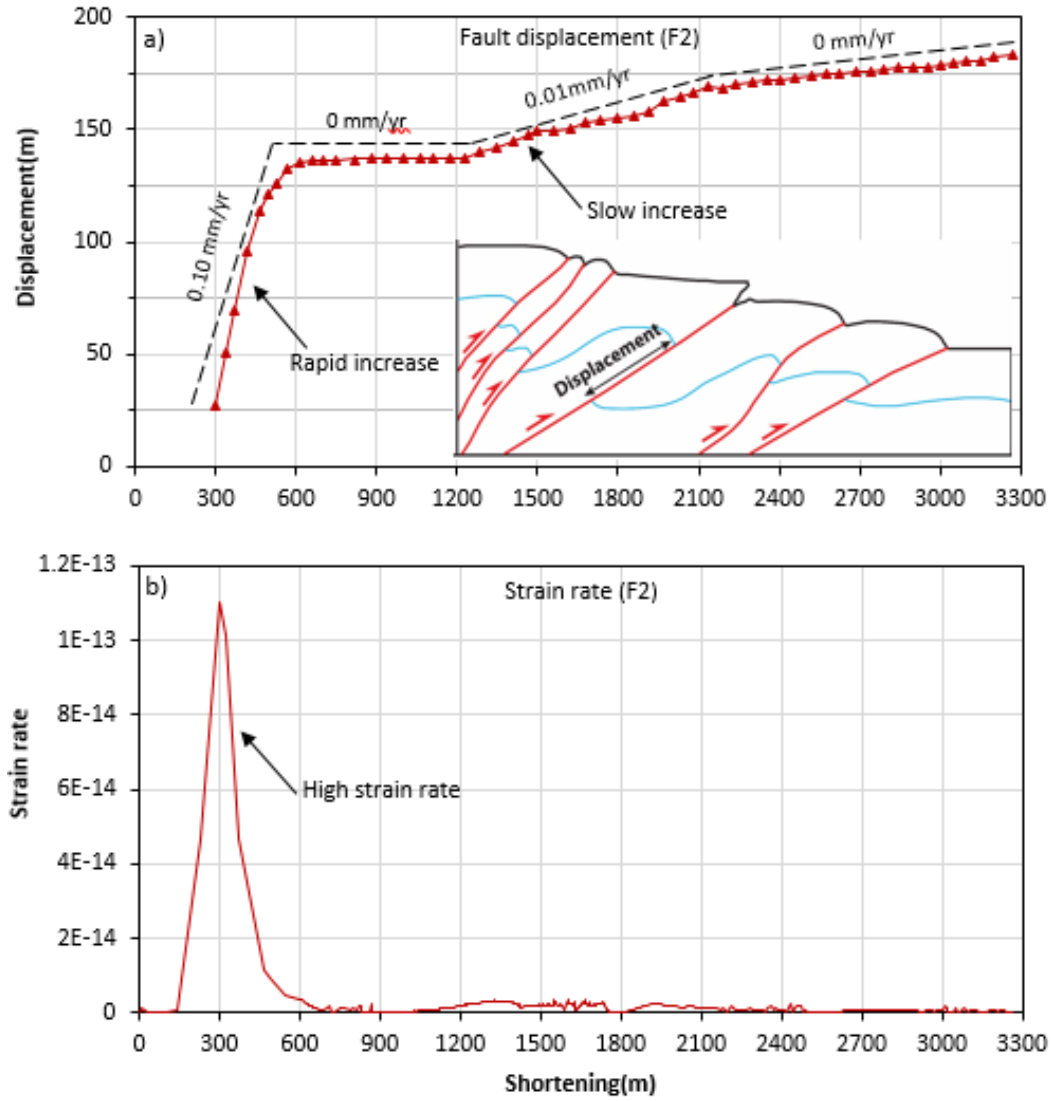

Figure 3.3 Fault displacement and strain rate of fault F2 versus shortening. (a) F2 displacement versus shortening shows that the displacement accumulates rapidly as the new thrust nucleates, followed by a slow and intermittent increase. The dotted line indicates the calculated slip rate. The inset shows how fault displacement is measured. The value with unit mm/yr next to the dotted line represents the slip rate of fault. (b) Strain rate against shortening showing F2 strain rate rapidly increases to a peak value of $1.1x10^{-13}$ s^{-1}*, followed by a significant drop to* $3.9x10^{-17}$ s^{-1} *at shortening 660 m. The strain rate then shows temporal and fluctuating variability at a much reduced rate* $3.8x10^{-15}$ s^{-1} *–* $3.5x10^{-14}$ s^{-1}*. For this and the subsequent figures, the shortening is a proxy for time.*

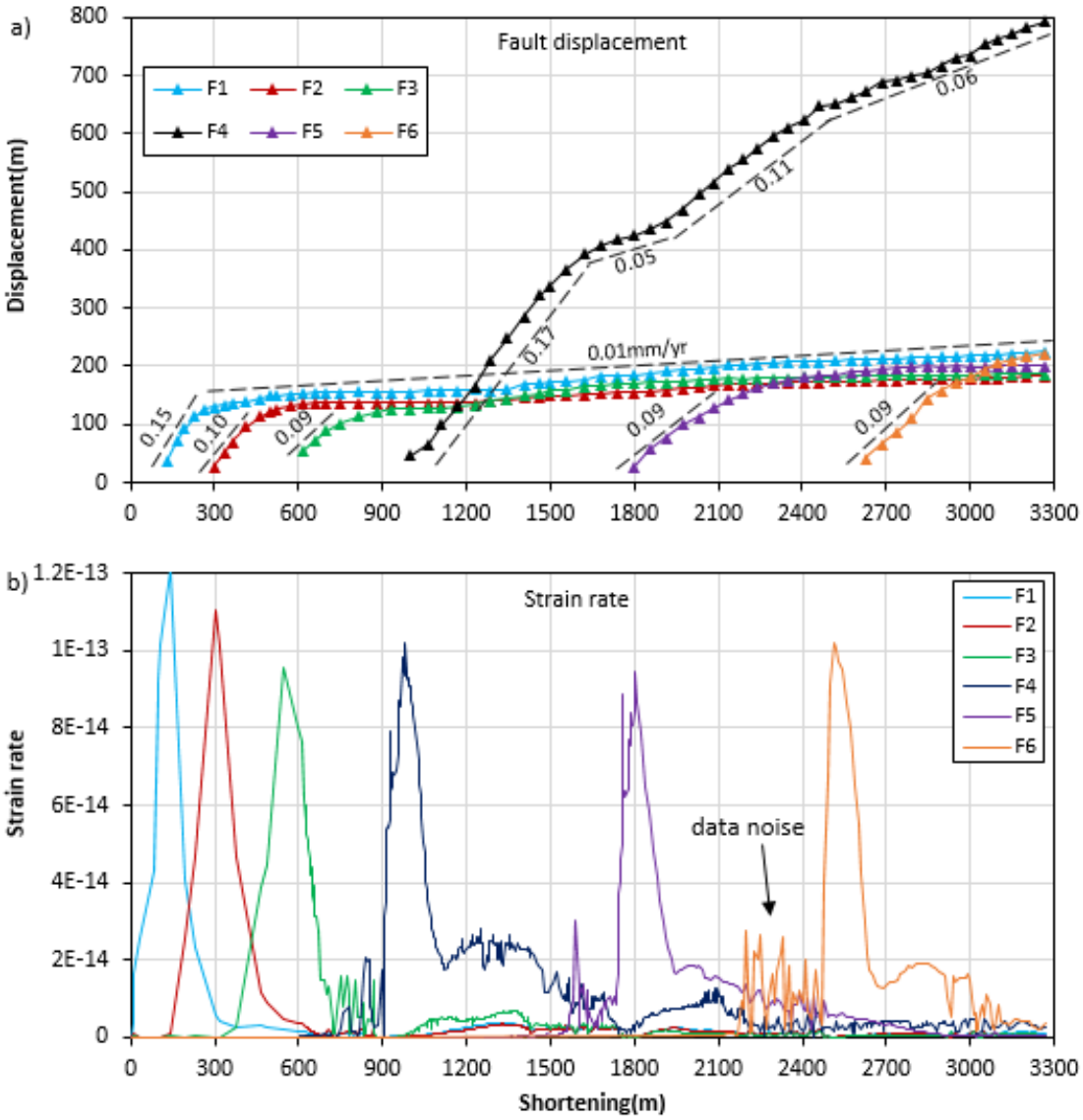

Figure 3.4 Timing relationships of fault displacement and strain rate. (a) Fault displacement versus shortening for faults F1-F6. Note the unit of slip rate is not displayed for each value for saving space. The total displacement of F4 (~793 m) is ~3-4 times of the other faults (183-225m), suggesting F4 plays a key role in accommodating shortening. (b) Strain rate against shortening for thrusts F1-F6.

Intermittent and fluctuating fault activity has been reported by previous studies through examining the change in fault displacement through time in scaled physical analogues (Dixon and Liu, 1992; Adam et al., 2005; Yamada et al., 2006) and dating the syn-tectonic sediments in a natural fault-related fold (Bergen et al., 2017). The minor changes of fault activity that can be monitored in the model are, generally, not resolved in natural examples due to the limited resolution of displacement and time in these studies. Based on the analysis of thrust F2, it is proposed that an individual thrust experiences two distinct stages: (1) rapid growth after thrust initiation corresponding to rapidly increased

fault displacement, high slip rate and high strain rate; and (2) subsequent growth corresponding to slowly accumulated fault displacement, low slip rate and low strain rate (*Figure 3.3*).

Fault displacement for all six faults F1-F6 is plotted against shortening to compare the patterns of fault growth and examine the strain distribution across the thrust wedge (*Figure 3.4a*). Apart from thrust F4, a rapid increase in displacement is observed for each thrust after its initiation, with high slip rates of 0.09-0.17 mm/yr (*Figure 3.4a*), followed by slow fault growth with gradually increased displacement and very low slip rate of 0.01mm/yr. For every two successive thrusts, the stabilized displacement of the older fault (e.g., F1) coincides with the formation of the younger thrust (e.g., F2). This signifies that the major strain is transferred to the front thrust as deformation proceeds in a piggyback mode of thrust development (*Figure 3.2* & *Figure 3.4*). This is in agreement with the previous observation from scaled physical analogue, where the frontal imbricate surfaces are new deformational sites where most of the displacement is taken up (Koyi, 1995). Between the high strain rate of F3-F6 formation (*Figure 3.4b*), three episodes of high-frequency variation of strain rate occur at shortening 600-900 m, 1500-1800 m and 2200-2500 m, which are considered as artefacts caused by the model and are not used in our analysis.

Despite similar patterns of rapid growth at the first stage, the displacement history of F4 is very different from the others (*Figure 3.4*). Most of the thrusts stabilize prior to the initiation of the next in sequence and, thereafter, accumulate displacement (*Figure 3.4a*) slowly at strain rates generally much less than 10^{-14} s^{-1} (*Figure 3.4b*). F4, however, continues to accumulate displacement after the initiation of F5 (*Figure 3.4a*) despite a reduced slip rate of 0.05 mm/yr at shortening 1740-1860 m. After that, it speeds up to a high slip rate of 0.06-0.11 mm/yr to accumulate large displacement through the rest deformation (*Figure 3.4a*). A total of 793 m displacement is accumulated at thrust F4, in contrast, only 179-222m of displacement is taken up on each of the other thrusts. Thus, F4 plays a dominant role, subsequent to its initiation, in accommodating strain across the entire wedge. In addition, the width of F4 shear zone (164m) is also larger than other thrusts (65-79 m) (*Figure 3.1* & *Figure 3.2*), suggesting the evolution of F4 incorporates some further materials.

3.3.3 Short-cut fault

A short-cut fault SF1 develops at the footwall of thrust F3, connecting in-sequence thrusts F3 and F4 (*Figure 3.1* & *Figure 3.2d*). To reveal its evolving history and effect on the growth pattern of connected individual thrust (i.e. F4), we monitor the strain rate of SF1 through time (*Figure 3.5b*). In addition to this, three marker horizons (at height above detachment of 150 m, 300 m and 450 m) are used to record the displacement along the F4 surface, which allows the examination of deformation propagation along a thrust zone (*Figure 3.5b*).

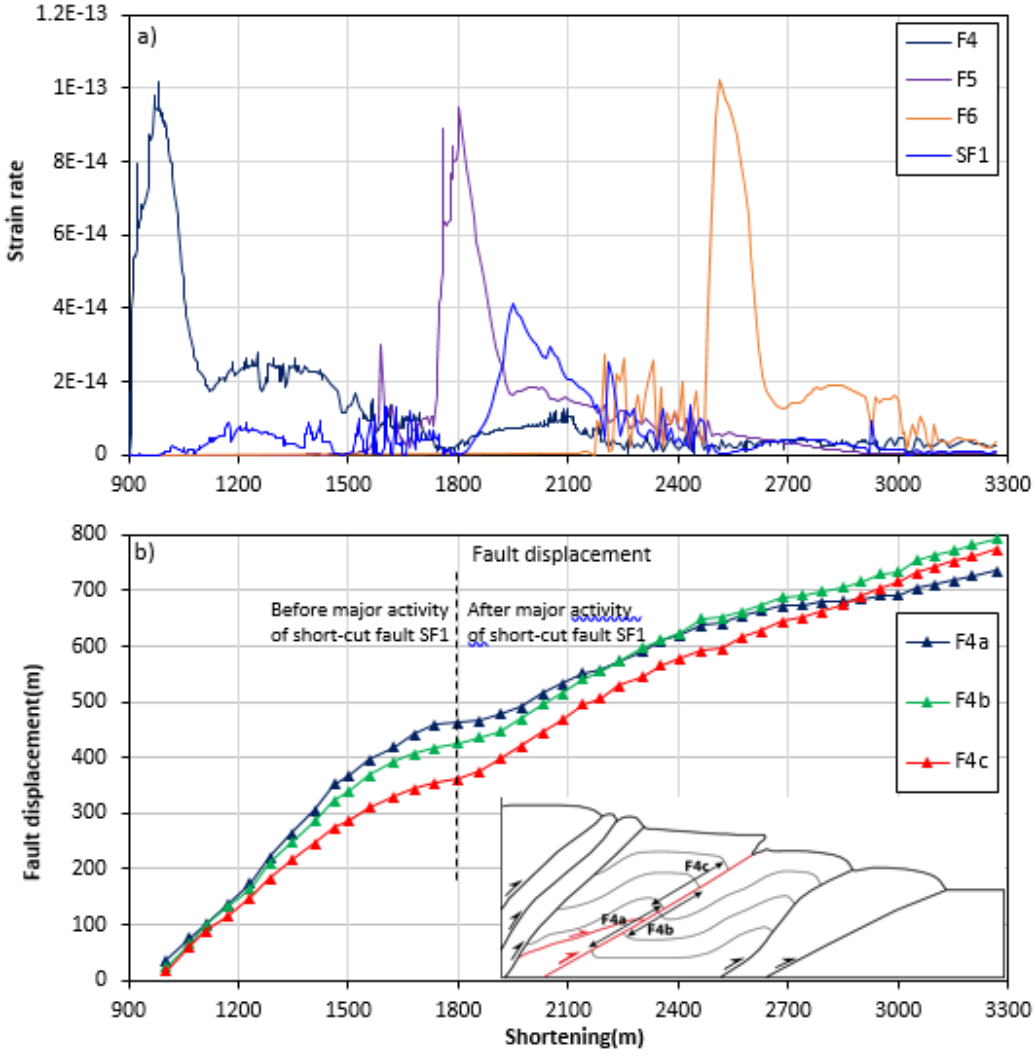

Figure 3.5 Plots of (a) strain rate of short-cut fault SF1 and (b) fault displacement of main thrust F4 against the amount of shortening.

Shortly after F4 develops (at ~1000 m shortening), the strain rate of SF1 starts to increase within a range of low value until 1800 m shortening (*Figure 3.5a*). This stage corresponds to diffused deformation in the folding region where the new fault is about to initiate and

cut through the existing fold, with its tip reaching the surface (Adam et al., 2005; Dotare et al., 2016; Yang et al., 2017), indicating minor strain accumulates prior to the formation of short-cut fault. After F5 forms (at ~1800 m shortening), SF1 experiences increased activity, with high strain rate until ~2400 m shortening, representing the stage of major short-cut fault development. The subsequent evolution of SF1 involves change in strain rate, but at much reduced values (*Figure 3.5a*).

Prior to the major activity of short-cut fault SF1, the displacement along F4 thrust zone decreases upward (*Figure 3.5b*), suggesting that the deformation of an individual thrust propagates from the detachment to the tip along the shear zone (Hughes and Shaw, 2015). After the major activity of SF1, the displacement of F4b, below the SF1 connection, becomes slow to increase and is eventually exceeded by the displacement of F4b and F4c, above the connection (*Figure 3.5b*).

In a fold-thrust belt, out of sequence thrusts (OOST) are those thrusts which do not conform to either a progressive forward-breaking or break-back sequence (Butler, 1987; Morley, 1988; McClay, 1992). In this study, the SF1 develops as a OOST, it initiates out of sequence after F4 at ~1000 m shortening and propagates through the already deformed thrust sheet between F3 and F4 (*Figure 3.1* & *Figure 3.2*). Despite an early initiation, the major activity on SF1 takes place at 1800m-2400m shortening after the formation of F5 (*Figure 3.5a*).

3.3.4 Fault dip

In granular material, the dip angle of shear bands relative to maximum compressive stress σ_1 varies (Buiter et al., 2016) between the Roscoe angle (Roscoe, 1970):

$$\theta_R = 45° - \psi/2 \quad (3\text{-}1)$$

the intermediate Arthur angle (Arthur et al., 1977):

$$\theta_A = 45° - (\varphi + \psi)/4 \quad (3\text{-}2)$$

and the Mohr-Coulomb (MC) angle (Coulomb, 1773):

$$\theta_C = 45° - \varphi/2 \quad (3\text{-}3)$$

where ψ is the angle of dilation (Roscoe, 1970) and φ internal friction angle.

To test the model results against the theoretical prediction, the Roscoe, Arthur and MC angles are computed for the model material parameters (*Figure 3.6*). The dip angles of F1-F3 evolve progressively throughout the thrust belt development, forming 3 distinct stages: 1) initial decrease from 30°-37° near Arthur angle of 36° to the Mohr-Coulomb angle of 27°; 2) subsequent increase to the Roscoe angle of 45°; then 3) eventual stabilization near the Roscoe angle through the rest of model deformation (*Figure 3.6*).

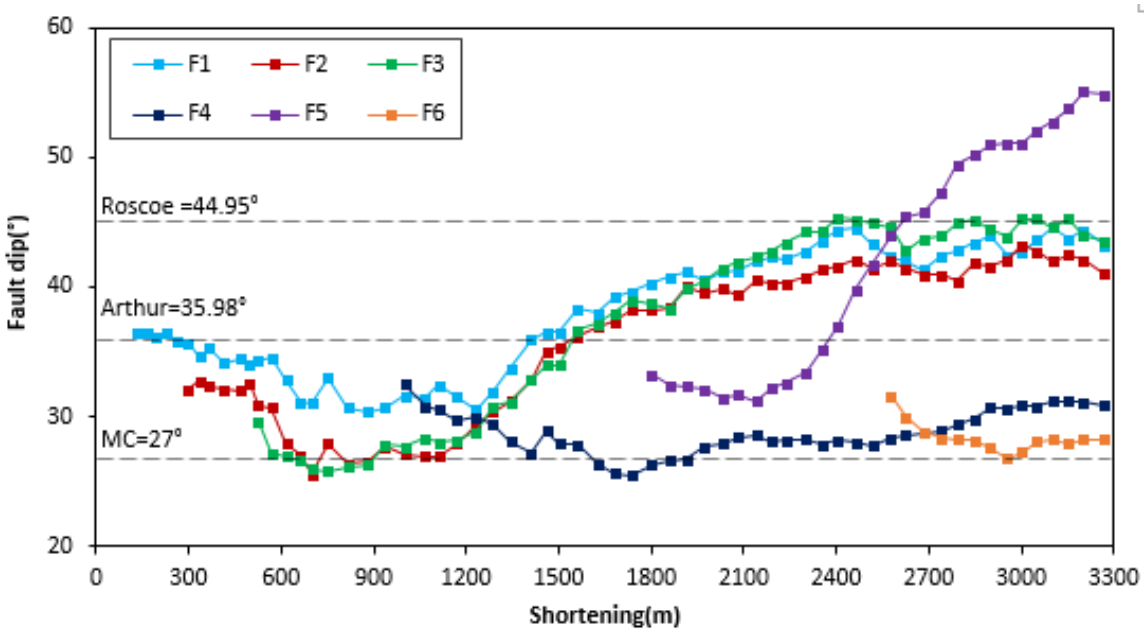

Figure 3.6 Dip angles of thrust faults (F1-F6) versus shortening. Theoretical dip angles of Roscoe (44.95°), Arthur (35.98°) and Mohr-Coulomb (MC, 27°) with respect to the orientation of maximum stress σ_1 are shown by horizontal grey dotted lines. Dips of fault F1-F3 are used to illustrate the distinct stages of fault dip evolution: decrease, increase, stabilization.

Mohr-Coulomb angles require sufficiently fine numerical mesh (Lemiale et al., 2008) and a well solved heterogeneity far away from the box that initiates the shear band and dynamic (not lithostatic) pressures (Kaus, 2010; Buiter et al., 2016). In most other cases, both Roscoe and Arthur orientations are observed and admissible (Lemiale et al., 2008; Kaus, 2010). With progressive contraction, wedge topography builds up (*Figure 3.2*). According to Coulomb Wedge Model, the orientation of maximum compressional stress σ_1 rotates to an angle ψ_b with the detachment (Dahlen, 1984), the fault dip relative to detachment calculated by subtracting ψ_b (6° in this study) from MC (Dahlen, 1984) therefore reduces, as is observed in *Figure 3.6*, with most of the dip decrease occurring in Stage 1. After a new thrust forms at the wedge front, i.e. F4-F6, it effectively rotates the earlier thrusts (F1-F5), leading to the increasing dip angle at Stage 2 (*Figure 3.2 & Figure 3.6*). Previous studies

using physical analogues have made similar observation of early formed thrusts being rotated and steepened by the growth of younger thrusts in the wedge front (Mulugeta, 1988; Hardy et al., 1998; Lohrmann et al., 2003; Koyi and Maillot, 2007; Wu and McClay, 2011; Nilfouroushan et al., 2012). At Stage 3, frontal accretion causes the early formed thrusts to become more distant from the deformation front, and the influence of growth of younger thrusts on older ones reduces. Eventually, the dip of early thrusts become stabilized as the system continues to advance (*Figure 3.2* & *Figure 3.6*).

F5 steepens significantly from 30° to 53° in the Stage 2 (after 2850 m shortening) that exceeds the Roscoe angle. Unlike other thrusts with straight fault surface, F5 develops as a bend fault with a steep ramp and two flats (*Figure 3.1* & *Figure 3.2*). The anomalous dip of F5 can be seen as a result of several controlling factors: the type of structural style, its rotation by the growth of frontal new thrust (i.e. F6). The high dip angle of an in-sequence thrust has also been observed in other models (Buiter et al., 2006; Buiter et al., 2016).

Theoretical prediction of fault orientation is mainly applicable to the initial fault development, the subsequent fault growth is often controlled by additional factors, such as material heterogeneity, mesh resolution, growth of frontal thrusts, changes in the orientation of maximum compressional stress, structural styles, etc.

3.4 Discussion

3.4.1 Growth of a thrust fault

Despite a steady shortening rate of 1.0×10^{-11} m/s (~0.3 mm/yr) for the entire system (*Figure 3.1*), the strain rate of an individual thrust changes over time, with high magnitude as the fault initiates at stage 1 and much reduced value at stage 2. The growth of a fold-thrust belt is characterised by the sequential development of imbricate thrust faults towards the foreland. For every two successive thrusts, the stabilized displacement of the older fault coincides with the formation of a younger thrust in front it, signifying that major strain is transferred to the front with wedge accretion (Koyi, 1995; Koyi et al., 2000). Previous authors (Mulugeta and Koyi, 1987; Koyi, 1995; Wu and McClay, 2011) suggest that early thrusts are rotated, and become locked and inactive as new thrusts form in the foreland accommodating the majority of displacement. Our results partly agree with this, but show that older thrusts remain partially active for long periods of the

thrust wedge development. Both displacement and strain rate of the thrusts in our model show temporal changes, with a second stage of slow growth (*Figure 3.2*, *Figure 3.3* & *Figure 3.4*) extending beyond the initial period of rapid growth. This is in agreement with previous experimental investigations (Dixon and Liu, 1992; Lohrmann et al., 2003; Yamada et al., 2006) and study of natural examples, i.e. Makran Accretionray Prism (Smith et al., 2012), which suggest the early-formed faults in the hinterland of a fold-thrust belt continue to accumulate displacement as deformation proceeds.

Slip rate variability has been reported from previous field based studies and numerical investigations on timescales of 10^2-10^5 yr, and has been attributed to a range of processes, including earthquake cycles, strain partitioning, orogenic wedge thickening, volcanic activity and gravitational process (McClymont et al., 2009; Hergert and Heidbach, 2010; Cowie et al., 2012; Gunderson et al., 2013; D'Amato et al., 2016; Bergen et al., 2017). In this study, we monitor the temporal variation of strain rate, thus providing greater resolution of the relative fault activity. As the strain rate of an individual fault varies significantly through time (*Figure 3.2*, *Figure 3.3* &*Figure 3.4*), there is no single value capable of representing the long-term state of fault activity. Given the use of fault slip rate in estimating earthquake recurrence intervals, variable slip behaviour should be considered in future assessment of seismic hazard.

3.4.2 Tectonic controls on the timing and relative fault activity

The tectonic control on fault growth is revealed through comparing the overall thrust wedge development with the relative fault activity through time. A cycle of wedge building starts as the wedge advances by frontal accretion (*Figure 3.7a*) which is characterised by diffuse deformation across the incipient folding in the wedge front (Mulugeta and Koyi, 1987; Dixon and Liu, 1992; Adam et al., 2005; Dotare et al., 2016), reducing the taper angle below critical (Gutscher et al., 1996, 1998; Yang et al., 2017). At this point, the new thrust has not developed yet, but is about to initiate as indicated by the dotted line in *Figure 3.7a*. The existing thrust (main thrust) is still active, defining the internal accumulation zone (IAZ) that is subjected to contraction, and shows persistent growth with moderate strain rate (*Figure 3.7a*), transporting the whole system towards the foreland along the basal detachment (Koyi et al., 2000). To facilitate this, existing thrusts are reactivated (*Figure 3.7a*) (Nieuwland et al., 2000; Yamada et al., 2006), as

demonstrated by evolution in strain rate and slow increase in fault displacement (*Figure 3.2*, *Figure 3.3* &*Figure 3.4*). A short-cut fault is about to initiate out of sequence to connect the main thrust and the thrust behind it as shown by the black dash line (*Figure 3.7a*).

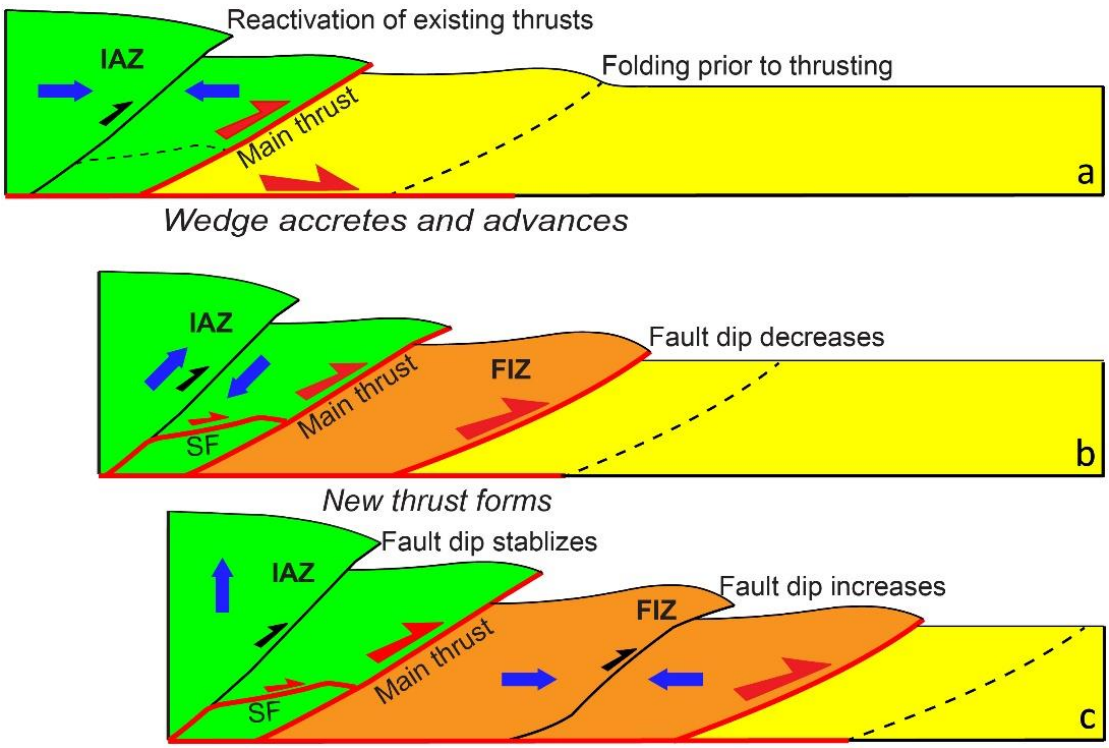

Figure 3.7 Schematic cartoon showing the evolution of fault displacement, fault activity, fault dip and the formation of short–cut fault in a developing fold-thrust belt. Red line represents active fault, black line denotes inactive or slightly active fault, dotted line indicates the forthcoming thrust, the size of arrow represents the level of fault activity and scale of fault displacement. IAZ is internal accumulation zone, FIZ the frontal imbrication zone, SF short-cut fault.

The rapid propagation of the thrust wedge ends up with the formation of a new thrust, breaking through the existing fold with its tip reaching the surface (*Figure 3.7b*) (Yang et al., 2017), which typically forms a frontal imbrication zone (FIZ). The new (frontal) thrust then shows significant activity and accommodates the majority of displacement while the older thrusts in the IAZ become inactive or slightly active with very low strain rate (*Figure 3.7b*), suggesting that the strain is transferred to the newly formed thrust surface. During this period, the main thrust effectively acts as the boundary between IAZ and FIZ, it has to grow continuously to adjust the deformation across the two deformation regions.

The entire wedge is then subjected to shortening and thickening to build the topography to critical (Gutscher et al., 1996, 1998), which leads to a decrease in dip angle for the new frontal fault (*Figure 3.7b*). Gunderson et al. (2013) observed a major deceleration in slip rate of the Salsomaggior fault to be coincident with orogenic wedge thickening due to the initiation of new thrust(s). This is in agreement with our model of relative fault activity during wedge thickening. A new short-cut fault cuts through the already deformed thrust sheet and shows activity, forming a typical horst. The dotted line ahead of the FIZ denotes the position of the next-formed thrust.

With further shortening, a new thrust forms at the wedge front, marking the start of a new cycle (*Figure 3.7c*). Due to continued frontal accretion and the growth of a new thrust, the earlier fault in the FIZ is rotated and steepened to very high angle, producing a bend fault with a steep ramp (*Figure 3.7c*). In contrast, the dip of old thrust in the IAZ is stabilized as the fault distance from the deformation front increases with time. The IAZ is thickened to a high elevation and is unable to take additional shortening, which is reconciled by the frontal compaction in FIZ. Both main thrust and short-cut fault show continuous activity as deformation proceeds.

The kinematic evolution of a thrust belt involves low-level activity of existing thrusts when moving the entire system forward as wedge accretes, but with the majority of strain accommodated by frontal thrust when building the wedge to critical. In a fold-thrust belt, the main thrust dividing the system into two tectonic regions (i.e. IAZ and FIZ) has to activate continuously to accommodate the deformation.

3.4.3 Strain distribution across a thrust wedge

As the material properties defined in this model do not include compaction, two primary components of deformation are thought to accommodate the overall shortening of a fold-thrust belt: thrusting and folding. The strain distribution across the wedge is quantified by monitoring the accumulated fault displacement in the thrust system. As shown in *Figure 3.4a*, of the total shortening (3268 m), 55% is taken up by thrusting (1811 m) with folding accounting for the remaining 45%.

Lohrmann et al. (2003) proposed that an internal accumulation zone (IAZ), composed of occasionally reactivated older thrusts, is separated by an OOST from the frontal

imbrication zone (FIZ), containing several constant active thrusts in a fold-thrust belt. The IAZ is characterised by diffuse deformation across the wedge while the FIZ shows localized shear displacement along distinct imbricate thrusts. As shown in *Figure 3.1* & *Figure 3.2*, the main thrust F4 divides the wedge into two deformation domains, with the frontal one (ahead F4) equivalent to FIZ and the behind one similar to IAZ. As it acts as a boundary to adjust deformation across two deforming regions, it has to grow consistently, accumulating large displacement.

Our results generally agree with the previous view that OOST accommodates great displacement within an active fold-thrust belt (Butler, 1985). However, it is worth noting that, the main thrust F4 is equivalent, but different from previously recognized OOST in natural systems as it forms in sequence after fault F3 (*Figure 3.2*). With additional shortening, evolution of F4 deforms additional material into the shear zone, expanding its width.

In an active fold-thrust belt, thrusting accommodates more strain than folding, and among the thrusts, the main thrust dividing the entire system into the internal accumulation zone and frontal imbrication zone can play a dominant role in accommodating strain.

3.4.4 Short-cut faults

Short-cut faults have been recognized in some areas where inversion tectonics develops (Underhill and Paterson, 1998; Mora and Parra, 2008). They generally form with a shallow dip in the footwall of a high-angle inverted fault, produced by reactivation of earlier listric normal faults. During the later compression, the upper, steeply dipping part of the fault surface is unable to take up the reverse slip leading to the development of a short-cut thrust with a lower dip in the footwall. In this study, pre-existing steep faults do not exist, but early thrusts steepen by rotation. For example, F3 steepens to 39°, at shortening 1800 m (*Figure 3.6*), and roots adjacent to the left corner of the model (*Figure 3.2*). With additional deformation, F3 cannot accommodate further slip along its high-angle surface and a short-cut fault SF1 is induced with a shallow dip of 19° (*Figure 3.2*).

Prior to the formation of SF1, the displacement along F4 decreases upwards (*Figure 3.5*), suggesting that individual thrusts propagate upward, as is also observed in scaled physical

analogues (Deng et al., 2014) and in natural examples (Hughes and Shaw, 2015). After SF1 forms, it shows continued activity as the wedge advances (*Figure 3.5a*) as displacement is transferred upward from the detachment. The connected lower section of F3, SF1 and upper section of F4 (*Figure 3.1* & *Figure 3.2*) acts as a path taking up some displacement. As a result, F4a reduces relative to F4b and F4c, changing the growth pattern of F4 (*Figure 3.2* & *Figure 3.5*).

3.5 **Conclusions**

By making refined measurements of thrust fault parameters within a 2-D numerical model, this study provides insights into the sequential development, growth and relative activity of thrusts fault during the kinematic evolution of a fold-thrust belt. The key findings are:

1. The precise timing of thrust fault activity can be monitored in the model. An individual thrust fault experiences two distinct evolving stages: (1) rapid growth immediately after its formation; (2) subsequent slow growth.

2. When a thrust wedge accretes, the existing thrusts reactivate, but at a lower strain rate, facilitating the forward propagation of the entire system. As soon as a new (frontal) thrust initiates, it experiences significant activity with high strain rate while the older thrusts undergo minor or negligible activity as the wedge builds to critical.

3. The model results indicate that thrusting accommodates a little more strain than folding in a growing fold-thrust belt.

4. A major thrust divides the entire system into two deforming regions. This thrust remains active throughout the subsequent development of the system and, hence, plays a key role in accommodating strain across the wedge.

5. Short-cut faults can develop between two imbricate thrusts and accommodate a component of shortening, changing the displacement pattern along an individual fault.

6. Thrust fault dip evolves through three different stages: initial decrease due to the rotation of the orientation of maximum compressional stress σ_1; subsequent increase

due to thrust rotation as frontal faults in front of it grow; and eventual stabilization as distance from the deformation front increases with time.

Using 2D finite element model, this study provides insights into the changes in fault growth, interaction between multiple faults, and the tectonic control on fault activity in a developing a fold-thrust belt. These results can be used to better understand the fault system development and its implication on hazard assessment.

Chapter 4 Fold-Thrust Belt Restoration Using New Area Balancing Methods

Abstract

Restoring a geological cross-section to its original, pre-deformational state is an important part of making a structural interpretation (Fossen, 2010). The conventional area balancing method uses a single regional slope, usually parallel to the basal detachment, to restore a deformed section to an initial rectangular shape. Most fold-thrust belts in areas of contraction exhibit a wedge or trapezium shape in cross-section with sedimentary sequence thinning into the basin. Although the initial regional slope of a stratigraphic layer is difficult to determine, it is unlikely to be parallel to the basal detachment fault, questioning the validity of many existing restorations.

To address this, two new, simple, quantitative solutions are developed to restore a thrust belt using various regional dips. This assumes that the initial shape is a general trapezium, allowing exploration of the original dip of the regional in controlling the shortening estimate. The methods are then tested against sandbox models and natural examples of fold-thrust belt from Hikurangi accretionary wedge and NW Borneo using a range of input parameters to evaluate the uncertainties in shortening with results being very sensitive to the dip of regional slope. This study highlights the significance of regional slope on area balancing restoration: a higher regional dip results in less shortening while a lower regional dip leads to more shortening. Accuracy of shortening estimate requires independent constraint of parameters, particularly the initial regional slope, not greater precision in their measurement. Hence, absolute values of shortening are probably not attainable in most thrust belts.

The new methods are generally applicable, since they are concerned mainly with the gross cross-section area of the system, rather than details of the lithology, rheology, fluid pressure or other factors that control the form and detailed expression of the final structure.

4.1 Introduction

Structural restoration is a technique that is applied to restore a strained geological cross-section to its original, undeformed state, and is an important part of making a structural interpretation (*Figure 4.1*) (Fossen, 2010). It is basically a tool used to predict the unknown initial geometry of a cross-section from its known final geometry and, hence, is concerned mainly with three elements:

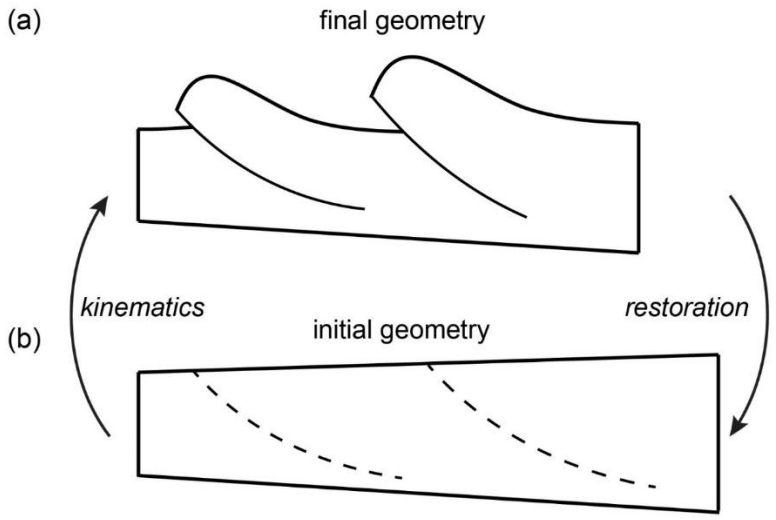

Figure 4.1 Schematic diagrams showing the concept of structural restoration. (a) strained geological cross-section with known final geometry, (b) restored retro-deformational state of cross-section with predicted initial geometry.

(1) The initial geometry, i.e. the original shape of the cross-section before deformation, which is usually unknown, but may be constrained by the pre-deformational history or setting (*Figure 4.1b*);
(2) The final geometry, which is generally known to some degree of accuracy and resolution from surface and/or sub-surface investigation (*Figure 4.1a*);
(3) The kinematics, i.e. the proposed movement path from initial geometry to final geometry, which generally involves assumption of various stages of tectonic deformation.

To perform a structural restoration, some form of balancing is employed as a fundamental principle (Chamberlin, 1910; Dahlstrom, 1969). This involves relating a geometrical measure in the deformed state to undeformed state, such as length, area or volume, which is generally assumed to remain unchanged (balanced). Line-length balancing presumes constant bed length both in deformed and undeformed states (Koyi

et al., 2004). Area balancing assumes that plane strain is operating during deformation to conserve the cross-sectional area (Chamberlin, 1910; Goguel, 1962; Dahlstrom, 1969; Hossack, 1979; Woodward et al., 1990).

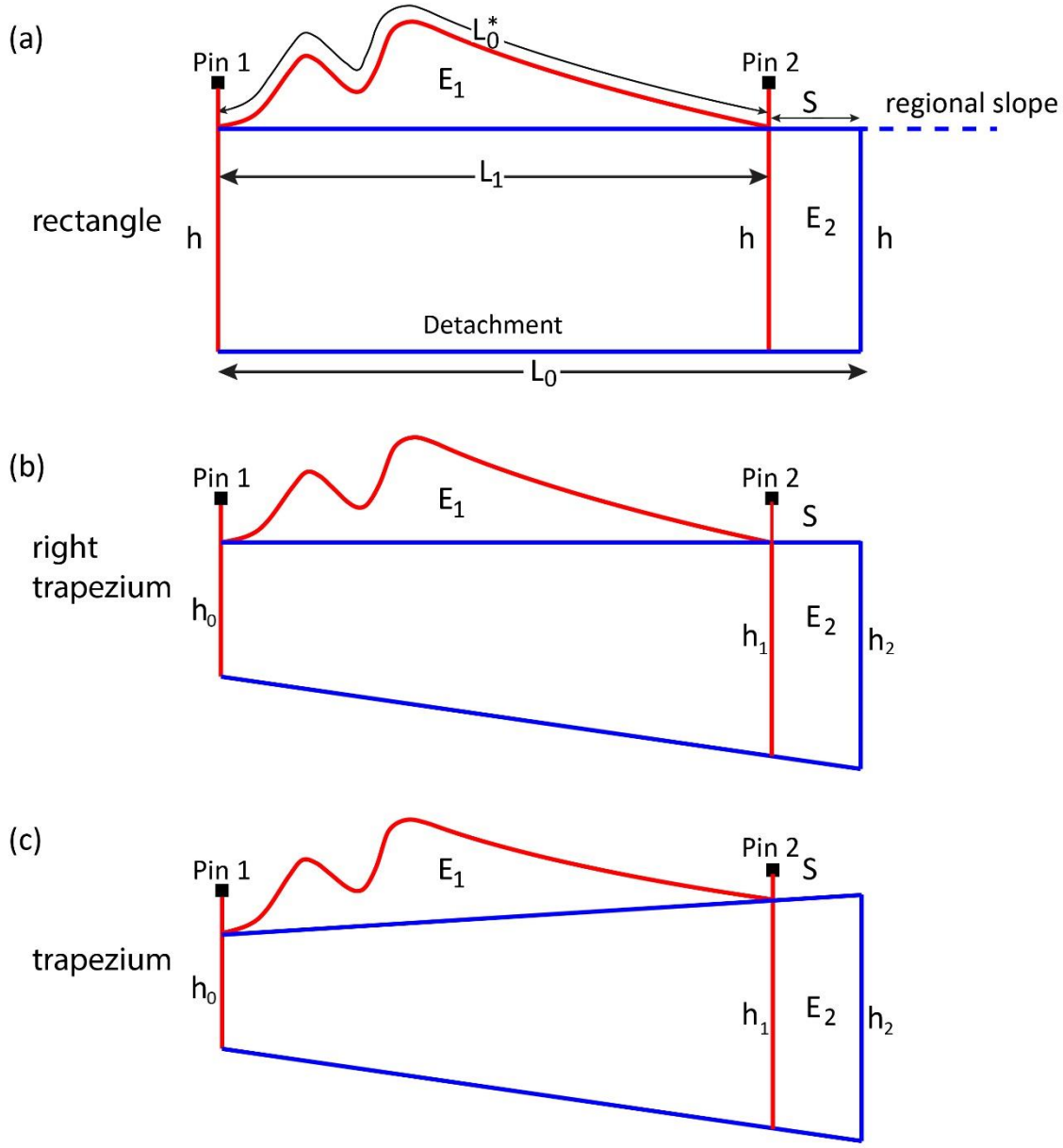

Figure 4.2 The relationship between excess area (E_1), shortening above detachment (S) and depth to detachment as formulated by Chamberlin (1910). L_0^* = curved bed length, L_1= length of deformed region, L_0 = restored length of cross-section, h/h_0 = depth to detachment at the front, h_1 = depth to detachment at the backstop of deformed section, h_2= depth to detachment at backstop of restored section. (a) horizontal regional slope and basal detachment; (b) horizontal regional slope and oblique basal detachment; (c) both oblique regional slope and basal detachment.

The notion of a balanced cross-section was first used by Chamberlin (1910) to predict the depth to detachment across a fold belt from detailed surface observations. This method provides the conceptual background for the use of models to predict structural geometries (e.g., Bucher, 1933; Goguel, 1962; Dahlstrom, 1969; Ramsay and Huber, 1987; Bulnes and Poblet, 1999; Butler, 2013). The principle of balancing is most clearly stated in the above works and there are many examples of its application. Structural restoration techniques may be used to calculate the orogenic shortening (Hossack, 1979; Boyer and Elliott, 1982; Mitra and Namson, 1989; McQuarrie, 2004; Judge and Allmendinger, 2011; Masini et al., 2011; Allmendinger and Judge, 2013). Balancing is widely used to validate structural interpretations or suggest the need for revisions (Bally et al., 1966; Dahlstrom, 1969; Boyer and Elliott, 1982; Dahlstrom, 1990; Woodward et al., 1990; Wilkerson and Dicken, 2001). Comparison of area and line-length balancing may be used to calculate depth to detachment (Chamberlin, 1910; Dahlstrom, 1969), indicate the presence of significant layer parallel strain (Sans et al., 2003; Koyi et al., 2004; Lathrop and Burberry, 2017), and evaluate the lateral compaction (Butler and Paton, 2010). Finally, structural restoration is used to interpret the deformation history (Yin and Kelty, 1991; Lickorish and Ford, 1998; Ghisetti et al., 2016).

The Chamberlin (1910) method was originally developed for sedimentary sequences with initially parallel layers and a planar basal detachment, i.e. constant bed length and thickness (*Figure 4.2a*). It uses the geometry of a folded layer to predict the detachment location underlying a fold. The regional is defined as the original position of this folded layer prior to deformation, and the excess area E_1 is the area of material in the fold that is uplifted by deformation to a position above its original strata level, i.e. regional slope (horizontal in this case, *Figure 4.2a*). The two vertical pin lines set up the boundaries of the strained section that is subjected to area balancing restoration.

The Chamberlin (1910) method involves three geometric parameters, obtained from the deformed cross-section: the length of folded layer L_0^*, the excess area above regional slope E_1 and the length L_1 between the two pin lines (*Figure 4.2a*). Based on the assumption of line balancing and area balancing

$$L_0^* = L_0 \quad (4\text{-}1)$$

$$E_1 = E_2 \quad (4\text{-}2)$$

where L_0 is the original bed length equivalent to the length of the undeformed cross-section, and E_2 is the area displaced above the detachment (*Figure 4.2a*)

The shortening S derived from bed length measurement is given by

$$S = L_0^* - L_1 \quad (4\text{-}3)$$

and the displaced area E_2 is determined by

$$E_2 = h*S = E_1 \quad (4\text{-}4)$$

where h is the depth to detachment. Note it is constant at the two pin lines because the regional and basal detachment are parallel in this model.

Rearranging formula (4) predicts the detachment depth

$$h = E_1/S \quad (4\text{-}5)$$

Equation (3) is substituted into (5) and solved for the depth to detachment to give

$$h = E_1 / (L_0^* - L_1) \quad (4\text{-}6)$$

The Chamberlin (1910) technique can be reversed to calculate orogenic shortening of a cross-section if the depth to detachment is known (Hossack, 1979; Woodward et al., 1990; Moretti and Callot, 2012).

$$S = E_1/h \quad (4\text{-}7)$$

By using a single regional slope that is parallel to basal detachment, the Chamberlin (1910) method restores a geological cross-section to a rectangle, representing the initial geometry (*Figure 4.2a*).

Despite significant progress in balancing cross-section by Chamberlin (1910) method, several problems arise from the underlying assumptions:

(1) the predicted depth to detachment (Equation 4-6) is often found to be substantially deeper than imaged (Faill and Nickelsen, 1999). This discrepancy is primarily caused by ignoring the layer parallel strain (i.e. penetrative strain), a significant amount of shortening that has been recognized both in scaled physical models and field observations (Sans et al., 2003; Koyi et al., 2004; Butler and Paton, 2010; Groshong et al., 2012; Moretti and Callot, 2012; Wiltschko and Groshong, 2012; Şengör and Bozkurt, 2013; Lathrop and Burberry, 2017). Bed length does not remain constant during deformation.

The shortening calculated using Equation 4-3 based on bed-length measurement is therefore insufficient to account for the overall shortening of a cross-section.

(2) The Chamberlin (1910) method produces an apparent rectangle for a restored cross-section with the upper surface defining a 'regional' parallel to a planar, usually horizontal, basal detachment (e.g., Dahlstrom, 1969; Hossack, 1979; Mitra and Namson, 1989; Butler, 2013; Schori et al., 2015; Hubbard et al., 2016). In fact, this is not the case for the most fold-thrust belts, where the basal detachment is typically dipping to the hinterland (Davis et al., 1983; Dahlen, 1990) (*Figure 4.2b*). The depth to detachment in the region of this kind varies, increasing from foreland to hinterland (h_0-h_2 in *Figure 4.2b*). If the regional slope remains horizontal, the restored cross-section is therefore a right trapezium (*Figure 4.2b*) rather than a rectangle (*Figure 4.2a*). This right trapezium is composed of two parallel sides (vertical in this case) equivalent to the boundaries of a retro-deformational cross-section, a horizontal line representing the regional slope and an oblique line representing the inclined detachment.

(3) In many geological settings, the initial regional slope of a stratigraphic layer need not be horizontal (e.g., Mishra and Mukhopadhyay, 2012). In many convergent plate boundaries, the thrust belts exhibit an overall wedge shape with a foreland-dipping topographic slope and a hinterland-dipping basal detachment, i.e. narrowing sedimentary sequence towards the foreland (Davis et al., 1983). This explicitly indicates that the initial regional slope of a sedimentary layer is likely to dip to foreland (*Figure 4.2c*), although the accurate initial geometry is unresolvable from the final geometry. In this paper we explore the idea of restoring to a general trapezium (*Figure 4.2c*), rather than a rectangle (*Figure 4.2a*) or right trapezium (*Figure 4.2b*).

We represent the undeformed section with a general trapezium (blue in *Figure 4.3*) that is pinned on the left. The trapezium sits on a fixed detachment with slope β and has a surface slope (α_0). Firstly, we consider moving a rigid, right-hand block to the left, assuming it acts as a vertically continuous 'end-plate', similar to the 'snow-plough' envisaged in the Coulomb taper model (Davies, et al., 1983). If the trapezium deforms homogeneously it will produce a new trapezium with greater surface slope (α) where the dash line resembles the resultant shape of the fold belt (*Figure 4.3*). Note that the surface slope α generalizes the first-order topographic relief of a fold-thrust belt in accordance with the critical taper wedge model by Davies et al. (1983). The excess area above the

regional is balanced by a trapezium of equal area to the right of the 'end-plate', which is the equivalent to the 'back-stop' used in many critical taper models.

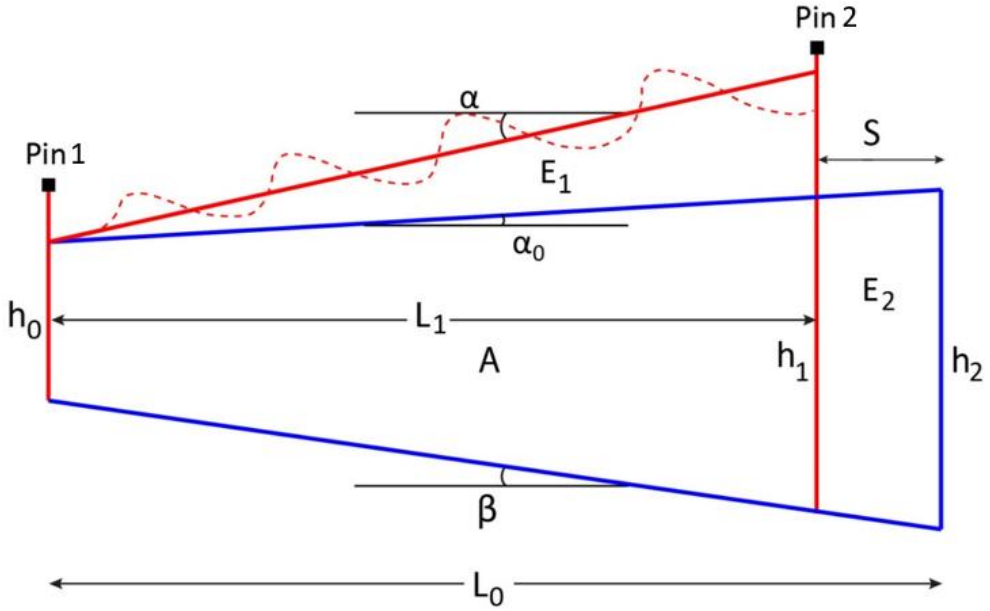

Figure 4.3 Model 1. A trapezium model of original (blue) and deformed (red) wedges to show the principles of area balancing restoration. α= topographic slope, β= basal dip, α_0 = dip of regional slope, E_1= excess area, E_2= displaced area above basal detachment, S= shortening, L_1= length of deformed section, L_0 = length of restored section, H_0= depth to detachment at the fixed pin line, H_1= depth to detachment at the mobile pine line, H_2= depth to detachment at backstop of restored section.

An alternative model (Model 2) assumes that the material to the right (hinterland) simply moves up the basal detachment with no internal deformation, and that there is continuity between this and the deforming wedge (*Figure 4.4*). This situation is approximated in many fold-thrust belts and will produce heterogeneous deformation in the wedge and produce an excess area above the regional. In this model the line connecting the top corners of the deformed wedge (OB in *Figure 4.4*) represents a pseudo-regional, linking the stratigraphy across the wedge. Note that this is not the true regional as the right-hand block has been displaced up the detachment.

4.2 Methodology

4.2.1 Model 1, trapezium shape

We assume that the original shape is a trapezium, with surface slope α_0 (blue in *Figure 4.3*), and is shortened by a distance S, with the material deforming to produce a

trapezium with slope α (red in *Figure 4.3*). The two vertical sides of the trapezium remain parallel. The front one is a fixed boundary (i.e. in x, z direction) and has no height change (i.e. h_0), whereas the 'back one' moves forward and allows slip parallel to it, thus the thickness within the pile changes from h_2 to h_1. This is similar to the setup of scaled sandbox models with a fixed wall in the front and a mobile wall in the back, imposing compression to the system (e.g., Schreurs et al., 2006). In this model, the known parameters that are essential to area-balancing restoration are dip of basal detachment β, length of section L_1 and the depth to detachment at the deformation front h_0 and at the backstop h_1. From these we can determine the final slope angle (α) and cross-sectional area A.

$$A = L_1 * L_1 (\tan \alpha)/2 + L_1 * L_1 (\tan \beta)/2 + L_1 * h_0 \quad (4\text{-}8)$$

Two model parameters, basal dip β and the depth to detachment h_0 at wedge front, are fixed during restoration. Generally, we only need to assume a value for the original topographic slope α_0 in order to determine the excess area (E_1) and, thus, the restored shortening of the cross-section (*Figure 4.3*). However, instead of using the excess area to restore a cross-section, as adopted in conventional area balancing method (e.g., Chamberlin 1910; Dahlstrom, 1969; Hossack, 1979), we use the area of the trapezium as a whole to restore it based on area conservation. Under these conditions, the assumed initial regional slope α_0 is utilized, in combination with the shortening S, to obtain the cross-sectional area A of the restored section (i.e. blue trapezium) (*Figure 4.3*), where

$$A = (L_1+S)*(L_1+S) *(\tan \alpha_0)/2 + (L_1+S)*(L_1+S) (\tan \beta)/2 + (L_1+S)*h_0 \quad (4\text{-}9)$$

The restored cross section area A is equivalent to the deformed cross-section area, which is a known parameter (*Figure 4.3*). The initial length of section L_0 is the sum of current wedge length and restored shortening:

$$L_0 = L_1 + S \quad (4\text{-}10)$$

Substituting (10) in (9) gives:

$$A = L_0 * L_0 * (\tan \alpha_0 + \tan \beta)/2 + L_0 * h_0 \quad (4\text{-}11)$$

Equation 4-11 is a quadratic equation with one unknown L_0, and can be rearranged as:

$$(\tan \alpha_0 + \tan \beta)/2 * L_0^2 + h * L_0 - A = 0 \quad (4\text{-}12)$$

the solution for the original wedge length L_0 therefore is

$$L_0 = \frac{-h \pm \sqrt{h^2 - 4(\tan\alpha_0 + \tan\beta)(-A)}}{2(\tan\alpha_0 + \tan\beta)} \quad (4\text{-}13)$$

Equation 4-13 gives two solutions for L_0, but only the positive one is physically possible.

The Equation 4-13 is substituted into 4-10 with rearrangement, and solved for the shortening S to give

$$S = \frac{-h + \sqrt{h^2 - 4(\tan\alpha_0 + \tan\beta)(-A)}}{2(\tan\alpha_0 + \tan\beta)} - L_1 \quad (4\text{-}14)$$

Although the excess area E_1 is not used in the restoration presented above, its value can be resolved by direct geometric analysis (*Figure 4.3*). The difference between the overall area A and the trapezium constrained by two pin lines, basal detachment and initial regional slope (*Figure 4.3*)

$$E_1 = A - (h + h_1) * L_1 / 2 \quad (4\text{-}15)$$

So far we have developed a theoretical model to restore a fold-thrust belt on the assumption of preserved cross-sectional area, termed as “trapezium method”. This method avoids the limits of traditional method that assumes single regional slope parallel to basal detachment restoring geological section to a rectangle, which is unlikely to represent the original shape of a deformed thrust belt. Instead, this model highlights the trapezium shape of a restored thrust belt (*Figure 4.3*).

Figure 4.5 shows a sequence of deformed wedges developed for the initial wedge of length 100 km, h_0 = 2.5 km, basal slope β = 2° and surface slope α_{01} = 1.1°, subject to shortening of 10, 20 and 30 km. Note the surface slope α of this trapezium cannot exceed the critical taper angle as predicted by Davies et al. (1983). If we consider this sequence as a forward model of the thrust wedge in red, then the other wedges could be considered as the restored shapes assuming different initial regional slopes (α_{03}, α_{02}, α_{01}), giving estimated shortening values S_{03}, S_{02} and S_{01}. These results are generalized in *Figure 4.5b*. The same discussion applies to the case where the deformation in the wedge is heterogeneous (*Figure 4.3*).

4.2.2 Model 2, assuming continuity and using pseudo-regional

The model in the previous section is very simple and assumes a homogeneous strain in the deformed wedge, with no deformation behind this, and a discontinuity in strain at the "back stop". In most fold-thrust belts there is some degree of continuity between the deformed and undeformed regions. If we assume that the material to the right

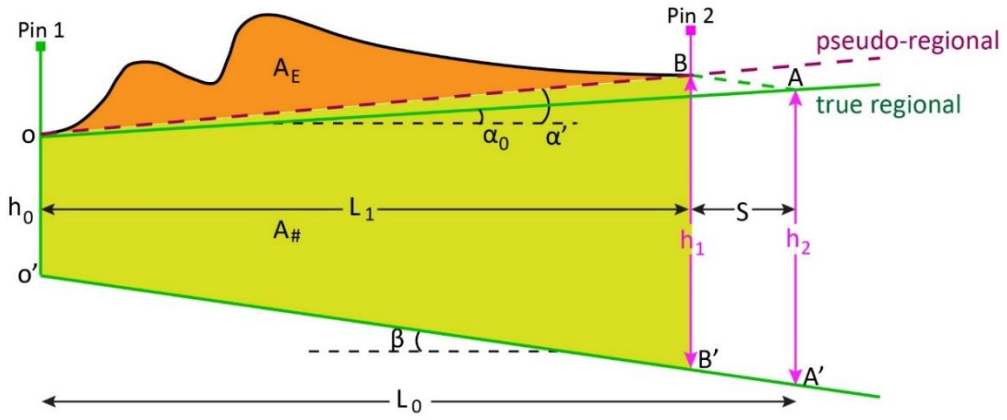

Figure 4.4 Model 2. A continuous trapezium model assumes that the material to the right (hinterland) simply moves up the basal detachment with no internal deformation, and that there is continuity between this and the deforming wedge. β= basal dip, α_0 = dip of regional slope, α' = dip of pseudo-regional, A_E= area above pseudo-regional, $A_\#$= the below the pseudo-regional (OBB'O'), S= shortening, L_1= length of deformed section, H_0= depth to detachment at the front, H_1= depth to detachment at backstop of deformed section, H_2= depth to detachment at backstop of restored section.

(hinterland) simply moves up the basal detachment with no internal deformation and that the deformation in the fold-thrust belt is heterogeneous and simply dies out to the vertical walls of the trapezium, then we have a situation as in *Figure 4.4*. Continuity between the deformed and undeformed blocks means that lengths $h_1 = h_2$, with the height of h_2 simply raising from A to B as the undeformed block slides up the basal detachment. Apparently, the slope of OB is different from the true regional of OA, and is defined here as the pseudo-regional. In this case it is useful to consider this pseudo-regional and determine the excess area above it (A_E) and the area of the trapezium below it, $A_\#$ (constrained by OBB'O'),

$$A_\# = ½ (h_0 + h_2) L_1 \quad (4\text{-}16)$$

Balancing these with the area of the original trapezium gives

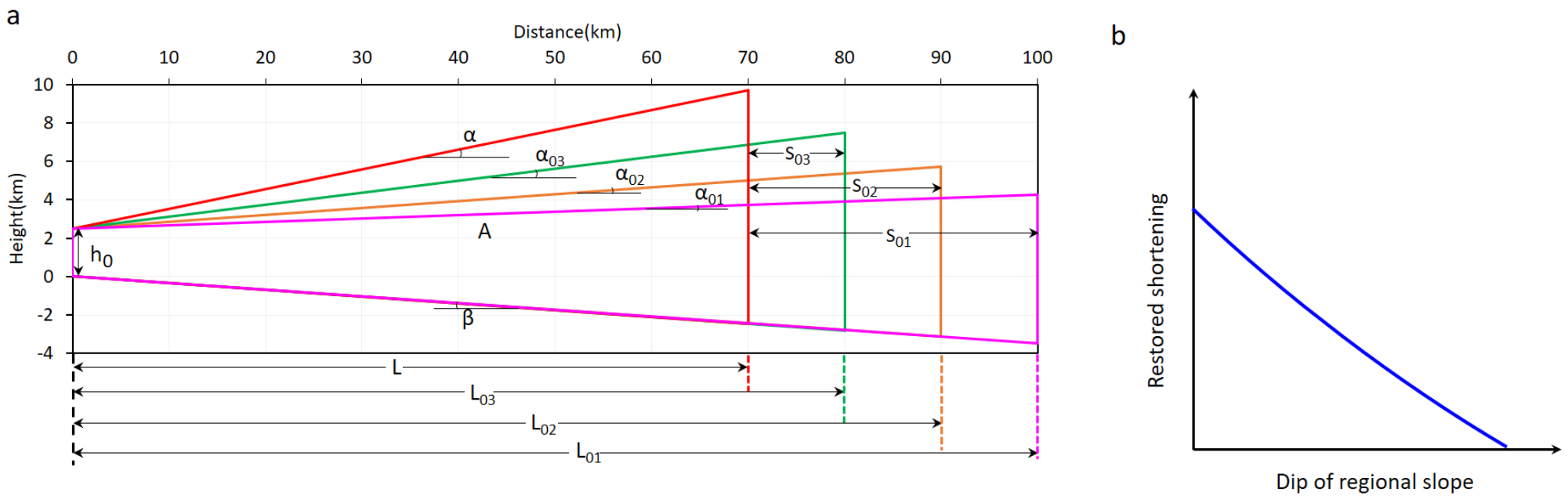

Figure 4.5 (a) Example of restoring a simplified thrust belt i.e. red trapezium using Model 1 with various regional slopes. α_{01}, α_{02} and α_{03} = the assumed regional slope, S_{01} ,S_{02} and S_{03} = the calculated shortening, L_{01} , L_{02} and L_{03} = the restored initial length of thrust belt. (b) The predicted linear relationship between restored shortening and dip of regional slope.

$A_0 = A_E + A_\#$ (4-17)

$A_O = ½ (h_0 + h_2) L_0$ (4-18)

Since:

$A_E = A_0 - A_\# = ½ (h_0 + h_2)*S$ (4-19)

Which on rearranging gives:

$S = 2 A_E / (h_0 + h_2)$ (4-20)

Equation 4-20 allows us to calculate the shortening directly from the area above the pseudo-regional.

4.3 Application to fold-thrust belts

4.3.1 Scaled physical analogue models

To validate the developed theoretical models, we used a scaled physical analogue example (Granado et al., 2017) where the initial geometry, final geometry and imposed shortening (*Figure 4.6a*), are known. The example has an initial surface slope of 3° (α_0), length of 75 cm (L_0), detachment depth at the wedge front of 6 cm (H_0) is subjected to 15 cm of shortening, creating a fold-thrust belt (*Figure 4.6a*).

Two horizons with well-defined initial slope are taken to perform the area balancing restoration using Model 1 (*Figure 4.3*): top layer (3°) and base of yellow layer (0°) (*Figure 4.6a*). This allows the direct comparison of restored shortening using different dipping bed layers.

Figure 4.6b shows the restoration section with an initial slope of 3° (blue trapezium), which yields 12.7 cm of shortening, a little less than the applied 15 cm shortening. In sandbox experimentation, it is fairly difficult to precisely define the dip of the model layer across the entire model. The 3° slope set by the model is likely a first-order estimate while the real value can be slightly less or more than that. Here we used a 2.5° initial slope to restore the cross-section, which gives rise to 14.7 cm of shortening, very close to the initial model settings. The 0.3 cm of difference in shortening can be attributed to errors of geometrical measurement, i.e. area, h_0, layer parallel shortening (e.g., Koyi et al., 2004) and lateral compaction (Butler and Paton, 2010).

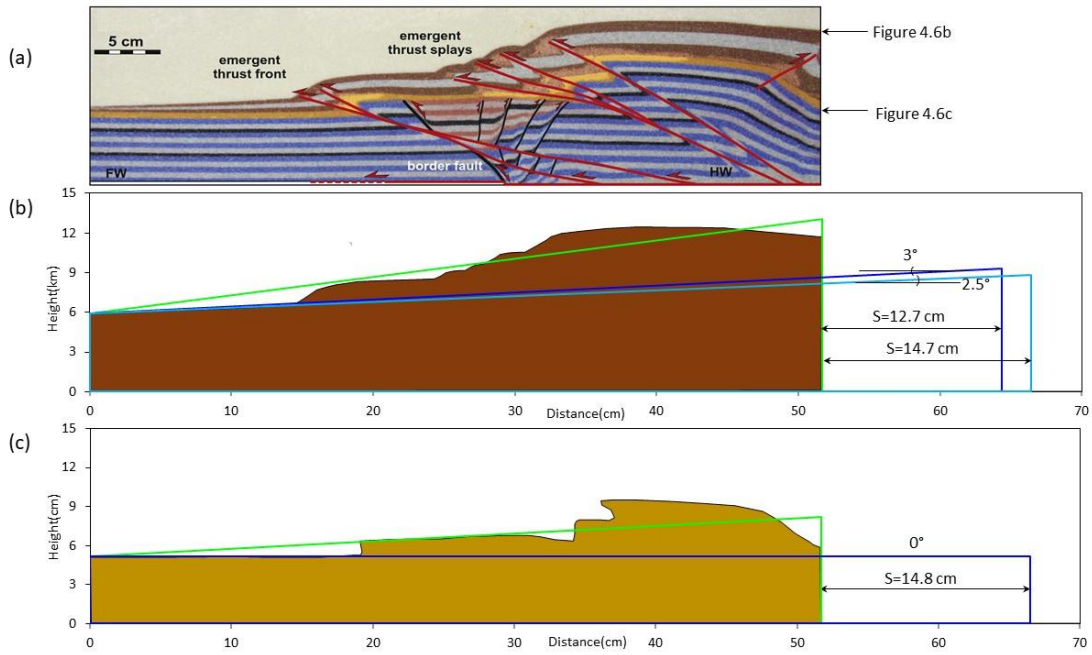

Figure 4.6 (a) Example of a sandbox model after 15 cm of shortening, after Granado et al. (2017), (b) restoration of the section using Model 1 for the top layer yielding 12.7 cm and 14.7 cm shortening, corresponding to 3° and 2.5° dip of regional slope, (c) restoration of the section using Model 1 for the horizontal base of yellow layer yielding 14.7 cm shortening.

The structural restoration with base of horizontal yellow layer (0° of initial slope) produces 14.8 cm shortening, roughly consistent with 15 cm of experiment value (*Figure 4.6c*). This also validates the experimental setting of the horizontal layer (0°).

From the settings of experimentation (Granado et al., 2017), we know the initial height h_2 (thickness of trapezium model) next to the mobile wall. The height maintains its value and moves forward as the undeformed block slides along the basal detachment (Model 2 in *Figure 4.4*). Based on this assumption, we then determine H_1 (BB') (H_1=h_2), and thus pseudo-regional OB (*Figure 4.7*). With these parameters, we can calculate the shortening of this experimental model using our theoretical Model 2 (*Figure 4.4*). From Equations 4-(4-20), we estimate 14.5 cm of shortening (*Figure 4.7*), very close to the experiment value of 15 cm. The slight underestimates in the shortening may be due to tectonic compaction, layer parallel shortening and lateral compaction (e.g., Koyi et al., 2004; Butler and Paton, 2010). But the overall good agreement between our area balancing restoration and the experiment values validates the theoretical models, that the models are able to perform structural restoration to estimate shortening based on area balancing. Further applications of the models to real-world examples are presented in the

following section.

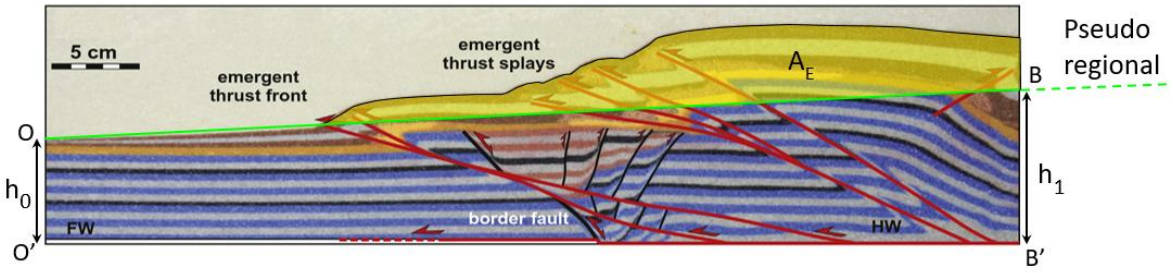

Figure 4.7 Restoration of the section using Model 1 producing 14.5 cm shortening, after Granado et al. (2017).

4.3.2 Hikurangi accretionary prism

The Hikurangi accretionary wedge is located above the subducting oceanic Pacific Plate along the eastern margin of North Island, New Zealand and its offshore convergent margin (Ghisetti, et al., 2016). Three depth-converted and geologically interpreted seismic profiles across the central Hikurangi margin were sequentially restored to study the last 2 Myr tectonic history of wedge development by Ghisetti et al. (2016). To test our model against natural examples, we took one of these (Transect T03 in Ghisetti et al., 2006), to carry out area balancing restoration using Model 1.

Figure 4.8a shows that the accretionary prism is dominated by imbricated thrusts and related folds that all sole out into one single detachment. Six stratigraphic units are interpreted with inferred age of present-day to 15±5 Ma from seafloor to depth, i.e., color grey to blue (*Figure 4.8a*). Among these units, the top yellow layer R3 appears to mark the top of pre-kinematic sediments of most anticlines with inferred age of 0.6±0.2 Ma, its geometry is interpreted to represent the overall topography of fold-thrust belt. The fold belt enveloped by horizon R3 is estimated to have 330.7 km^2 of cross-section area A, 1.9 km of detachment depth at the front (h_0) and 85.7 km of length (L_1) (Ghisetti et al., 2016). Using these parameters, we created a simplified trapezium model and superimposed on the accretionary prism (black trapezium in *Figure 4.8b*).producing an overall match in shape between our model and example. A horizontal regional is assumed to restore the black trapezium to blue trapezium, yielding 8.2 km of shortening (*Figure 4.8b*). We then tested a range of regional slopes from -0.3 to 0.6 °, which produced shortening results ranging between 13.5 – 0.4 km (*Figure 4.8c*).

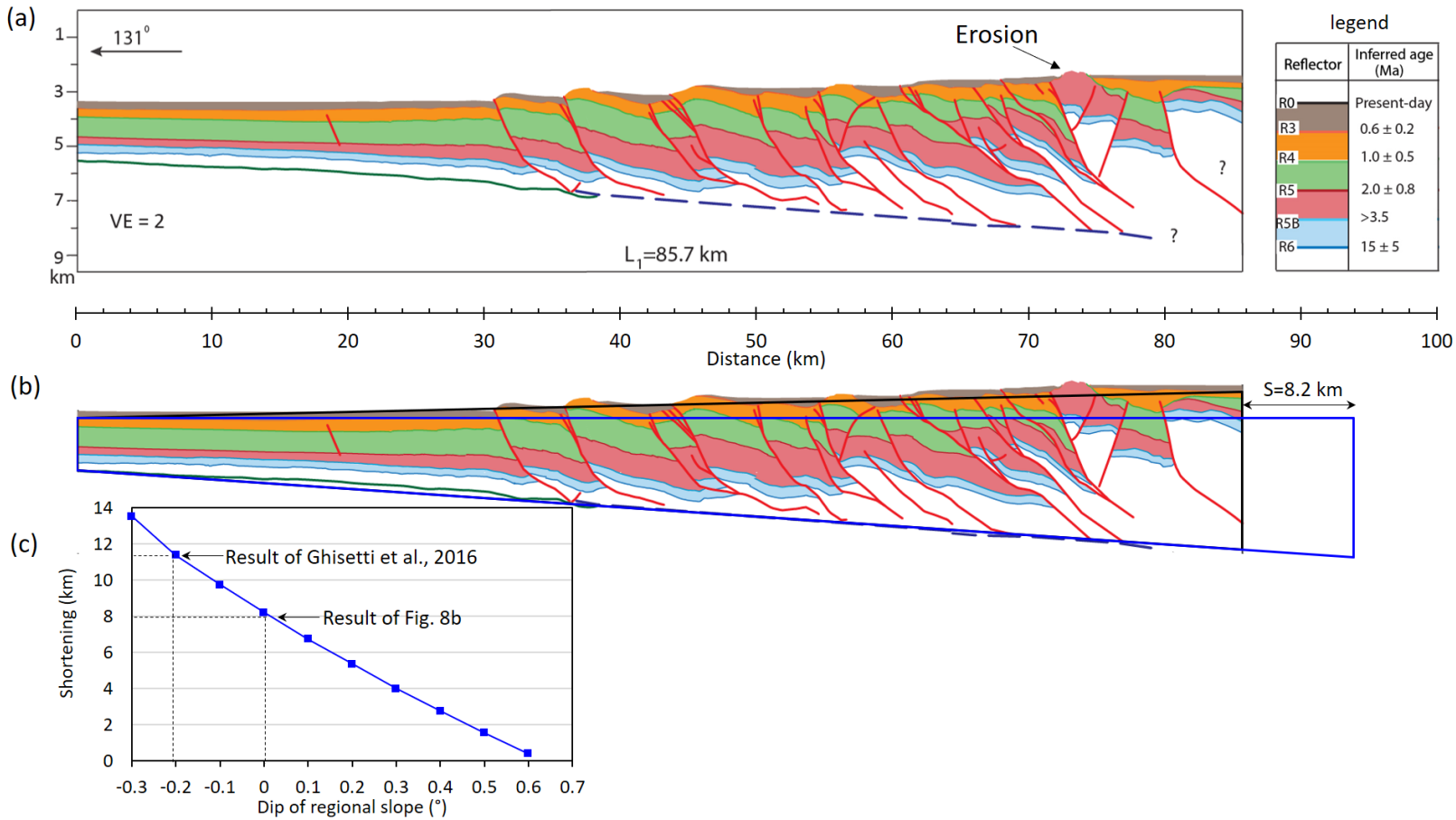

Figure 4.8 *Restoration of a fold-thrust belt across Hikurangi accretionary prism. (a) The depth converted and structure interpreted 2D seismic profile (Ghisetti et al., 2016). (b) The restored fold-thrust belt with a horizon regional slope yielding 8.2 km of shortening. (c) Plot of estimated shortening against a range of input dips of regional slope (-0.3-0.6°).*

The overall trend of shortening is consistent with the theoretical prediction (*Figure 4.5b*), the estimated shortening is inversely correlated with dip of regional slope.

Ghisetti et al. (2016) estimated 11.6 km of shortening accommodated during the deposition of R5-R3 by sequential restoration essentially based on bed length measurement, which exceeds the 8.2 km of shortening across the thrust belt estimated using a horizontal regional (*Figure 4.8b*) A few factors are thought to contribute to the difference. Firstly, the horizon R3 does not exclusively mark the top of kinematic sediments, at the landward area, it is actually preserved in a post-kinematic sequence (*Figure 4.8b*). So the layer R3 does not document all the deformation, particular in the landward area of the thrust belt, and will be an underestimate of the shortening. Secondly, erosion is observed at the crest of a fold, which leads to the removal of part of Horizon R3 and underlying horizon R4. This effectively causes less cross-section area, and thus underestimates shortening. Thirdly, the assumption of 0 degree at minimum for regional slope might be wrong. The horizon R6 is observed to dip landward right in front of the fold-thrust belt, which may indicate that the regional can also dip to hinterland, i.e. with a negative regional slope.

The extended initial regional slope below 0 degree allows additional shortening to be estimated (*Figure 4.8c*), and the plot of the Ghisetti et al. (2016) result into our data indicates -0.2 ° of initial regional slope (*Figure 4.8b*), i.e. the landward dipping initial regional slope. Clearly, without good control on the regional slope, the shortening estimated by area balancing method is highly variable, suggesting that shortening estimates will be poorly constrained.

4.3.3 NW Borneo fold-thrust belt

The NW Borneo continental margin is well known from drilling and seismic reflection data related to hydrocarbon exploration (*Figure 4.9*) (Hinz et al., 1989; Ingram et al., 2004; Morley et al., 2008; Hesse et al., 2009; Morley, 2009a; Hesse et al., 2010b). The NW Borneo fold-thrust belt (FTB) is developed on the deep water slope in the middle Miocene-Holocene shallow marine sequences (Morley, 2009b). Previous 2D seismic data shows an extensive train of elongated folds that verge seaward, spaced 5-15 km apart and oriented NE-SW (Hinz and Schluter, 1985; Hinz et al., 1989; Morley, 2009a). Ten

thousand square kilometres of 3D seismic datasets was acquired by Petroleum Geo-Services (PGS) in 2000 and 2001 across the deep-water area of Brunei (Morley, 2009a), and was then processed by PGS in 2001. Three 2D seismic lines spaced 17-20 km were extracted and used in this study along the 3D volume (Fig. 9). To focus the analysis, we described the results derived from section 4000 in detail, while the remaining results obtained from section 2300 and 6000 are presented, but without detailed description. *Figure 9* shows the 2D seismic profile 4000 with five horizons being mapped from shallow to deep levels (H0-H4) within the pre-kinematic sedimentary sequences. The FTB has folds and associated imbricate thrusts that sole out at depth into one detachment, South China Sea Unconformity (SCSU) (Morley, 2009a), exhibiting a classic trapezium geometry with topographic slope dipping to foreland and basal detachment dipping shelfward (*Figure 4.9b*) Area balancing is preformed between two pin lines shown in *Figure 4.9*

Figure 4.9

4.3.3.1 Restoration of a profile 4000

Horizon H0 is partly eroded at the crest of fold (Gee et al., 2007; Morley, 2007a; Morley, 2009b), it was reconstructed based upon the geometry of underlying sedimentary layer, i.e. H1 (*Figure 4.9b*).This inevitably leads to some inherent errors on the structural interpretation. Due to the reduced seismic resolution at depth, Horizon H4 is the lowest mapped horizon and part of it is still interpreted with less confidence. To minimize the errors and uncertainties inherited from mapping the thrust wedge geometry, we only use the most confident seismic horizons H1-H3 to conduct the restoration.

Horizon H1 is mapped as one of the top layers of the pre-kinematic sediments, its geometry is thought to represent the overall topography of the thrust belt. With well imaged basal detachment and two defined boundaries, the thrust belt enveloped by horizon H1 is taken as an example for area balancing restoration using our trapezium method (Equations 4-(8-15)). We created a simple trapezium model equivalent to the deformed thrust belt example with same cross-section area A, wedge length L_1, depth to detachment at the front stop h_0, and basal dip β (2.0°) as indicated by the red trapezium (*Figure 4.10a*). This model is then superimposed on the fold belt example of section 4000, producing a good match of overall geometry between these two (*Figure 4.10a*), validating

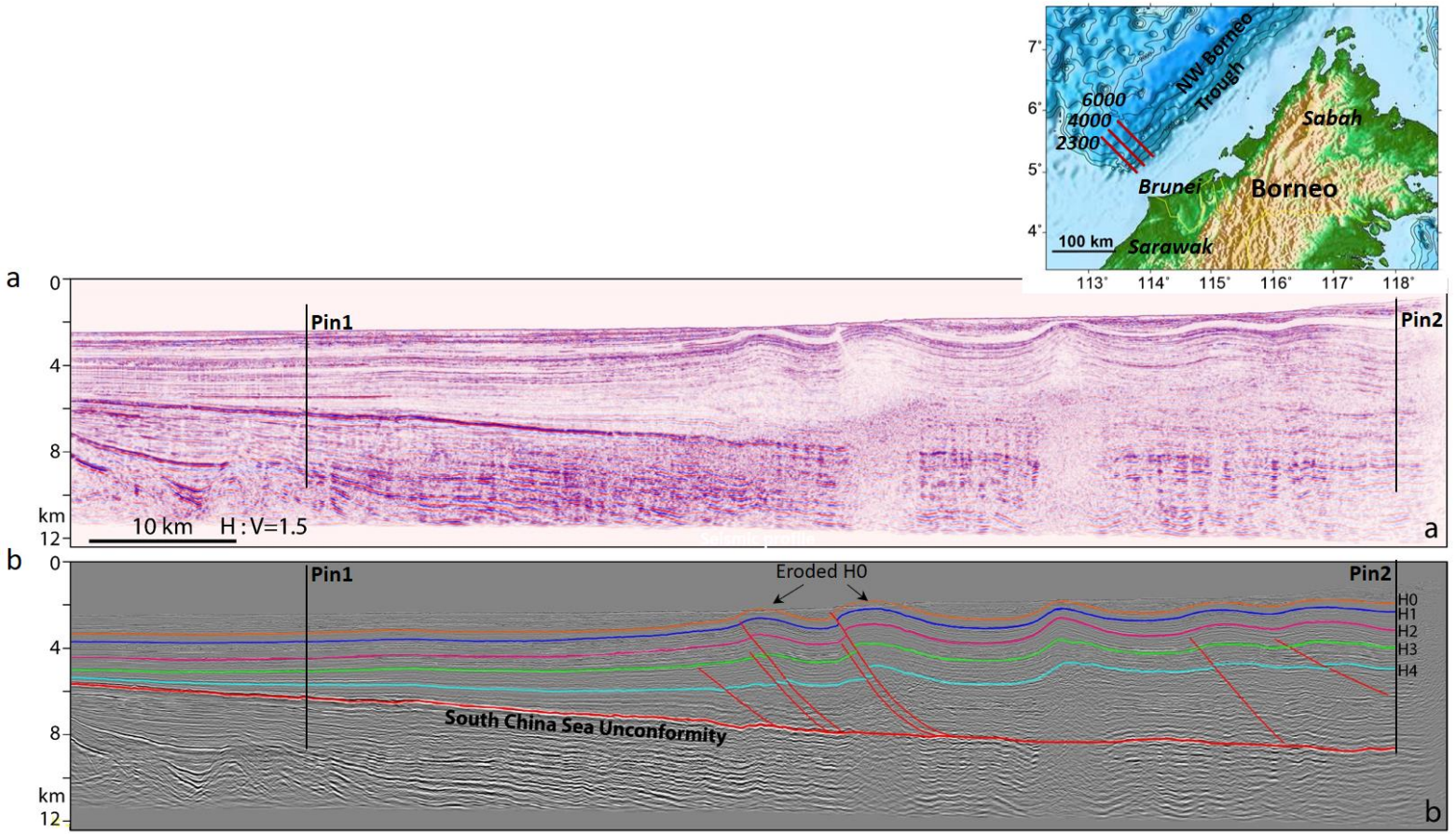

Figure 4.9 (a) Uninterpreted 2D depth converted seismic line 4000 (VE=1.5) across the Brunei portion of NW Borneo deep water fold- thrust belt (for location see Inset), (b) interpreted 2D depth converted seismic profile 4000 with 5 horizons and a basal detachment (South China Sea Unconformity) mapped from shallow to deep levels. Two vertical pine lines define the main deforming region in this thrust belt subjected to area balancing restoration.

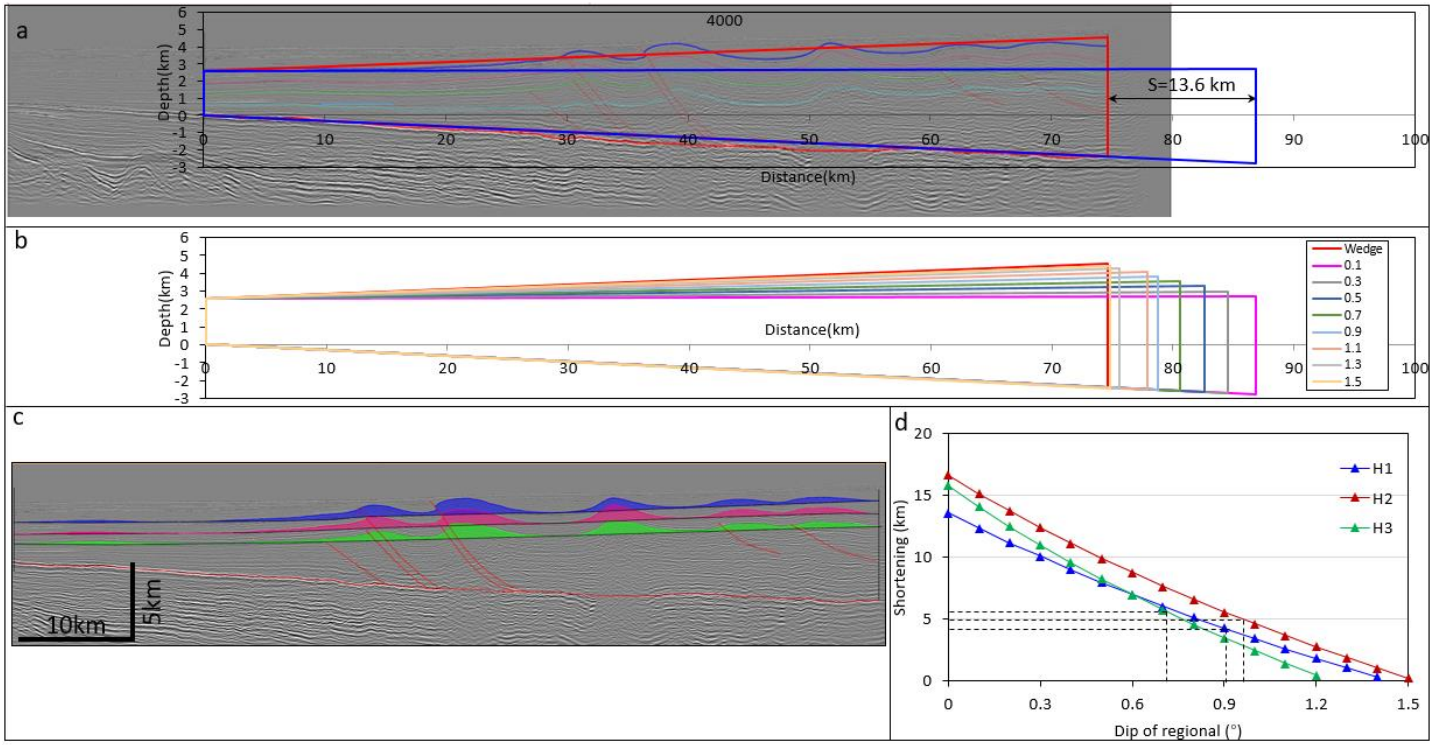

Figure 4.10 (a) Restoration of the thrust wedge enclosed by horizon H1, basal detachment and two pin lines with an arbitrary horizontal regional slope yielding ~13.6 km of shortening. (b) Restoration of the same cross-section, but with a range of regional dips (0.1-1.5°), giving rise to a range of shortening values.(c) estimation of excess area with pseudo-regional for Horizons H1-H3. (d) Plots of results of Model 1 and Model 2 to constrain the optimal shortening and corresponding initial regional slope, the dotted lines indicate the results derived from Model 2.

the definition of model geometry. We then progressively restored the model trapezium, maintaining h_0 and β. The blue trapezoid in *Figure 10a* represents the restored thrust belt with an arbitrary horizontal regional, α_0=0°, which yields 13.6 km of shortening. We repeated the area balance using a range of initial regional dips from 0-1.5° (*Figure 4.10b*). These give a variety of shortening estimates ranging between 0.2-12.2 km, indicating that the shortening estimated by area balancing is highly sensitive to the select of regional dip. In *Figure 4.10c*, we assume a series of pseudo-regionals by linking the hinterland thickness of the wedge with the synclines formed between the thrust related folds. This is almost certainly an overestimate of the dip of the pseudo regional as it ignores any deformation to the hinterland of pin 1. We measure the area above the pseudo-regional for horizons H1-H3, which is used in combination with Model 2 to estimate the shortening. The Model 2 results are plotted into the shortening values estimated by Model 1, which gives a narrow range of shortening 4.2-5.7 km, corresponding to regional slope 0.7-1.0°. This is thought to represent a minimum estimate for the shortening of this section.

4.3.3.2 Application to other cross-sections of the NW Borneo FTB

To examine the variation in the overall geometry and restored shortening along strike across the NW Borneo FTB, we also carried out structural restoration for fold-thrust belt in section 2300 and 6000, applying both models 1 and 2 (*Figure 4.11)*. Similar to the observations made in section 4000, the angle of regional dip plays an essential role in the determination of orogenic shortening. A higher regional dip leads to less shortening while a lower regional dip results in more shortening. By projecting the results of Model 2 into the shortening range of Model 1, we estimate 4.6-5.7 km of shortening and correspondent 1.2-1.4° of regional slope for section 2300, 3.6-4.9 km of shortening and correspondent 0.7-1.0° of regional slope for section 6000 (*Figure 4.11d)*. If the recognition of H1-H3 as pre-kinematic sediments is valid, these horizons are expected to have accommodated similar amount of shortening. The varied shortening for different horizons may reflect the complex deformation history of thrust belt, and uncertainties of structural interpretation (Bond et al., 2012; Bond, 2015), various amount of layer-parallel strain that each horizon accommodates (Koyi et al., 2004). Despite prominent difference in wedge parameters across these three sections, such as wedge length L_1, depth to detachment at front stop h_0, angle of basal dip β and area of cross-section A, the calculated shortening

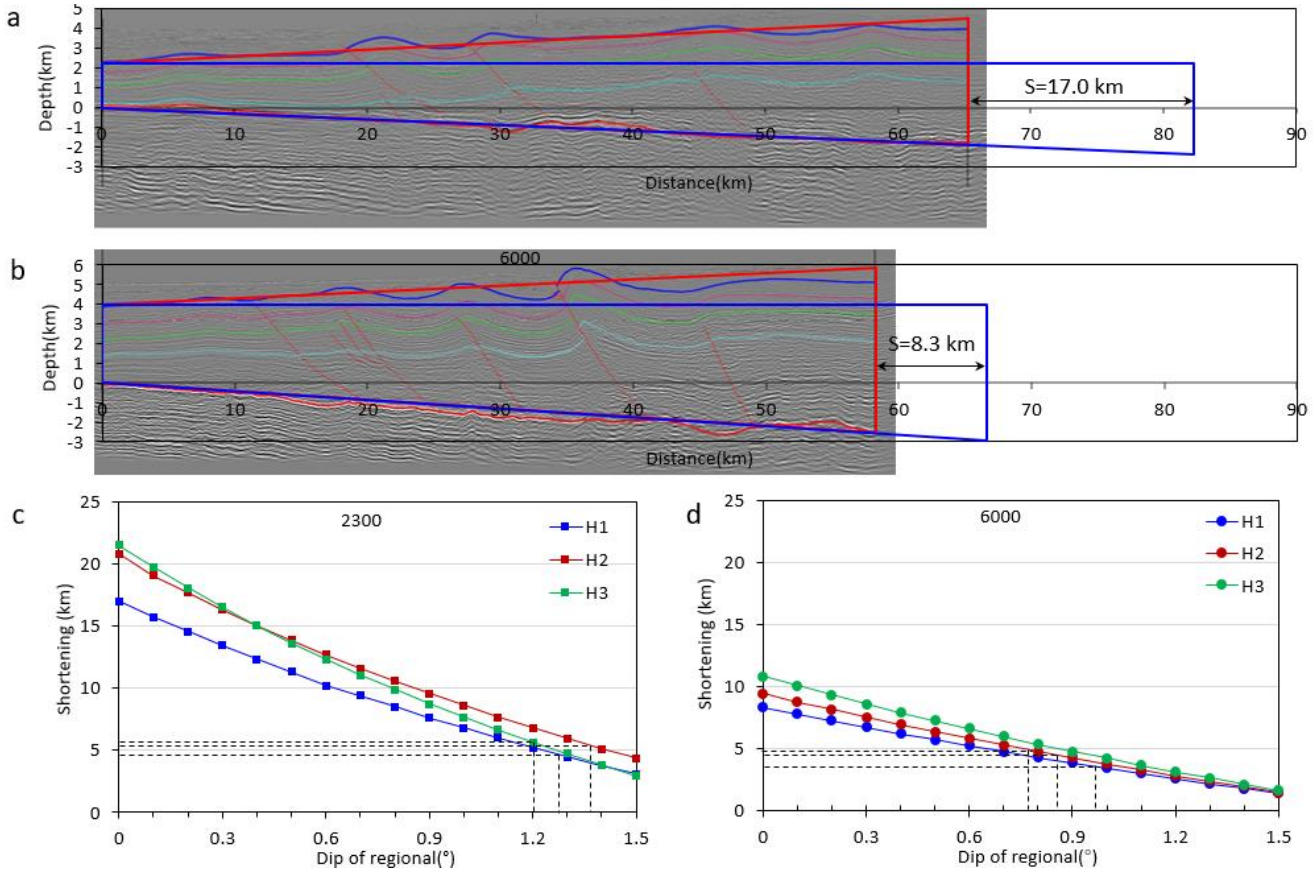

Figure 4.11 (a) Restoration of the thrust wedge in section 2300 with a horizontal regional slope yielding ~17.0 km of shortening. (b) Restoration of the thrust wedge in section 6000 with a horizontal regional giving rise to 8.3 km shortening. (c) Plots of results of Model 1 and Model 2 to constrain the optimal shortening and corresponding initial regional slope for section 2300. (c) Plots of results of Model 1 and Model 2 to constrain the optimal shortening and corresponding initial regional slope for section 6000, the dotted lines indicate the results derived from Model 2.

appears to show a distinct trend, decreasing from Section 2300 to Section 6000, i.e., from southwest to northeast. This trend is roughly consistent with shortening variation of Sabah portion of NW Borneo FTB estimated by sequential restoration in the adjacent region (Hesse et al., 2009, 2010b), some 50-100 km northeast of this study area. This effectively demonstrates that, whilst, the results derived from the models have large inherent variability due to uncertainty in the input parameters, they may still be capable of predicting the overall trend of orogenic shortening along strike in a thrust system.

4.4 Discussion

4.4.1 Uncertainties and Limitations

Any balancing method is subject to uncertainties in (A) the geometry of the deformed area, (B) the assumed shape of the restored area and (C) the validity of the balancing conditions (conservation of length, area, etc).

4.4.1.1 Type A

Type A errors are based mainly on the structural mapping and interpretation of the fold-thrust belt (including imaging and correlation of horizons, recognition of facies changes, erosion, etc.) and the location of detachment. The structural interpretation determines the cross-sectional area and final length of section that are two critical parameters in any area balancing. The limited resolution of seismic data causes some inherent errors in structural interpretations, which is often accompanied by unresolved sub-seismic deformation. This is known to be a major source of error in line-length balancing, generally leading to an underestimate of the overall shortening (e.g., Sans et al., 2003; Koyi et al., 2004; Allmendinger and Judge, 2013).

Erosion is operating to some extent during structural deformation, typically leading to the removal of material from a geological cross-section. Hence, it reduces the bed-length and cross-sectional area, causing underestimate of shortening.

The basal detachment exerts a first-order control on estimating cross-section area, and thus structural restoration. The theoretical models generally assume a single basal detachment underlying the entire thrust belt. Some real world examples are found to have incorporated multiple detachments with various depth (i.e. Corredor et al., 2005),

which are likely to have involved several stages of deformation in relation to shortening. The single detachment approximation in this study (and most others) will inevitably ignore the different stages of deformation and related shortening, leading to uncertainties in final shortening estimates.

4.4.1.2 Type B

The shape of the restored section is a major unknown, which most existing methods treat by simplifying to a sequence of parallel layers or assuming a horizontal regional slope. As outlined in section 4.2.1 and the examples in section 4.3, small changes in the slope of the regional can produce significant changes in the restored section and in estimated shortening. Despite progress of applying various regional slopes to estimate shortening using Model 1, the simplified straight line of original slope is still unlikely to represent the true shape. For instance, the shape of sedimentary layers in front of the Hikurangi accretionary prism are not planar, but curved. So the simplified straight line in theoretical models are likely to have incorporated some errors and uncertainties.
Furthermore, in natural system, the deformation front in a thrust belt propagates forward through frontal accretion with increasing contraction. The trapezium model presented here assumes that the position of the deformation front is fixed (*Figure 4.3*), resembling the settings of some physical analogue models (Schreurs et al., 2006). Therefore this model only restores the overall shape of thrust belt, irrelevant to its spatial position.

4.4.1.3 Type C

Layer-parallel strain and lateral compaction are widely recognized in both physical analogue models and natural examples (e.g., Sans et al., 2003; Koyi et al., 2004; Butler and Paton, 2010; Sengor and Bozkurt, 2013). These are thought to cause a reduction in cross-section area, bed length and volume, that are difficult to assess from the current structures. Their contribution to structural shortening remains poorly constrained, as such the shortening quantified by the models will usually be a minimum estimate in thrust systems.

Tectonic compaction (i.e. loading) are thought to have considerable effects on the cross-section area, challenging the assumption of area balancing. The estimated cross-section area in this study does not involve the contribution of tectonic compaction may only

represent a component of the overall area, causing underestimation of shortening.

4.4.2 Applications to fold-thrust belts

Our theoretical development of area balancing restoration, structural interpretation and the application discussed in sections 4.2 & 4.3 suggest that the dip of initial regional slope plays a critical role in quantifying the excess area, and hence, the orogenic shortening of a geological cross-section. Previous studies have paid little attention to this in the estimation of shortening (Chamberlin, 1910; Dahlstrom, 1969; Hossack, 1979; Mitra and Namson, 1989; Woodward et al., 1990; Epard and Groshong, 1995; Groshong et al., 2012; Wiltschko and Groshong, 2012; Butler, 2013; Wang et al., 2018). The estimation of excess area using a simplified initial regional slope (Mitra and Namson, 1989; Wiltschko and Groshong, 2012; Schlische et al., 2014), implicit in most applications of area balancing restoration ignores the dependency on the dip of the regional. The traditional method is valid only if a geological cross-section is composed of layer-parallel sedimentary sequences above a single basal detachment (Chamberlin, 1910). However, this simplistic geometry does not reflect the complexity of structural features in natural thrust systems, such as taper shape of thrust belt with sedimentary sequence thinning towards the foreland and thickening towards the hinterland, complex fault related folds, forward and backward vergent imbricate thrusts and duplex (Boyer and Elliott, 1982; Davis et al., 1983; Dahlen, 1990; DeCelles et al., 1998; McQuarrie, 2004; Fitz-Diaz et al., 2011).

4.4.3 Comparison with other structural restoration techniques

Apart from area balancing restoration, previous authors also used sequential restoration method that usually involves bed-length balancing to reconstruct the tectonic history of a fold-thrust belt (McQuarrie, 2004; Corredor et al., 2005; Hesse et al., 2009, 2010b; Masini et al., 2011; Ghisetti et al., 2016), which is largely based on bed-length measurement. The restored shortening by this technique is typically cited as a minimum estimate (Allmendinger and Judge, 2013) as bed-length does not preserve during deformation (Epard and Groshong, 1995; Koyi et al., 2004; Butler and Paton, 2010; Groshong et al., 2012; Wiltschko and Groshong, 2012; Şengör and Bozkurt, 2013; Lathrop and Burberry, 2017). To avoid the restriction of bed-length change, the Area-depth-strain (ADS) method has been proposed to predict the detachment depth, estimate the displacement along

detachment and detect sub-resolution deformation based on the relationship between the excess area of multiple stratigraphic horizons on a cross section and their relative depths (Epard and Groshong, 1993; Groshong et al., 2012; Wiltschko and Groshong, 2012; Schlische et al., 2014). This method is independent of the length measurement and therefore insensitive to bed-length changes. But it still involves the quantification of excess area using a single, mostly horizontal regional slope. Application of ADS method generally deals with individual fault-related fold, not an entire fold-thrust belt. A thrust belt is generally composed of a series of folds and thrusts that deform the stratigraphic layers, resulting in complex structures. This makes it difficult to accurately determine the un-deformed regional slope of each stratigraphic layer across the entire section, hence limiting the use of ADS method in the system of this kind.

In contrast, our models take the system as whole, simply restore it back to pre-deformed state with various regional dips. The results derived from this new method allow a comparison of shortening against the selected regional dips, and examine the sensitivity of excess area and shortening to the change in regional dips (e.g.,

Figure 4.11).

4.4.4 Application to gravity driven fold-thrust belt system

A gravity driven deformation system on passive margins, i.e. offshore Brazil, Gulf of Mexica, Nigeria delta, Orange basin, is commonly composed of an extension on up-dip slope and contraction on the down-dip slope with the two domains connected by a basal detachment (Rowan et al., 2004; Morley et al., 2011). The purely gravity-driven system is thought to be kinematically self-contained such that the stratal shortening represented by the contractional structures, including the thrust and folds developed on the lower slopes, must balance the net extension accommodated higher on slopes (Butler and Paton, 2010). Although these trapezium models are introduced for a contractional fold-thrust belt, the same principles apply in extension (*Figure 4.12*). If the regional slope for a sedimentary layer is well constrained from the up-dip slope to the down-dip slope, we should be able to restore the system and examine if it is self-contained (i.e. extension equals to contraction). This allows to quantify the contribution of extension, and regional, plate-scaled movement if available, to the development of FTB.

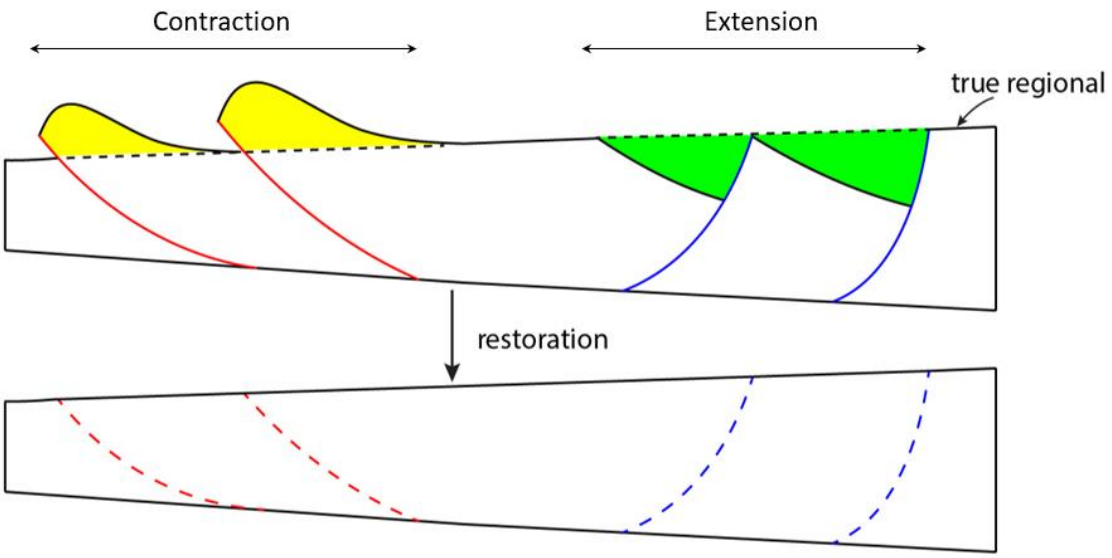

Figure 4.12 Schematic diagram showing the expansion of the application of Model 1 from pure contraction to combined extension and contraction deformation in a gravity driven system, with overall shortening = 0.

4.5 Conclusion

In this paper, we developed two new and simple quantitative solutions to area balance a thrust wedge based on conserved cross-section area, assuming an initial trapezium shape. The new methods generalize the usual assumption of a rectangular initial geometry, allowing various regional slopes to be used. They are then tested against scaled physical analogues and natural examples of fold-thrust belt from Hikurangi accretionary wedge and NW Borneo margin using a range of input parameters.

The results show a good agreement between our theoretical calculation and real experiment results, i.e. 14.5 - 14.8 cm shortening by models versus 15.0 cm shortening by experiment (*Figure 4.6* & *Figure 4.7*). The NW Borneo FTB are estimated to have accommodate 3.6 - 5.7 km of shortening, corresponding to 0.7 - 1.4 ° of regional slope.

A higher regional dip results in less excess area and less shortening while a lower regional dip leads to more excess area and more shortening. Absolute values of shortening are probably not attainable in most thrust belts. Accuracy of shortening estimate requires independent constraint of parameters, particularly the initial regional slope, not greater precision in their measurement.

This study highlights the significance of regional slope on area balancing restoration. The

new method is generally applicable, since it is concerned mainly with the gross cross-section area of the system and is irrespective of the lithology, rheology, fluid pressure or many other factors that control the form and detailed expression n of the final structure.

Chapter 5 Structural Development of the Northwest Borneo Fold-Thrust Belt, Offshore Brunei

Abstract

Using high-resolution 3D seismic data, we investigate the origin, geometry, structure and tectonic evolution of the deepwater fold-thrust system in the Brunei sector of the NW Borneo continental margin. Our new results demonstrate the presence of three types of anticlinal fold: fault-propagation folds (dominant); detachment folds (minor); and fault-bend folds (only one example). For each individual fold, the structural style varies significantly along strike, which we interpret to reflect lateral changes in the magnitude of folding, the basal décollement strength, and inherited pre-contraction structure (pre-existing carbonate platforms with topography). Associated with many of the folds, thrust faults appear to initiate at depth and propagate up-dip as demonstrated by up-dip decreasing displacement. Fault dip is closely related to fault or fold style; low fault dips (18-39°) are associated with both incipient faults and fault-propagation folds, whereas steeper fault dips (>39°) are associated only with fault-propagation folds. Fault spacing decreases towards the northeast where the thrust system impinges upon pre-existing carbonate platforms that appear to act as obstacles, blocking the forward propagation of the thrust belt. From foreland to hinterland, there is an increase in shortening marked by pronounced steps at thrust structures but characterized by a gradual change across pure folds. Thrusting plays a primary role over folding in strain accommodation. A major mismatch between the shortening determined using the conventional bed-length measurement and revised area-balancing method indicates that bed length is not conserved: ~83% of the shortening shown by area balancing is not seen in bed length. This highlights the inadequacy of the simple bed-length method for estimating shortening. The low taper angle of the NBFB (mostly <6°) implies a high basal fluid pressure (>0.7 of lithostatic pressure). This estimated overpressure is interpreted to result from rapid burial, disequilibrium loading, in situ generation of hydrocarbons, and fluids, including hydrocarbons, driven laterally from the shelf seaward following an oceanward lateral decrease in lithostatic pressure. This study provides new evidence for the gravity-driven origin of the Northwest Borneo Fold-thrust Belt: (1) two distinct stages of fault activity and associated fold growth are identified in some parts of the may be a

consequence of changing rates of sediment input and loading through time, (2) fault activity is distributed across much of the fold thrust belt rather than being focused exclusively at the toe. We interpret that the NBFB results from a combination of gravitational tectonics driven by deltaic sedimentation (primary) and crustal shortening driven by collision of plate tectonics (secondary).

5.1 Introduction

The continental shelf and slope areas of NW Borneo, lying offshore Brunei and the Sabah and Sarawak provinces of Malaysia, are well known from drilling and seismic reflection data related to hydrocarbon exploration (*Figure 5.1a*) (e.g., James, 1984; Levell, 1987; Hinz et al., 1989; Sandal, 1996; Petronas, 1999; Ingram et al., 2004; Morley et al., 2008; Hesse et al., 2009; Morley, 2009a; Hesse et al., 2010b; Morley et al., 2014).

The shelf is dominated by prograding shallow marine clastic sediments of Middle Miocene to Holocene age (*Figure 5.1b*), which locally attain thicknesses in excess of 10 km (Morley, 2007b; Hesse et al., 2009). The Miocene–Holocene depocentre in Brunei is known as the Baram Delta Province (Morley, 2009a). The shelf sequence is heavily deformed, with both extensional and compressional structures, including kilometre-scale, syn-sedimentary normal faults (growth faults), shale diapirs, thrusts and inversion-related anticlines (Sandal, 1996; Morley et al., 2003; Van Rensbergen and Morley, 2003; Morley et al., 2008; King et al., 2009).

Beyond the shelf break, the continental slope dips steeply (1-3°) to the NW into the Northwest Borneo Trough (a.k.a. the Sabah Trough). The slope consists of Middle Miocene-Holocene clastic deposits (Levell, 1987). Based on seismic facies we interpret these to be turbidites and mass transport deposits, interbedded with hemipelagic and pelagic sediments (see also Hazebroek and Tan, 1993). The slope is affected by thin-skinned folding and thrusting (James, 1984; Levell, 1987; Hinz et al., 1989; Sandal, 1996; Petronas, 1999; Ingram et al., 2004; Morley, 2009b; Morley et al., 2014). We herein refer to this general domain as the NBFB (Northwest Borneo Fold-Thrust Belt).

Previous work based on 2D and 3D seismic data shows that the NBFB consists of a series of elongated folds that verge seaward, spaced 5-15 km apart and oriented NE-SW (James, 1984; Hinz and Schluter, 1985; Hinz et al., 1989; Sandal, 1996; Schlüter et al., 1996;

Morley, 2009a). The NBFB extends the length of Sabah and Brunei and terminates offshore Sarawak (*Figure 5.1a*). The folds are mostly associated with imbricate thrusts that sole out at depth into one or two décollements (Hinz et al., 1989; Ingram et al., 2004; Franke et al., 2008; Hesse et al., 2009, 2010b) (*Figure 5.1*). The principal and deepest décollement lies at the base of the Mid Miocene - Holocene clastic wedge.

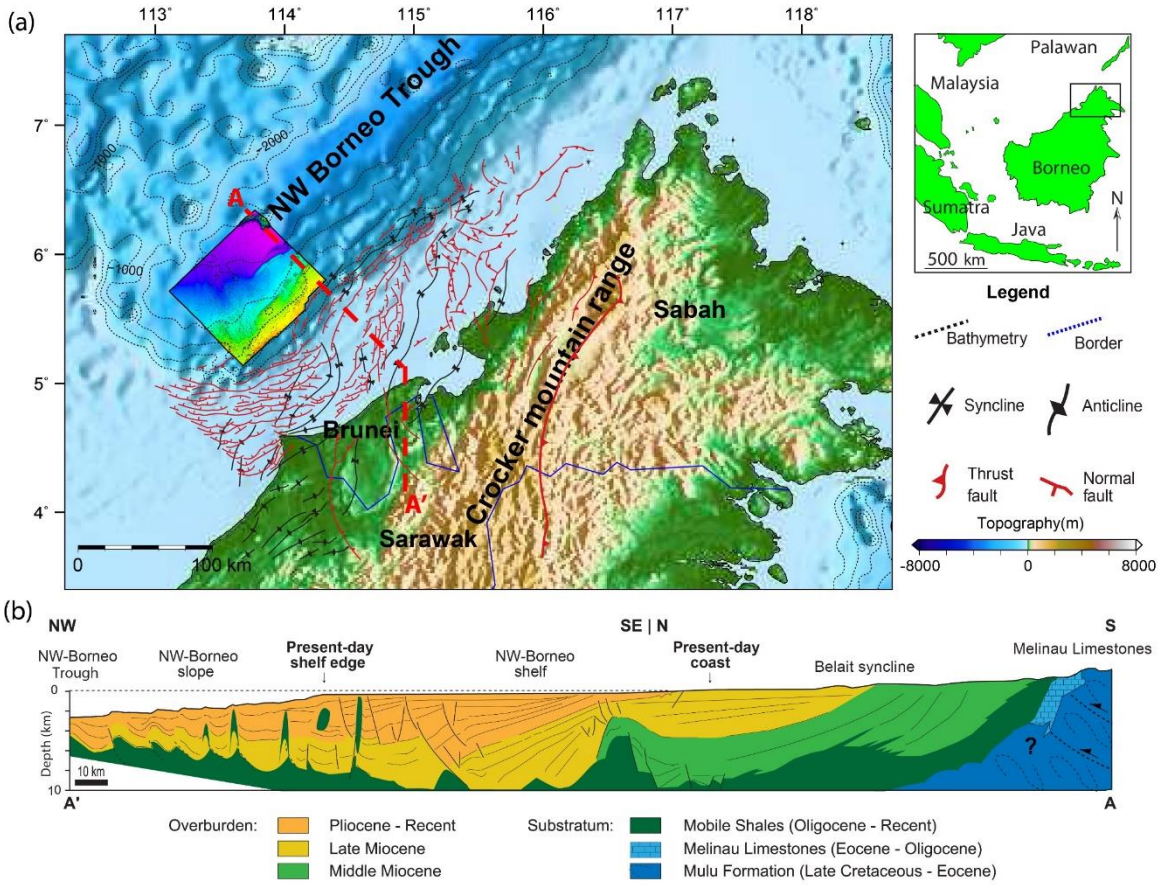

Figure 5.1 (a) Regional map of NW Borneo showing the key tectonic elements of the study area and location of the 3D seismic data, after Morley (2009a). Bathymetric contours are 500 m intervals. (b) Regional cross-section across NW Borneo along line A-A' (after Hess et al. (2009).

The existence of active collision, regional compression or subduction has been long debated (Sapin et al., 2013). Mechanisms for generating the Miocene to Recent fold-thrust belt are therefore as follows: (1) the old subduction zone is reactivated, possibly driven by far-field stresses from the Australia–Indonesia collision zone, deformation around Sulawesi, or from collisional events in the Phillippines (e.g., Hinz et al., 1989; Simons et al., 2007; Franke et al., 2008; Cullen, 2010; Sapin et al., 2001); or (2) deformation is primarily a gravity-driven phenomenon (e.g., Hazebroek and Tan, 1993;

Hall and Morley, 2004; Hall et al., 2008; Hall, 2013). Between these two end-member mechanisms, some authors also suggest a combined mechanism of gravitational deltaic tectonics and far-field regional stresses/regional compression (e.g., Ingram et al., 2004; Morley, 2007b; Hesse et al., 2009, 2010b; King et al., 2010a) To resolve this debate, detailed examination of fault and fold activity in relation to its potential driving mechanism is required.

In the past, studies of the NBFB have identified and interpreted regional unconformities, geometries and structures of hydrocarbon traps, fold styles, structural shortening, seismic velocity of folds and thrusts (Hinz et al., 1989; Ingram et al., 2004; Franke et al., 2008; Hesse et al., 2009, 2010b; Steuer et al., 2014), and mass transport processes and depositional elements (McGilvery and Cook, 2004; Gee et al., 2007; McGilvery and Cook, 2013) using mainly 2D seismic lines, but the temporal-spatial variation and development of the compressional structures in this system remain poorly understood. Morley (2007a, 2007b, 2009a, 2009b) studied the growth of folds and oblique thrust faults, the role of sedimentation in the topographic evolution of the NBFB, and normal faulting at fold crests using the shallow portion of a 3D seismic volume (1s TWT below seafloor). But the strain partitioning between thrusts and folds, structural characteristics at depth e.g., geometry and displacement of thrust faults at depth, and the structural relationship between folds and faults and the underlying basal décollement have not been examined. Previous studies also investigated the present-day stress across the continental margin of NW Borneo (Tingay et al., 2005; King et al., 2009; Tingay et al., 2009; King et al., 2010b), showing that the margin has three tectonic provinces: an inner shelf inverted province (σ_H is NW-SE, margin-normal), an outer shelf extensional province (σ_H is NE-SW, margin-parallel), and a slope to abyssal plain compressional province (σ_H is NW-SE, margin-normal).

Despite considerable research and exploration efforts in the deep-water NW Borneo region in recent years, there are still many questions concerning the nature, structural development and tectonic history of the NBFB. Specific questions include: What are the structural styles of the NWFB and how do they change along strike? How do the faults grow and propagate? What is the fault activity history? How is strain distributed across different structures? What are the décollement properties? To answer these questions, we used a 3D seismic dataset from offshore Brunei, to conduct 2D and 3D seismic

interpretation, structural style classification, structural reconstruction, strain measurement, and mechanical analysis.

5.2 Methods

Ten thousand square kilometres of 3D seismic datasets acquired and processed by Petroleum Geo-Services (PGS) in 2000 and 2001 across the deep-water area of Brunei were used (*Figure 5.1a*). This is the same dataset used by Morley (2007, 2009a).

Well penetrations exist in the most landward/updip of the structures (Schlüter et al., 1996 and reference herein), but are not available to this study. However, since there are no well penetrations of the main body of the NBFB, this is not a major issue.

The V_0-K method (Marsden, 1992) was used to depth convert the seismic data as explained below

$$V_i = V_0 + K*Z \quad (5\text{-}1)$$

$$V_i = dz/dt \quad (5\text{-}2)$$

The first formula states that the instantaneous velocity V_i, increases linearly with depth Z; V_0, is a constant and K the rate of velocity increase compaction factor (Marsden, 1992). The second equation states that the instantaneous velocity is the rate of change of depth with time. Here, a fixed seismic velocity of 1.5 km/s is adopted for V_0, i.e. sea water in this case, and an acceleration factor 0.8 km/s per km is employed for K.

Seismic interpretation, depth conversion, structural restoration and strain quantification were conducted using Petrel 2014 and Midland Valley 2D Move. In addition to standard seismic analyses, we created edge maps of the seafloor and a shallow horizon (Horizon H0) to highlight the slope of the study area as an indication of fold distribution (*Figure 5.2* & *Figure 5.2b*). A total of nine 2D NW-SE trending seismic lines spaced 17-20 km across the Brunei sector of NBFB were extracted (*Figure 5.2c*). For quantitative structural analysis, we systematically measured fault displacement, dip, and spacing, and strain across the fold-thrust belt using 2D Move software.

5.3 Regional Context

5.3.1 Tectonic history and setting

The formation of the continental margin of NW Borneo was strongly influenced by the evolution of the South China Sea during the Oligocene-Early Miocene (Hinz and Schluter, 1985; Hinz et al., 1989). During the Late Cretaceous, the proto-South China Sea (SCS) oceanic crust was being subducted south-southeastward beneath NW Borneo (Hinz and Schluter, 1985; Hinz et al., 1989; Hall, 1996; Morley, 2002; Hall et al., 2008; Hall, 2013; Cullen, 2014), creating a major orogenic and magmatic mountain belt in Borneo and developing the Crocker-Rajang accretionary wedge. Subduction continued until the latest Early Miocene (Morley, 2007b), at which time the proto-SCS ocean had been consumed, and NW Borneo overthrust the leading edge of the Dangerous Ground Microcontinent (DGM) (James, 1984; Levell, 1987; Hazebroek and Tan, 1993; Hutchison, 1996; Hutchison and Misra, 1996; Sandal, 1996). In the final stages of convergence, Northern Borneo experienced major uplift and significant contractional deformation causing the emergence of much of Sabah and the present central Highlands of Borneo, e.g. Crocker Mountain Range (*Figure 5.1*)(Hamilton, 1979; Rangin et al., 1990; Tongkul, 1991; Tongkul, 1994; Hutchison, 1996; Tate, 2001; Hall, 2013; Cullen, 2014), as documented in the late Early Miocene to middle Miocene folded sedimentary units onshore NW Borneo (Tongkul, 1994; Sandal, 1996; William et al., 2003; Hesse et al., 2009). The resulting uplift and erosion of the Crocker-Rajang accretionary belt became the main source of sediment for the continental margin of NW Borneo (Gee et al., 2007).

The southern, highly attenuated, margin of the DGM forms the basement to the North Borneo margin. The deformation prior to docking of the DGM with Borneo in the late Early Miocene was dominated by extension, evidenced by horst and graben containing synrift sediments in the pre-Mid Miocene section below the NBFB (e.g., Ahmad et al., 2004; Hutchison, 2005; Madon et al., 2013; Cullen, 2014).

On the shallow NW Borneo shelf, late Neogene contraction coincided with the development of major syn-sedimentary normal faults within an up to 10-km-thick late Neogene deltaic overburden (*Figure 5.1b*) (Hesse et al., 2009). This “thin-skinned”, gravity-driven extensional deformation was superimposed on older, deep-seated convergence-related compressional structures and generated, particularly in the southern

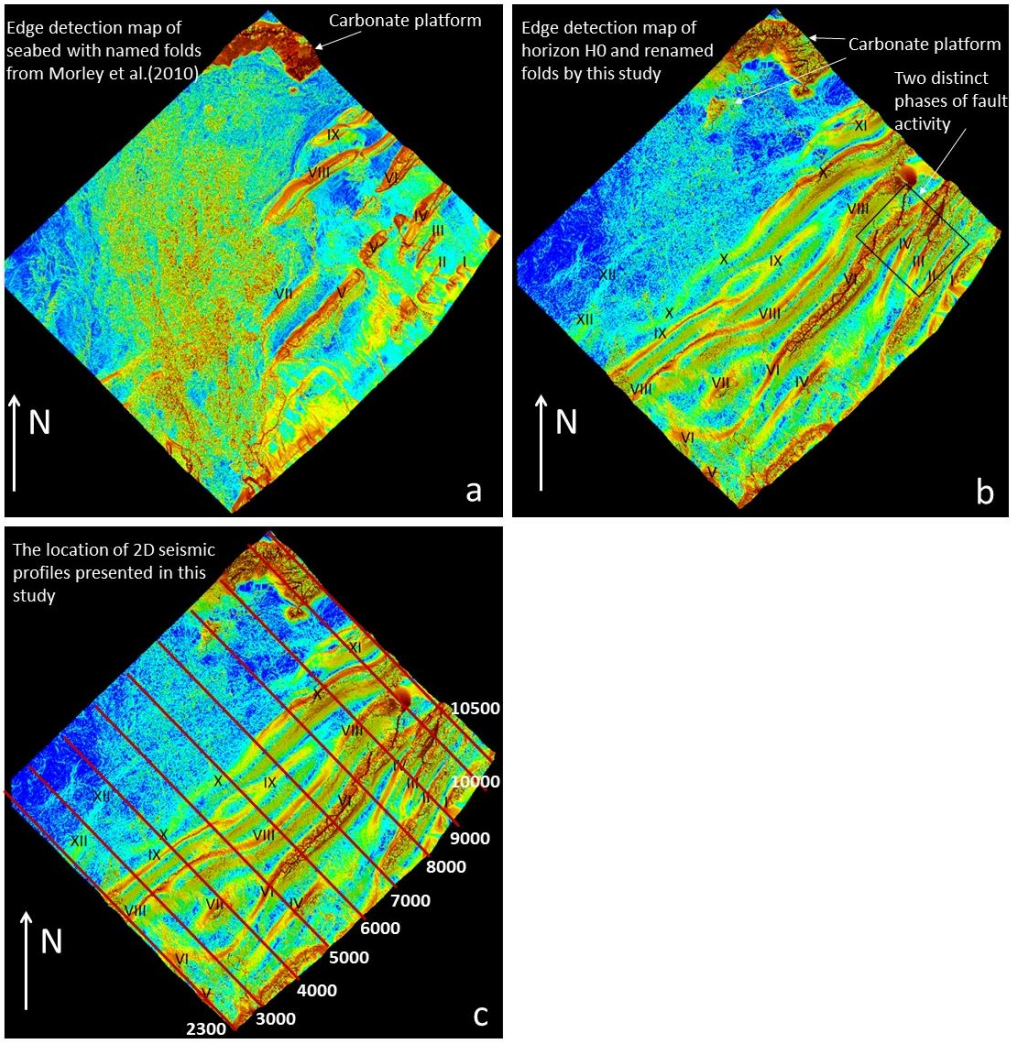

Figure 5.2 Edge detection maps. In each case, the darker brown/red shading indicates increased slope dip on the outer/seaward limbs of the anticlines. (a) Edge detection map of the seafloor reflection for the slope region of offshore Brunei Darussalam from 3D seismic volume (from Morley et al., 2010), with fold interpretation and numbering from Morley et al. (2010) study. (b) Edge detection map of seismic horizon H0 beneath the seabed (see Figure 5.3 for depth and geometry) from this study. I-XII denotes individual numbered folds interpreted in this study. (c) Location of 2D seismic profiles and numbered folds.

part of the NW Borneo shelf, a multitude of complex tectonic features that are influenced by both extensional and contractional tectonics (Morley et al., 2003; Morley et al., 2008; Hesse et al., 2009; King et al., 2010b). The interference of extensional and compressional features primarily affected the sedimentary sequence landward of the present day shelf break (Hess et al., 2009) (*Figure 5.1b*). Seaward of the shelf break, a purely contractional

fold-thrust belt developed (Ingram et al., 2004), affecting Middle Miocene to Recent sediments. This fold-thrust belt has been primarily interpreted to be driven by gravity, and linked to the extension on the shelf (e.g., Hazebroek and Tan, Sapin et al., 2013; Hall, 2013) (*Figure 5.1b*).

5.3.2 Deeper stratigraphy and potential positions of the NBFB basal décollement - previous studies

Beneath the NW Borneo continental margin, the NBFB is underlain by a prominent regional unconformity that is marked by a seismic reflector of high-amplitude, high-continuity, and positive polarity (Hinz et al., 1989; Hazebroek and Tan, 1993; Hess et al., 2009; Hess et al., 2010a). This unconformity has been given a range of names, and ascribed different ages in different regions by different authors. Levell (1987) named this the Deep Regional Unconformity (DRU), while others, such as Balaguru and Hall (2008), refer to this as the Mid Miocene Unconformity (MMU), and others, such as Cullen (2010, 2014), Xu et al. (2016), refer it more generically as the South China Sea Unconformity (SCSU). In this paper we use the term SCSU because the unconformity in this study area is not always deep, and its age is unconfirmed.

This SCSU is interpreted as the top of Nido carbonates of Oligocene to Late Early Miocene age (e.g., Kudrass et al., 1986; Levell, 1987; Hinz et al., 1989; Hazebroek and Tan, 1993; Schlüter et al., 1996; Franke et al., 2008; Cullen, 2014; Steuer et al., 2014), which is overlain by well bedded, but poorly lithified Middle Miocene and younger hemipelagic-pelagic sediments and prograding shelf/slope clastic sediments (Levell, 1987; Hazebroek and Tan, 1993). The latter form the sedimentary section deformed by the NBFB. The SCSU dips gently southeastwards at a depth of 4-8 km beneath the NBFB (e.g., Hinz et al., 1989; Ingram et al., 2004; Morley, 2007b; Franke et al., 2008; Hess et al., 2009; Cullen, 2010, 2014; Xu et al., 2016). Further landward, a deep high-amplitude seismic reflection event has been interpreted as the extension of the SCSU, continuing to dip gently southeastwards, at a depth of 10-12 km below the NW Borneo shelf (Morley, 2007b; Hess et al., 2009). The 2D seismic data suggests the unconformity dip increases from SE to NW along the margin: it is 2°–3° in SE offshore Brunei, increasing to a maximum of 7° in NE offshore Sabah, with an overall along-strike average of 3.8° (Hinz and Schluter, 1985; Hinz et al., 1989; Schlüter et al., 1996; Yan and Liu, 2004; Morley, 2007b; Hesse et al., 2009).

The thrust fault planes of the NBFB appear to converge onto a common décollement surface most likely located at a major rheological boundary in the sediment pile. Some authors have interpreted this to be the SCSU or equivalent (Hinz et al., 1989; Franke et al., 2008; Hess et al., 2009). Others propose it may form at a slightly shallower stratigraphic level, possibly related to overpressured clay or shale, such as the Setap Shale, overlying the SCSU (Ingram et al., 2004; Morley et al., 2009; Cullen, 2014).

5.4 Results

5.4.1 Fold-Thrust Belt Stratigraphy

The NW Borneo Slope Fold-Thrust Belt (NBFB) is developed in a wedge of deep-water, clastic-dominated Middle Miocene-Holocene sediments. These form a wedge that thins northwestward (seaward), mostly by gentle and progressive onlap onto a major basal unconformity (the SCSU). This deep water wedge terminates abruptly to the NW against the steep southern flank of a major regional carbonate high, the Dangerous Grounds (e.g., Cullen, 2014).

The SE part of the wedge is strongly affected by folding and thrusting within the NBFB. The base of the wedge is an angular, in places, erosive, unconformity (SCSU), and the basal surface of the overlying wedge shows major onlap. However, within the wedge, there are no identifiable major regional seismic unconformities. There are local unconformities within the shallow syn-kinematic section, showing local erosion and onlap related to active fold deformation, but these are not of regional extent. There are also widespread discontinuities of small vertical amplitude (<100 m scale) related to remobilization of slope sediment as mass transport deposits (Gee et al., 2007; McGilvery and Cook, 2004), but these do not represent regional tilting and can be considered to be part of the gross stratigraphy. Therefore the wedge as a whole can be considered as a grossly conformable unit. The lack of unconformities within the wedge contrasts with previous studies working further upslope, which highlight significant correlatable unconformities on the upper slope and shelf (e.g., Levell, 1987; Hinz et al., 1989; Schluter et al., 1996; Franke et al., 2008). This is to be expected because (i) the deepwater region consists of lower-relief anticlines separated by less deformed areas, whereas in the updip region, the structures are more closely spaced and higher amplitude, and (ii) small

changes in relative sea level are likely to result in erosion at shallower water depths.

Stratigraphic surface mapping

Previous studies have defined gross stratigraphic units within the wedge based on their seismic and structural characteristics; these studies have focused on the shelf/upper slope further upslope than this study (Bol and Van Hoorn, 1980; Levell, 1987; Hinz et al., 1989; Schlüter et al., 1996; Ingram et al., 2004; Franke et al., 2008). In this study, we mapped 7 surfaces; the seafloor, 5 marker horizons of high amplitude and lateral continuity within the NBFB wedge (H0 to H4, from young to old), and the SCSU at the base of the wedge. We have determined the approximate equivalence of horizons H0-H4 to the published stratigraphy, based on seismic character matches to published sections, but our primary purpose here was to identify and map regionally correlatable seismic horizons for structural analysis, rather than to study specific chronological or geological units defined by others. Therefore surfaces H0-H4 do not correspond directly to the published stratigraphic divisions. Surfaces H0 to H4 are conformable seismic horizons, but as noted above, they may correlate to unconformable boundaries updip.

Horizon H4 is the deepest mappable seismic horizon of moderate-high amplitude and lateral continuity that is traceable throughout the NBFB. It forms the base of the pre-kinematic sedimentary sequences with inferred late Early Miocene to early Middle Miocene age based on its relationship with the SCSU and overlying horizon H3.

Horizon H3 (early Middle Miocene) forms the top of a low frequency band of parallel reflectors. Although surface H3 is not unconformable in the seismic data, it is provisionally correlated to "Unconformity C" of Franke et al. (2008), which may in turn be the deepwater equivalent of the ‘Deep Regional Unconformity’ (DRU), a major break in sedimentation recognised offshore and onshore (Bol and van Hoorn, 1980; Levell, 1987).

Horizon H2 (early Middle Miocene) is correlated to Unconformity B of Hinz et al. (1989), Schluter et al. (1996) and Franke et al. (2008), with an inferred age of 12-14 Ma. However, given the time transgressive nature of this horizon further upslope, it may be as young as Late Miocene and thus roughly coincide with the ‘Shallow Regional Unconformity’ (SRU) (e.g., Levell, 1987; Tan and Lamy, 1990; Rice-Oxley, 1991).

Horizon H1 represents a narrow band of high amplitude reflectors within low-amplitude reflectors, and is equivalent to Horizon A of Franke et al. (2008) and Horizon II at the

Early/Late Pliocene boundary of Levell (1987). Hinz et al. (1989) interpreted this horizon to represent the base of the upper Pliocene sediments.

Table 5-1 Seismic Horizons used in this study and their relationship to other studies (after Franke et al., 2008)

Horizon	**Estimated age**	**Equivalent horizons from other studies**	**Horizon and overlying unit properties from this and other studies**
H0	Early Pleistocene	Horizon B (Morley, 2009)	Base of infill of synclinal mini-basins Top of pre-deformation (pre-kinematic) sequence with respect to majority of folds in frontal NBFB
H1	Early/Late Pliocene boundary, 3.6 Ma	Unconformity A (Hinz et al., 1989; Franke et al., 2008)	Truncation surface with minor onlap. Associated with open anticlines and synclines with a general NW-SE orientation (compressional tectonic).
H2	Late Miocene, 10 Ma	Shallow regional unconformity (SRU); unconformity B (Schlüter et al., 1996; Franke et al., 2008) Upper intermediate unconformity (UIU)(Levell, 1987)	Evidence for an erosional unconformity and onlap above the horizon, interpreted as a rise in sea level (see Franke et al., 2008; Levell, 1987).
H3	Early Middle Miocene(?), 16 Ma	Unconformity C (Hinz et al., 1989; Schlüter et al., 1996; Franke et al., 2008)	Base of thrust-deformed section. Potentially related to the end of active subduction along the BW Borneo Trough in the early Middle Miocene.
H4	Late Early Miocene(?), 17 Ma		Base of prominent seismic reflections representing pre-kinematic sedimentation.
SCSU	Oligocene to Late Early Miocene, 17-33 Ma	Horizon D (Kudrass et al., 1986; Hinz et al., 1989; Schlüter et al., 1996; Franke et al., 2008)	Top of carbonate unit originating from the Dangerous Grounds region.

Horizon H0, equivalent of horizon B of Morley (2009a), is located near the base of a higher amplitude, laterally continuous reflection package that represents the infill of the synclinal mini-basins forming between the active folds (piggy-back basins). It is also interpreted to mark the top of the pre-kinematic sequence with respect to the majority of the folds in the frontal FTB, and we infer an age of early Pleistocene based on its relationship with underlying horizon H1.

Whilst some highly discontinuous to chaotic sequences are present, in general the reflectors are continuous and sub-parallel (e.g., Morley, 2009a). The age and nature of each marker horizon and their relationship to other studies is listed in *Table 5-1*. As this study concentrates on the deepwater FTB developed after the formation of SCSU, the seismic reflections and related structures underlying the SCSU are not described.

5.4.2 Structural styles

To analyze the thrust system, the folds and related faults are numbered. Numbering increases from the hinterland (landward) to the foreland (seaward).

Morley (2009b) used a edge detection map of the seabed to highlight increased slope dips on the seaward/outer anticlines compared with the upper slope, thus defining 9 anticlines, I-IX, across the NBFB, offshore Brunei (*Figure 5.2a*). However, this approach is probably insufficient since some anticlines are buried and lack seafloor expression. Therefore here we created a surface map of horizon H0 up to 1 km beneath the seafloor, representing the top of the syn-kinematic sequence with respect to the majority of folds, to identify more structures relative to Morley's study and increase the representativeness of the analysis. As shown in *Figure 5.2b*, the new results visualize additional high-slope areas that correspond to the limbs of anticlines. We therefore defined 12 anticlines (folds I-XII), trending NE-SW, parallel to the NW Borneo trough (Fig. 2b).

In terms of structural style, three principal types of fault-related folds have been recognized in natural thrust systems around the world: fault-bend folds (FBFs) (Suppe, 1983; Mueller and Talling, 1997; Hubert-Ferrari et al., 2007; Lu et al., 2017), fault-propagation folds (FPFs) (Suppe and Medwedeff, 1990; Hardy and Ford, 1997; Carena and Suppe, 2002; Khalil and McClay, 2002; Hughes and Shaw, 2015) and detachment folds (DFs) (Grando and McClay, 2004; Chen et al., 2005; Gonzalez-Mieres and Suppe, 2006).

FPFs generally contain a planar or listric thrust fault, verging to the foreland, while the FBF has flat-ramp-flat fault geometry and the ramp governs the development of the fold. Both FPFs and FBFs displace sedimentary layers. In contrast, a DF is characterized by folded layers without displacement, underlain by a basal décollement. Interpretation of structural style and the underlying décollement is also a function of data resolution and image quality, and this is particularly true for detachment folds where there is no layer displacement.

Based on these fold categories, we structurally interpreted the 2D/3D seismic data, defined fold structural styles and spatial distribution, and investigated the fault and associated fold development and propagation in time and space. Here we present results of interpretation of seven of the 2D seismic profiles extracted from the 3D volume.

Seismic profile 2300 traverses the southwest section of the FTB (*Figure 5.2* & *Figure 5.3*), with seismic horizons H0-H4 and SCSU mapped and five of the regional folds identified (folds XII, IX, VIII, VI and V; *Figure 5.3*). Folds XII and V are detachment folds without obvious fault displacement of the sedimentary layers. Fold XII appears to be detached onto the SCSU (*Figure 5.3*). The position of this fold may be a function of minor topography on the SCSU (although this could be a seismic artefact) and may be an example of the effect of existing décollement geometry on structural development (e.g., Macedo and Marshak, 1999; Huerta and Harry, 2012). By contrast, the décollement position relative to fold V is poorly imaged. Several high-amplitude reflectors above the SCSU are crosscut by chaotic seismic facies here, interpreted as evidence for mobile shale diapirism (Van Rensbergen and Morley, 2003). Folds IX, VIII are interpreted as fault-propagation folds with high-level confidence, because their stratigraphic horizons are displaced by basin-vergent thrust faults whose displacement seems to decrease up-dip. In contrast, fold VI shows major characteristics of a décollement fold, without obvious displacement of sedimentary layers. This fold appears to interact with a shale diapir, characterized by the same chaotic seismic facies as observed at fold V, but part of seismic horizons H3 and H4 at the core of fold VI are truncated by this diapir, leading to uncertainties in geometry as highlighted by the dashed lines. Fold VI is therefore classified as a décollement fold cored by a shale diapir.

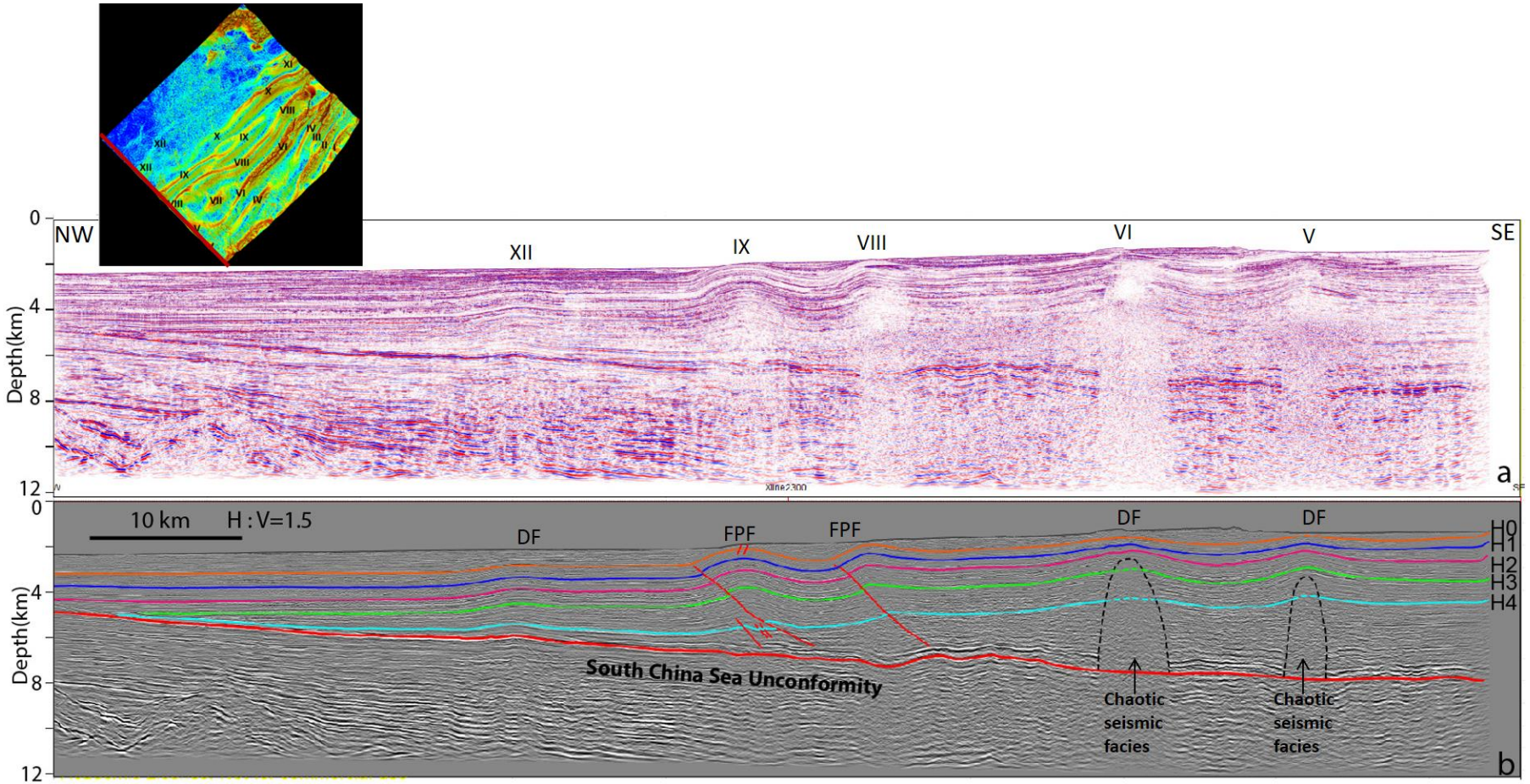

Figure 5.3 (a) Uninterpreted and (b) interpreted 2D depth-converted seismic line 2300 with 1.5 x vertical exaggeration. The interpreted horizons (coloured lines, H0-H4) are mainly within the pre-kinematic sedimentary sequences highlighting important characteristics of the structures including fold and thrust shapes. DF denotes detachment fold, FPF denotes fault-propagation fold. Inset is surface map of horizon H0 with seismic line location indicated.

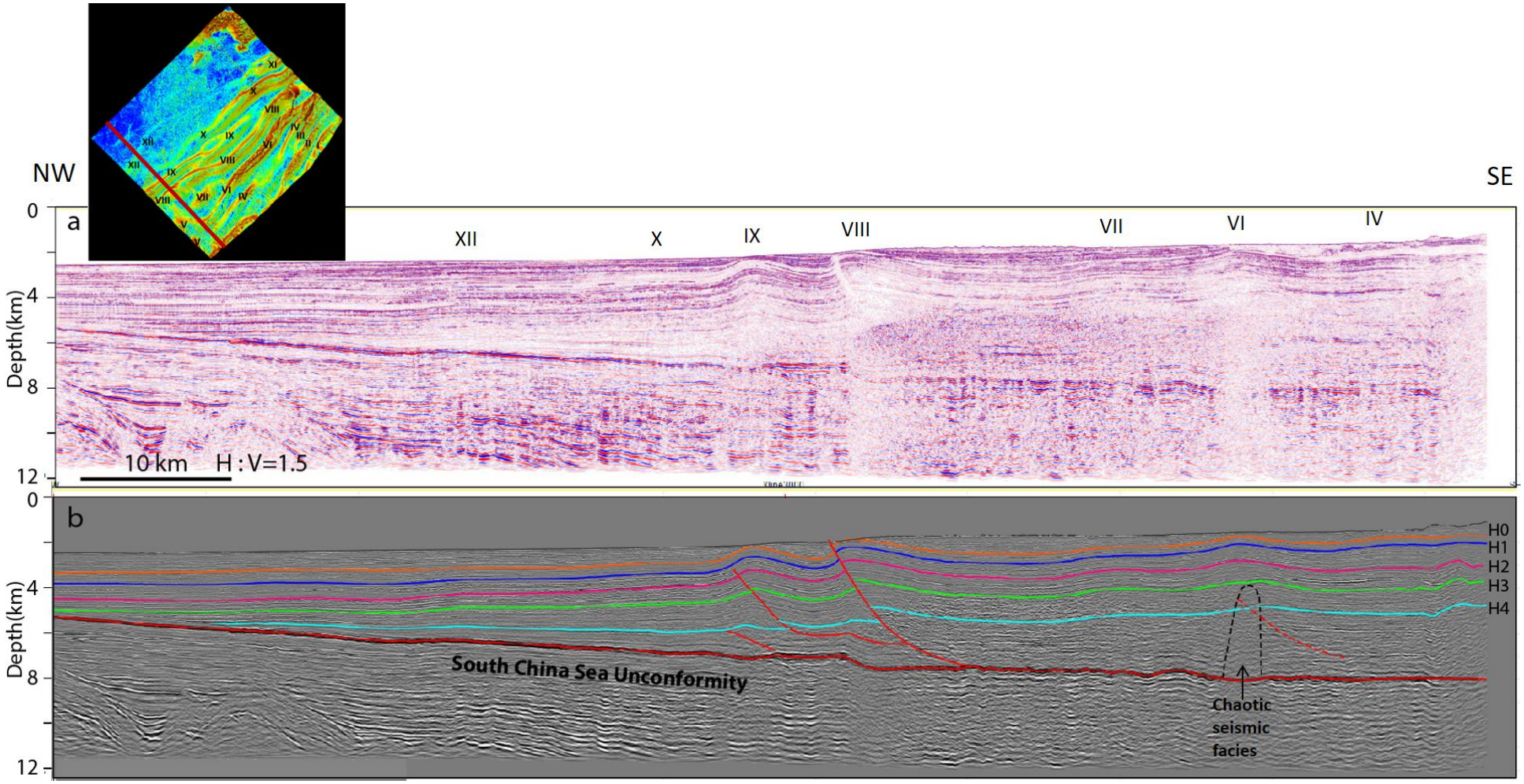

Figure 5.4 (a) Uninterpreted and (b) interpreted 2D depth-converted seismic line 3000 (1.5 x vertical exaggeration).

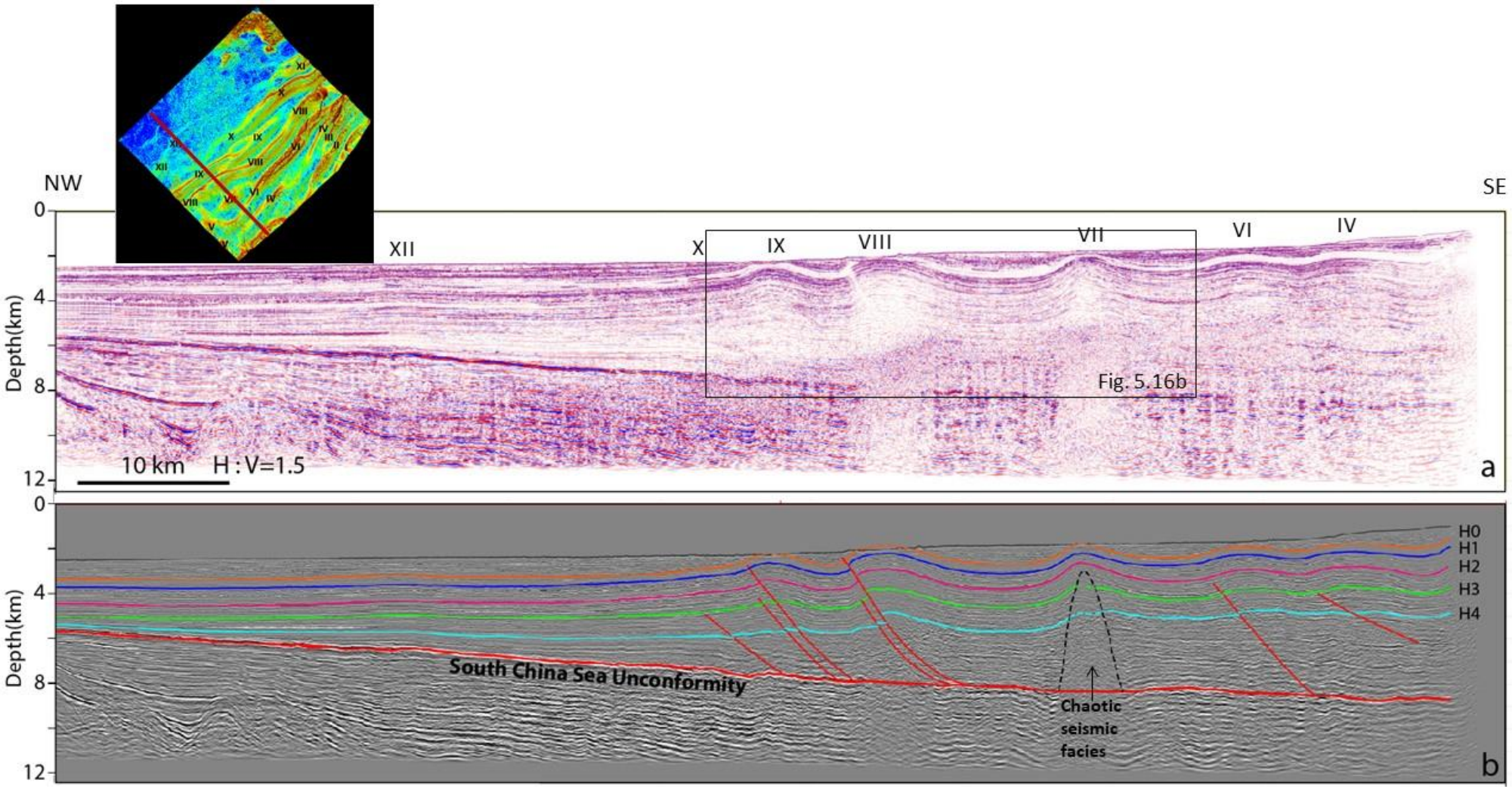

Figure 5.5 (a) Uninterpreted and (b) interpreted 2D depth-converted seismic line 4000 (1.5 x vertical exaggeration).

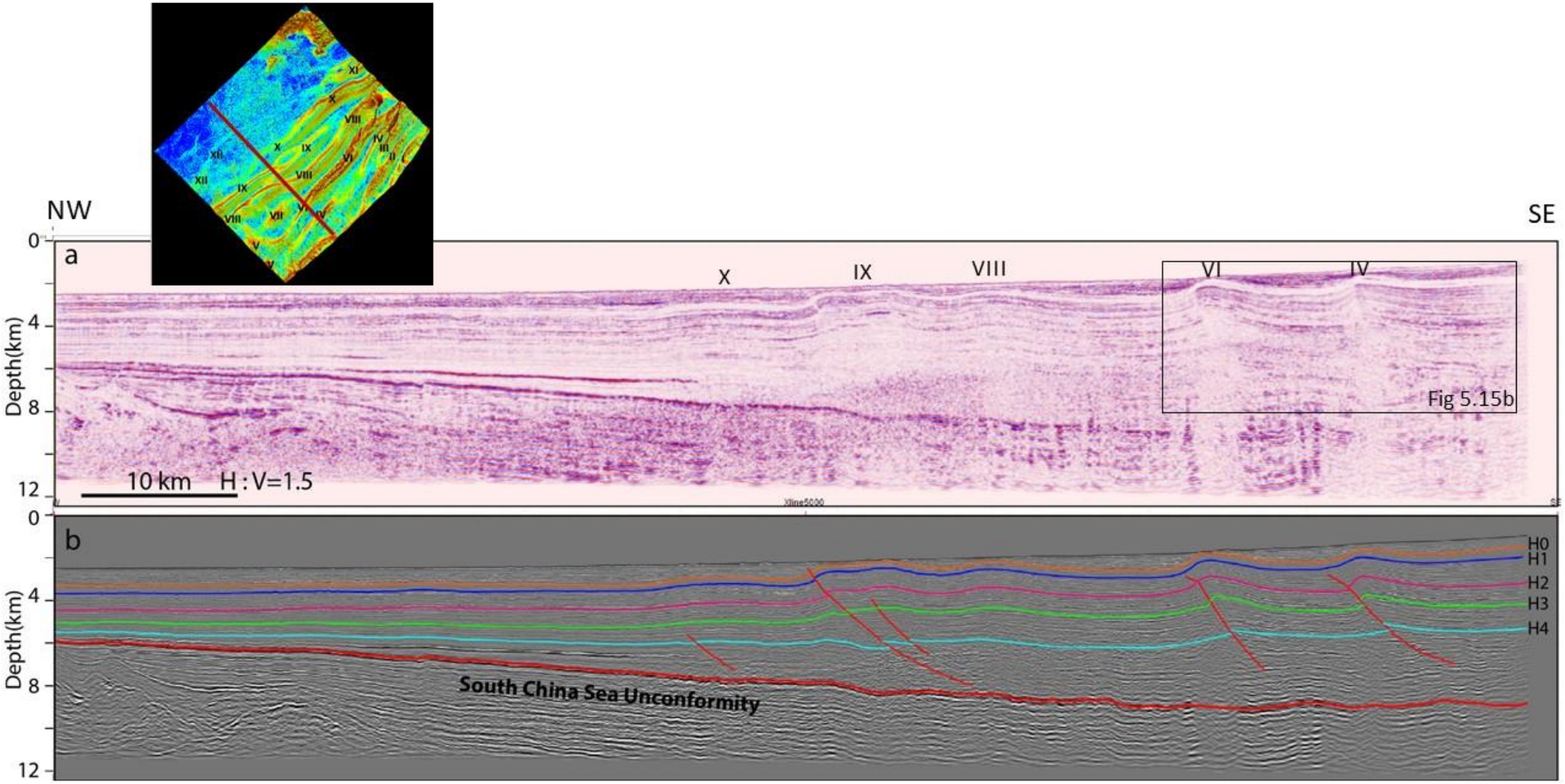

Figure 5.6 (a) Uninterpreted and (b) interpreted 2D depth-converted seismic line 5000 (1.5 x vertical exaggeration).

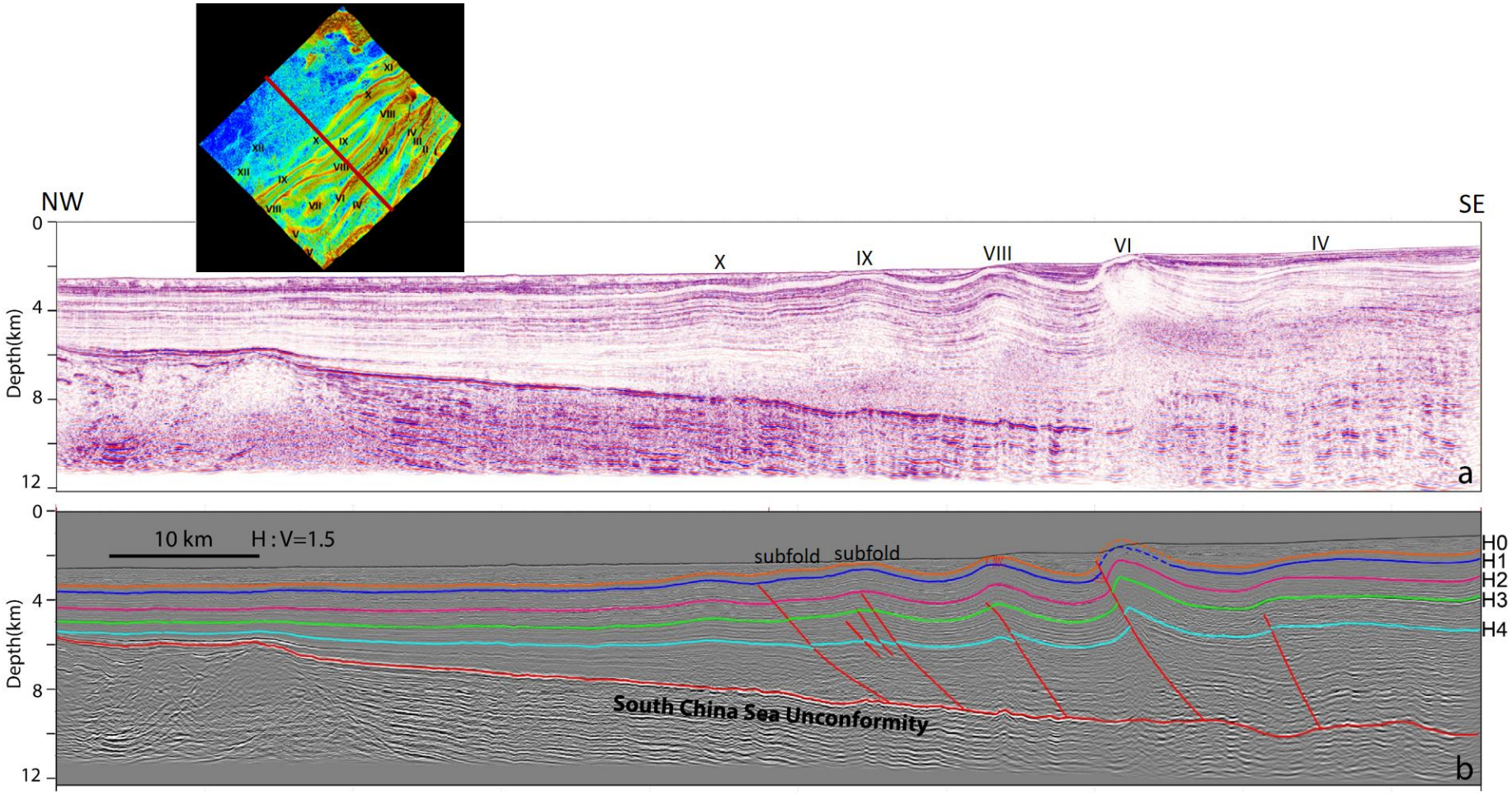

Figure 5.7 (a) Uninterpreted and (b) interpreted 2D depth-converted seismic line 6000 (1.5 x vertical exaggeration).

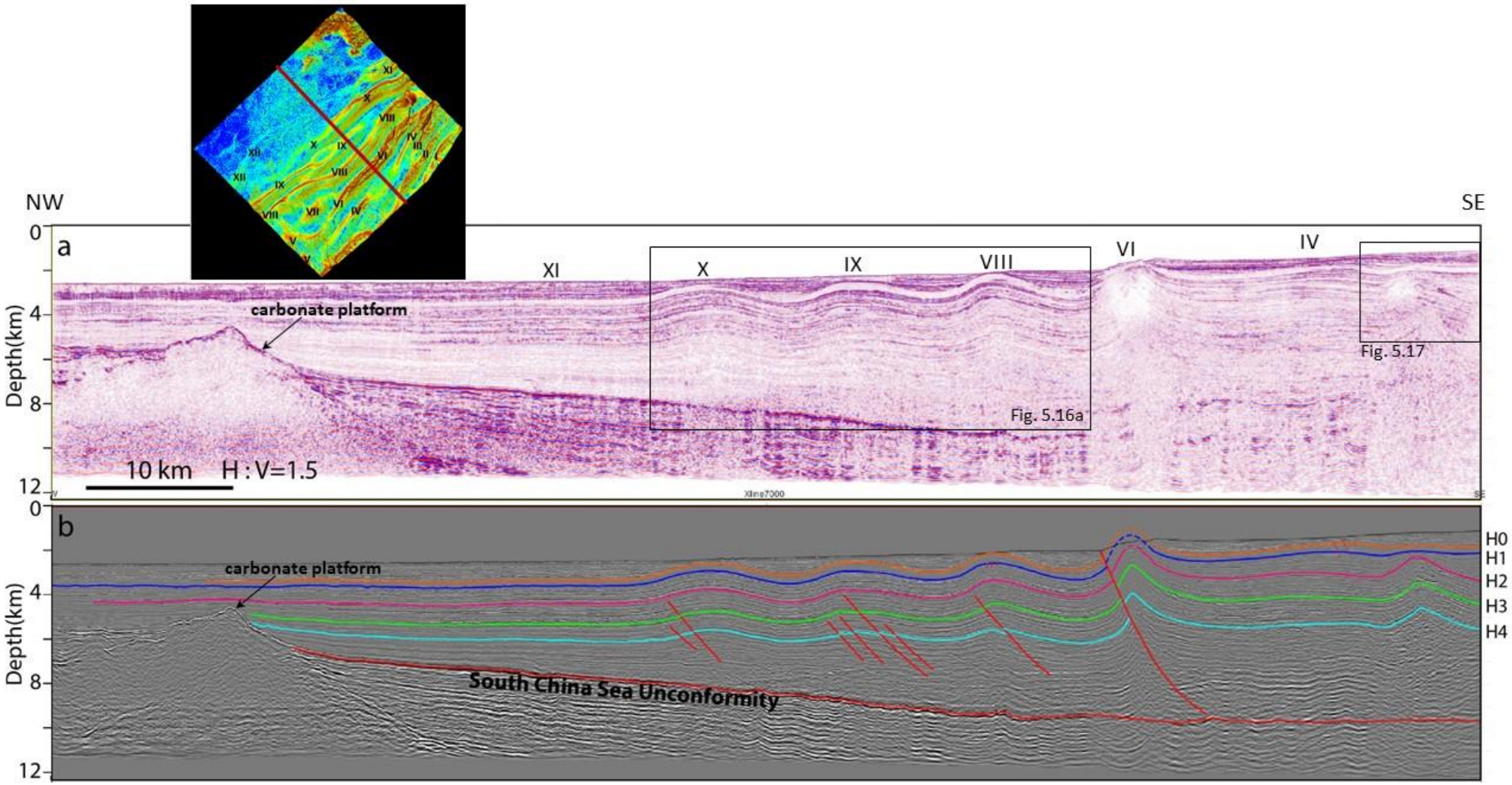

Figure 5.8 (a) Uninterpreted and (b) interpreted 2D depth-converted seismic line 7000 (1.5 x vertical exaggeration).

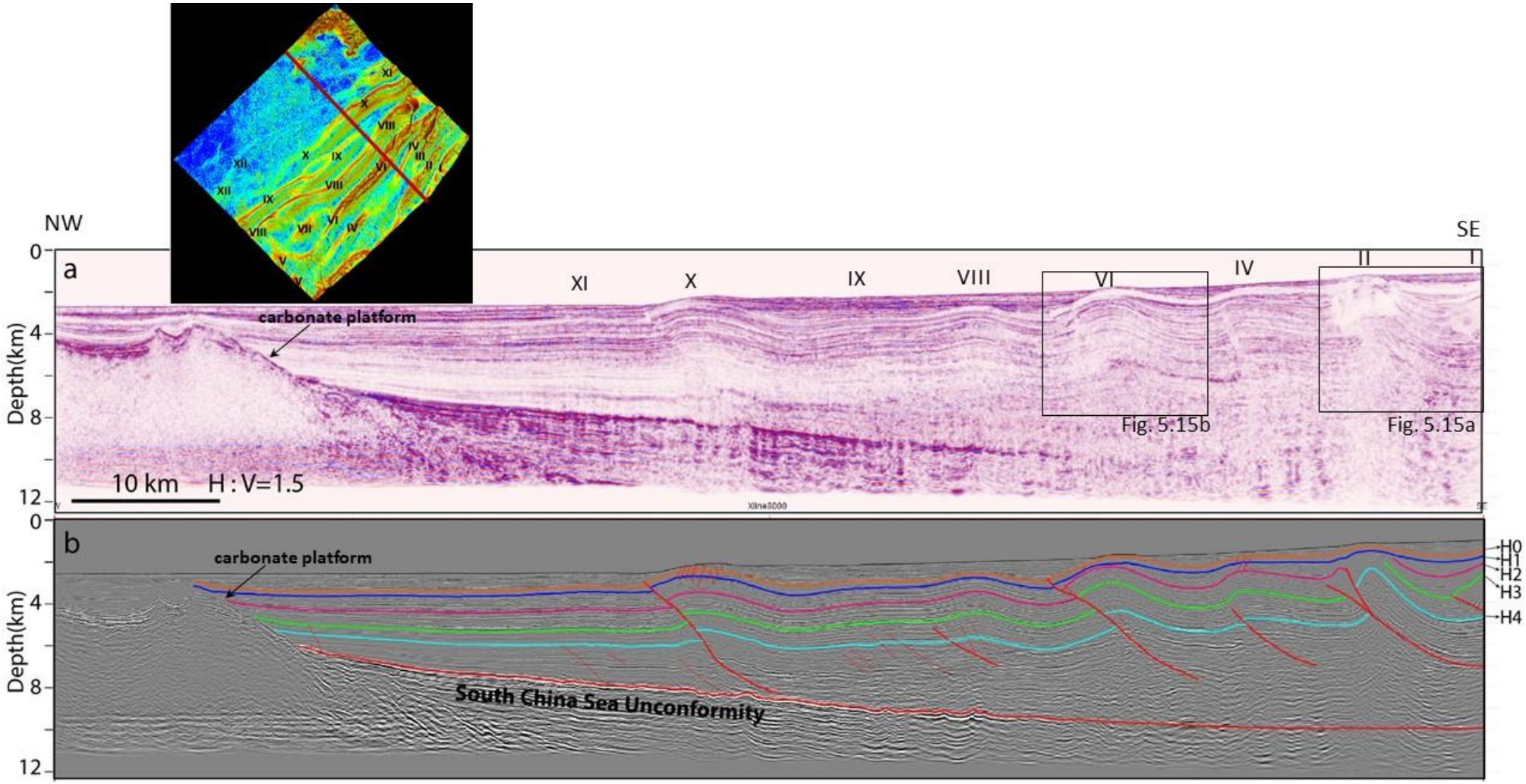

Figure 5.9 (a) Uninterpreted and (b) interpreted 2D depth-converted seismic line 8000 (1.5 x vertical exaggeration).

Profile 3000 (7 km NE of 2300) crosses seven folds: XII, X, IX, VIII, VII, VI and IV (Figure 5.4), but only three anticlines are clearly imaged: IX, VIII, VI. Fold IX is a fault-bend fold while Fold VIII and VI are fault-propagation folds, with one or more seismic horizons displaced by thrust faults. The lower portion of the thrust fault of fold IX shows a typical ramp-flat-ramp geometry, and appears to inherit the shape of the underlying SSCU. This adds to the evidence that pre-existing décollement topography influences fault/fold development. The chaotic seismic facies seen in profile 2300 is also observed within fold VI here, and interpreted as a shale diaper. The remaining four folds (XII, X, VII, IV) are detachment folds characterized by very large inter-limb angles of up to 160˚and long wavelength, and are interpreted as at the early stage of fold development (Hesse et al., 2010c).

Profile 4000 (10 km NE of 3000) images folds XII, X, IX, VIII, VII, VI and IV (*Figure 5.5*). As on profiles 2300 and 3000, fold XII is typical of a décollement fold, but with some evidence of structural inheritance here. The amplitude of fold X is almost negligible on this profile, suggesting fold X terminates nearby. As seen in the Horizon H0 surface map (*Figure 5.2c*), only a slight trace of fold X is visible seaward of fold IX on this profile, whereas it has increasing amplitude northeast of profile 4000, indicating it initiates at Northeast and propagates to Southwest. Folds IX and VIII have clear, well imaged geometries, and each has a secondary, shorter parallel fault that lies in the footwall of the major, longer fault, ~1 km apart. Fold VII is interpreted as a décollement fold due to a lack of displacement, however the décollement itself cannot be resolved. Folds VI and IV are fault-propagation folds displacing horizons H3-H4 and H4, respectively.

Profile 5000 is located in the Central-SW of the study area, and traverses 5 folds, X, IX, VIII, VI, and IV (*Figure 5.6*). Fold X is primarily a fault-propagation fold at an early stage with only the deepest horizon, H4, slightly displaced. Fold IX is typical of a fault-propagation fold where all stratigraphic horizons are being displaced by a major thrust fault. A minor fault is observed 2-3 km landward of this major fault, displacing horizons H3 and H4. It is difficult to tell where this minor fault roots or its relationship to the major fault because of reduced seismic resolution. Fold VIII presents as a décollement fold on this profile. Further landward, folds VI and IV show the characteristics of fault-propagation folds with three horizons (H2-H4) displaced. These faults appear to initiate at depth, and then propagate up towards the fault tip with decreasing displacement.

Profile 6000 (10 km NE of 5000) traverses folds X, IX, VIII, VI, IV (*Figure 5.7*). Fold X still exhibits some characteristics of a décollement fold without obvious displacement of the sedimentary layers, as on profiles 4000 and 5000. In contrast to Fold X, fold IX appears to be more complex structurally, consisting of two sub-folds. The seaward sub-fold is interpreted as a fault-propagation fold with two gently-dipping limbs. This sub-fold seems to act as the forelimb of the primary fold IX that is clearly also a fault-propagation fold. Three sub-parallel thrust faults are observed associated with fold IX, one major and two minor. Further landward, folds VIII, VI and IV are all fault-propagation folds with relatively simple structure. Fold VI has significant thrust displacement of the sedimentary layers and there is also significant seabed displacement forming a prominent scarp up to 500 m.

Profile 7000 (10 km NE of 6000) images folds XI, X, IX, VIII, VI and IV (*Figure 5.8*). Fold XI has very minor, almost negligible deformation relative to that on other profiles, because this profile crosses the structure's SW tip (see inset of H0 surface) and is at the very initial stage of development. The remaining folds are fault-propagation folds. Unlike the simplified model of a fault-propagation fold (FPF) (Suppe and Medwedeff, 1990; Hardy and Ford, 1997), some of the FPFs here incorporate a set of parallel and unrooted faults. Fold VI shows enhanced deformation on this profile, with two of the stratigraphic horizons (H3 and H4) eroded at the fold crest and forming a 2-3 km wide scarp on seafloor. Similar to fold XI, fold IV is also at its initial growth stage with minor deformation. Shown in the surface map (*Figure 5.2c*), this profile (7000) transects the saddle of fold IV characterized by low-fold relief where the two distinct fold segments have not yet fully connected, supporting its early stage of development. At the landward end of this profile, a décollement fold is imaged deforming horizons H2-H4. This fold appears to be no longer active; its growth ceased when the stratigraphic layer overlying H1 started to deposit and the thickness of subsequent sedimentary layers remains constant. It is therefore not imaged in the H0 surface map or numbered (*Figure 5.2b*).

Profile 8000 (10 km NE of 7000) traverses folds XI, X, IX, VIII, VI, IV, II (*Figure 5.9*). Fold XI shows the characteristics of a décollement fold with two incipient faults at depth which have yet to displace any stratigraphic horizons. These incipient fault traces are interpreted as a result of increased shortening across fold XI. In contrast, fold X shows the distinct characteristics of a fault-propagation fold with all sedimentary sequences displaced by a major seaward-verging thrust. At the crest of this fold, normal faulting is

developed as a product of gravity-induced deformation, outer arc/crestal bending and crestal collapse (e.g., Berberian, 1979; Avouac et al., 1992; Morley, 2007a).

Further landward, fold IX shows negligible deformation on this profile. It is difficult to determine if this is a fault-propagation fold despite a set of four parallel minor thrust faults observed at depth. Unlike the major thrust that controls the growth of adjacent fold X, these four thrusts show minimal displacement. The adjacent fold VIII is a fault-propagation fold supported by three faults: one major low-angle thrust, and two secondary high-angle reverse faults. The high-angle faults are interpreted as a result of structural adjustment: with increasing shortening, the strain is adjusting between folding and thrusting. Similar to fold X, fold VI is also a typical fault-propagation fold, with its growth largely controlled by a thrust fault and with prominent seafloor expression. Among the remaining three folds, IV and II are all fault-propagation folds, which appear to have experienced multiple stages of fold growth and fault activity. In addition, fold II has been subjected to erosion by slumping (Gee et al., 2007; Morley, 2009b), leading to truncation of horizons H2 and H3 at the fold crest. The geometry of fold I is not revealed in this profile because only a minor part of its forelimb is visible.

Thus, across the NBFB, fault-propagation folding (FPF) is the most common structure type (*Table 5-2*), primarily appearing as a series of interdigitating folds that produce distinct seafloor relief and significant displacement of up to 1.4 km of pre-kinematic sedimentary layers. In contrast, the less common detachment folds observed are primarily young (*Table 5-2*), immature folds that are largely buried with no/minimal seafloor expression and minimal displacement of stratigraphic horizons. *Table 5-2* shows fold type and change across or along strike for the NBFB. There is only one fault-bend fold observed, which is interpreted to result from the topography on the underlying SCSU. Variation in structural style along strike of an individual structure is common in the NBFB. For instance, Fold VI changes from DF to FPF towards the NE (increasing in seismic line number) while Fold IX changes from DF to FPF towards the SW. The foreland is dominated by detachment folds due to fold immaturity in the frontal part of the FTB. There is variation in fold style across strike, but without a clear pattern. Processes affecting these patterns will be investigated below, in particular factors influencing along-strike variation such as fold initiation and propagation history (Section 5.5.1).

Table 5-2 Summary of fold styles in this study

Seismic profile	Folds (seaward (XII) to landward (IV) across-strike)								
	XII	XI	X	IX	VIII	VII	VI	V	IV
SW 2300	DF			FPF	FPF		DF	DF	
3000	DF		DF	FBF	FPF	DF	DF		
4000	DF		FPF	FPF	FPF	DF	FPF		FPF
5000			FPF	FPF	DF		FPF		FPF
6000			DF	FPF	FPF		FPF		FPF
7000		DF	FPF	FPF	FPF		FPF		DF
NE 8000		DF	FPF	DF	FPF		FPF		FPF

DF= Detachment fold, FPF= Fault-propagation fold, FBF=Fault-bend fold

5.4.3 Fault geometry

The thrust faults in the NBFB are mostly associated with folding, and their structural development plays a fundamental role in controlling the kinematic growth and propagation of folds. Here we quantify fault dip, displacement and spacing, and ultimately use these data to examine fault development and associated fold growth in space and time. For this section, we use all faults including the fault-propagation fold faults, the fault-bend fold fault and any associated incipient faults.

5.4.3.1 Fault dip

As illustrated in *Figure 5.3* & *Figure 5.9*, most of the thrust faults are characterized by a listric or curved geometry rather than planar (and we note these are depth sections therefore fault dip with depth is not a function of velocity). A single dip value is therefore not sufficient to represent the overall fault dip. To better characterize the fault shape, we use the cut-offs of the mapped horizons to define fault segments. The fault segment below horizon H4 is not included since its geometry is not well resolved in the data. Fault

dip is measured here for all faults, i.e., primary mature faults (FPFs and the FBF) and incipient faults, with FPFs dominating (*Figure 5.10*). Incipient faults are defined as structures where a fault plane reflector is imaged but actual slip was unresolvable, i.e. probable minor or immature faults). We note that the dips obtained are apparent dips in the direction of the seismic profile, however analysis of the 3D dataset indicates they are close to true dips i.e., the 2D sections are broadly perpendicular to the structural trend.

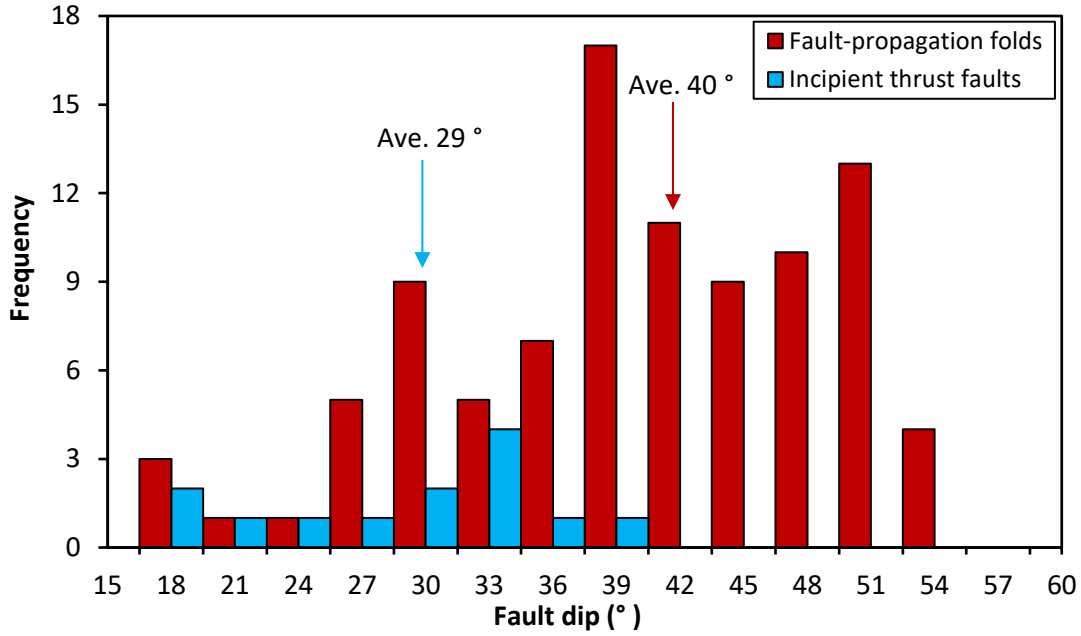

Figure 5.10 The distribution of average weighted fault dips for all major faults (FPFs and FBF) and incipient thrust faults.

The dip angle for incipient faults is 18-39° (*Figure 5.10*), with a relatively high proportion of dips around 30-36° and a median value of 29°, roughly in accordance with the theoretical prediction of the Mohr-Coulomb criteria (Coulomb, 1773). For fault-propagation folds (and the fault-bend fold), dips have a wider range of 18-54°, averaging 40°. The majority of faults associated with FPFs and the FBF have fault dips >35°, i.e., larger than for incipient faults. We note that a longer fault that propagates to very shallow levels displacing all marker horizons is divided into more fault dip segments relative to a short fault and therefore a longer fault may statistically dominate the results.

Previous mechanical modeling suggests that fault-propagation folding is favored at higher fault ramp dips (Hughes and Shaw, 2014), similar to observations in this study (see *Figure 5.10*). Scaled physical analogue modelling shows that an incipient fault nucleates with low angle in association with a low-relief décollement fold in the front of a foreland-vergent

thrust system (Wu and McClay, 2011). The incipient fault then breaks through the sedimentary layers of the décollement fold with its tip reaching the surface, forming a fault-propagation fold as contraction continues, also accompanied by fault rotation and steepening. This highlights the changes of fault/fold type and fault dip in a growing fold-thrust system. In our study, the fault-propagation folds (and fault-bend fold) represent mature structures, and their associated faults have attained relatively high dip angles. However, we note that the fault dips measured here represent a snapshot of fault dips, and precise details of the original fault dip or its evolution is difficult to quantify.

5.4.3.2 Fault displacement

Fault displacement is quantified for all FPFs and the FBF. We quantified fault displacement from the separation of stratigraphic horizons and then plotted this as a function of distance up-dip along the fault (*Figure 5.11*); a "distance-displacement plot"(Hughes and Shaw, 2015). A steady decrease in fault displacement up-dip is observed, suggesting the faults initiate at depth and propagate up-dip. Moreover, the gradient in displacement appears constant, supporting the growth behavior of these thrust faults. This is similar to observations made in other thrust systems such as the Niger Delta passive-margin fold-thrust system and the Sierras Pampeanas of Argentina (Hedlund, 1997; Hughes and Shaw, 2015).

The fault separation for each horizon is also plotted as a function of along-strike distance from southwest to northeast, with a measurement every 10 km (*Figure 5.12*). The thrusts are numbered according to their associated folds. For this analysis, only the four folds that extend across the whole study area are included, i.e., those imaged on each profile (*Figure 5.12*). These faults are largely blind, therefore no displacement is available for H0 (*Figure 5.12*). The data are plotted together with the same displacement axis to highlight the magnitude of growth that each fault/fold attains.

Along-strike, a thrust/fold propagates laterally with decreasing displacement. The area where the fault/fold structure initiates is expected to attain the maximum displacement along the fault length (e.g., Higgins et al., 2009) and therefore its initiation location should be identifiable. For fold/fault IX (*Figure 5.12a*), the fault displacement for each horizon generally decreases towards the northeast, particularly for the deepest/oldest Horizon H4, suggesting a northeastward propagation. This is reinforced by the observation that

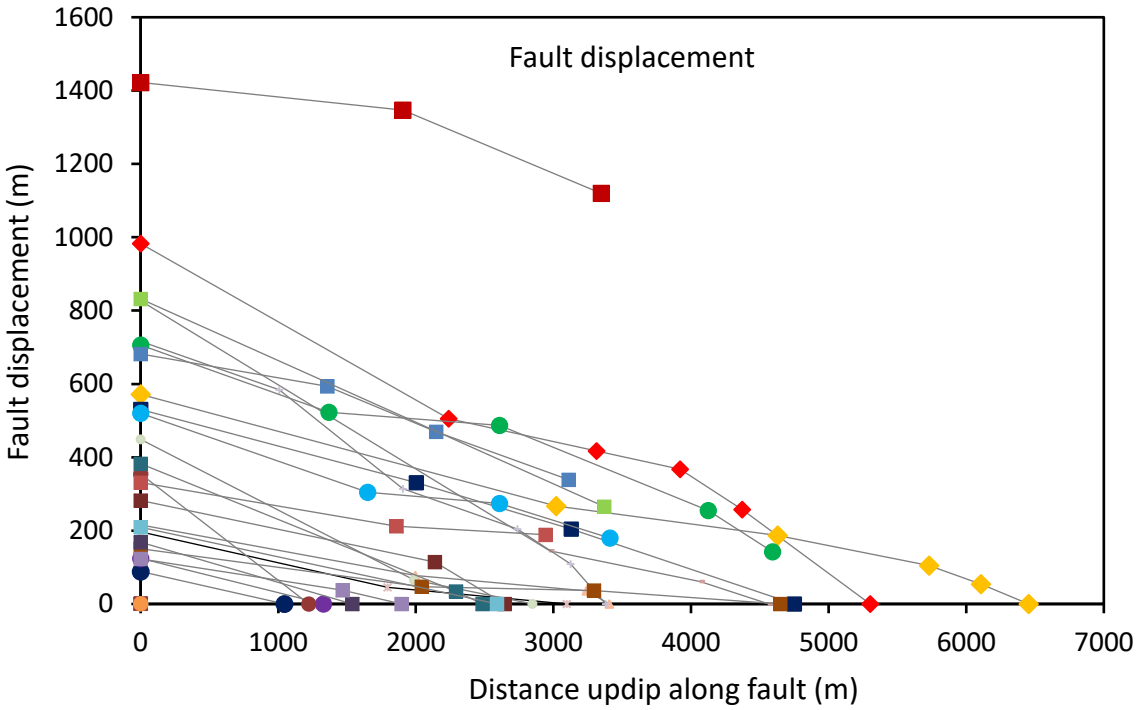

Figure 5.11 Compilation of displacement-distance measurements for all major thrust faults related to fault-propagation folds and the fault bend fold.

the number of seismic horizons displaced by fold/fault IX and VIII decreases northeastward. The maximum displacement of fault IX at ~2 km along strike suggests initiated here or further southwest, outside the data area. For fault IX, a pronounced increased fault displacement of H1-H4 is observed at 35 km deviating from the general decreasing displacement along-strike trend, implying a different position for the fault/fold (IX) initiation. An anomaly of very low displacement of H4 is observed at 20 km, which may be an artefact of uncertain interpretation exaggerating the low. However, because all horizons (including H1-H3) show a pattern of increased displacement at 35 km, the suggestion of this position for fault/fold initiation is still supported.

Contrasting slightly with fold IX, the fault of fold VIII is likely to have initiated at 10 km along strike where the maximum displacement of each horizon is located (*Figure 5.12b*). Fault displacement diminishes laterally in both directions suggesting it propagated both NE and SW. Another anomaly of relatively high displacement of H4 observed at 63 km is also likely an artefact.

For fold/fault VI, fault displacement decreases towards the southwest (*Figure 5.12c*), contrasting with fold/fault IX and VIII and suggesting southwestward fault propagation.

Due to surface erosion (McGilvery and Cook, 2004; Gee et al., 2007; McGilvery and Cook, 2013), the displacement for horizon H1 cannot be determined at 75 km.

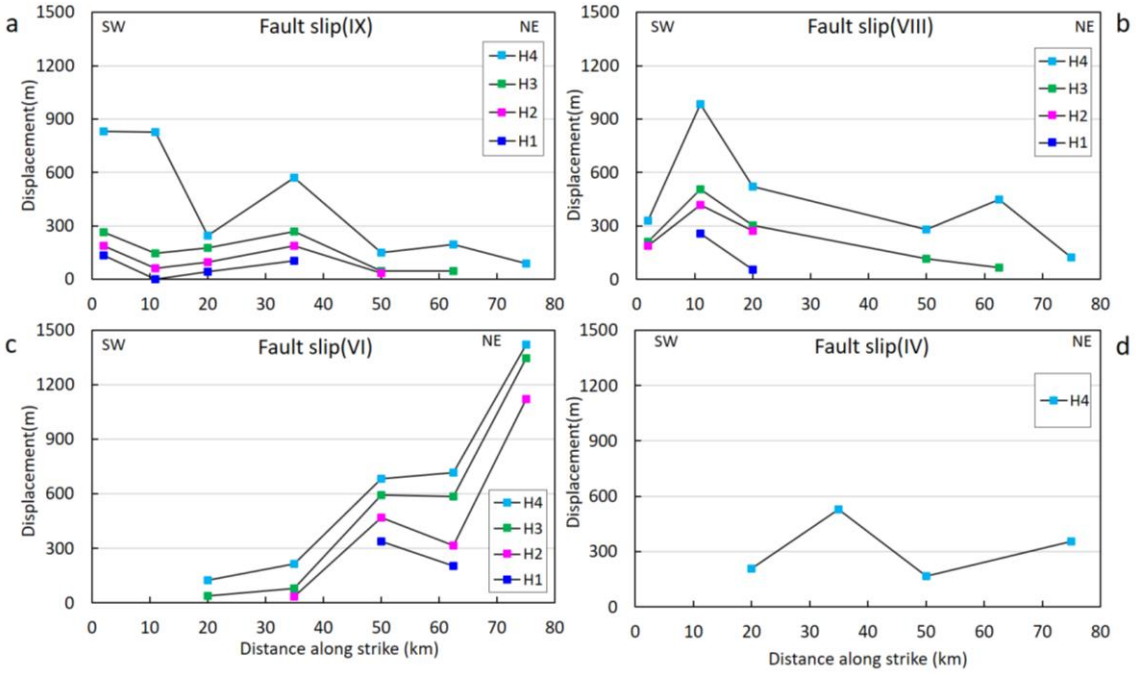

Figure 5.12 The fault displacement-distance relationship for seismic horizons H1-H4 for folds IX, VI, VIII and IV. Note distance is determined by along-strike distance rather than along-fault plane distance as in Figure 5.11.

Fold/fault IV is still at the early stage of initiation with the majority of deformation at depth, therefore only the deepest/oldest marker horizon (H4) is displaced northeast of 20 km (*Figure 5.12d*) and by only a small amount. However, the H0 surface map (*Figure 5.3b*) can also be used to visualize this fold shape and geometry to better evaluate fault/fold growth history. The largest fold IV limb slope occurs in the northeast (*Figure 5.3b*), decreasing southwestward to become very small at 20-25 km, then increasing again. These two sections of high slope are located at 10-50 km and 75-100 km along-strike (*Figure 5.3b* &*Figure 5.12d*), and are interpreted to represent the initiation regions of two folds that have propagated towards each other into the area of lower slope and then linked. The maximum displacement of 530 m for fault IV occurs at 35 km where the fault is interpreted to initiate and coinciding]with the first area of high slope, and then propagates principally towards the northeast with limited southwest propagation. However, another potential position for fault initiation is at 75 km, corresponding to the second high slope area (75-100 km) (*Figure 5.2b*).

5.4.3.3 Fault spacing

We defined fault spacing as the surface distance between the major thrust faults and apply this to the fault-propagation folds, excluding small or negligible-displacement incipient faults (*Figure 5.13*). Fault spacing fluctuates both along and across the margin, from 3 to 26 km, particularly across the margin in the southwest (e.g., profile 4000 in *Figure 5.5*). Fault spacing is on average larger and more variable in the southwest, and decreases and stabilizes towards the northeast, with overall average spacing ranging from 8-16 km (red dot, *Figure 5.13*). This is similar to the observation made by Hinz et al. (1989) for the adjacent Sabah portion of the NBFB where spacing varies between 3 and 15 km and generally tends to decrease towards the northeast.

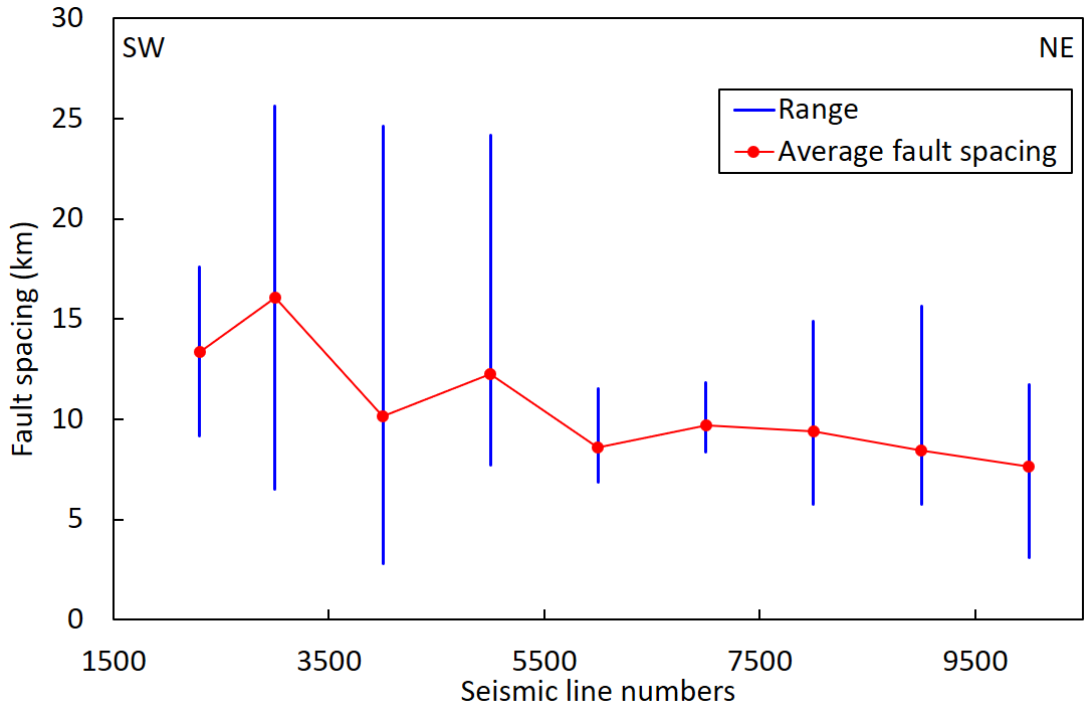

Figure 5.13 Plot of average fault spacing for each seismic line, with range of values indicated by blue bars. Fault spacing shows an overall decreasing trend towards the northeast (i.e. increase of seismic line number).

Fault spacing is thought to be sensitive to the stress field within a fault population (e.g., Cowie and Roberts, 2001; Roberts et al., 2004), thickness of sedimentary pile (depth of décollement) (Soliva et al., 2006), and nature of the décollement surface (Corredor et al., 2005). The controls on fault spacing in this study area will be discussed in detail in Section 5.5.1.

5.4.4 Fault activity

Active faults and associated folds develop distinctive stratigraphic geometries resulting from the interactions of sedimentation and deformation, which provides a quantifiable record of deformation history (Suppe et al., 1992; Hardy et al., 1996; Hardy and Ford, 1997; Shaw et al., 2004; Shaw et al., 2005; Gonzalez-Mieres and Suppe, 2006).

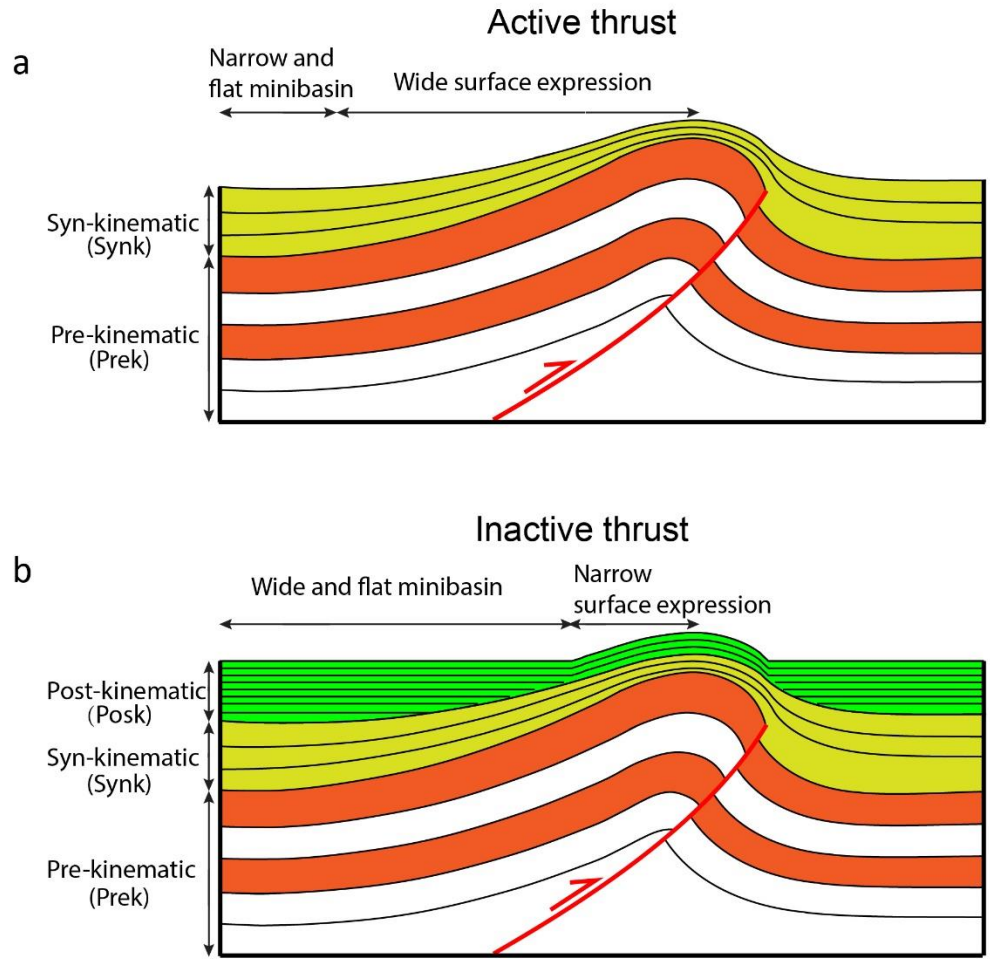

Figure 5.14 Schematic cartoon of (a) active and (b) inactive thrust faults showing effect of underlying structure activity on overlying sediments.

Modern seismic data with excellent images of growth sequences, allow us to extract this record of deformation in detail (Gonzalez-Mieres and Suppe, 2004). In cross-section, continuous activity of a thrust fault may be accompanied by persistent growth of a fault-related fold, e.g., an FPF. This coupled structure typically forms a sedimentary growth fan of syn-kinematic sediments in the hanging wall, thinning towards the anticlinal crest, i.e. the structural high, overlying the pre-kinematic sequence which has layer thickness unaffected by faulting (*Figure 5.14a*). Syn-kinematic sediments filling a mini basin (piggy-back basin) between active structures will also include growth strata and indicate

fault/fold activity history through growth, tilting and unconformities. Syn-kinematic sequences are also generally folded in one or more limbs of the structure (Shaw et al., 2005). In bathymetry data, one expects to see a relatively wide slope of folded syn-kinematic sequence and a narrow, flat, mini-basin associated with an active thrust (*Figure 5.14a*). Once a thrust fault becomes inactive and associated folding stops, post-kinematic sediments progressively fill the space created by the tilted hanging wall fold limb, widening the flat basin and narrowing the exposed slope (*Figure 5.14b*). The lowermost post-kinematic sequence tends to onlap the syn-kinematic sequences in some cases (Jackson and Hubec, 2017). All of these features can be used to assess fold/fault activity history.

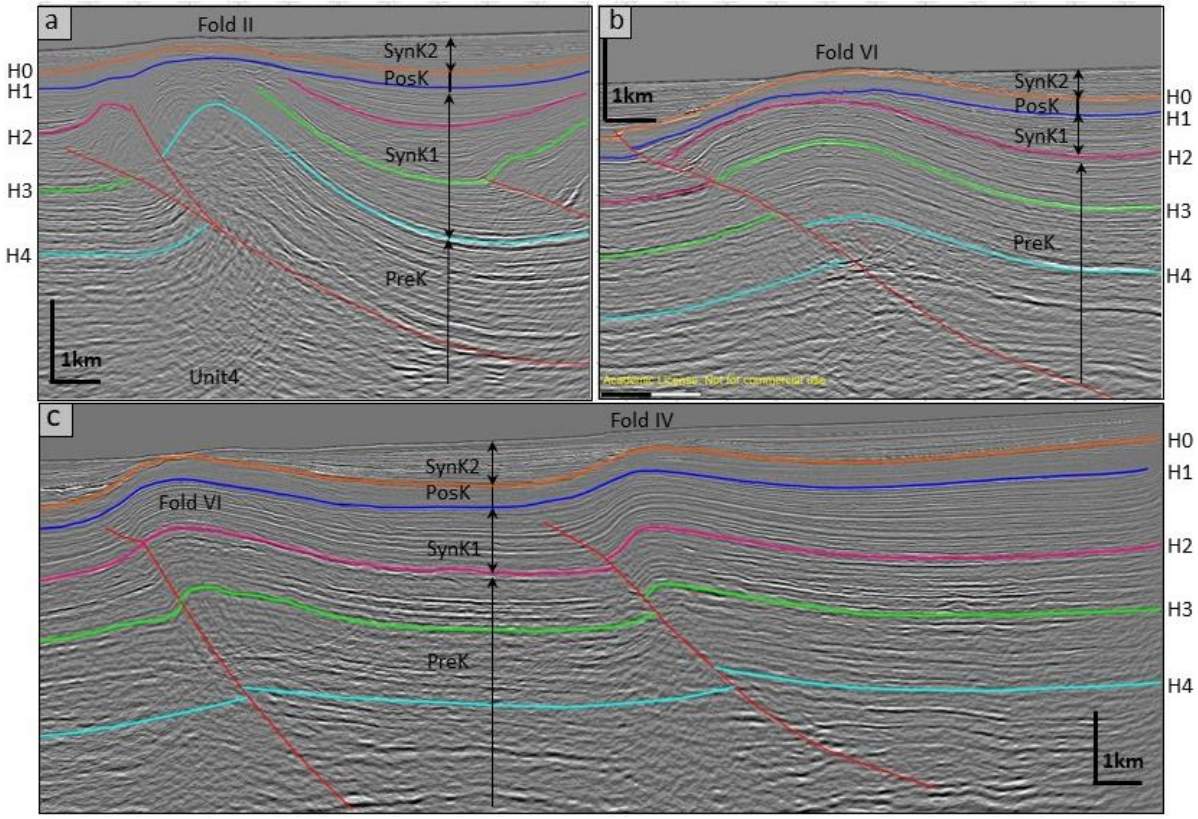

Figure 5.15 Seismic line examples of folds/faults with two stages of fault activity and associated fold growth. Fault activity is during deposition of SynK1 and SynK2.

Examples of stratigraphic patterns related to fault activity in the study area are shown in *Figure 5.15*, *Figure 5.156* & *Figure 5.17*, with folds grouped in these figures based on a shared pattern of growth history. Units are identified in each case based on distinct periods of fold/fault activity. In *Figure 5.15a*, four kinematically-distinct stratigraphic units are recognized in association with fold II: PreK, the pre-kinematic sequence below horizon H4; SynK1, the first syn-kinematic sequence between H4 and H1; PosK, the post-kinematic

sequence between H1-H0; and SynK2, the syn-kinematic sequence between H0 and the seafloor. Fold II activity begins as soon as PreK1 starts to deposit, which is accompanied by backlimb rotation.

This first stage of fold growth ceases when PosK starts to deposit, which maintains constant sedimentary thickness. Fold growth resumes as SynK2 starts to deposit, and lasts until the present-day, deforming the seafloor. Therefore, the two syn-kinematic units (SynK1, SynK2) result from two distinct stages of fault activity and associated fold growth. Folds VI and IV are also interpreted to have experienced two distinct phases of growth (*Figure 5.15b* & *Figure 5.15c*).

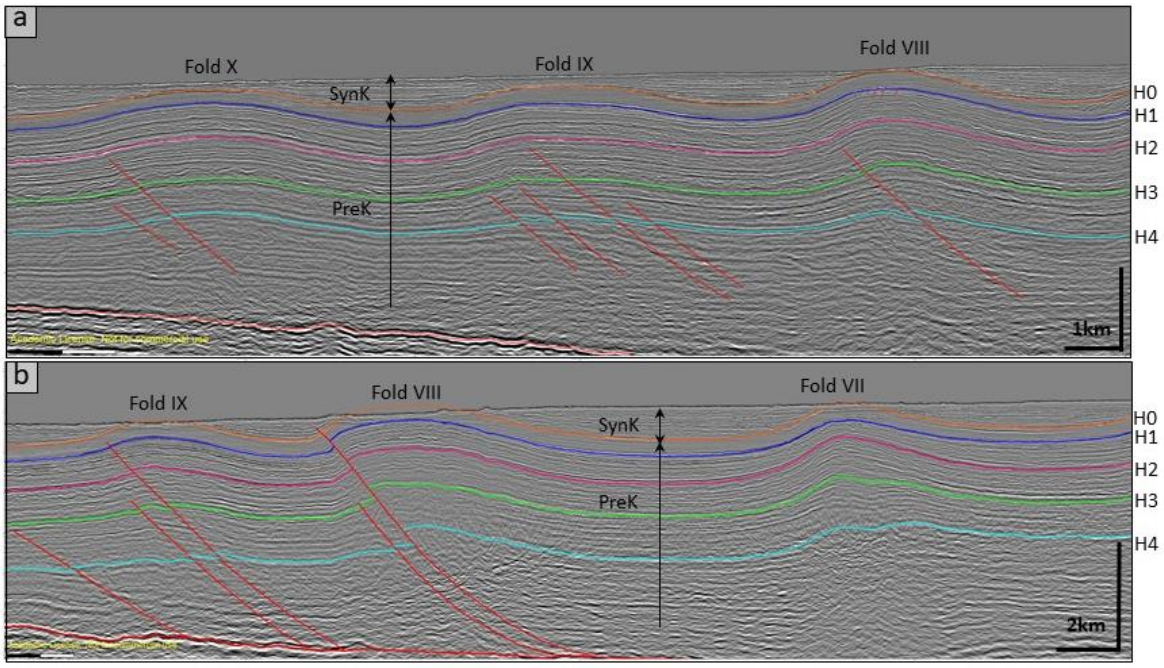

Figure 5.16 Examples of one stage of fault activity and associated fold growth, with present-day continuing activity. Fault activity is during deposition of Synk.

In *Figure 5.16a*, Folds X, IX and VIII appear to experience similar growth history to each other – a single and continuous growth phase to present day. Two kinematically-distinct stratigraphic units are associated with fold X and adjacent folds IX, VIII and VII: PreK, a pre-kinematic sequence below H0 with relatively constant thickness; and SynK, a syn-kinematic sequence from H0 to the seafloor with fan geometry thinning towards the fold crest. A similar sedimentary sequence is seen for Fold IX, VIII and VII (*Figure 5.16b*), indicating fold growth from H0 to the present day.

In *Figure 5.17*, we identified three successions associated with activity of an unnamed fold: PreK, a pre-kinematic sequence below horizon H2; SynK, a syn-kinematic sequence

between H2 and H1; and PosK, a post-kinematic sequence above H1. Rapid growth of this fold starts after H2 and ceases at H1. This fold is presently inactive, lacking seafloor expression. Fold VIII has a similar pattern of activity, with major growth from H1 to a time between H0 and the present day, but is not presently active.

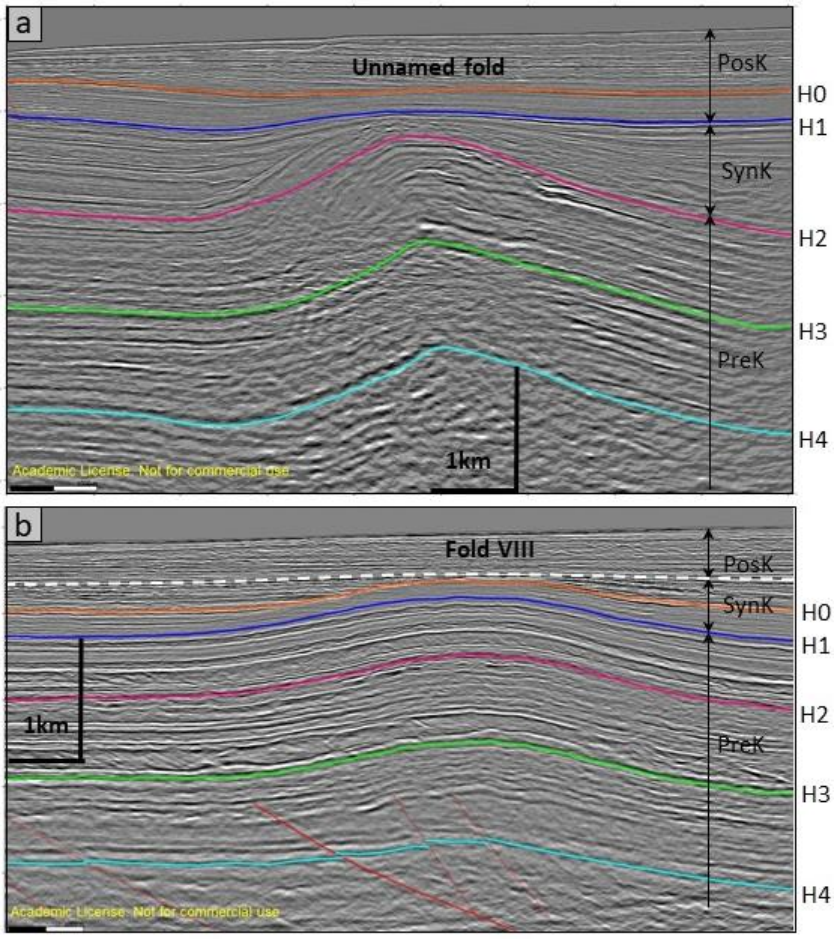

Figure 5.17 Examples of one stage of fault activity and associated fold growth for a presently inactive fault. Fault activity is during deposition of SynK.

5.4.5 Quantification of shortening

In this study we apply the two common methods used to quantify shortening; bed-length measurement and area balancing restoration. The comparison of bed-length shortening and area-balanced shortening allows us to estimate the missing strain. We also examined strain partitioning between different structures to evaluate whether faulting or folding dominates in accommodating shortening. Taking the bed as a whole, the conventional bed-length measurement method quantifies shortening by subtracting the length of the deformed bed from the restored original bed length (e.g., Chamberlin, 1910, Dahlstrom, 1969; Mitra and Namson, 1989). Instead, here we cut the bed into a number of 2-km-long

segments, then calculate the individual shortening of each segment and sum these for the cumulative shortening across the FTB. The plot of cumulative shortening against across-strike distance from foreland to hinterland (*Figure 5.18*) is expected to show each fault as a step whilst a fold appears as progressive change in the shortening curve. This revised method provides information both for the total bed-length shortening and the strain partitioning between faults and folds across a FTB, i.e. where major strain is taken up and hence which structures are responsible.

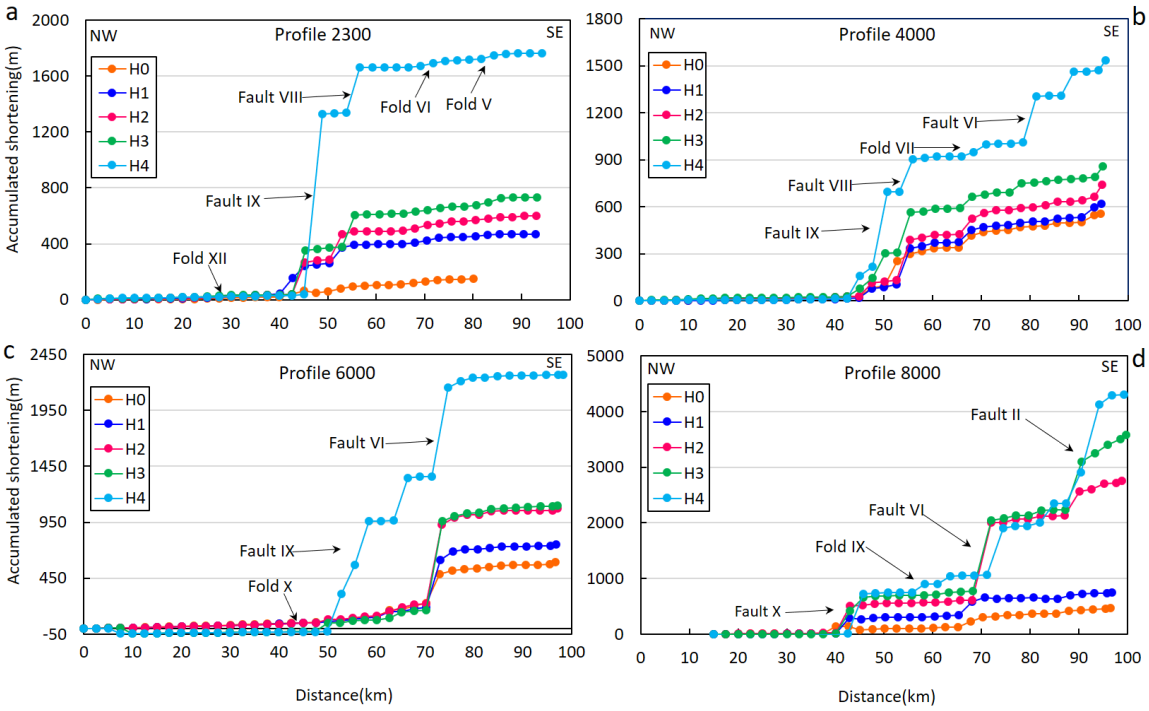

Figure 5.18 Plot of accumulative shortening derived from the five horizons (H0-H4) on four seismic profiles against along-strike distance.

5.4.6 Bed length balancing

Figure 5.18 shows cumulative shortening from the bed length measurement against distance from NW to SE for 4 of the seismic profiles. In profile 2300, shortening varies with depth (*Figure 5.18*): Horizon H4 at depth produces large shortening while H0 (close to the seafloor) yields small shortening, indicating propagation from depth, attaining greatest displacement at depth (*Figure 5.11* & *Figure 5.12*). Because of this process, shortening derived from a single bed is not representative of the overall shortening and several beds have to be utilized to more accurately quantify shortening. Another prominent feature is that the cumulative shortening rises rapidly at 45-49 and 54-57 km distance across-strike. This is particularly so for Horizon H4 and at the thrust fault

positions (IX and VIII). In contrast, the accumulated shortening increases gradually at 25-30, 69-74 and 82-87 km distance at the locations of the three folds (XII, VI and V; *Figure 5.18a*). Similar observations are also made with profile 4000, 6000 and 8000 (*Figure 5.18c-d*). The pattern of increased shortening is marked by pronounced steps at thrust structures but characterized by a gradual change across pure folds. For one measurement (3 km long segment), the maximum shortening accommodated by thrusting is as high as 928 m (Fault IX in profile 2300, *Figure 5.18a*) whereas the maximum shortening accommodated by folding is only 150 m (Fold IX in profile 8000, *Figure 5.18d*). Other fold-faults on this and other profiles show a similar pattern and ratio of shortening. We therefore conclude, in this fold-thrust belt, that thrusting dominates over folding in strain accommodation.

5.4.6.1 Area balancing

A revised area balancing solution was proposed by Yang et al. (in prep.; Chapter 4) to reduce the uncertainties of estimating shortening, such as the choice of the regional slope (Wiltschko and Groshong, 2012). The principles and detailed analysis of this improved method, also used here, are described fully in Yang et al. (in prep; Chapter 4). The revised area balancing method allows shortening of a cross-section to be better constrained by allowing the use of various regional slopes while the conventional methods only uses an arbitrary, often horizontal, regional slope to calculate shortening.

Three horizons (H1-H3) from three seismic profiles are used for area balancing using this revised method and compared with other shortening methods (*Table 5-3*). The values from the revised area balancing are larger than those derived from the bed-length measurement. This difference is attributed to several deformation mechanisms, such as layer-parallel shortening, lateral compaction, ductile deformation, pressure solution, sub-seismic deformation (Koyi et al., 2004; Butler and Paton, 2010; Şengör and Bozkurt, 2013; Lathrop and Burberry, 2017) which are not accounted for by bed-length measurement techniques.

5.4.6.2 Missing strain

As above, the difference between shortening derived from the bed-length and area mechanisms. Butler and Paton (2010) reported a significant mismatch between the minimum extension (44 km) and slip on thrusts (19-25 km) in a gravity-driven fold-thrust

system from Orange Basin, offshore Namibia, using the bed-length method amounting to

Table 5-3 Shortening using bed-length measurement and area balancing

Horizon	LS (km)	AS (km)	MS (km)
Seismic profile 2300			
H1	0.5	4.6	4.1
H2	0.6	5.3	4.7
H3	0.7	5.7	5.0
Seismic profile 4000			
H1	0.6	4.2	3.6
H2	0.7	5.0	4.3
H3	0.9	5.7	4.8
Seismic profile 6000			
H1	0.8	3.6	2.8
H2	1.1	4.4	3.3
H3	1.1	4.9	3.8

LS=line length balanced shortening, AS=area balanced shortening, MS=missing strain.

18-25% of total strain. We interpret that this difference could either be a real difference between extension and contraction in this system, or could be a function of the inaccuracies of the bed-length method or a greater potential for inaccuracy/underestimation for the contractional measurement. Butler and Paton (2010) suggested this was due to lateral compaction and volume loss and they named this mismatch “missing strain” that is not visible in a present-day snapshot of a structural system.

Unfortunately, the lack of constraints on the effect of lateral compaction and volume loss and layer parallel strain in this study prevents further quantification of their contribution to shortening. Therefore, the shortening difference we measure by comparing the bed-length measurement and area balancing results (*Table 5-3*) is taken as a whole, and named “missing strain” (e.g., Butler and Paton, 2010). This shows that up to 2.8-5 km is

missing across the entire NBFB from the conventional bed-length measurement and that a simple line-balanced restoration cannot account for the overall shortening. Our revised area balanced method produces a more realistic estimate, however it still involves uncertainties, such as location of the regional slope, décollement depth and interpretation of folds and faults (Wiltschko and Groshong, 2012; Wang et al., 2018).

The missing strain identified here raises the importance of the method used to quantify strain and of the need to understand the roles of penetrative deformation and lateral compaction in partially lithified strata. These effects could have significant implications for hydrocarbon systems such as reservoir volume estimation, subsurface prediction of structural geometries using theoretical models based on conserved bed-length (Shaw et al., 2005), and fluid expulsion pathways (Butler and Paton, 2010). Quantification of missing strain is also important for the general understanding of tectonic process, and strain distribution and localization in a contractional deformation system.

5.4.7 Taper angle and properties of the basal décollement

In the NBFB, the thrust fault planes predominantly sole out at a common décollement surface. This is likely to be preferentially located at a major rheological boundary in the sediment pile. Previous studies have suggested it may be related to overpressured clay or shale, such as the Setap Shale, overlying the SCSU (Ingram et al., 2004; Morley et al., 2007; Cullen, 2014). Evidence for the Setap Shale has been identified across other parts of the margin, including directly in boreholes, and through interpretation of shale diapirs and related structures in the fold-thrust system (e.g., Levell, 1987, this study; Hinz et al., 1989; Hutchison, 2004; Ingram et al., 2004; Franke et al., 2008; Hesse et al., 2009, 2010b; Hesse et al., 2010a; Cullen, 2014). Here we comment on the seismic properties of the décollement surface which the thrusts sole into and on other lines of evidence for the properties of the basal décollement.

The surface appears to be an interval just above the SCSU. In contrast to the SCSU, the décollement, if it sits just above the SCSU as interpreted here, does not have a distinct, high-amplitude, positive reflector. Instead, it is characterized by low amplitude. However it may still represent a mechanical contrast between overlying and underlying sequences, possibly related to overpressured clay or shale, such as the Setap Shale overlying the Oligocene–early Miocene ‘basement’ (e.g., Ingram et al., 2004), but this contrast may not

be sufficient to generate a high amplitude reflector.

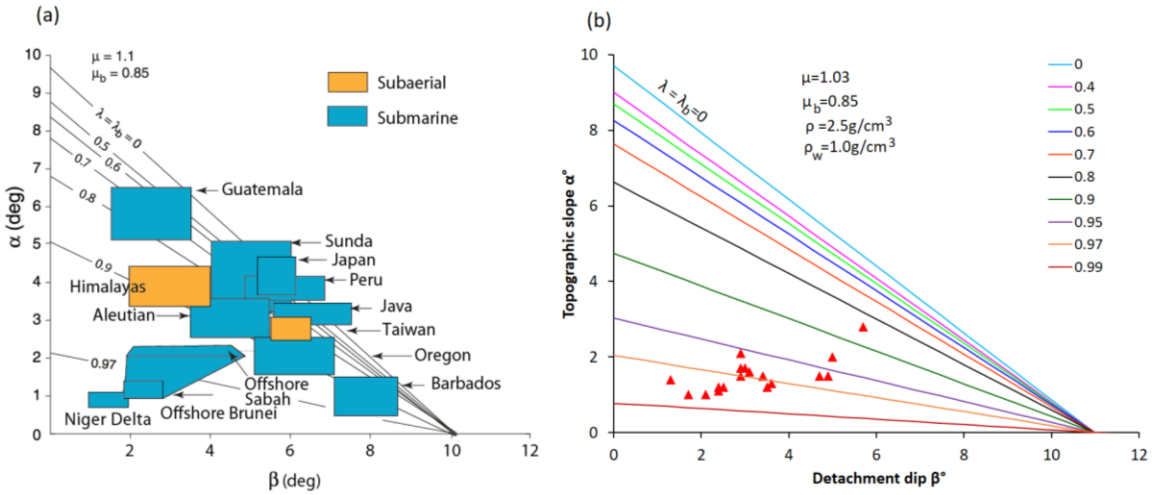

Figure 5.19 (a) Relationship between pore-fluid pressure ratio (λ), surface slope (α), and basal décollement dip (β) for fold-thrust belt at critical taper assuming known material properties, Coulomb material behaviour and constant fluid pressure across the wedge (from Dahlen, 1984). (b) Plot of measured taper angles from the NBFB (red triangles). Fluid pressure ratio across the wedge is interpreted as high at 0.9-0.99.

Critical taper theory explains the first-order geometry of a fold-thrust belt as a function of the internal strength of the wedge and the strength of the basal décollement (Davis et al., 1983; Dahlen et al., 1984). This theory was initially developed to study accretionary prisms at convergent plate boundaries, but has also been expanded to investigate the mechanics of gravity-driven deep-water fold thrust belts (Bilotti and Shaw, 2005; Mourgues et al., 2014). Critical taper theory predicts the fluid pressure ratio for the wedge interior and basal décollement (λ and λ_b) for fold-thrust belt examples from a broad range of settings (Davis et al., 1983) (*Figure 5.19a*). This earlier compilation is now somewhat outdated as the datasets used were more limited and of lower resolution and accuracy, and it tended to ignore the variability of taper angle within individual systems. Generally, the magnitude of the wedge taper is inversely correlated with the effective friction of the basal décollement linked to basal fluid pressure (*Figure 5.19a*).

Thanks to increased data collection and advances in reflection seismic imaging, we are now able to image the geometry of a fold-thrust belt in greater detail and assess variations in taper angle along strike. In this study, the taper angle is measured from 19 2D seismic profiles from the NBFB 3D volume. The results show that the taper angle is small and generally increasing from southwest to northeast (profile 2300 to 10500; *Table*

5-4). Within this overall trend, the taper angle predominantly lies below 6° (range = 2.7-8.5°), but with outliers of 7-9°. Given the overwhelmingly low taper angle, the fluid pressure ratio along the base of wedge is predicted as high as 0.9-0.99 (*Figure 5.19b*).

Table 5-4 Measured taper angles in the study area.

seismic profile	α(°)	β(°)	Taper (sum of α and β) (°)
2300	1.4	1.3	2.7
2500	1	1.7	2.7
3000	1	2.1	3.1
3500	1.2	2.5	3.7
4000	1.2	2.4	3.6
4500	1.1	2.4	3.5
5000	1.5	2.9	4.4
5500	1.7	2.9	4.6
6000	2.1	2.9	5
6500	1.6	3.1	4.7
7000	1.5	3.4	4.9
7500	1.7	3	4.7
8000	1.2	3.5	4.7
8500	1.3	3.6	4.9
9000	1.5	4.9	6.4
9500	1.5	4.7	6.2
10000	2	5	7
10500	2.8	5.7	8.5

These results (*Figure 5.19b*) are an end member scenario where the fluid pressure is unrealistically assumed constant across the profile i.e., $\lambda = \lambda_b$. It has been suggested that in some low taper angle deepwater fold-thrust systems, the pore pressure ratio is lower in the wedge interior and higher along the basal décollement (Davis et al., 1983; Bilotti and Shaw, 2005). Therefore here, a range of assumed internal pore pressure ratio are used, and a range of values for basal pore pressure ratio are then estimated (*Figure 5.20*). Four internal pore pressure ratio (λ=0.8-0.5) are taken to estimate the basal fluid pressure ratio λ_b using the critical taper theory (*Figure 5.20*). For each scenario, a range of λ_b values

are predicted to give a range of relationships between topographic slope and basal dip, i.e. the color lines shown in *Figure 5.20*. With the measured taper angles (red triangles) from our interpreted seismic data, we can approximate the appropriate range of basal pore pressure ratios. Again, the majority of likely basal pore pressure values that fit our measured taper angles sit within the range, 0.7-0.95, i.e., are high values, suggesting that elevated basal pore fluid pressure is indeed the dominant cause of the low-taper angle of the NBFB.

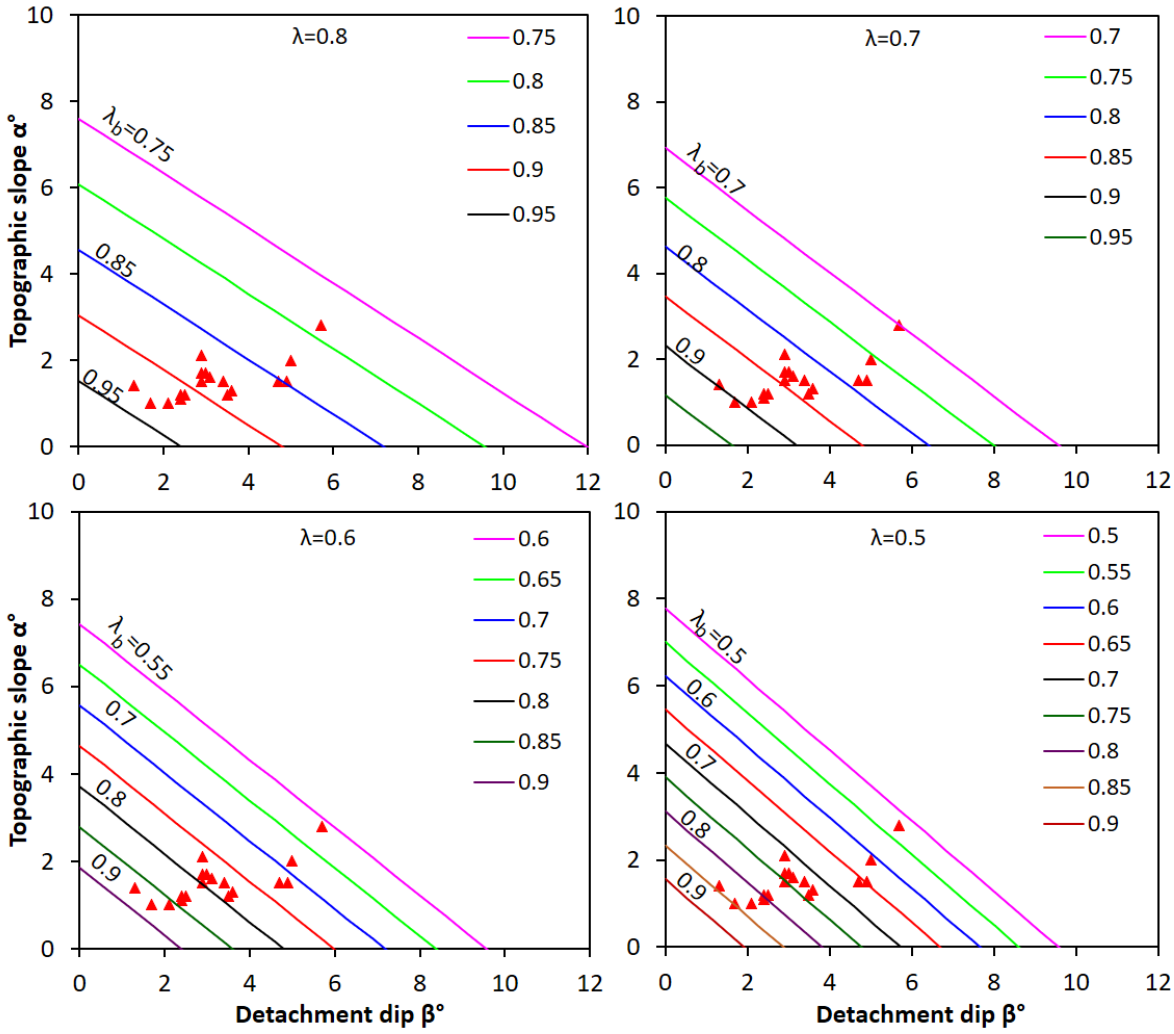

Figure 5.20 The relationship between pore-fluid pressure ratio (λ), surface slope (α), and basal décollement dip (β) for a fold-and thrust belt at critical taper, assuming varied fluid pressure ratio across the wedge. The red triangles denote the measured taper angles from the NBFB in this study. An assumed λ=0.8-0.5 for internal wedge material is used.

Reports of mobile shale diapirs in the deep water region of the NW Borneo margin (Morley et al., 2003; Van Rensbergen and Morley, 2003; King et al., 2009; Morley et al., 2014) and interpreted in this study (e.g, *Figure 5.3* & *Figure 5.5*) provide supporting

evidence for local overpressure. The potential role of overpressured shale and evidence for low taper angle will be discussed further below (Sections 5.5.1 & 5.5.3) with reference to the potential physical properties of the décollement.

5.5 Discussion

5.5.1 Controls on the geometry and structural style of the NBFB

We have shown significant variations in structure along and across strike of the NBFB in fold style, growth and activity history. How do these features compare with other parts of this margin and with other thrust systems worldwide? Can specific controls and processes explain the structural variations?

Structural variation of fold style

A previous study classified four types of fold in the Sabah portion of the NBFB (50-100 km NE of this study area) with respect to the fold inter-limb angle (Hesse et al., 2010b) , but this is mainly a geometry-based definition probably with limited structural significance. In our study, we identified three types of folds: fault-propagation folds (which dominate); detachment folds (less dominant); and fault-bend folds (rare) based on the style of folding. For each structure, there is an obvious spatial variation along strike in fold geometry and style. For instance, Fold X is a buried décollement fold in the SW (*Figure 5.4* & *Figure 5.7*), but becomes a fault-propagation fold towards the NE (*Figure 5.9*) with increasingly significant seafloor expression.

Structural variation of fold style along-strike in a fold-thrust system has been recognized in many other locations, including the Niger delta (Corredor et al., 2005; Higgins et al., 2007; Higgins et al., 2009), Sabah/NW Borneo (Totake et al., 2018), Zagros (Barber et al., 2016), Subandean Argentina (McGroder et al., 2015), Himalayan Orogen (Yin et al., 2006), and Oregon (Mackay et al., 1992; MacKay, 1995) and Costa Rica accretionary prisms (Shipley et al., 1992). Potential factors controlling this variation include rock/sediment heterogeneity, irregular basement topography, lateral variation in sediment input and storage, changes in along-strike stress regime, and pore fluid pressure/strength variation of the basal décollement or interior materials.

From this study, we suggest that a fold initiates as a low-relief detachment anticlinal fold,

marking the position of a future incipient thrust, as also observed in analogue models (Wu and McClay, 2011). With further contraction, the fold propagates laterally with reducing shortening. At this stage, an incipient fault breaks through the sedimentary layers where the fold initiated and accrues thrust displacement, with a change in fold style from detachment fold to fault-propagation fold. Fold growth is subsequently controlled largely by the underlying thrust fault (*Figure 5.18*) (e.g., Koyi, 1995). In the area where the propagating fold terminates, the fold remains as a detachment fold, but this structure may eventually become a fault-propagation fold with sufficient additional shortening. The same fold structure therefore expresses different structural style along-strike due to varying amount of shortening and maturity. There is only one example of fault bend fold (FBF) which we interpret to reflect the topography of underlying basement (see below).

The effects of basement morphology

In this study, we interpret that the décollement of the NBFB sits just above the SCSU and therefore is heavily influenced by the morphology of the SCSU. We also presume that the décollement forms parallel to the prominent reflector of the South China Sea Unconformity (SCSU), and its first-order geometry is planar and dipping landward, consistent with the basal geometry of critical taper wedge models (Davis et al., 1983; Dahlen, 1990). However, its local geometry is variable and in places has topography (forming a flat-ramp-flat). This variation in morphology clearly affects the resulting fold geometry and style, for example fault-bend fold IX inherits the shape of the underlying SCSU (*Figure 5.4*). The SCSU is a significant stratigraphic boundary (see Introduction) and marked by a high amplitude reflector, therefore a strength contrast is interpreted across the SCSU (e.g. Ingram et al., 2004). Hence we might expect the relatively weaker overlying materials to mimic the geometry/topography of the basement, i.e. the SCSU. In general though the SCSU is predominantly planar and therefore most folds of the NBFB do not show structural inheritance.

Rock heterogeneity and basal décollement properties

All stratigraphic units of the NBFB above the SCSU appear to be of similar seismic facies, and they are dominated by the shallow marine siliciclastic and hemipelagic sediments from borehole interpretations and projections (Levell, 1987; Schluter et al., 1996 and reference herein; Morley, 2007b). Within these units, shale diapirs and gas pipes are

interpreted from the chaotic seismic facies in the core and base of some folds (e.g., Sandal, 1996; Van Rensbergen and Morley, 2003; this study; Morley, 2007a; Paganoni et al., 2016; Paganoni et al., 2018). These particular folds are mostly symmetric detachment folds and not the basinward-vergent, asymmetric, fault-propagation folds (see labeled fold examples in *Figure 5.3a*). Clearly shale diapirism plays a role in affecting fold shape and style. Evidence for shale diapirism also supports that mud-rich fluids exceeding lithostatic pressure and hence overpressured pore-fluid pressure are present here (see also Morleyb, 2007). If at the appropriate stratigraphic level and/or appropriate fluid pathways are available, the overpressured shales could play a role in weakening the basal décollement and in turn be responsible for inducing the development of symmetric detachment folds (e.g., Davis and Engelder, 1985; Rowan et al., 2004). A weak basal décollement of low basal shear stress could explain the measured low taper angles. The seismic interpretation of the décollement surface supports this interpretation generally – the décollement appears to not coincide with positive polarity reflector of the SCSU boundary but probably sits just above. The lack of a prominent reflector at the décollement suggests that overpressure, if present, is insufficient to generate a reflector or there is a relatively thin discrete zone that cannot be resolved in the seismic data at this depth.

Sediment thickness

The NBFB itself is interpreted to be mainly composed of homogeneous, siliciclastic, mud-rich sediments/sedimentary rocks. The undeformed sediment wedge in front of the NBFB also represents future sediment availability and shows some variability in thickness. To investigate the role of sediment thickness (both pre-kinematic and syn-kinematic overlying the NBFB) we compared thickness with structural style and, below, with fault spacing. For example, the thickness of the pre-kinematic units of fold VIII reduce from southwest to northeast, i.e. profile 3000 to 8000, but the fold style remains the same, i.e. a fault-propagation fold (*Figure 5.3* & *Figure 5.9*). Therefore the pre-kinematic sequence thickness in this case has very limited effect on the structural style that develops. The syn-kinematic sequences with respect to most folds in the NBFB are consistently thin across the FTB, <1 km thickness beneath the seafloor (*Figure 5.3* & *Figure 5.9*). With a relatively homogeneous syn-kinematic sediment thickness, the role of its variation on fold-thrust belt width, number of imbricate thrusts or taper angle cannot be easily tested. However

the changes in structural style we observe across and along strike cannot be explained be any change in syn-kinematic sedimentation variability.

Controls on Fault spacing and Forward Propagation of the Fold-Thrust Belt

In a region of likely homogeneous stress field and basal décollement properties, a thicker sedimentary layer tends to develop wider fault spacing. The Brunei portion of the NBFB shows an overall decrease of fault spacing from southwest to northeast, whilst the stress field is unvarying (normal to the NE-SW trending fold-thrust belt (King, 2010)), and importantly sediment thickness is increasing to the northeast (*Figure 5.13*) (Hesse et al., 2010b). This result contradicts expected correlations (between fault spacing and sediment thickness), and another factor must control fault spacing here.

In the northeast where fault spacing is reduced, there is increased topography on carbonate platforms of Oligocene – Early Miocene age with the overlying sedimentary sequence onlapping (Cullen, 2014) but minimal topography elsewhere (*Figure 5.8* & *Figure 5.9*) (Hinz and Schluter, 1985; Hinz et al., 1989; Schluter, 1996, Franke et al., 2008; Steuer et al., 2013). This topography appears to act as an obstacle to the forward propagation of the fold-thrust belt, leading to the squeezing of fold-thrust belt and hence reduction in fault spacing in the northeast. Similar effects are seen in other fold-thrust belts, e.g, basement ridge collision/subduction locally reducing fault spacing in the Makran accretionary prism (Smith et al., 2012).

The maturity of a thrust system may also affect the relative fault spacing. When a new thrust fault initiates, its distance from the adjacent fault landward is relatively wider with respect to other thrusts, e.g., in the frontal tectonic wedge of the NW Himalaya (Bose et al., 2009), and in scaled physical analogue models (e.g., Wu and McClay, 2011, Yamada et al., 2006). In the southwest area of the NBFB (this study), this tends to widen the fault-thrust belt and increase the average fault spacing, i.e., the outermost frontal Fold XII is 15-20 km from the adjacent (2^{nd}) fold, whereas the spacing between the 2^{nd} and 3^{rd} fold is 5-10 km on seismic profiles 2300, 3000 and 4000 (*Figure 5.3* & *Figure 5.5*). However, this contrast in spacing is not observed in the northeast area of the NBFB (seismic profiles 6000, 7000 and 8000; *Figure 5.7* & *Figure 5.9*). We believe this may be a result of increasing influence of basement topography (carbonate platforms) and/or potentially

greater maturity of these structures (suggested by smaller interlimb angle, steeper fault dips; see also Hess et al., 2010a).

Growth/development

Quantification of fault displacement shows the growth of individual thrust faults in this fold-thrust belt. We observe that the faults initiate at depth and then propagate upwards with decreasing displacement up-dip with a constant displacement gradient (*Figure 5.11*).

Considering along-strike displacement variation as a proxy for fault initiation location and propagation patterns, our analysis (*Figure 5.12*) shows that the position of fault initiation and direction of fault propagation is not consistent for each structure, despite an apparent trend of southwestward propagation suggested by increased seafloor expression and fold-related slope in the northeast (*Figure 5.2*). We infer that this spatial variation of fold initation and propagation reflects the complexity of structural development of the fold-thrust system, i.e., the growth pattern of an individual new fold/fault may develop independently relative to the overall structural development/propagation direction. We also observe multiple displacement highs along strike for an individual structure, which we interpret to represent separate initiation locations of fault segments that subsequently linked. Similar observations are also made in the Ostler fault zone, New Zealand (Davis et al., 2005), the Niger Delta deep water FTB (Higgins et al., 2007; Higgins et al., 2009), the Sabah part of the NW Borneo FTB (Totake et al., 2018) and in scaled analogue models (Cowie et al., 2006; Schreurs et al., 2006).

In summary, we conclude that the variation of fold style along strike is primarily a result of the degree of fold deformation/shortening, topography/ geometry of basement, and the frictional strength of the basal décollement. The stress field, nature of the décollement and thickness of the input sedimentary pile may jointly govern the initial fault spacing in a fold-thrust belt, but subsequent fault development, structural shortening, and presence of geological obstructions/basement topography play a larger role in determining the evolving and ultimate fault spacing.

5.5.2 Kinematics of the fold-thrust belt: Driving mechanisms

On the NW Borneo continental margin, two competing mechanisms have been proposed for the generation of the fold-thrust belt: (Mechanism 1) basement involved crustal

shortening driven by collisional plate tectonics (Hinz, et al., 1989); and (Mechanism 2) gravity-related tectonics driven by delta deposition (Tan and Lamy, 1990; Hazebroek and Tan, 1993). The following summarizes evidence and arguments for these mechanisms from previous studies and new results from this study.

Evidence from previous studies supporting Mechanism 1:

I. A relative motion based on GPS data between NW Borneo and the fixed Sunda Plate of the order of 4-6 mm/yr, attributed to convergence across the NW Borneo Trough (Socquet et al., 2006a; Socquet et al., 2006b; Simons et al., 2007; Sapin et al., 2011; Sapin et al., 2013). However, we note this is a very low rate of convergence.
II. A net component of regional compression based on comparison of shortening across the toe fold-thrust system versus extension across the continental shelf, using structural restoration (Hesse et al., 2009; King et al., 2010a).
III. The development of the NBFB contemporaneously with collisional events southeast of Borneo, especially those in Sulawesi and the main Australia-Sundaland collision in the Timor Sea area (e.g.,Hall, 1996; Morley, 2007b).
IV. The presence of Late Miocene-Pliocene inverted structures on the inner shelf and onshore Brunei (Morley et al., 2003; Tingay et al., 2003; Tingay et al., 2005).
V. An existing compressive stress-field evidenced by borehole analysis in the coastal area, i.e. the inverted province with timing coincident with the NBFB activity (King et al., 2009, 2010b).

Evidence from previous studies supporting Mechanism 2:

I. GPS data, in a fixed NW Borneo reference frame, showing that the NW Borneo coastal area moves towards the NW independently from the rest of Borneo Island, moving SW to W (Sapin et al., 2013). This supports separate movement of the coastal region and potentially the area immediately offshore, and is compatible with extension and gravitational movement downslope.
II. Evidence for cessation of subduction of the proto-South China Sea oceanic crust beneath NW Borneo in the Early Miocene with Neogene deformation along the NW Borneo trough postdating this collision (Sapin et al., 2013; Hall, 2013). This includes the absence of seismicity below or landward of the trough and volcanism such as might be associated with an actively subducting slab (Hall, 2013).

III. Significant extensional normal faulting in the shelf area that is connected to the toe thrusting downslope and associated with an underlying basal décollement (Hess et al., 2009; Morley et al., 2008).

New evidence from this study:

I. We propose that the two distinct phases of fault activity and fold growth we observe (e.g., *Figure 5.15*) may support the gravitational driving origin of this system, because these can indicate changing rates of sediment input and loading through time rather than likely more continuous deformation as might be expected from convergence. However, we also that these two phases of fault activity are only observed in the northeast of the NBFB for folds II-VI (*Figure 2b*), covering a small area of 25 km (along strike) x 30 km (across strike). Therefore this multiphase activity could be a local phenomenon, and may not be driven by wider sediment input changes.

II. The present-day fault activity and fold growth is extensively distributed across the entire NBFB (e.g., *Figure 5.5*, *Figure 5.6* , *Figure 5.9* & *Figure 5.16*; see also, Morley, 2007b), rather than localized at the toe. The majority of strain being focused at the toe tends to be more common for plate convergence-driven systems and has been observed in scaled physical experiments (e.g., Davis et al., 1983; von Huene and Scholl, 1991; Koyi, 1995; Gutscher et al., 1996; Koyi et al., 2000; Wu and McClay, 2011), numerical models (e.g., Willett et al., 1993; Fuller et al., 2006), and natural examples (e.g., Park et al., 2002; Kopp and Kukowski, 2003; Adam et al., 2004). However it is important to point out that fault activity more widely distributed across a prism is observed within several active accretionary systems (e.g., Smith et al., 2012; Cook et al., 2014).

Putting together all of these lines of evidence, we conclude that the NBFB resulted from a combination of gravitational tectonics (Mechanism 2) and crustal shortening driven by plate convergence (Mechanism 1), but predominantly driven by gravitational tectonics.

5.5.3 The mechanics of the NW Borneo Fold-Thrust Belt

Based on the critical taper theory (Davis et al., 1983), the very low taper angles of the majority of the NFTB (< 6°) predict the fluid pressure ratio λ_b at the base of wedge to be > 0.7 (*Figure 5.19* & *Figure 5.20*), inferring overpressure. This prediction is supported by

evidence for high pore-fluid pressures on the shelf (from well data, e.g., Sandal, 1996; Van Rensbergen and Morley, 2003; Tingay et al., 2005; Morley et al., 2008), and in the deep-water area where many shale diapirs, mud pipes, and gas chimneys affect the cores of anticlines (Van Rensbergen et al., 1999; McGilvery and Cook, 2003; Ingram et al., 2004; Morley, 2008; Morley et al., 2014). Ingram et al. (2004) also suggested that the décollement in the Sabah portion of the NBFB is located at a major rheological boundary in the sediment pile, possibly related to overpressure, and the décollement may, mark the contact between the Setap Shale and the Oligocene–early Miocene 'basement' (Hess et al., 2010a; Cullen, 2004). High basal fluid pressures are also proposed for other gravitational fold-thrust belts, including the Niger Delta (Bilotti and Shaw, 2005).

In terms of structural response, a weak basal décollement is proposed to induce symmetric detachment folds, promotes the forward propagation of deformation, widens the fold belt and reduces the taper angle (e.g., Davis, et al., 1983; Davis and Engelder, 1985; Rowan et al., 2004). These correlations agree with our observations in the NBFB where a broad zone of synchronously active folds and thrusts are developed (*Figure 5.8*) to elevate the back of the system to attain a critical taper, causing deformation across the whole section (*Figure 5.3* & *Figure 5.9*), further supporting that the basal décollement is weak. Morley (2007b) suggests that the critical taper is attained at low values in the Brunei NBFB probably because it is a region of high sedimentation rates, with the sediments being derived directly from the shelf area. Consequently, disequilibrium compaction produced zones of highly overpressured marine shales as thick as several kilometers, later augmented by in situ hydrocarbon generation (Morley, 1992; Morley, 2007b; Morley et al., 2008), and by fluids, including hydrocarbons, driven laterally from the shelf offshore following an oceanward lateral decrease in lithostatic pressure gradient (Van Rensbergen and Morley, 2003; Tingay et al., 2005; Morley et al., 2008). These factors are likely collectively responsible for development of overpressure which in turn probably controls décollement properties, prism taper, and shale diapirism within the fold-thrust belt.

We conclude that the Brunei sector of the NBFB is comparable to other thrust systems with high sedimentation rates and low taper angle, such as the Niger Delta which is also driven by gravity (Bilotti and Shaw, 2005; Smith et al., 2012).

5.6 Conclusions

This study investigates the origin, geometry, structure and tectonic evolution of the NW Borneo Slope Fold-Thrust Belt based on examination of modern seismic data to undertake structural analysis, structural restoration, strain measurement and mechanical analysis. Key results are:

- Three types of fold are recognized: fault-propagation folds which dominate, detachment folds, and fault-bend folds (one example only). For each fold, its structural style varies significantly along strike, controlled by the magnitude of deformation/shortening the fold has attained, by topography and by strength of the basal décollement. Detachment folds tend to develop early and evolve into fault-propagation folds once thrust faults initiate.
- Along strike, the overall structural propagation direction is southwestward however the position of individual fault initiation is not consistent and the direction of fault propagation not consistently to the southwest. The identification of multiple displacement highs on individual structures suggests that multiple fault segments initiated and eventually linked to form longer structures.
- Using an improved area balancing restoration method, a significant amount of missing strain is estimated from bed-length measurement (accounting for 83% of the total shortening across the FTB). This highlights the inadequacy of the simple bed-length measurement for shortening.
- In the NBFB, faulting plays a dominant role over folding in strain accommodation.
- The low taper angle of the NBFB (≤ 6°) suggests a high basal fluid pressure (λ_b>0.7). The predicted overpressure is interpreted to result from a combination of high sedimentation input (i.e. rapid burial), disequilibrium loading, and potential gas generation and hydrocarbon maturation at depth.
- Different phases of fault activity are identified in some parts of the NBFB that may be a consequence of changing rates of sediment input and loading through time, and fault activity is distributed across much of the fold thrust belt rather than being focused exclusively at the toe.
- We interpret that the NBFB results from a combination of gravitational tectonics driven by deltaic sedimentation (primary) and crustal shortening driven by collision of

plate tectonics (secondary). The results of this study and previous observations suggest that gravity may dominate the fold thrust belt process in the present day.

Chapter 6 Comparison of Fold-Thrust Belts Driven by Plate Convergence and Gravitational Failure

Abstract

Submarine Fold-thrust belts (FTBs) are formed by the deformation of sedimentary sequences as a result of subduction of oceanic plates at active margins, gravitational failure at many passive margins, or a combination of these two at both types of margin. A key question is: Is the FTB driven by gravitational failure basically the same as the FTBs driven by plate convergence or are there fundamental differences? Deepwater FTBs in the toes of gravity-driven linked systems display many elements of structural style that are similar or even identical to those in FTBs driven by plate convergence. However, some structural style elements and elements of fold-thrust belt development history differ between the two systems.

To address this, we used examples from various tectonic settings (end members and hybrid systems) to conduct detailed structural analysis in terms of geometry, structure, strain distribution, shortening rate, deformation history, and tectonic process. The new results suggest: (1) The energy source in gravity-driven systems is the gravitational potential energy within the sediment material itself that is being deformed to create the slope extension and downdip contraction, whereas it is the movement of stressed lithospheric-scale tectonic plates, which lies outside the local sediment pile and within the broader crust and lithosphere that is not deformed by the thrusting and folding; (2) the energy in gravity-driven systems is resupplied by sediment input from large river deltas and deformation tends to be episodic linked to major episodes of sediment input. Whereas in a system driven by plate motions, the energy is resupplied by movement of a boundary upon which force is acting, and tends to be continuous, and less episodic; (3) the thrust faults of both systems are predominantly basinward-verging thrust faults. Backthrusts and back rotation appear to only be observed in the purely or predominantly plate-convergence driven systems; 4) the rate of shortening across plate convergence-driven systems is high (e.g., 1.9-6.1 cm/yr in Hikurangi, 3.7-4.6 cm/yr in the Makran), and generally continuous on a long time scale. Whereas across the contractional domain of gravity-driven systems, shortening is slow (e.g., 1.4-2.0 mm/yr in the Niger delta, 2.3-3.6

mm/yr in Orange basin and 0.8 mm/yr in the Para-Maranhao basin) and more variable through time; (5) For both driving mechanisms, the fold-thrust belt propagates forward with new thrust initiation at the toe, but fault activity differs slightly. Focused activity at the toe of the FTB driven by plate convergence is more common but not observed in gravity-driven systems. Activity across much of the FTB is observed for both systems, but activity focused in the rear to middle of the FTB is only observed in gravity-driven systems; (6) plate-driven system is primarily limited by rate of plate motion i.e., the rate at which the plate is fed into the FTB, whereas in a system driven by gravity, the movement is limited (resisted) by the strength of the sediments and detachment.

6.1 Introduction

Three main tectonic settings can host Fold-Thrust Belts (FTBs): (1) subduction zones associated with oceanic-continental or oceanic-oceanic plate convergence at active margins, in the form of submarine accretionary wedges (*Figure 6.1a*) (e.g., Davis et al., 1983; Moore and Silver, 1987; von Huene and Scholl, 1991), (2) the subaerial foreland of orogeny associated with continental-continental plate collision or intracontinental shortening (e.g. Rodgers, 1949; Coward, 1983; Buiter, 2012) and (3) the contractional toes of gravity-driven linked systems of extension and contraction, most commonly developed on passive continental margins where the sediment sequence lies above a weak décollement (salt, overpressured mud or shale) (e.g., Rowan et al., 2004; Hamilton and De Vera, 2009; Butler and Paton, 2010; Butler and Turner, 2010; Morley et al., 2011; Wu et al., 2015; Scarselli et al., 2016) (*Figure 6.1b*). Note that FTBs may have components of both plate convergence and gravitational deformation, creating hybrid systems, such as the Makran accretionary prism (Grando and McClay, 2007), and the NW Borneo FTB (Levell et al., 1987; Hinz et al., 1989; Ingram et al., 2004; Hess et al., 2009; King et al., 2010a).

Understanding of the geometry and processes of FTBs began with the study of onshore fold belts that were driven by continent-continent collision, such as the Scottish Moine Thrust Belt (Peach et al., 1907), the Canadian Rockies and the Alps (e.g. Bally et al., 1966, Dahlstrom, 1969, 1970; Price and Mountjoy, 1970). This setting dominated our paradigm of FTBs to such an extent that the classic paper of Boyer and Elliott (1982) entitled "Thrust Systems" makes no mention of any other context.

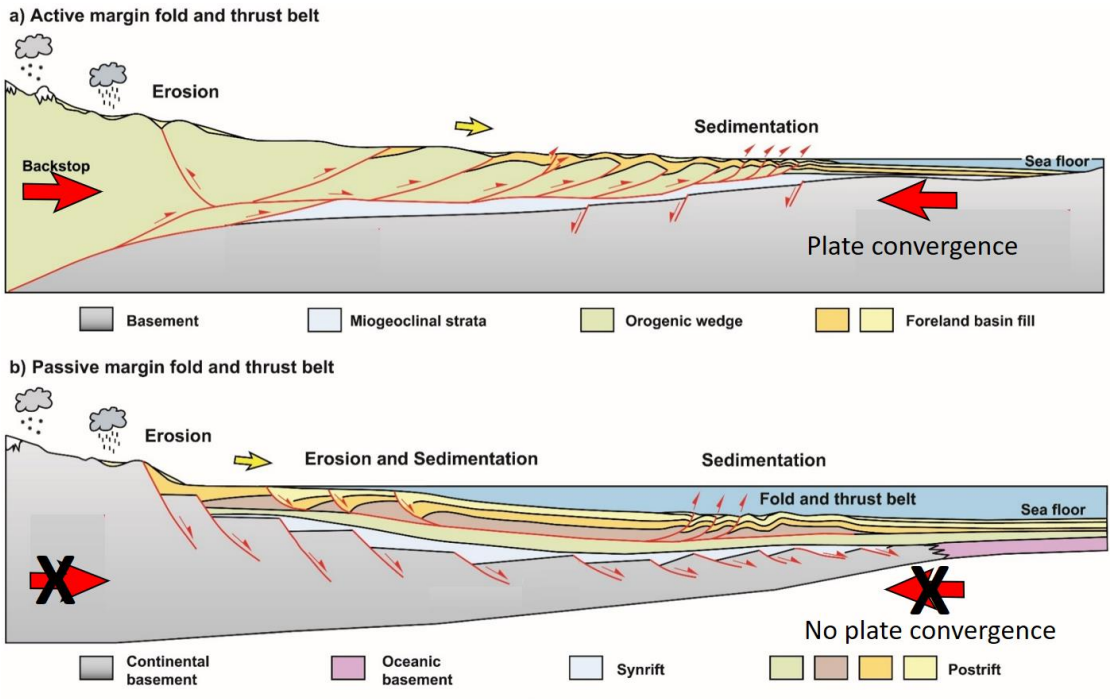

Figure 6.1 Conceptual cartoon showing fold-thrust belts driven by (a) plate convergence and (b) gravitational failure.

From the 1970s onwards, largely through the use of marine 2D reflection data, information on accretionary wedges in zones of oceanic subduction emerged, revealing that these consist of thrust systems with close relation to onshore FTBs (e.g. Moore and Curray, 1980; von Huene et al., 1979; Westbrook, 1975; Davis *et al.,* 1983). Continuing study of accretionary wedge systems, motivated in part by the need to assess geohazard potential including earthquakes, tsunamis and landslides through understanding of properties of the underlying plate boundary (e.g., Westbrook et al., 1982; White, 1982; White and Louden, 1982; Moore and Silver, 1987; Westbrook et al., 1988; Moore et al., 1990; Morgan and Karig, 1995), has confirmed that accretionary systems form a continuum with FTBs in continental collision settings.

Information on a different class of FTB began to emerge in the 1990s, spurred by the move of petroleum exploration into progressively deeper water on passive continental margins. These deep water passive margin toe-thrust belts in the toes of gravity-driven linked systems were initially identified on 2D reflection seismic data, and later supported by 3D seismic data and exploration drilling. The first published examples came from the US Gulf of Mexico (e.g., Wu et al., 1990, Weimer and Buffler, 1992, Trudgill et al., 1995, 1999; Diegel et al., 1995, Peel et al., 1995, Rowan et al., 2000). Examples from other

basins have subsequently been published, e.g. Niger Delta, Orange Basin and offshore Brazil (Rowan et al., 2004; Corredor and Shaw, 2005; Bilotti and Shaw, 2005; Granado et al., 2009; Morley et al., 2011; Scarselli et al., 2016; Cruciani et al., 2016,2017). As data emerges across the world, it appears that gravity-driven FTB systems may develop in every passive margin where a major source of clastic sediments feeds onto a margin that includes a potential décollement.

A key question is: Is this new class of FTB basically the same as the FTBs driven by plate convergence or are there fundamental differences? Deepwater FTBs in the toes of gravity-driven linked systems on passive margins display many elements of structural style that are similar, or even identical, to those seen in FTBs driven by plate convergence. However, some structural style elements or elements of fold-thrust belt development history may differ between FTBs driven by plate convergence and gravity.

This chapter compares examples of FTBs from gravity-driven systems and from systems driven by plate convergence to document similarities and differences in structural style and tectonic evolution. It examines whether the difference in tectonic setting, and the different boundary conditions, may give rise to differences in structure, behaviour and evolution.

Morley et al. (2011) argued that that dividing FTB systems into gravity-driven and plate-convergence-driven cases does not encompass all types of offshore FTB, and proposed a more complex classification based on the driving mechanism, tectonic setting, and detachment type. However, this classification appears to be too specific with many sub-types, affecting the structural comparison between them. Here we choose to use the conventional classification, simplified as gravity-driven, plate convergence-driven, or a hybrid system.

Despite significant similarities between gravity-driven and plate convergence-driven FTBs, such as wedge shape, fold and thrust structure/geometry, presence of large-scale horizontal shortening (e.g., Rowan et al., 2004, Morley et al., 2011), there are significant differences in mechanism and deformation.

In a plate convergence-driven system:

1. The convergence zone lies within a system whose boundary surfaces are moving, and upon those bounding surfaces, forces are acting, in the form of plate-scale stress

fields. Therefore energy is continually fed into the system and plate motion is the primary energy source for deformation in the subduction/collisional zone.

2. Naturally, body forces (in the form of gravity) act upon the region of deformation within the convergence zone. These play a significant part in controlling the local tectonic processes within that zone, but they do not provide the energy that powers them.
3. The rate of plate convergence is governed by global plate motions. Therefore the long-term rate of shortening within the convergence zone is independent of the geometry and strength of the deforming wedge, or of the strength of the décollement. The system will not stop if these conditions become unfavourable to easy deformation.
4. Within the plate convergence system, the entire subduction zone can experience deformation because the convergence applies to the whole lithosphere. However the frontal fold-thrust belt/accretionary wedge is typically thin-skinned.

In a gravity-driven system:

1. The FTB lies within a system whose boundary surfaces are not moving relative to one another. Therefore no energy is fed into the system across the bounding surfaces.
2. Body forces (in the form of gravity) act upon the region of deformation. In addition to playing a significant part in controlling the local tectonic processes within that zone, these forces provide the energy that powers them (Peel, 2014).
3. The rate of tectonic contraction is governed by the dynamics of the local gravity-driven linked system. Therefore the rate of shortening is dependent on the geometry and strength of the deforming system, and on the strength of the décollement. The system may stop, or indeed may never start, if these conditions are unfavourable.
4. The gravity-driven linked system soles out on a basal décollement, a layer that is relatively weak normally as a result of lithology and/or fluid pressure. Basement rocks are typically stronger than continental margin sediments, and as a result basement is unlikely to form part of the linked system and deformation is isolated to regions above basement. Gravity-driven linked systems are therefore thin-skinned.

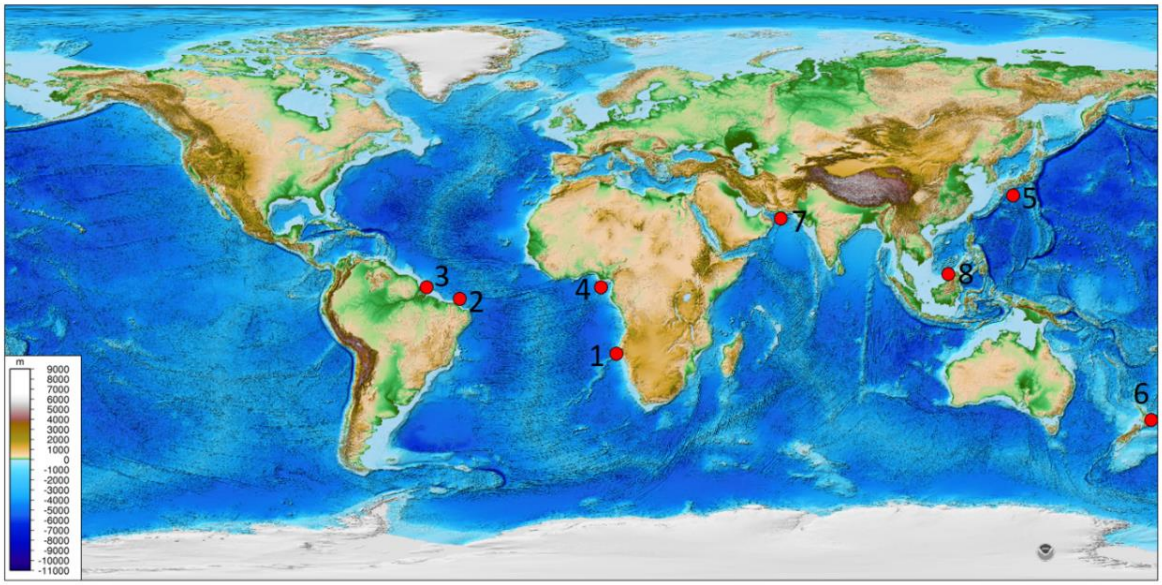

Figure 6.2 Global digital elevation map (DEM), showing locations of submarine fold-thrust belts presented in this study. 1= Orange Basin, offshore Namibia, 2= Para-Maranhao Basin, offshore Brazil, 3= Amazon Fan, 4= Niger Delta, 5= Nankai Accretionary Prism, offshore Japan, 6= Hikurangi Accretionary Prism, New Zeland, 7= Makran Accretionary Prism, Iranian margin, 8= NW Borneo.

In a hybrid system:

1. The shortening at the toe of the system is driven by both plate convergence and by updip extension that may act contemporaneously or separately. The relative role of each is likely to vary between hybrid systems and through time.
2. Energy is fed into the system by body forces and by movement of the boundaries.

To investigate the impacts of the differences in driving mechanisms, submarine Fold Thrust belts, which are better imaged by seismic reflection data than their subaerial counterparts (Butler and Paton, 2010) are used here to carry out the in-depth examinations of multiple (8) examples of FTBs from a range of end member and hybrid systems(Figure 6.2). This paper is the first detailed study of the differences and similarities in terms of driving mechanisms, geometries, structural styles and tectonic history. Specifically, we (1) describe the geometry of the structures, (2) examine the interaction of the structures involved in the system, i.e. folds, faults and basal detachment, (3) investigate the timing of deformation within and between the contractional and extensional parts of the systems, (4) quantify the strain distribution and

partitioning in the system, and (5) explore the tectonic and mechanical control on the FTBs.

6.2 Workflow

Key methods used in this study are seismic interpretation, tectono-stratigraphic mapping, structural analysis, strain measurement and deformation quantification. These were applied to a series of fold-thrust belts from one end member of driving mechanism to the other and selected for the quality of their seismic datasets, imaging of seismic stratigraphy and deformation, and prior interpretative studies. To apply the methods, we developed a simple workflow: (1) map the stratigraphic units in a cross-section of FTBs based primarily on previous interpretations; (2) identify the deformation-related sedimentary successions, i.e. basement, pre-kinematic, syn-kinematic and post-kinematic, based on the relationship between structural development (thrusting, folding and uplifting) and deposition timing (growth strata); (3) group the different types of fault, i.e. normal fault, detachment fault, basinward/seaward-vergent thrust fault and/or landward-vergent thrust fault; (4) analyse the timing of folding and faulting of individual structures in a system; (6) quantify the amount of contraction, extension or both, as relevant, as a proxy for strain distribution and partitioning in examples with well-imaged stratigraphy and displacements; and (5) evaluate the deformation initiation and propagation location, timing and patterns. We aim to map these different tectono-stratigraphic elements consistently between datasets. The same colour scheme is used in figures to highlight comparable structural features and stratigraphic sequences, which allows direct comparison between datasets.

6.3 Examples of submarine fold-thrust belts

6.3.1 Gravity-driven fold-thrust belts

6.3.1.1 Orange Basin, offshore Namibia

The Orange Basin is located on the volcanic-rifted South Atlantic passive margin, offshore southern Namibia and South Africa (Granado et al., 2009). A large delta system (Orange River) transports a significant volume of material into the basin, generating a classic gravity-driven fold-thrust belt with extension in the upslope region and contraction in the

downslope region with the two connected by an underlying seaward-dipping basal detachment (*Figure 6.3*). To highlight the characteristics of sedimentation and deformation, we remapped the tecton-stratigraphic successions and structural features based on previous interpretations, using a consistent colour scheme (e.g., Granado et al., 2009; Butler and Paton, 2010; Morley et al., 2011; Scarselli et al., 2016).

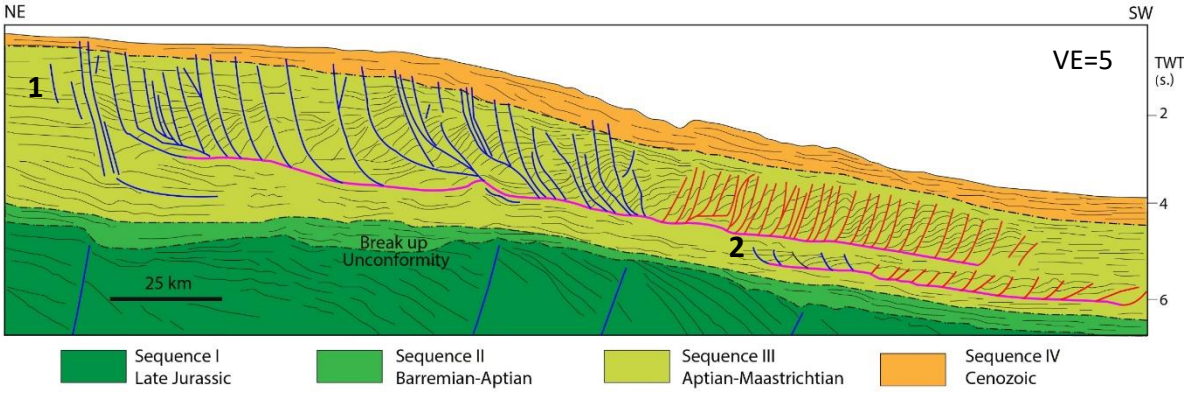

Figure 6.3 Interpretation of a seismic reflection profile across the gravity-driven Orange Basin system, offshore Namibia, from the outer shelf to slope, after Granado et al. (2009), Morley et al. (2011) and Scarselli et al. (2016). The vertical exaggeration is 5. Interpreted units are stratigraphic sequences.

Four distinct stratigraphic units separated by three regional unconformities are interpreted with inferred age of Late Jurassic to Cenozoic (*Figure 6.3*). Sequence I is deformed by landward-dipping extensional growth faults, seaward-dipping reflectors (SDRs) and associated grabens and half grabens, reflecting the crustal extension/syn-rift phase (Granado et al., 2009; Scarselli et al., 2016). The transition to seafloor spreading in the Orange Basin has been associated with the Barremian "break up" unconformity that truncates both the SDRs and the infill of the marginal rift basins, and separates Sequence I from the overlying Barremian-Aptian, sub-parallel strata of Sequence II (Scarselli et al., 2016). Sequence II is a transgressive succession of terrestrial sandstones intercalated with basaltic lava and overlain by marine sediments (Gerrard and Smith, 1982; Wickens and McLachlan, 1990; Light et al., 1993; Séranne and Anka, 2005; Mello et al., 2011; Scarselli et al., 2016). The late Lower Cretaceous sequence III and Cenozoic sequence IV are composed of marine post-rift deposits. Sequence III shows more complicated tectono-stratigraphic evolution with flat-lying strata overlain by prograding clinoforms in association with widespread regional growth listric faulting (up-slope) and thrusting and

folding (downslope). Overlying Sequence IV is characterised by prograding clinoforms and slope failures.

We differentiate fault types in the interpretation: normal faults are blue, basinward/seaward-verging thrust faults are red, landward-verging thrust faults are black, detachment fault(s) are pink. For poorly resolved fault geometries, a dashed line is used.

In sequence III, the area affected by gravitational deformation can be sub-divided into two systems, a landward/upslope major system (1), and a seaward/downslope minor system (2) (*Figure 6.3*). The minor system (2) forms in the frontal deep sequence below the compressional system associated with (1). It has a length of 88 km, and deforms a very thin pile of material (0.3s two-way time (TWT)) and is therefore unlikely to have a significant effect on the entire deformational system. For the major gravity-driven system (1), the extensional domain is linked downslope to a contractional domain via a structurally complex and poorly imaged transition zone of ~4 km width (*Figure 6.3*, *Table 6-1*). The extensional domain is ~133 km wide and the contractional zone is narrower, ~84 km wide (*Figure 6.3*, *Table 6-1*). The extensional domain includes predominantly SW-dipping listric normal faults with fault spacing of 3-10 km. The contractional domain includes SW-directed imbricate thrust sheets with more narrowly spaced thrust faults (~3 km). All thrust sheets terminate in asymmetric SW/seaward-verging fault related folds, interpreted in 2D as fault-propagation folds. The shortening rate across this contractional domain is estimated as 2.3-3.6 mm/yr (Cruciani et al., 2017). Most faults within the extensional and contractional domains are detached onto a common, detachment that dips gently seaward (1-2°) and is interpreted to be controlled by overpressured shale (Scarselli et al., 2016). Due to unresolved stratigraphic detail within Sequence III, we are not able to quantify the deformation characteristics of the normal growth faulting and thrust sequences and hence across the whole system. But clearly some normal faults propagate upwards into Sequence IV, while the thrust faults are limited to Sequence III. Both fault systems are buried without surface expression and are likely not presently active. The majority of deformation takes place during deposition of Sequence III (Aptian-Maastrichtian).

6.3.1.2 Para-Maranhao Basin, offshore Brazil

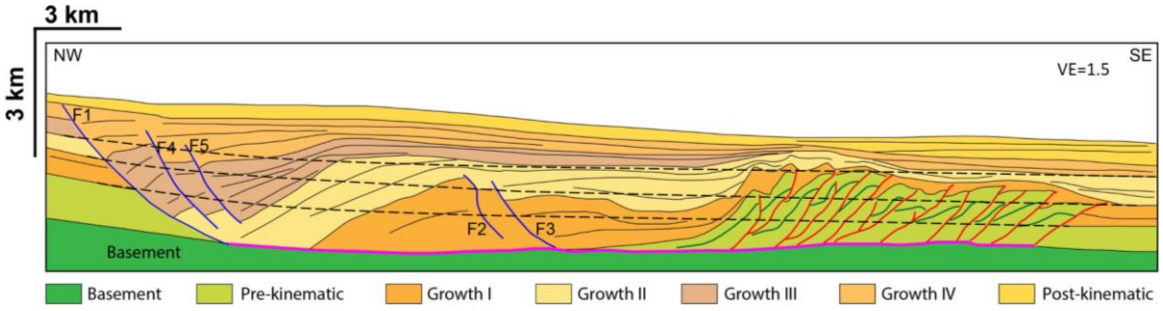

Figure 6.4 Interpretation of a seismic profile showing architecture of a gravity-driven system, Para-Maranhao basin, offshore Brazil (after Zalan, 2005; Butler and Paton, 2010). The vertical exaggeration is 1.5. Interpreted units are structural sequences.

The Para-Maranhao basin is located on the South American continental margin, offshore Brazil. An FTB is formed as the downslope expression of large-scale gravitational failure upslope (Butler and Paton, 2010, *Figure 6.4*). The overall deformational system is 38 km wide, composed of a 19 km wide extension region and 16 km wide contraction region that are underlain by overpressured mudstone (*Figure 6.4*; Butler and Paton, 2010). Seven tectono-stratigraphic sequences and associated structural features are interpreted within an example seismic section (*Figure 6.4*). From deep to shallow levels, these are Basement, Pre-kinematic, Growth I, II, III, IV and Post-kinematic. Each growth sequence represents a discrete stage of fault/fold growth. To better explain the growth history of extensional faults in relation to deformation initiation and development (migration and localization), we number all the interpreted normal faults in order of timing of initiation based on analysis of the growth stratigraphy.

Fault F1 is the primary listric extensional fault with a cumulative displacement of ~14.7 km measured as the offset of top Pre-kinematic sequence, it dominates strain accommodation in the extensional domain. It is initially induced by the deposition of Growth I as gravity failure, its subsequent growth created a prominent half-graben basin filled with Growth sequences II-IV. The overlying Post-kinematic sequence marks the cessation of fault F1 growth (*Figure 6.4*). During the continuous growth of F1, accommodating the majority of strain during Growth sequences I-IV, a component of strain is distributed elsewhere within the extensional zone. The first phase of strain

migration leads to the formation of normal faults F2 and F3, 8-10 km basinward of F1 (*Figure 6.4*), which deform Growth sequence I and part of Growth II. A second phase of strain migration occurs landward as two normal faults F4 and F5 initiate 2 km into the hanging wall of F1. These faults initiate within Growth sequence II, and continue through Growth sequences III and into IV.

In contrast, all thrust faults of the contractional domain appear to initiate and grow synchronously, with initial activity coincident with the significant growth of major normal fault F1 as documented by Growth sequence I (*Figure 6.4*). This demonstrates the genetic link between the contraction and extension in this gravity-driven system. Later thrust and associated folding activity is more localized in the rear of the contractional domain, as documented by the thinning and deformation of Growth sequences II, III and IV. The deposition of post-kinematic material marks the cessation of the entire system, onlap onto developed topography is observed within this sequence particularly in the landward part of the contractional domain (*Figure 6.4*). It is estimated that the shortening rate of this contractional domain is as low as 0.8 mm/yr (Cruciani et al., 2017).

These results highlight the characteristics of self-powered deformation within a gravity-driven system. The extension of normal faults in the upslope/landward slope region supplies the driving force and energy source to drive thrusting and folding on the downslope. Once the driving force ceases, the compressional deformation stops.

In terms of deposition, the majority of sediments are syn-kinematic sequences that attain thicknesses up to ~3 km in the graben basins related to extensional faulting, while a relatively thin pile of sediments of (<1 km) thick is deposited as pre-kinematic sequences. The stratigraphic thickening in this gravity-driven system is attained mainly by deposition, rather than strain through shortening and thrust repetition in the plate convergence-driven system.

To estimate the magnitude of deformation, three stratigraphic horizons are used to carry out the area balancing analysis and strain measurement, i.e., the tops of the Pre-kinematic (Horizon 1), Growth I (Horizon 2), and Growth II (Horizon 3) sequences (*Figure 6.4* & *Figure 6.5*). The regional slope is estimated based primarily on the present-day bathymetry (i.e. top of Post-kinematic) that is formed when the system is inactive and therefore likely reflects the initial sedimentary slope prior to deformation. For each layer,

the area encompassed by the regional slope, faults and selected layer is quantified to evaluate the magnitude of extension and contraction.

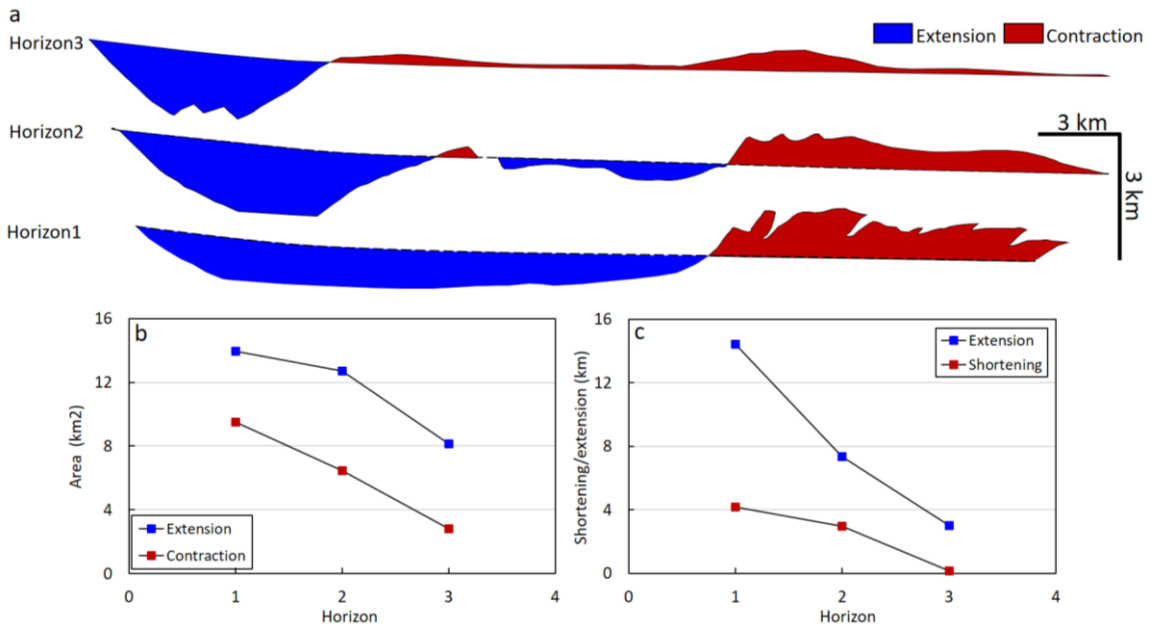

Figure 6.5 Quantification of extensional and contractional deformation across the gravity-driven linked system, Para-Maranhao basin, offshore Brazil (Figure 6.4). (a) Extensional area and contractional area constrained by estimated regional slope, interpreted faults and selected stratigraphic horizons, (b) plot of area of extension and contraction for each horizon, (c) plot of strain of extension and contraction for each horizon. Horizon 1 is top of Pre-kinematic, Horizon 2 is top of Growth 1, Horizon 3 is top of Growth II (see Figure 6.4).

The area balancing of Horizon 1 shows that the extension is directly connected with contraction without an obvious temporal transition in this system (*Figure 6.5a*), differing from that observed in the Orange basin, offshore Namibia (*Figure 6.3*). Regarding width, the extensional domain extends 21 km basinward whereas the contractional domain is only 13 km wide. By the time of Horizon 2, the extensional domain has propagated only 0.3 km basinward while the contractional domain propagated 1 km basinward (*Figure 6.5a*). By Horizon 3, the extension has retreated slightly, 0.8 km landward, while the contraction has propagated landward significantly, ~9.3 km. The measured 8.1-14 km^2 extensional area from the three horizons is much larger than that of contractional area, 2.8-9.5 km^2. The difference is attributed to layer parallel shortening, lateral compaction, and ductile deformation (Koyi et al., 2004; Butler and Paton, 2010, and reference herein). The strain across the extensional and contractional domains is also measured as the difference between restored and current bed length for each selected horizon (*Figure*

6.5c). The results show that strain in the extensional domain is 4.2-14.4 km (relative to each horizon) and much larger than for the contractional domain (0.2-4.2 km). This is in agreement with the area balancing analysis across the two domains (*Figure 6.5b*). Not unexpectedly, strain is greatest for the deepest horizon and shows a general pattern of decreasing upwards (*Figure 6.5a*).

We note this seismic section is mapped primarily based on its tectonic history without emphasis on stratigraphy. The top of the Pre-kinematic sequence for thrusting may be diachronous, and the thrust faults may have in fact developed in a piggyback sequence, rather than synchronously. However, the continuous growth of the thrusts at the rear of the contractional domain is evident (*Figure 6.4*), which continues until the extensional faulting stops.

6.3.1.3 Amazon fan, offshore Brazil

The submarine Amazon Fan lies off the NE coast of Brazil, near the mouth of the Amazon River. It is characterised by a wedge of clastic sediment up to 10 km thick deposited since 10 Ma (Cobbold et al., 2004) (*Figure 6.6a*). The extensional faults have formed across the prograding delta slope and contractional folds and faults have formed seaward of it. In the present-day, the system is composed of a 131 km wide extensional domain and 90 km wide contractional domain, separated by a 11 km wide transition zone of minor deformation (*Figure 6.6a*, *Table 6-1*) beneath the rear of the downslope region.

A 2D seismic profile across this system interpreted by previous authors (Cobbold et al., 2004; Morley et al., 2011) is analysed here, with five tectono-stratigraphic horizons and sequences mapped previously from deep to shallow levels (*Figure 6.6a*). In this example, Basement is defined as the sequence purely deformed by syn-rift extension (as indicated by deeper normal faulting), pre-dating the gravitationally-driven system. The top of this unit is marked by the Top Cenomanian. The rifting-related extension terminates between the top Cenomanian and top Cretaceous and this unit (medium green colour) is partly syn-rift and partly post-rift (*Figure 6.6a*). The Pre-kinematic sediments (light green) thin basinward. This would produce a prominent topographic relief/slope (presuming they did not infill earlier topography with seaward topographic highs) and resulting gravitational energy enabling the system to deform. The deformation initiates immediately after the deposition of the Top Cretaceous, and is subsequently driven by deposition of the

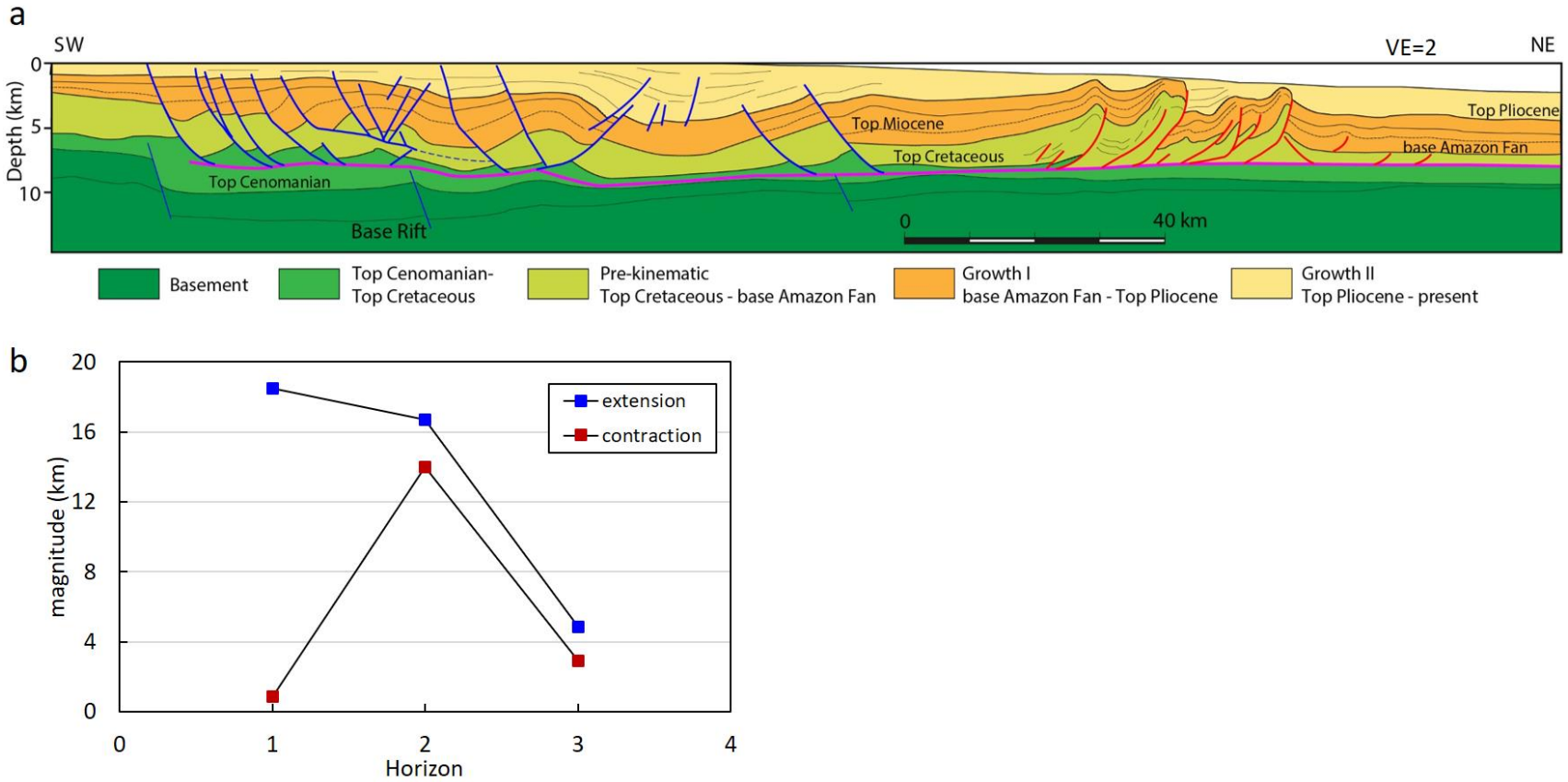

Figure 6.6 (a) Interpretation of a seismic reflection profile across the gravity-driven Amazon Fan system, offshore Brazil from outer shelf to slope (after Cobbold et al., 2004; Morley et al., 2011). Interpreted units are stratigraphic sequences. The vertical exaggeration is 2. (b) Quantification of extension and contraction across this system using 3 stratigraphic horizons. Horizon 1 is the Top Cretaceous, Horizon 2 is the base Amazon fan, Horizon 3 is the Top Pliocene.

Amazon fan, forming a gravity-driven extensional system on the updip slope linked to contraction at the toe of the slope (*Figure 6.6a*). The normal faults are predominantly regional, dipping basinward with a few outliers of counter-regional normal faults dipping landward, however the thrust faults are typically basin/seaward-vergent. The detachment (interpreted to sit at/in overpressured shale) is developed between the Top Cenomanian and Top Cretaceous in the extensional domain and the landward region of the contractional domain (medium green), but coincides with the Top Cretaceous for the more seaward part of the contractional domain based on previous interpretations (Morley et al., 2011). The majority of normal and thrust faults detach onto this level.

In terms of growth/activity history, the linked system starts to deform as soon as the Top Cretaceous deposits, and continues to the present-day with some normal faults extending to the seafloor and the thrust faults dying out at their tips beneath seafloor. The buried nature of the thrust faults has been interpreted to result from low uplift and high sedimentation rates (Shaw et al., 2005), but the Growth II succession above the Top Pliocene thins towards the anticlinal crests demonstrating continued activity of the thrust faults in the most recent depositional phase (*Figure 6.6a*).

Extensional and contractional strain across the system have been quantified using three sedimentary layers separated by the following horizons: (Horizon 1) Top Cretaceous, (Horizon 2) base Amazon Fan, and (Horizon 3) Top Pliocene, using the same method as described for the Para-Maranhao basin above. The results show a strain difference and pattern between the extensional and contractional domains (*Figure 6.6b*). This can be generally explained by lateral compaction commonly recognized in a poorly lithified sedimentary succession, e.g. Orange basin of offshore Namibia (Butler and Paton, 2010). We note that the strain difference between extension (17.6 km) and contraction (1.9 km) documented from the deepest horizon (Horizon 1, Top Cretaceous) is very large with respect to the other horizons, i.e. 6.4-9.1 times (*Figure 6.6b*). However, this anomaly is interpreted to result from errors in interpretation. For example, there are only 1-2 thrust faults interpreted relative to 11 normal faults, which is obviously unbalanced in such a large gravity-driven system (*Figure 6.6b*). Therefore, we suggest that the Top Cretaceous should be above the basal detachment across the contractional domain, rather than beneath it. In addition, correlation of horizons and stratigraphic units between the extensional and contractional domains may not be completely accurate.

6.3.1.4 Niger delta, offshore Nigeria

The Niger Delta is located on the West African continental margin, and it displays well-developed zones of a large delta province with an onshore to shelfal zone of growth fault controlled depocentres, a belt of shale diapirs around the outer shelf-slope area, and a fold-thrust belt in the slope area (e.g., Evamy et al., 1978; Doust and Omatsola, 1989; Morley and Guerin, 1996; Haack et al., 2000; Ajakaiye and Bally, 2002) (*Figure 6.7*). A transition zone of minor deformation is 41 km wide, separating the extensional and contractional domains that are 93 km and 69 km wide, respectively (*Table 6-1*). The basal detachment dips gently seaward beneath the extensional domain and landward beneath the contractional zone (*Figure 6.7*), and has been interpreted as within/at overpressured, compacted shale (Biollit and Shaw, 2005).

The interpreted seismic profile crosses the Niger delta, Gulf of Guinea, and consists of four principal tectono-stratigraphic sequences: Basement, Cretaceous, Pre-kinematic and Syn-kinematic (*Figure 6.7*). The Basement is the oceanic crust subjected to extension

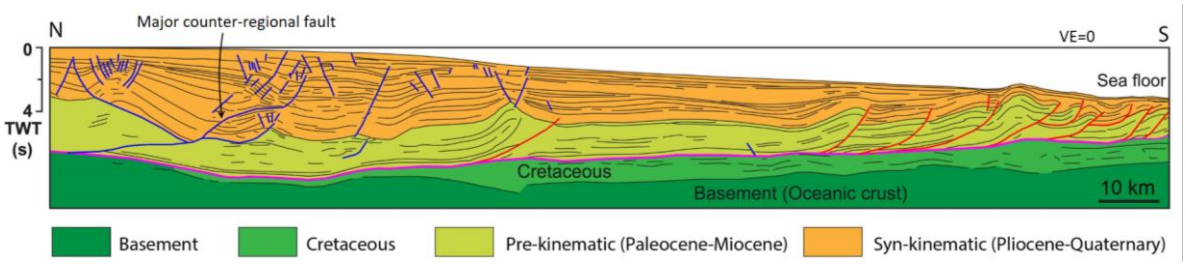

Figure 6.7 Interpretation of a seismic reflection profile across eastern lobe of offshore Niger Delta, Gulf of Guinea, showing structural styles of a gravity-driven fold-thrust belt (after Ajakaiye and Bally, 2002; Wu and McClay, 2011). No vertical exaggeration. Interpreted units are stratigraphic sequences.

during the crustal stretching/syn-rift phase. The overlying post-rift sequence is deposited during the Cretaceous ("Cretaceous" sequence) and the Pre-kinematic sequence is deposited during the Paleocene to Miocene. This sequence is then deformed by extension on the shelf and compression on the slope during the Plio-Quaternary as documented by the Syn-kinematic sequence. In terms of structural style, the extensional domain is characterised by both regional and counter-regional normal faults. This includes a major counter-regional, listric normal fault which detaches onto the primary detachment and this fault includes the thickest Syn-kinematic sequence in this section, indicating its

dominance in accommodating extension. Deformation in the extensional domain is dominated by the two listric normal faults (one regional, one counter-regional) while a minor component of deformation is distributed across a number of additional minor, rootless planar normal faults. In contrast, deformation in the contractional domain is distributed across a number of major imbricate thrust faults. The shortening rate across this contractional domain is estimated as 1.4-2.0 mm/yr (Cruciani, 2017). A maximum shortening of 17-25 km is estimated across the contractional domain (Corredor et al., 2005, *Table 6-1*). Wu and McClay (2011) reported that in this system the sequence of thrusting tends to young offshore, and most folds and thrusts verge basinward, typical for a critical wedge model. Studies from an adjacent area report examples of out-of-sequence thrusting, synchronous deformation and break-back sequences, with some folds displaying pop-up and triangle-zone geometries, and a series of back-thrusts (e.g., Morley et al., 2003; Corredor et al., 2005). Therefore there are clear variations in structural style along strike and the contractional domain is unlikely to be a simple piggyback thrust sequence throughout.

Similar to the observation made in the Para-Maranhao basin, the thickened upslope region is typically attained by the deposition of a thick syn-kinematic sequence (the primary deformational phase in the Plio-Quaternary for the Niger Delta), which in turn powers the system as the source of gravitational potential energy.

In terms of deformation history, the initiation of extension is marked by the formation of the major counter regional listric normal fault in the middle of the domain, which is accompanied by the deposition of the thickened syn-kinematic sequence. Subsequently, deformation propagates mainly basinward with a component of landward propagation. The initiation and continuation of shortening coincides with the growth of normal faults as documented by the Syn-kinematic sequence of the Pliocene-Quanternary (*Figure 6.7*). In the present day, the major contractional deformation appears to occur in the middle of the contractional domain where fold growth significantly deforms the seafloor relative to surrounding areas (*Figure 6.7a*). We note the end of this section probably does not image the entire seaward part of the contractional domain.

6.3.2 Plate convergence driven fold-thrust belts

6.3.2.1 Nankai accretionary prism, offshore Japan

The accretionary Nankai subduction margin forms where the Philippine Sea Plate converges and subducts beneath SW Japan and Eurasia, and is the location of regular subduction earthquakes. It is a typical plate convergence-driven FTB end member. A cross section across the prism (Muroto transect) shows the characteristics of fold and fault geometry and the associated sedimentary sequence across a width of 21 km (*Figure 6.8*). Building upon previous work (e.g., Moore and Silver, 1987; Moore et al., 1990; Hills et al., 2001; Bangs et al., 2004; Gulick et al., 2004; Wu and McClay, 2011), we mapped faults and four key tectono-stratigraphic sequences: Basement, Miocene, Pre-kinematic and Syn-kinematic (*Figure 6.8*). The basement here is oceanic crust of the subducting plate, while the Miocene sediments are the subducted sedimentary materials overlying basement.

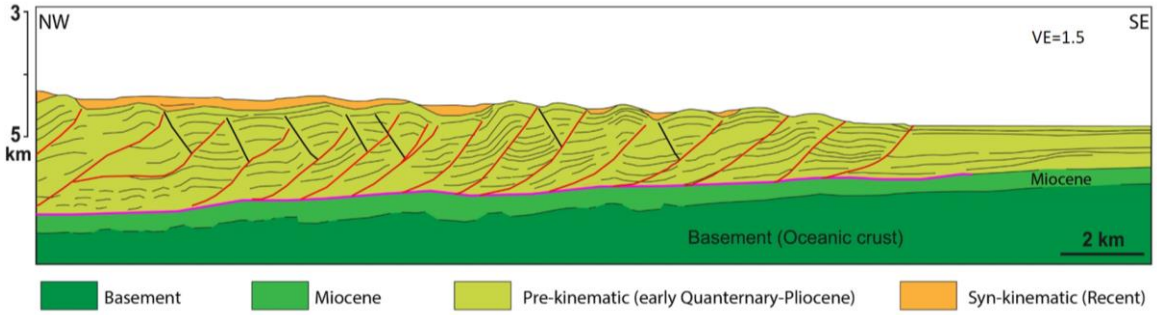

Figure 6.8 Interpreted seismic reflection profile across Nankai Accretionary prism (Muroto transect), Japan, a plate-convergence driven system, after Moore and Silver. (1987), Moore et al. (1990), Wu and McClay. (2011). The vertical exaggeration is 1.5. Interpreted units are stratigraphic sequences.

Bangs et al. (2004) mapped the amplitude of the subduction thrust reflector from the trench into the seismogenic zone using 3D data supported by drilling data, and showed that the décollement forms within the lithologically homogeneous Lower Shikoku Basin facies along a high-amplitude reflection. It is a major boundary for both physical and mechanical properties (Moore et al., 2001) between the underthrusting Miocene sequence and Pliocene-early Quaternary pre-kinematic sequence, and dips 6-8 ° landward (*Figure 6.8*). The reflector is predominantly negative polarity beneath the prism attributed to high porosities beneath the décollement, and decreases in amplitude and becomes less negative towards the rear of the prism (Bangs et al., 2004).

The Nankai fold-thrust belt is formed of a well ordered array of closely spaced (1–2 km) basinward-vergent thrusts with associated folds. Several of these thrusts, primarily further landward, have developed landward-verging backthrusts in the shallow part of the section (<1 km beneath seafloor) (*Figure 6.8*). The majority of the discrete thrusts separate the fold-and-thrust sequences of the accretionary wedge and sole out into the basal detachment (*Figure 6.8*, see also Bangs et al., 2004).

The deforming sediments (Pre-kinematic), attaining thicknesses up to 3 km, are input sediments being continuously supplied by the subducting oceanic plate. This sequence is time transgressive, and the thrusting sequence is therefore not synchronous, but likely younging basinward (e.g., Moore et al., 1990, 2001a, 2001b). The syn-kinematic sediments experience only minor deformation, and thin (< 0.3 km), in contrast to the pre-kinematic sequence which is significantly deformed, and relatively thick (up to 2 km). This shows that the thickening of plate convergence-driven FTBs is attained by shortening and thrust repetition and not the build up of syn-kinematic sediment thickness, in contrast to the thickening being produced by deposition of the deformed syn-kinematic sequence within gravity-driven FTBs.

6.3.2.2 Hikurangi accretionary prism, offshore New Zealand

The Hikurangi accretionary prism is located above the subducting oceanic Pacific Plate on the eastern margin of the North Island, New Zealand (Barnes et al., 1998; Barnes et al., 2010). It is a typical plate convergence-driven FTB. The present-day convergence rate is estimated as 1.9-6.1 cm/yr (Wallace et al., 2009). In the example profile (*Figure 6.9*), a ~89 km wide prism is interpreted with seven stratigraphic horizons of inferred age 30+/5 Ma to present by previous authors (Ghisetti et al., 2016). Here we reinterpret the sequence to highlight its tectonic history while maintaining the previously interpreted stratigraphic horizons. This allows direct comparison of structural initiation development with sediment deposition.

The sedimentary material within the thrust belt is dominated by the Pre-kinematic sequence with three thin Growth successions (I-III) deposited at shallow depths, <1 km beneath the seafloor (*Figure 6.9*). This prominent contrast in sediment thickness is similar to that observed in Nankai accretionary prism (*Figure 6.8*). The Growth I sequence is deposited during the development of the early thrusts now at the rear of the wedge. The

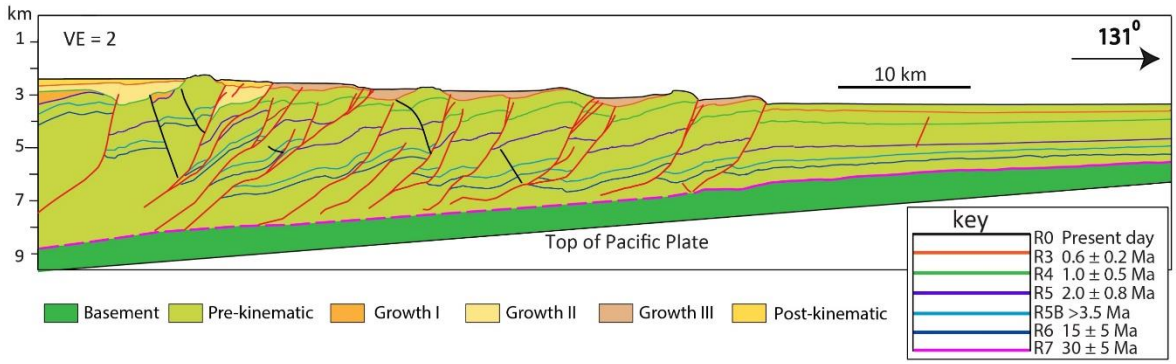

Figure 6.9 Interpreted seismic reflection profile across Hikurangi accretionary wedge, offshore North Island, New Zealand (after Ghisetti et al., 2016). Eight stratigraphic horizons are mapped with inferred age of 30+/5 Ma to present day. The vertical exaggeration is 2. Interpreted units are structural sequences.

overlying Growth II sequence extends 10 km further basinward relative to Growth I, indicating the forward propagation of the wedge with formation of additional thrusts. Growth III is deposited beyond the previously developed thrust faults, and extends to the deformation front across the majority of fold belt, representing the latest stage of significant deformation of a wider zone (~35km). The wedge deformation is therefore characterised by forward propagation involving sequential (Growth I and II) and synchronous (Growth III) development of thrust faults.

The structures in this cross section are dominated by basinward/seaward-verging imbricate thrust faults and associated fault propagation folds. Minor faults are observed splaying off the shallow portion of a few major thrust faults, and 4-5 rootless backthrusts are observed in the hanging wall of some of the major imbricate thrusts. Some major thrusts show listric geometry with an increasing fault dip upward (*Figure 6.9*, note these are depth sections so no velocity effects on fault dip). In terms of amount of contraction, Ghisetti et al. (2016) estimated a total of 16.6 km shortening accommodated by thrusting and folding since the deposition of Horizon R5 (*Figure 6.9*) by using sequential restoration.

6.3.3 Combined gravity- and plate convergence-driven fold-thrust belts

Unlike the end member scenarios driven entirely by gravity, e.g., Niger Delta, or plate convergence, e.g., Nankai, a hybrid system of fold-thrust belt might be expected to inherit the structural characteristics of both types of system. The Makran is a subduction zone with a gravitational element at least in part of the along-strike system (observed on part of the Iranian margin, e.g., Grando and McClay, 2007) and NW Borneo is a gravity system with a possible subduction element (e.g., Hess et al., 2009; King et al., 2010a).

6.3.3.1 Makran accretionary prism, offshore Iran

Of global subduction zones, the Makran has the largest documented input sediment section, as a result of Indus Fan subduction, and the widest accretionary wedge system (~350 km, e.g., Smith et al., 2012). It is formed as a result of subduction of the Arabian plate beneath the Eurasian plate throughout the Cenozoic (Harms et al., 1984). The average convergence rate is ~4.0 cm/yr approximately northward, varying from 3.65 cm/yr in the western Makran to 4.2 cm/yr in the eastern Makran (DeMets et al., 1990). More recently Vernant et al. (2004), based on GPS data, have estimated convergence velocities of 2.7 cm/yr in the western Makran. In the west, offshore Iran, a regional N-S geological cross-section (*Figure 6.10*) shows that the margin is also deformed by extension on the shelf (47 km width domain) in the form of major listric growth faults, and compression further downslope (85 km width domain seaward of the extensional zone) forming the seaward part of the accretionary prism (Grando and McClay, 2007). There is no obvious transition zone separating these two domains. We note that shale diapirism is also a characteristic of this and other parts of the margin (see *Figure 6.10*). The submarine accretionary prism, characterised by thrusts and associated folds, at least in this part of the margin, is therefore interpreted to result from a combination of plate convergence and gravitational failure. To analyse and quantify the contribution of each driving mechanism, we carry out an in-depth analysis of fault activity and fold growth by looking at the detailed pattern, geometry and distribution of the syn-kinematic sequence. The stratigraphy is interpreted as both sedimentary units (*Figure 6.10a*) and deformation-related units (*Figure 6.10b*), building on previous interpretations (e.g., Grando and McClay, 2007). This profile traverses the shelf area, slope basins and outermost Makran accretionary prism.

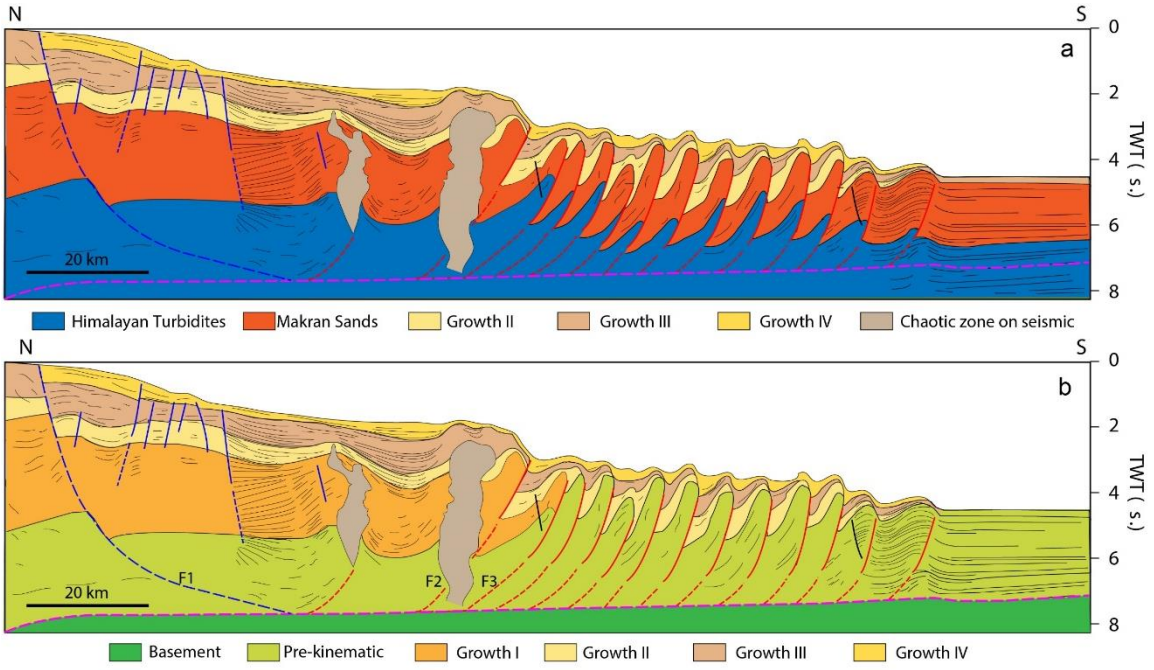

Figure 6.10 Interpretation of a seismic reflection profile across the hybrid system western Makran accretionary prism, offshore Iran. (a) Stratigraphy-based interpretation with stratigraphic sequences, (b) Structure-based interpretation with structural elements. The vertical exaggeration is 6. After Grando and McClay (2007).

From deep to shallow levels, six stratigraphic units are mapped (*Figure 6.10a*): the Himalayan Turbidites, Makran Sands, Growth II, Growth III, Growth IV and Chaotic zone on seismic (from Grando and McClay, 2007). As part of this study, the cross-section is then structurally reinterpreted to highlight its deformation history (*Figure 6.10b*). Three types of deformation-related sedimentary successions are mapped: (1) Basement, defined as the material below the basal detachment that is not involved in deformation; (2) Pre- kinematic, the sediments deposited before the onset of deformation; and (3) Growth (broken into units I-IV), the sediments deposited during deformation. We note that the top of oceanic basement sits below the base of this seismic profile and is not equivalent to "basement" as defined here. Note the Growth sequences II, III and IV and the Chaotic zone in *Figure 6.10a* match the deformation-related units in *Figure 6.10b*, in accordance with the interpretation of Grando and MaClay (2007). The chaotic zones could be indicative of shale diapirs, narrow shale pipes or gas chimneys (Morley et al., 2011).

The gently north-dipping (sub-horizontal) basal detachment is developed within the Himalayan Turbidites, separating the "Basement" from the overlying Pre-kinematic sediments (*Figure 6.10a & Figure 6.10b*). The primary listric normal fault (northern end of

profile) and all basinward/seaward-verging thrust faults detach onto this level (*Figure 6.10b*), whereas the more minor normal faults (between faults F1 and F2) and the two minor landward-verging thrust faults (or backthrusts) in the contractional domain appear to be rootless, dying out at depth with negligible displacement. These rootless faults are interpreted as secondary structures and have very limited effect on the overall development of Makran accretionary prism.

In an evolving thrust system, the pattern and distribution of growth strata documents the history of tectonic evolution. Growth sequence I represents the first stage of deformation, and is thickest in the extensional domain, including in the half-graben basin created by the major extensional fault F1, with a thinner section preserved in the hanging walls of thrust faults F2 and F3 (*Figure 6.10b*). The distribution of Growth I indicates the coincidence of activity of extensional and thrust faults in this coupled system. This first-stage deformation extends as far as thrust fault F3 but not beyond, and involves the landward part of the Makran Sands sequence (*Figure 6.10a*). Subsequently, three stages of deformation are recognized, denoted Growth II, III and IV and these phases appear to involve the entire extensional to contractional system as demonstrated by the broad distribution of the growth sequences marking a change in activity and extent of the system between Growth I and II.

The thicknesses of Growth units II, III IV change within the hanging walls of the thrust faults (primarily thinning towards the crest), but have more constant thickness across the normal fault hanging walls, in particular near primary listric normal fault, F1 (*Figure 6.10b*). This suggests that major deformation is focused in the contractional (FTB) domain with minor deformation in the extensional domain since Growth II. Therefore, gravitational failure may have only played a role in driving thrust faults F2 and F3 (*Figure 6.10b*), with subsequent conractional deformation driven primarily by plate convergence. However, it is possible that additional normal faults exist upslope (beyond the northern end of the seismic profile) with larger displacements and extension, and that these are responsible for generation of the thick Growth sequences in the extensional domain (in particular Growth I, *Figure 6.10b*), and therefore gravity may play a larger role in this system.

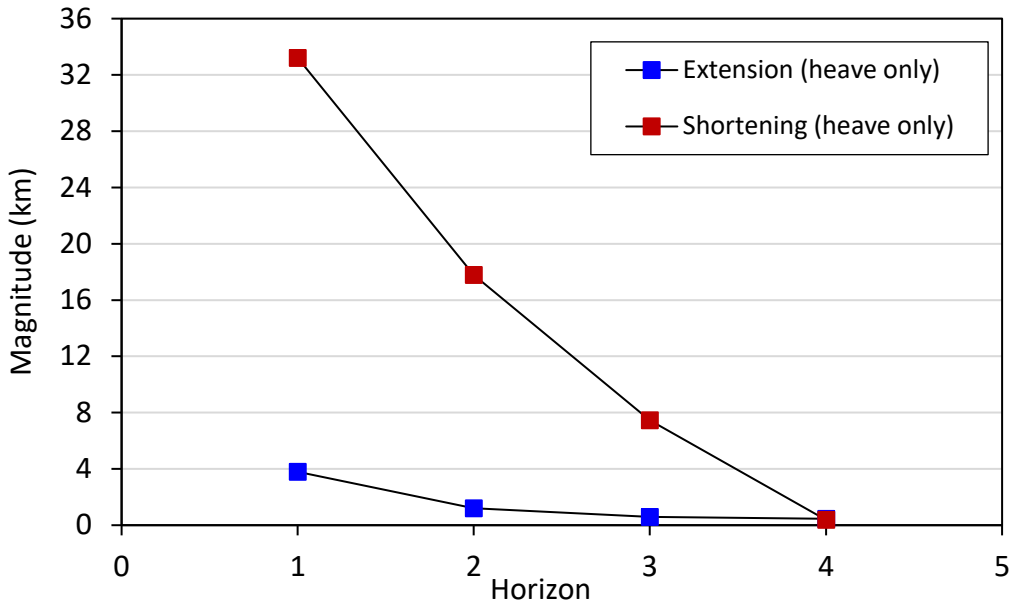

Figure 6.11 Plot of extension and contraction (heave only) across the hybrid system Makran accretionary prism for four stratigraphic horizons. Horizon 1 is top of Himalayan Turbidites, Horizon 2 is top of Makran Sands, Horizon 3 is top of Growth II, Horizon 4 is top of Growth III (Figure 6.10a).

To validate this observation, we further quantify the magnitude of deformation documented by sedimentary layers across the extensional and contractional domains. Because this is a time section, we choose to measure fault heave as a proxy for strain and relative strain distribution. Four stratigraphic horizons are used to carry out the strain measurement: top of Himalayan Turbidites (Horizon 1), top of Makran Sands (Horizon 2), top of Growth II (Horizon 3) and top of Growth III (Horizon 4) (*Figure 6.10a*). The results show fault heave decreases updip from the deepest (1) to shallowest horizon (4) for both the extensional and contractional domains. We note that heave relative to displacement does change with depth for these listric faults, in particular the normal faults, and therefore will artificially generate/exaggerate a decreasing upward heave. The heave of the extensional faults amounts to 0.6-3.8 km for Horizons 1-3, which is 6.8-11.4% of the 7.5-33.2 km heave of the thrust faults, demonstrating the dominance of thrusting over normal faulting in accommodating strain in this system (*Figure 6.11*). In contrast, the heave of Horizon 4 (the shallowest horizon) in both the extensional and contractional domains is very low, 0.4-0.5 km. This is interpreted as the effect of updip propagation of deformation and the buried nature of the thrust faults, i.e. lack of fault displacement. Horizon 4 in the contractional domain is the top of Growth III (*Figure 6.10a*), which is

largely affected by folding, and not by fault displacement. Because this study only quantifies fault heave, not fold shortening, as a component of deformation (*Figure 6.1*), the overall deformation is largely underestimated in particular for Horizon 4.

We conclude that the Makran accretionary prism is predominantly a plate convergence-driven system (Growth II- IV) with minor gravitational contribution primarily in the first growth stage (Growth I), however additional extensional faulting beyond the profile used may change this interpretation.

6.3.3.2 NW Borneo deepwater fold-thrust belt, offshore Brunei

The NW Borneo deepwater fold-thrust belt is interpreted to result from a combination of gravitational instabilities and active regional collision (e.g., Ingram et al., 2004; Morley, 2007b; Hesse et al., 2009; Hesse et al., 2010a; King et al., 2010a). To resolve the initiation, propagation and distribution of deformation across the NW Borneo FTB, tectonostratigraphic units are remapped based on previous interpretations (*Figure 6.12*; Morley et al., 2011).

Six stratigraphic units are mapped from deep to shallow levels: Middle Miocene and Older, Middle Miocene, Upper Miocene, Upper Miocene-Pliocene, Pliocene and Pleistocene-Holocene (*Figure 6.12a*). The system is composed of two deformational domains: upslope extension (46 km wide) and downslope contraction (85 km wide), connected by a common underyling detachment interpreted as preferentially located at a weak formation, i.e. over-pressured mudstone, (e.g., Van Rensbergen and Morley, 2003; Ingram et al., 2004; Morley, 2007b) (*Figure 6.12b*). Similar to the Makran prism (*Figure 6.10a*), there is no observed transition zone between the two deformational domains. The detachment fault is developed within the deepest/oldest unit: Middle Miocene and Older. Its first-order geometry is characterised by a ramp-flat-ramp shape, excluding the estimated landward trace (dashed line). Four major, landward-dipping normal faults and the majority of thrust faults appear to sole out into this basal detachment (*Figure 6.12a*). The remaining normal faults are basinward/seaward dipping, and either die out at depth or intersect with another fault while the remaining thrust faults are up to 2 km above the detachment, characterized by decreasing displacement updip (*Figure 6.12a*).

To reinterpret tectonic history, we mapped eight deformation-related sequences: Basement, Pre-kinematic, Growth I, II, III, and IV, and Post-kinematic (*Figure 6.12b*). The

first stage of deformation (Growth I) initiates in the extensional domain where the maximum cumulative displacement is attained by two conjugate normal faults F1 and F2, forming a graben. Deformation then propagates predominantly basinward with a small landward component characterised by decreasing fault displacement as documented by Growth II. This second stage of deformation (Growth II) involves the majority of the normal faults and two thrust faults at the rear of the contractional domain. During this stage, most normal faults (including all basinward-dipping faults) become inactive with fault tips dying out within Growth II, but three landward-dipping normal faults remain active. Deformation during this stage propagates ~10-12 km basinward due to the formation of the two new thrusts (F3 and F4). The third stage of deformation (Growth III) is characterised by continuous activity of three primary landward-dipping normal faults and 3-4 newly activated thrust faults basinward/seaward of F3 and F4. This stage involves an additional 15 km of basinward propagation of deformation. The fourth stage (Growth IV) marks the cessation of growth of the three landward-dipping normal faults and formation of one new thrust fault, ~20 km basinward. The final (fifth) stage of deformation (Growth V and Post-kinematic) is more complex, with all normal faults inactive but the majority of thrusts beyond F4 active (*Figure 6.12b*). If this cross-section includes all extensional structures across the margin, then this final stage of thrusting (Pleistocene-Holocene) must have been driven by regional active collision with an absence of gravitationally-driven deformation. This agrees with measured convergence in the present-day between NW Borneo and Sundaland (4-6 mm/yr, Simons et al., 2007; Sapin et al., 2011, 2013) and the more downslope shortening relative to upslope contraction predicted using sequential restoration by Hess et al. (2009), King et al. (2010b). However, the convergence rate is low relative to typical subduction zone end members.

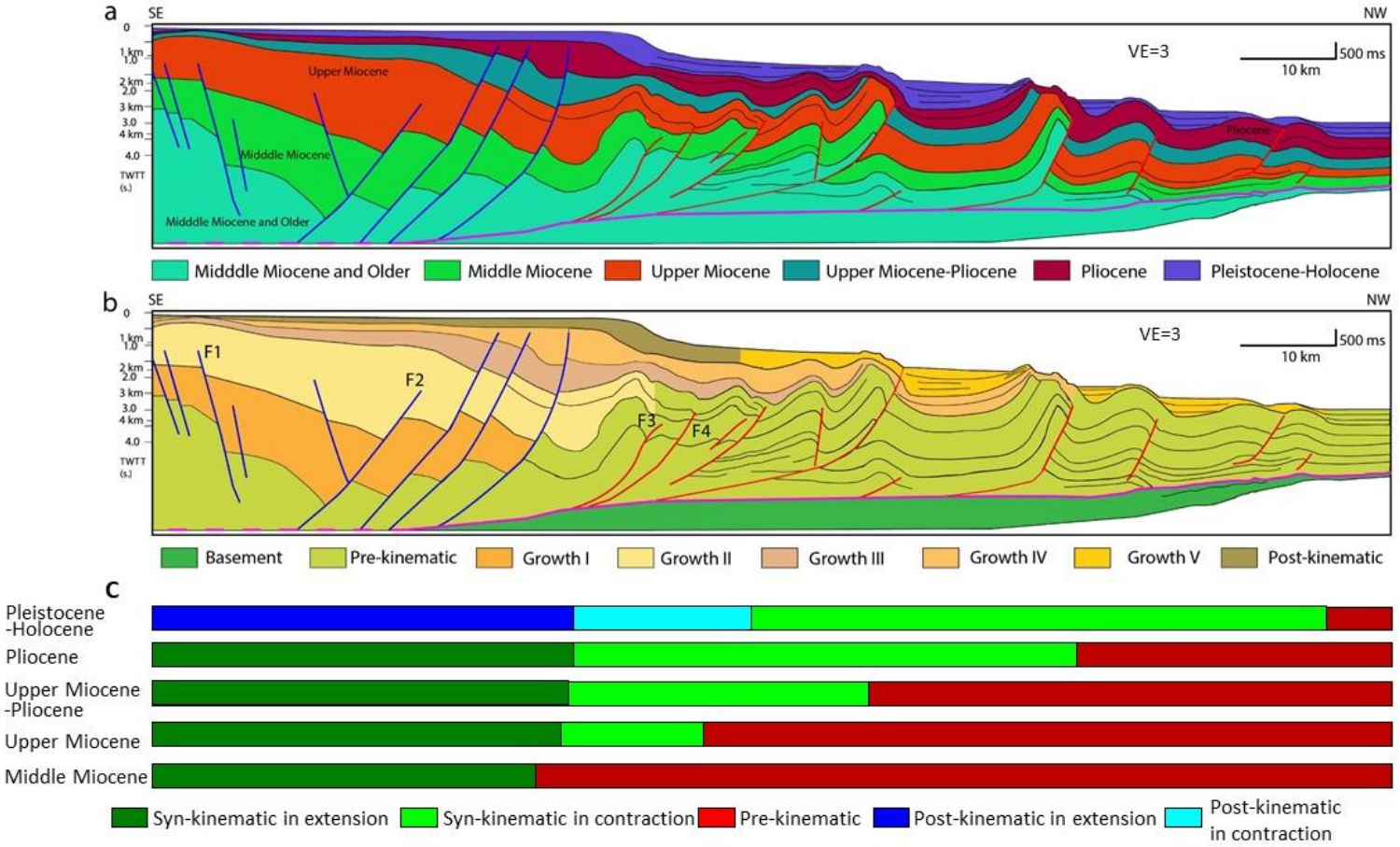

Figure 6.12 Interpretation of a seismic reflection profile across the hybrid system NW Borneo continental margin. The profile crosses extension in the shelf area and contraction beneath the slope. (a) Stratigraphy-based interpretation; (b) structure-based interpretation; c) schematic of the five stratigraphic units broken down across strike into the tectono-stratigraphic units for extension and contraction. The vertical exaggeration is 3. After Morley et al. (2011).

To highlight the deformation history, we created a schematic of the five stratigraphic units broken down across strike into the tectono-stratigraphic units for extension and contraction (Figure 6.12c). The width of each unit correlates to the interpreted seismic section above, which shows the position/extent of deformation at each stage. The maps shows that extension initiates in the Middle Miocene, and then propagates mainly upwards with only minor forward propagation (dark green), and ceases during or just before the Pleistocene-Holocene (dark blue). In contrast, contraction initiates later during deposition of the Upper Miocene. Subsequently, it propagates forwards significantly as highlighted by the basinward/seaward extent of the bright green bars (Syn-kinematic in contraction). In the Pleistocene-Holocene, the rear of the contractional domain, i.e. early formed thrusts and folds, is inactive (light blue, Post-kinematic in contraction) but there is continuous deformation of a wide zone of thrust and folds in the outer part of the FTB (light green).

Our structural analysis indicates that, in general, the NW Borneo fold-thrust belt is predominantly a gravity-driven system with a minor contribution from plate-scale shortening produced by far-field plate-convergence, in particular during the recent Pleistocene-Holocene stage.

Table 6-1 The parameters of fold-thrust belt examples used in this study.

Fold-thrust belt example	**Parameters**											
	Width (W) (km)	**W_E (km)**	**W_C (km)**	**W_T (km)**	**T_H (km)**	**T_F (km)**	**Detachment dip and properties**	**Extens-ion (km)**	**Shorte-ning (km)**	**Faults**	**Folds**	**Activity history**
Orange basin, offshore Namibia	255	133	84	4	3.7 s	2.3 s	Gently seaward dipping, overpressured shale			Dominant regional listric normal faults, seaward-verging imbricate thrusts	Asymmetric fault propagation folds (FPFs)	Younging seaward?
Para-Marahao basin, offshore Brazil	38	20	16	0	2.7	2.0	Gently seaward dipping, overpressured mudstone	3.0-14.4	0.2-4.2	A major and several small regional listric normal faults, seaward-verging imbricate thrusts	Asymmetric FPFs	Normal faulting migrates seaward and landward, folds younging seawards?
Amazon fan, offshore Brazil	232	131	90	11	10.1	8.0	Gently seaward dipping, overpressured and compacted shale	4.8-18.5	0.9-14	Dominant regional and few counter regional listric normal faults,	Asymmetric FPFs	Younging seawards, recent activity focused on the rear of

										seaward-verging imbricate thrusts		contractional domain
Niger delta, offshore Nigeria	203	93	69	41	6.4 s	2.2 s	Gently seaward dipping at extension and landward dipping at contraction, overpressured, compacted shale		17-25	Two major Listric regional and counter regional listric faults and a number of rootless planar normal faults, seaward-verging imbricate thrusts	Asymmetric FPFs	Younging seawards, the recent activity is focused in the middle of contractional domain
Nankai (Muroto) accretionary prism, offshore Japan	27	0	21	0	2.0	0.9	6-8° landward dipping, overpressured mudstone/shale			Seaward-verging imbricate thrusts, a few landward-verging thrusts	Asymmetric FPFs	Younging seawards with poorly resolved thrust sequence
Hikurangi accretionary prism, offshore New Zealand	89		55		6.4	2.9	Moderately landward dipping, weak detachment ?		16.6	Dominant seaward-verging listric and planar imbricate thrusts and a few planar backthrusts,	Asymmetric FPFs	Younging seawards, deformation involves initial piggyback sequence and

										splay faults		subsequent synchronous folding
Makran accretionary prism, offshore (and onshore) Iran	178	47	85	20.4	7.6 s	2.7 s	1-3° landward dipping, weak detachment ?	0.5-3.8	0.4-33.2	A major listric normal fault, several rootless planar normal faults, dominant seaward-verging imbricate thrusts, two planar backthrusts	Asymmetric FPFs	Younging seawards, deformation involves initial piggyback sequence and subsequent synchronous folding
NW Borneo fold-thrust belt, offshore Brunei	131	46 45.9	85	85.4	8.00	2.5-3	Gently landward dipping, Overpressured shale	0.5-6	4-7	A few major counter regional listric normal faults, many rootless planar normal faults, dominant seaward-verging imbricate thrusts, two rootless planar backthrust	Asymmetric FPFs	Younging seawards, deformation involves initial piggyback sequence and subsequent synchronous folding

W=Width of whole section, W_E=width of extension, W_C= width of contraction, T_H=thickness of upslope or hinterland, T_F=Thickness of foreland. Please note for time sections, the thickness is measured in seconds two way time, so the value is followed by unit s.

6.4 Discussion

6.4.1 Driving forces and energy source

The energy source of gravity-driven systems is the release of gravitational potential energy (PE) within the linked system (Peel, 2014). For large-scale passive margin systems, it is energy contained within the sediment pile itself, i.e., within the body of material that is being deformed (the deformed syn-kinematic sequences in the hanging wall of upslope extensional faults in *Figure 6.3*, *Figure 6.4*, *Figure 6.6* & *Figure 6.7*), where the energy is supplied to the linked system through the means of body forces that are applied to the moving sediments. The system is contained within outer boundaries that do not need to move. Natural gravity-driven systems generally require the existence of a height difference between the ends of the system, usually in the form of a surface slope, e.g. the estimated surface slope in the Para-Maranhao basin, offshore Brazil (*Figure 6.4*). The greater the height difference, the greater the potential energy and the more potential for development of a gravity-driven system. This height difference can change through time dependent on the rate of addition of sediments or as the slope system deforms and sediments are incorporated. It is worth noting that the gravitational PE could also exist in a system that did not have any initial surface height difference, and this can in principle drive lateral motion if the density of sediments changes laterally. But there is no known major example of an active gravity-driven FTB powered solely by lateral density differences without initial surface expression/slope.

In contrast, the energy source of plate-convergence driven systems it is the movement of stressed lithospheric scale-boundary, which lies outside the local sediment pile. It is supplied to the FTB through the means of boundary forces (relative plate motions) applied to a moving boundary. The FTB system is contained within outer boundaries that do need to move.

As a consequence, the sediments in gravity-driven FTBs are dominated by the significantly deformed syn-kinematic sequences, typically >3 km in thickness, that power the system in the form of gravitational potential energy, particularly in the extensional domain, with much thinner pre-kinematic sequences, <1 km (*Figure 6.3*, *Figure 6.4*, *Figure 6.6* & *Figure 6.7*). In contrast, the plate convergence-driven FTBs are typified by thick pre-kinematic

sequences (2-7 km) with very thin (<0.5 km) and slightly deformed syn-kinematic sequences across the system (*Figure 6.8* & *Figure 6.9*). We conclude that the thickening is attained by deposition of the syn-kinematic sequence in the gravity-driven system whereas it is attained by shortening and thrust repetition in the plate convergence-driven system (*Table 6-2*).

6.4.2 Resupply and renewal of energy, and the link to deposition

A system whose energy supply is not recharged will ultimately slow down and stop. Gravity-driven systems can arise on slopes without energy resupply, but as they move, they use up the energy, and so will slow down and ultimately stop. Furthermore, by Le Chatelier's Principle, movement of any dynamic system that is close to equilibrium tends to change the system in such a way as to oppose movement. For example, in a gravity-driven linked system, movement of material deepens the upslope extensional area and shallows the downslope contractional area (*Figure 6.4*), thus decreasing the overall slope (Rowan et al., 2004). In order for a system to continue for long periods of time, and to accumulate large lateral displacements, the energy supply needs to be recharged. Energy recharge within gravity-driven systems can be any process that adds new (sedimentary) material which has PE by virtue of its position, or any process which increases the PE of the existing material. In natural gravity-driven systems, this recharge most commonly occurs by addition of new sediment in the updip part of the slope, such as observed thick syn-kinematic deposits in the half graben basins created by extensional fault growth (e.g., *Figure 6.4*, *Figure 6.6* & *Figure 6.7*). However, relative tectonic uplift of the updip/upslope part of the system (e.g., by basement faulting or regional tilting) can also increase the PE of the system, e.g., the gravity potential energy between the uplifting mountains and lowlands in New Guinea, Southern New Zealand and Himalaya-Tibet (Copley et al., 2009; Copley et al., 2011).

Consequently, there is a common genetic linkage between the development of large scale gravity-driven systems and major sediment input. The locations of gravity-driven systems tend to be linked to major sedimentary systems in particular major river deltas (e.g., the Niger, Mississippi, Orange rivers), and the timing of major episodes of movement are probably linked to major episodes of sediment input. Thus there is commonly a hard-wired genetic link between deformation and sedimentation in gravity-driven systems.

In a system driven by plate convergence, the energy enters the system by movement of a boundary upon which a force is acting. The energy is consumed by deformation, by processes such as the raising up of sedimentary material within the orogenic wedge. The energy is resupplied by ongoing plate convergence and further movement of the boundary. This will occur regardless of whether there is a major sediment input, or whether the margin is sediment starved and is purely reliant on maintenance of the convergence between the plates. The addition of sediment (i.e., the syn-kinematic sequence) to such a system will modify the response of the system, and change the structural style. For instance, previous studies indicate that high syn-tectonic sedimentation widens a plate convergence driven FTB, reduces the number of imbricate thrusts and the taper angle, and inhibits the fault activity (Storti and McClay, 1995b; Wu and McClay, 2011; Buiter, 2012; Fillon et al., 2012; Wang et al., 2013). The addition of sediment seaward of the deformation front fills the basin of proto-thrust and supplies the sediment to be accreted, thrusted and folded in the form of the pre-kinematic sequence (e.g., *Figure 6.10*). But it is not a necessary component to power the system, which is demonstrated by the significant deformation, but very thin syn-kinematic sequence <0.5 km in the Nankai, and Hikurangi accretionary prisms (*Figure 6.8* & *Figure 6.9*). The thickness of the incoming sedimentary section at a subduction zone does however have a major control on the scale and extent of the FTB. The largest sedimentary sections exist where submarine fan systems are being accreted, e.g., Indus (Makran), Bengal (Sumatra-Myanmar), and width and thickness of the FTB is clearly linked to thickness of the input sequence (e.g., Smith et al., 2012; McNeill and Henstock, 2014).

6.4.3 Structural styles

6.4.3.1 Normal faults

In the gravity-driven system, listric normal faults tend to dominate, often soling out deeply into the primary detachment, whereas planar normal faults are in the minority and are often rootless, dying out above the detachment (*Figure 6.3* & *Figure 6.10*). In terms of fault dip direction, the regional (seaward-dipping) normal faults dominate over any landward-dipping normal faults in the extensional domain. Regarding strain localization in the extensional domain, the listric normal faults dominate strain accommodation with respect to planar normal faults, as demonstrated by the significant

displacement of listric normal faults (up to 14 km) and negligible displacement (less than 0.3 km) of planar normal faults in the Orange basin, Para-Maranhao Basin, Amazon Fan and Niger delta (*Figure 6.3*, *Figure 6.4*, *Figure 6.6* & *Figure 6.7*).

This observation is also applicable to the hybrid deformational system examples presented here (NW Borneo and Makran). For NW Borneo, gravitational failure is interpreted as dominant whereas for the Makran, gravitational failure is interpreted as a minor driver of fold-thrust belt development. For the purely plate-convergence driven (accretionary) systems examined here (Nankai, Hikurangi) and elsewhere, there is no evidence for major normal faulting, although minor extension is sometimes associated with anticlinal crestal flexure or collapse. We note however that erosional convergent margins, often controlled by subducting basement topography, commonly include significant extensional fault systems and associated subsidence (e.g., Costa Rica, e.g., Ranero and von Huene (2000)).

6.4.3.2 Thrust faults and related folds

The thrust faults in the contractional domain of the example fold-thrust belts in this study are predominantly basinward- or seaward-verging imbricate thrusts detached onto a basal detachment (*Figure 6.3* & *Figure 6.10*). Several major thrust faults in the Hikurangi accretionary prism are not detached (*Figure 6.9*), but this may be a function of seismic resolution, i.e. unresolved structures at depth. Backthrusts are only observed in the purely or predominantly plate-convergence driven fold-thrust belts, such as Nankai, Hikurangi and Makran (*Figure 6.8*, *Figure 6.9* & *Figure 6.10*). These faults typically arise in the hanging wall of imbricate thrusts as secondary conjugate structures with minor displacement. Back rotation of thrusts is also only observed at the rear of the plate convergence-driven or dominated system such as Nankai, Hikurangi and Makran (*Figure 6.8*, *Figure 6.9* & *Figure 6.10*, *Table 6-2*). However, both backthrusts and back rotation are absent from the purely or predominantly gravity-driven systems (*Table 6-1Table 6-2*).

Rowan et al. (2004) suggest the fold structural style in FTBs is independent of the driving mechanism, and is largely dependent on the nature of detachment. However, the folds in these systems detached, many of which may be controlled by overpressured shale and mudstone, are dominated by fault-propagation folds (*Figure 6.3* & *Figure 6.12*, *Table 6-1*). This contradicts the statement of Rowan et al. (2004) that symmetric, low-relief

detachment folds most commonly arise above a weak basal detachment, i.e. salt, overpressured shale, and asymmetric folds, basinward-vergent imbricate thrusts are mostly developed above a strong basal detachment.

The basal detachment typically dips gently seaward in the gravity-driven system but dips landward/towards the hinterland in the plate convergence-driven system (*Table 6-1Table 6-2*). The presence of a seaward-dipping surface slope supplies the gravitational potential energy for the gravity-driven system, which leads to the formation of a seaward-dipping basal detachment. In contrast, the plate convergence-driven system is part of a subduction zone where the plate boundary (basal detachment) naturally dips landward.

6.4.3.3 Strain distribution

In a gravity-driven system, the upslope extensional strain is larger than the downslope contractional strain and decreases from deep to shallow levels, such as 3.0-14.4 km (extension) vs 0.2-4.2 km (contraction) in the Para-Maranhao basin and 4.8-18.5 km (extension) vs 0.9-14.0 km (contraction) in the Amazon system (*Figure 6.5* & *Figure 6.6*). We attribute this apparent difference to lateral compaction (Butler and Paton, 2010), layer-parallel shortening (Koyi et al., 2004), and sub-seismic deformation. In the hybrid Makran system, the much reduced extension (heave only) of 0.5-3.8 km is significantly less than the contraction (heave only) of 0.4-33.2 km (*Figure 6.11*), which demonstrates the dominant driving mechanism of plate convergence on FTB deformation. In the Sabah portion of the hybrid NW Borneo FTB (some 50-100 km NE of this study area), previous authors Hess et al. (20099, 2010a) reported a net shortening (0-4 km) relative to extension for the most recent time period (Late Pliocene-Holocene), while in the Brunei portion (this study area), King et al. (2010a) reported 2 km net shortening relative to extension for the last 0.5 Ma, attributed to regional plate convergence. We therefore suggest that quantification of extensional and contractional strain in a system can help to determine the driver of the system.

6.4.4 Deformation initiation and propagation

In general, a piggyback deformation sequence is observed in each FTB system regardless of driver, where deformation initiates adjacent to the upslope extensional region for a gravity-driven system, or in the hinterland/rear of the FTB in a purely plate convergence-

driven system, and progressively propagates basinward through time (*Figure 6.3* & *Figure 6.12*, *Table 6-1*). For those systems with a poorly resolved syn-kinematic stage (i.e., we use one syn-kinematic/growth unit throughout), such as the Orange basin, Niger delta and Nankai prism (*Figure 6.3*, *Figure 6.7* & *Figure 6.8*), previous studies (e.g., Morley, 2003; Corredor et al., 2005) and this study suggest that the sequence of thrusting tends to young offshore, but there are instances of out-of-sequence thrusting, synchronous deformation or break-back sequences on a number of thrusts and folds

In the gravity-related system (including the hybrid system), deformation initiates in the extensional domain in the form of normal faulting, followed rapidly by the formation of thrust faults in the contractional domain, showing the genetic link between extension and contraction. For instance, Growth I in the Makran prism, offshore Iran (*Figure 6.10*), and Growth sequence I in the Para-Maranhao basin, offshore Brazil (*Figure 6.4*), represent both the extension and contraction domains. In the system driven purely by gravitational failure, extensional deformation is controlled by major listric faults soling out deeply into the detachment that continue to grow until the system runs out of energy and ultimately stops (*Figure 6.3, Figure 6.4, Figure 6.6 & Figure 6.7*). During this process, a range of minor, short-lived normal faults initiate in and deform the hanging wall basin created by the growing major listric fault, and a portion of deformation migrates to these small faults (e.g., Para-Maranhao basin, Amazon Fan, Niger Delta, *Figure 6.4*, *Figure 6.6* & *Figure 6.7*). There is no consistent direction for minor deformation to propagate within the extensional part of the system; it can be either basinward or landward. In the contractional domain of a gravity-driven system, deformation initiates across a wide zone of synchronous thrust faults (e.g., Para-Maranhao basin and Niger delta, *Figure 6.4* & *Figure 6.7*) that form contemporaneously with the initial growth of the major listric fault. The subsequent deformation tends to become localized on a few continuously growing thrust faults either at the rear (e.g., Amazon Fan, *Figure 6.6*) or in the middle of the contractional domain (e.g., Niger Delta, *Figure 6.7*).

In summary, despite observed differences between individual examples, a few characteristics appear to be universal in the gravity-driven system: deformation propagates from extension to contraction but rapidly after extensional deformation initiates; deformation in the extensional domain is typically dominated by one or more major listric faults; deformation in the contractional domain initiates synchronously on

multiple thrust faults; following initiation, deformation localizes onto a few major structures within each domain with a small portion of deformation then accommodated across small and short-lived faults.

These observations made for the purely gravitational system are also applicable to the system driven mainly or partly by gravity, e.g., NW Borneo. The interpreted syn-kinematic sequence allows differentiation of the two driving mechanisms in this example, showing that pre-Pleistocene deformation includes activity on both extensional and contractional structures (interpreted as driven by gravity) but Pleistocene-Holocene deformation is entirely contractional and extensional faults are inactive, resulting from convergence only. In the Makran prism, early activity of the gravity-driven extensional structures (Growth I sequence, *Figure 6.10*) drive the formation of the earliest thrusts at the rear of the contractional domain, followed by Growth II-IV sequences with extensional inactivity and the primary driver of contraction interpreted as plate convergence, continuing to the present day.

6.4.5 Rates of movement

The rate of movement in the FTBs driven by plate motion is governed by the absolute and relative motions of the plates. Although there will probably be local and short term variations in the rate of shortening within the system, and longer term plate convergence rates can change, the rate is constant and continuous on a relatively long time scale. In contrast, within a gravity-driven system there is no extrinsic constraint on the rate of movement. Rates of shortening are generally very slow in gravity driven FTBs, such as 1.4-2.0 mm/yr in the Niger delta, 2.3-3.6 mm/yr in the Orange basin and 0.8 mm/yr in the Para-Maranhao basin (Cruciani et al., 2017), whereas rates of convergence are much higher at plate convergent systems, such as 3.7-4.2 cm/yr in the Makran (DeMets et al., 1990) and 1.9-6.1 cm/yr in Hikurangi (Wallace et al., 2009) (*Table 6-2*). It is also possible for gravity-driven movement to be much faster and even catastrophic and highly variable. This is because sediment flux to the margin via deltaic systems can change significantly in response to regional climate change and surface processes or change in morphological structure of the delta system (e.g., lobe switching).

The entire crust/lithosphere is involved in plate-convergence driven systems, even though the frontal portions (often the entire FTB being examined here) are typically thin-skinned.

Moreover, both the total amount of shortening and the deformation rates are usually substantially higher than in gravity-driven FTBs. The rate of shortening across plate-convergence driven FTBs is continuous on a long time scale and very high in magnitude (e.g. 1.9-6.1 cm/yr in Hikurangi, 3.7-4.6 cm/yr in Makran), being of one to two orders of magnitude higher than those of the gravity-driven system (see also Rowan et al., 2004).

6.4.6 Limiting factors

In a system driven by gravity, the stress field acting on the sediment is primarily a function of surface relief. Movement is resisted by the strength of the sediments and therefore sediment strength is also a factor, in particular strength of the detachment/décollement. Many of the detachments in this study are interpreted to be dominated by overpressured shale or mudstone or have evidence for high pore fluid pressure/porosity based on seismic properties (*Table 6-1*), resulting in a relatively weak detachment. If the stress applied is reduced, the strength increases, or the geometry changes in such a way as to increase the resistance, movement would slow. If the resistance increases to the point that the stress is insufficient to move the sediment, movement will cease. Unless the geometry is changed in such a way as to increase the stress (through sediment deposition) (*Table 6-2*), or weaken the detachment, the system will remain frozen. Thus the critical limiting factors are (1) stress and (2) strength of the detachment.

In a plate convergence-driven system, movement is also resisted by the strength of the sediments/detachment (*Table 6-2*). So if the geometry or material properties change in such a way that the stress is insufficient to move the sediments, the system will temporarily stop. However, the plates continue moving and the boundary of the FTB (detachment/décollement) continues moving at a rate determined by the plate convergence rate. In a locked system this results in the stress increasing and the stress will increase until the system breaks and the sediments once again move. We note that on a much shorter timescale, i.e., within the earthquake cycle of 100's years, stress applied does change through time. The impact of this effect on the Coulomb taper and stress regime within the forearc has been analysed by Wang and Hu (2006). However, on the scale of the seismic data and time periods involved in this study, these effects will not be observed. Thus the plate-driven system is not limited by the strength of the materials

involved in the FTB; the ultimate limiting factor is the rate at which the plate is fed into the FTB. On a large scale, the plate motion rate is effectively constant, and the plates will continue moving at the same speed over a long timescale. But the overall geometry and structure of the FTB will be affected by the properties of the internal and basal materials.

Table 6-2 The characteristics of the fold-thrust belts relative to system/driving mechanism.

Parameter	**Systems**		
	Gravity	**Plate convergence**	**Hybrid**
Energy	Gravitational potential energy (PE) contained within the deforming sediment pile itself	Gravitational PE within the crust/lithosphere outside the local deforming sediment pile	Both (either can dominate in a specific system and may change through time)
Surface slope	1-4 °	1-6°	1-2°
Dominant process of thickening	Deposition	Strain (shortening and thrust repetition)	Both (either can dominate in a specific system)
Control on state of stress	Surface slope (controlled by depositional processes)	Tectonic shortening rate, strength of décollement	Both (either can dominate in a specific system)
Detachment dip direction	Varies; most gently basinward, some landward	Landward	Seaward in gravity-dominated system and landward in plate convergence-dominated system
Net contraction	Low	High	Low in gravity-dominated system and high in plate convergence-dominated system
Fault vergence	Seaward	Seaward dominant, landward also observed	Dominant seaward Very few landward
Back thrusts	No	A few	No in gravity-dominated system and a few in the plate convergence-dominated system
Back rotation of thrusts	No	Some degree	No in gravity-dominated system and

			some degree in the plate convergence-dominated system
Strain localization	Major listric faults and imbricate thrusts	Imbricate thrusts	Both major listric faults and imbricate thrusts
History	Extension quickly leads to contraction. Forward propagation of thrust activation. Activity across wide zone of fold-thrust belt (sometimes focused in the rear-middle region) but not focused at the toe.	Contraction only. Forward propagation of thrust activation. Activity typically focused at the toe or across much of the fold-thrust belt.	Forward propagation of thrust activation. Activity can be focused at the toe or across much of the fold-thrust belt.
Overall shortening rate	Low (0.8-5mm/yr), pulsed	High (1.9-6.1 cm/yr), constant	Low in gravity-dominated system and high in the plate convergence-dominated system

6.5 **Conclusions**

This study examines the geometry, structure and tectonic history of submarine fold-thrust belts induced by plate convergence, gravitational failure and a combined mechanism (hybrid system). The new results indicate the following:

1) The energy source in gravity-driven systems is within the sediment pile itself which is deformed to create upslope extension and downslope contraction, while in plate convergence driven systems, it is the movement of stressed lithospheric scale-boundary, which lies outside the local sediment pile.
2) As a consequence, a prominent difference between the two systems is that the syn-kinematic sediments are thick (up to 6-7 km) and highly deformed (extensional faulting) in the gravity-driven system (*Figure 6.3*, *Figure 6.4*, *Figure 6.6*, *Figure 6.7*), whereas they are thin (<0.5 km) and only slightly deformed (minor folding) in the plate-motion driven system (*Figure 6.8* & *Figure 6.9*). The thickening is attained by deposition (of the syn-kinematic sequence) in the gravity-driven system, whereas it is attained by shortening and stratigraphic repetition by thrusting in the plate convergence-driven system (*Table 6-2*).

3) The energy in gravity-driven systems is resupplied by sediment inputs from large river deltas (Niger, Mississippi, Orange rivers, etc), and the timing of major episodes of movement is probably linked to major episodes of sediment input. In a system driven by plate convergence, the energy is resupplied by movement of the plates and the plate boundary, which will occur regardless of sediment input.
4) The thrust faults of both systems are predominantly basinward/seaward-verging imbricate thrusts detached onto a basal detachment. Backthrusts and back rotation appear to only be observed in the purely or predominantly plate convergence-driven fold-thrust belts, (*Table 6-1 Table 6-2*). The anticlinal folds in both systems are dominated by asymmetric fault-propagation folds (*Figure 6.3* & *Figure 6.12*, *Table 6-1*) and many of the detachments appear to be weak and/or controlled by overpressured shale. This contrasts with the interpretation of Rowan et al. (2004) that asymmetric folds, and basinward vergent imbricate thrusts develop above a strong basal detachment.
5) In gravity-driven systems, deformation in the extensional domain initiates on a small number of major listric faults and then becomes more distributed across multiple normal faults. In the contractional domain, for both driving mechanisms the fold-thrust belt propagates forward with new thrust initiation at the toe. However, fault activity differs slightly between the two systems. Focused activity at the toe of the FTB is more common for plate-driven systems but not observed in gravity-driven systems. Activity across much of the FTB is observed for both systems, but activity focused in the rear to middle of the FTB is only observed in gravity-driven FTB systems.
6) The rate of shortening across plate convergence-driven fold-thrust belts is very high (e.g. 1.9-6.1 cm/yr in Hikurangi, 3.7-4.6 cm/yr in the Makran), and generally continuous on a long time scale. In contrast, within a gravity-driven system, the rate of shortening across the contractional domain is very slow (e.g., 1.4-2.0 mm/yr in the Niger delta, 2.3-3.6 mm/yr in Orange basin and 0.8 mm/yr in the Para-Maranhao basin) and more variable through time.
7) In a system driven by gravity, the movement is resisted by the strength of the sediments and detachment. Thus the critical limiting factors are stress and strength of the sediments/detachment. A plate-driven system is primarily limited by plate motion rate i.e, the rate at which the plate is fed into the FTB.

Chapter 7 Conclusions

This thesis investigated the dynamics of fold-thrust belts from individual structures, i.e., faults and folds, to the entire system, i.e., wedge topography, cross-sectional area, and basal properties by using and analysing numerical models and natural examples in great detail. This leads to the following conclusions of several key aspects of the fold-thrust belt system.

7.1 The kinematics of a fold-thrust belt

The kinematics of a fold-thrust belt is investigated with a set of numerical models. A thrust belt system is typically composed of three distinct regions: the thrust wedge (main deformation zone), pre-wedge (incipient folding), and an undeformed region. We find that the thrust wedge grows episodically and cyclically (see also Byrne and Fisher, 1987; Gutscher et al., 1996, 1998; Fitz-Diaz et al., 2004; Ji et al., 2008; Ruh et al., 2012). A cycle of wedge building starts as frontal accretion occurs, which is accompanied by a rapid increase in wedge width, reducing the taper angle below critical. In response to this, the wedge interior rapidly propagates forwards into a region of incipient folding (see also Wu and McClay, 2011), while the taper angle progressively increases to a constant apparent critical value (~10°). The significant shortening of the wedge occurs immediately after a new thrust initiates at the failure front, leading to a decrease in wedge width. Successive widening of the wedge and subsequent shortening and thrusting maintain a reasonably constant taper angle. Therefore, the fold-thrust belt evolves cyclically, through a combination of rapid advancement of the wedge and subsequent gradual, slow wedge growth. The new model results also highlight that there is clear, although minor, deformation (0-10 m horizontal displacement) in front of the thrust wedge, not observed or highlighted before. Without this discrete deformation, the system is not able to proceed forward.

7.2 Fault activity and interaction in an evolving fold-thrust belt

In a growing fold-thrust belt, the activity of individual faults and their interactions are investigated using 2D finite element models by tracking the evolution of fault displacement (see also Koyi et al., 2000; Sun et al., 2016), slip rate (e.g., Cowie et al.,

2012, Bergen et al., 2017) and fault dip. Our new results highlight two distinct stages of individual fault evolution: 1) rapid growth with significantly increased displacement and high strain rate after initiation, 2) subsequent slow but continued growth with slowly accumulated displacement and low strain rate. When a thrust wedge advances, existing thrusts are reactivated to facilitate this process (Nieuwland et al., 2000; Yamada et al., 2006), which is quantitatively highlighted here by strain rate along the existing faults, but not highlighted or observed before. As a new thrust initiates at the wedge front, the entire wedge is subjected to shortening and thickening to obtain a critical taper, accompanied by significant activity of the frontal thrust and minor or negligible activity of the early-formed thrusts. Short-cut faults have been recognized in some areas where inversion tectonics develops (Underhill and Paterson, 1998; Mora and Parra, 2008). They have been interpreted to generally form with a shallow dip in the footwall of a high-angle inverted fault, produced by reactivation of earlier listric normal faults. In our results, short-cut faults are observed to develop with a shallow dip (~11°) between two imbricate thrusts, and slip on the short-cut fault is found to accommodate a component of shortening, changing the displacement pattern along an individual fault (i.e. up-dip decrease in displacement beyond where the short-cut fault merges). Across the thrusts of the wedge, a single major fault plays a key role in accommodating strain, with total displacement ~3-4 times that of the other imbricate thrusts. Fault dip progressively changes through time, with three distinct stages: (1) initial decrease to the Mohr-Coulomb angle due to rotation of maximum compressional stress σ_1, (2) subsequent increase, (3) final stabilisation as distance from the deformation front increases with time.

7.3 Restoring a fold-thrust belt

The conventional area balancing method has long been used to predict detachment depth, construct subsurface structure and quantify tectonic shortening of a geological cross-section. This method generally produces an apparent rectangle for a restored cross-section with presumed planar, parallel, and usually horizontal regional slope and basal detachment (e.g., Chamberlin, 1910; Dahlstrom 1969; Hossack, 1979; Mitra and Namson, 1989; Butler, 2013; Schori et al., 2015; Hubbard et al., 2016). However, most fold-thrust belts exhibit a wedge or trapezium shape in cross-section, thinning towards the basin (e.g. Chapple, 1978; Davies et al., 1983). Although the initial regional slope of a stratigraphic

layer is difficult to determine, it is unlikely to be parallel to the basal detachment fault, questioning the validity of many existing restorations. Here we developed two new, simple solutions to quantitatively restore a fold-thrust belt, exploring the role of regional slope in the shortening estimate. The results derived from the application of model solutions to sandbox models and natural fold-thrust belts from the Hikurangi accretionary prism and the NW Borneo margin fold-thrust belt highlights that the regional slope is indeed significant in area balancing restoration: a higher regional dip results in reduced shortening while a lower regional dip leads to increased shortening. Accuracy of the shortening estimate requires independent constraint of parameters, particularly an accurate measure of the initial regional slope, rather than greater precision in their measurement. Hence, we find that absolute values of shortening are probably not attainable in most thrust belts, but their accuracy can be improved using this new method.

The new methods can generate more accurate measures of shortening and are generally applicable, since they are concerned mainly with the gross cross-sectional area of the system, rather than the details of the lithology, rheology, fluid pressure or other factors that control the form and detailed expression of the final structure.

7.4 The tectonics of the NW Borneo fold-thrust belt

In Chapter 5, we investigated the origin, geometry, and structural development of the NW Borneo slope fold-thrust belt (Brunei sector) using high-resolution 3D seismic data. Our new results highlight the presence of three different types of anticlinal fold and their relative dominance, evolution and variation along and across the FTB: fault-propagation folds (dominant); detachment folds (minor); and fault-bend folds (only one example). This contrasts markedly with many continental FTBs, where fault bend folding is assumed to predominate. For each individual fold, the structural style varies significantly along strike, which we interpret to reflect lateral changes in the magnitude of folding, the basal décollement strength, and inherited pre-existing structure (carbonate platforms generating topography). Thrust faults appear to initiate at depth and propagate up-dip as demonstrated by up-dip decreasing displacement. Fault dip is closely related to structural maturity with fault dip increasing as the fault and fold matures. Fault spacing responds to

basement topography and this topography also blocks forward propagation of the fold-thrust belt.

In terms of strain localization, we find that thrusting plays a primary role over folding in strain accommodation. By using the bed-length measurement and refined area-balancing solution, we highlight that bed length does not remain constant during deformation and bed-length method cannot accurately quantify deformation. The low taper angle of the NBFB (mostly <6°) implies a high basal fluid pressure (>0.7 of lithostatic pressure), which can be interpreted to result from rapid burial, disequilibrium loading, in situ generation of hydrocarbons, and fluids, including hydrocarbons, driven laterally from the shelf seaward following an oceanward lateral decrease in lithostatic pressure. From evidence of two distinct stages of fault and fold activity, distribution of present-day contractional deformation across the entire NBFB rather than at the toe, and the present-day extensional inactivity but contractional activity, we conclude that the NBFB results from a combination of primary gravitational tectonics and secondary crustal shortening driven by plate convergence, with the latter dominating currently.

7.5 Comparison of fold-thrust belts induced by plate convergence and gravitational failure

Chapter 6 investigated the similarities and difference between fold-thrust belt driven by plate convergence and gravitational failure. The new results suggest (1) the energy source in gravity driven systems is within the sediment material itself that is being deformed to create the slope extension and downdip contraction, while it is the movement of lithospheric-scale boundaries in the plate-convergence driven systems, which lies outside the local sediment pile; (2) it is resupplied by sediment input from large river deltas and deformation tends to be episodic linked to the episodes of sediment input in gravity drive system whereas by movement of a boundary upon which force is acting in plate-convergence driven system; (3) the thrust faults of both systems are predominantly basinward-verging thrust faults. Backthrusts and back rotation appear to only be observed in the purely or predominantly plate-convergence driven systems; (4) the rate of shortening across plate-convergence driven system is high, and generally continuous on a long time scale. Whereas across the contractional domain of gravity-driven system, it is very slow and more variable through time; (5) the plate-driven system is limited by

plate motion rate, i.e. the rate at which the plate is fed into the FTB, whereas the gravity-driven system is resisted by the strength of the sediments and detachment.

7.6 The relevance of the numerical model to real-world examples and its limitations

Although numerical modelling is a robust tool to investigate the long-term structural behaviour and the influences of rock rheologies on the tectonic evolution of fold-thrust belts (e.g., Buiter, 2012; Ruh, 2013; Buiter et al., 2016), a few limitations appear to be universal in its applications. For instance, boundary conditions are generally simplified in numerical models to resemble that of a natural system. In crustal-scale compressional numerical experiments, shortening is mostly modelled by inward movement of a mobile wall (or a backstop) into the deformable material domain, with push-type experiments (e.g., Burbidge and Braun, 2002; Simpson, 2009; Cruz et al., 2010; Yang et al., 2017), or by dragging the material towards the backstop, with conveyor-type (pull type) experiments (e.g., Stockmal, 2007; Ruh et al., 2012; Ruh et al., 2013). In most models, the backstop is defined with ultra-strong material properties that act as the boundary of deformation and remain undeformed during the experiment. There is a striking rheology contrast between the deforming material domain and the backstop. However, a natural system does not generally include a distinct boundary, and generally has a gradual transition of rock properties across the foreland fold thrust belt and the hinterland. Numerical modelling captures the first-order boundary conditions and rock mechanics that exist in natural systems, but not the exact scenarios. Further, some essential processes operate to accommodate a significant portion of strain in natural systems, but are not implemented in numerical experiments, such as lateral compaction, layer-parallel strain, and gravity loading accompanied by porosity reduction (Koyi et al., 2004; Butler and Paton, 2010; Şengör and Bozkurt, 2013; Lathrop and Burberry, 2017). In addition, most numerical models are built on equations for conservation of mass assuming incompressibility (i.e., sediment compaction is neglected) (Ruh, 2013).

There are also resolution differences between numerical experiments and geological observations. Numerical modelling enables us to visualize the structural behaviour of discrete faults in unprecedented detail, but part of this detailed information is difficult to validate by geological investigation. For example, the strain rate of a shear band derived

from numerical modelling allows the systemic examination of its change through time (e.g., Cowie et al., 2012, see also chapter 3). However, the slip rate of a natural fault can be determined over a certain period of time dependent on the method used, e.g., over decades (i.e., GPS observation) to a million years or even longer (i.e., geological observation). Slip rate variability is reported in some field-based studies (e.g., Gunderson et al., 2013; Bergen et al., 2017), but often a complete set of observations over a range of timescales is not available and detailed temporal changes within a time period remains unclear. Likewise, geological observation only documents the resultant structures after long-term evolution, i.e., a static view. They therefore cannot easily be compared with the temporal structural deformation available from numerical models. These significant information gaps between numerical models and geological observations require further efforts to narrow in both fields.

7.7 Future work

A few topics essential to the understanding of the tectonics of fold-thrust belts are not fully addressed by this research, and are therefore considered for future study.

7.7.1 Fold systems in a growing fold-thrust belt

Individual folds can be characterised by many attributes such as trend, length, width, amplitude, wavelength, vergence, and strain. The mechanics of individual folds has generally been investigated by previous authors in the form of the Fault-bend fold, Fault-propagation fold (including tri-shear model) and Detachment fold (e.g. Suppe, 1983; Jamison 1987; Suppe & Medwedeff 1990; Mitra 1990; Erslev, 1991; Suppe et al., 2004; Shaw et al., 2005). These models also highlight individual fold growth behaviour by limb rotation and kink-band migration, fold amplification, growth strata deformation, and rates of folding. However, folds typically occur as a system (i.e. a range of multiple folds) that can affect both local and regional geology and folds/faults tend to interact within the system. The fold system as a whole is important because the interconnected folds can provide large reservoirs of trapped resources, such as hydrocarbons and groundwater. Fold growth, propagation, interaction and associated deformation zones are areas of increased shortening, and connectivity, and these factors affect the reservoir and trap potential. Fold systems are also associated with fault networks in a fault-related fold

system. In a region of predominantly buried thrust faults, examination of the fold system may provide insights into the underlying fault networks that are essential for providing pathways for fluid flow allowing migration, entrapment and escape of resources (e.g., Aydin 2000) and can generate important geohazards. In summary, how a fold system works collectively, how individual folds interact, and how fold and fault systems interact within a single fold-thrust belt are processes that remain poorly resolved in favour of study and our understanding of individual structures.

7.7.2 Further 3D analysis and temporo-spatial evolution ("4D") of the Northwest Borneo fold-thrust belt (NBFB)

The analysis of structures from a set of 5-10 km spaced 2D seismic profiles within the 3D volume to examine the along-strike variation of fold style and its controlling factors are likely to have ignored local changes that should be evident in the 3D volume. 3D seismic interpretation has generally only been carried out in the shallow portion of the volume from the offshore Brunei section (<1-2s below seafloor), and the surface maps produced are only used to number the folds, but not to characterize the 3D shape of the fold structures and associated deformation. The structural restoration was performed only using 2D profiles in an attempt to estimate the shortening across the NBFB, which do not include the effects of lateral compaction, tectonic loading, or layer-parallel strain and volume change.

To fully understand the details of the structure of the FTB and how the FTB has evolved through time, further 3D analysis is required, to fill the gaps mentioned above. This involves future work on 3D seismic interpretation (i.e. sedimentary surface mapping, fault plane mapping, strain contouring, and volume calculation), 3D structural restoration (i.e. conserved volume). By implementing age control on the sedimentary layers into the results of 3D seismic interpretation, it should be possible to decipher the temporal and spatial evolution of this system (4D). Several additional parameters may be acquired from such future work: 3D strain distribution, shortening rates, deposition rates, and layer-parallel compaction, and their changes in space and time.

7.7.3 Numerical modelling of the gravity-driven fold-thrust belt

We have shown the insights into the episodic growth of a fold-thrust belt induced purely by plate convergence using numerical solution (Chapters 2 and 3). The numerical model of a gravity-driven fold-thrust belt has not yet been developed or presented. This leads to limits on the understanding of the mechanics of this system, such as stress state, displacement field, strain rate, strain distribution and localization, as well as their temporal and spatial variations, and analysis of differences with the plate-convergence system. Gravity driven fold-thrust belts have been compared with those driven by plate convergence in this thesis (Chapter 6), and this has highlighted significant differences and similarities in geometry, structure and tectonic history between the two. To fully understand their mechanics, numerical modelling is required. For example, numerical modelling of these two systems with the same rock properties, failure criterion, model size and resolution, but different boundary conditions (related to convergence or gravitational failure) allows us to examine their kinematic behaviour and links between mechanism and process in greater detail, such as topography, fault and fold geometry, fault space, displacement, strain distribution and localization, stress field and deformation rates.

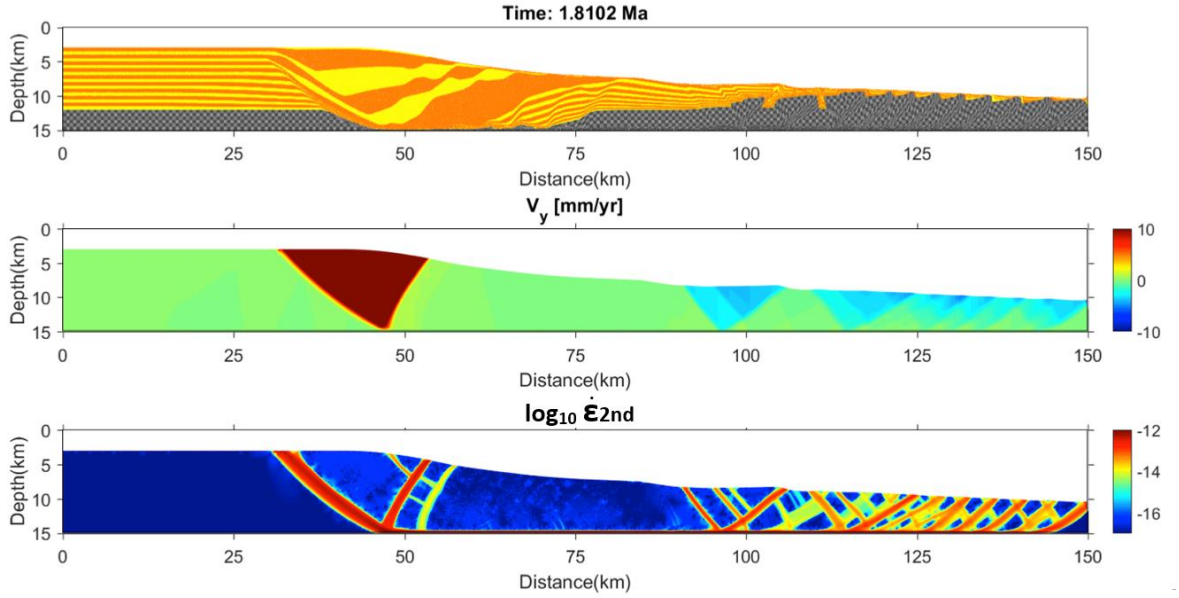

Figure 7.1 Results of numerical modelling of a gravity-driven fold-thrust belt. (a) Resultant extension and contraction coupled deformation system, the yellow and brown represent the syn-kinematic sequence while the grey donates the pre-kinematic sequence. (b) Vertical velocity field across the system, the positive value (towards red in colour bar)

represents downward movement while the negative value (towards blue in colour bar) indicates upward movement. (c) Second invariant of the strain rate tensor across the system, the high value in colour bar corresponds to large strain rate. The deformation is driven by the growth of delta in form of gravitational potential energy, the cell size is 400 m x 300 m, the delta grows by sediment deposition of 0.4 cm/yr and forward propagation of 1 cm/yr, the model here shows the results after 1.8 Myr of evolution. This is the result after 4012 time steps.

In fact, we have begun to develop a simple gravity driven model using the Finite element method (in collaboration with Jonas Ruh) (*Figure 7.1*). In this numerical experiment, the model is initially 150 km long and 15 km thick with the cell size of 400 m X 300 m in rectangle. We implemented a progradational delta with increasing height difference as it propagates forward to generate the gravitational potential energy. The delta grows by sediment deposition of 0.4 cm/yr and forward propagation of 1 cm/yr. The left boundary, right boundary and surface are all of free slip whereas the basement is fixed. There is no external force imposed to the system, the deformation is driven exclusively by gravitational failure on upslope. Initial results highlight the upslope extensional domain, that is typically localised along a few major listric faults and their hanging wall half graben, and that deformation is broadly distributed across a range of discrete thrust faults in the downslope contractional domain. This model is currently built only with a certain range of input parameters, and the mechanical controls on its deformation pattern have yet to be explored. Further work will involve the evaluation of the effects of internal and basal strength, rheology of the sedimentary layers, failure criterion, and surface processes (including sediment input) on the overall fold-thrust belt development and on individual structures.

7.7.4 Final comment

One of the primary aims of this thesis was to use different methods and examples in order to explore the development of fold-thrust belt systems. It is important to combine geological observations made through field investigation and seismic interpretation, with viable and appropriate kinematic models, supported by numerical modelling of the long-term mechanics, in order to more fully understand the evolution of fold-thrust belts such as the NW Borneo and Makran. Field observations can be incorporated into numerical

models to test the role and importance of features or processes, such as fault propagation, distinct stages of fault and associated fold activity, and fold style evolution through time. Many observations made in the gravity-driven systems also require further validations, such as how deposition controls system thickening, the genetic links between extension and contraction in association with sediment flux into a gravity-affected system, and what controls the predominantly synchronous rather than in-sequence development of folds within the fold-thrust belt.

Appendix A Stability and sensitivity test of Finite Element Model built with Abaqus 6.14

1. Model set-up

This numerical experiment was generated to test the stability of the modelled wedge that is initially in the stable field of the critical taper theory when translated horizontally. A brittle wedge with surface slope of 20° is pushed by inward movement of the mobile wall over a horizontal base (β=0°). The width and height of the stable wedge are 3000 m and 1047 m, respectively (Fig. A1). The moving wall is in direct contact with the base, therefore a sharp velocity discontinuity is formed at the left corner (Buiter et al., 2016). This experiment should create a stable wedge maintaining the original shape without internal deformation as predicted by the Coulomb Wedge Model (Davis et al., 1983; Dahlen, 1984).

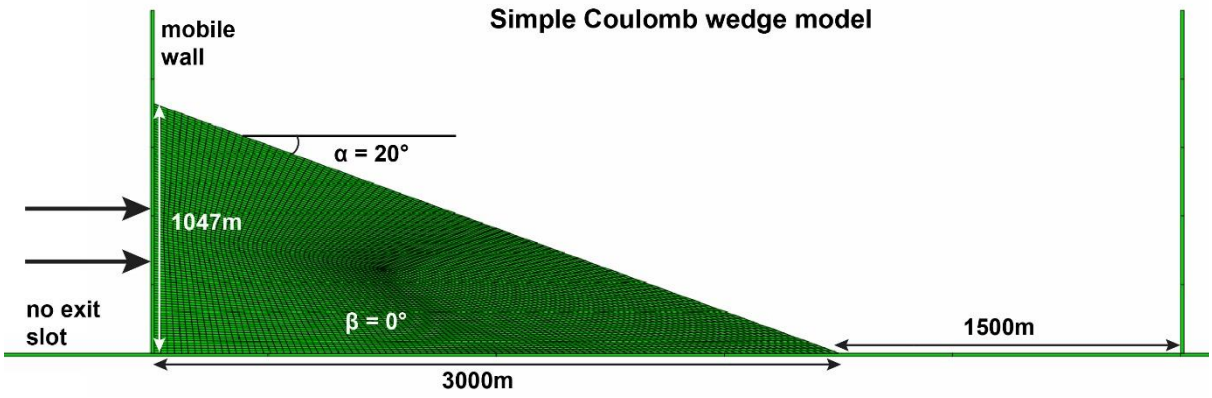

Figure A1 Setup of a simple Coulomb Wedge Model, a wedge of brittle material with a stable slope of 20 ° is pushed by a mobile wall over a horizontal base. The width and height of the stable wedge is 3000 m and 1047 m, respectively.

2. Model results

For a wedge that is translated in a stable field, the analytical solutions for the parameters can be derived to quantify the wedge behaviour. The model results are visualized from their material field, pressure field and strain rate field after 500 m, 1000 m and 1500 m of translation (Fig. A2). As shown in Figure A2a, all the model runs maintain the initial surface

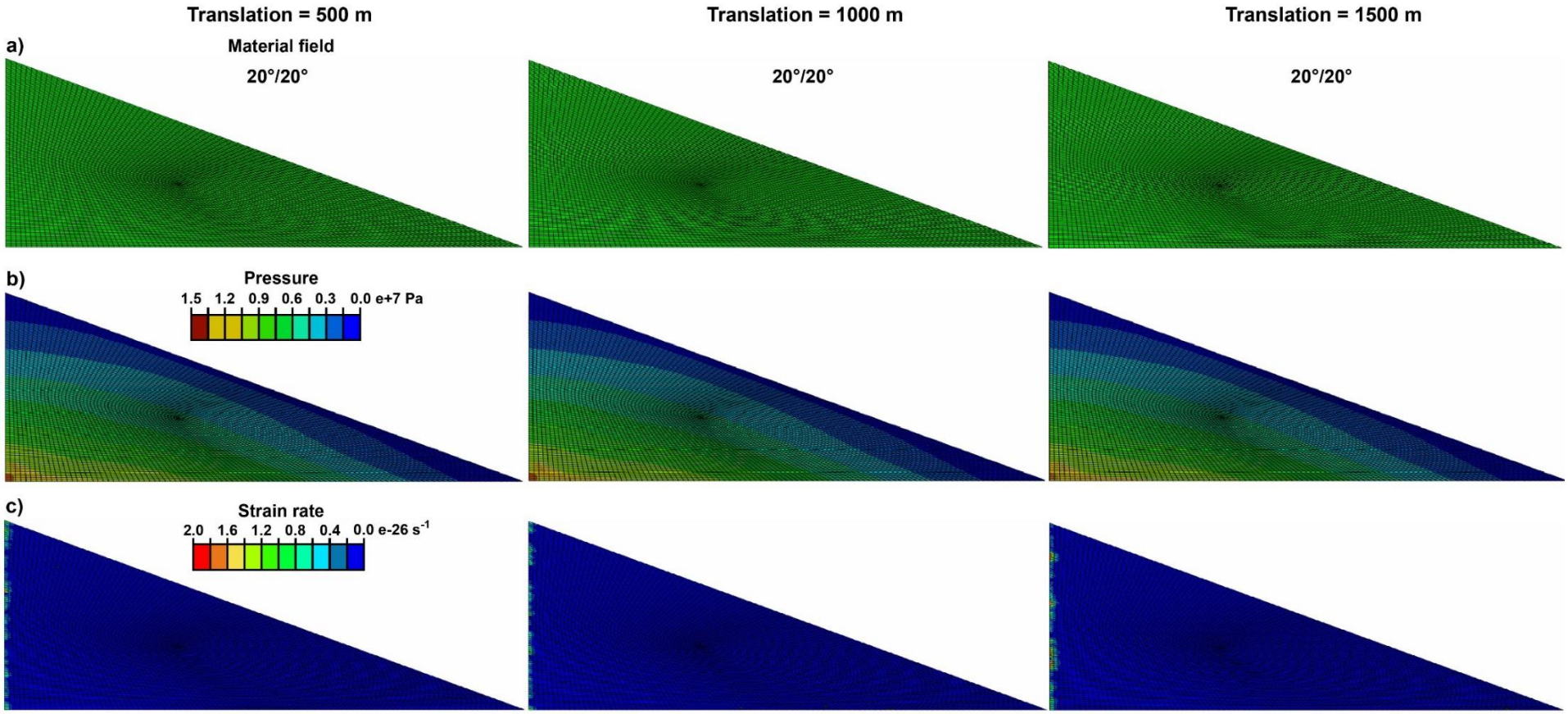

Figure A2 The model results after 500 m, 1000 m and 1500 m of translation. (a) Material fields, the model result is shown with the true resolution. The numbers are the values for surface slope of pre translation and post-translation. (b) Pressure field. (c) Strain rate field.

slope of 20°, and do not show obvious internal deformation, which agrees the theoretical predication of critical taper theory (Davis et al., 1983; Dahlen, 1984). A stable wedge that does not experience external forces apart from gravity is expected to have a lithostatic pressure field (Buiter et al., 2016). The models shows a pressure field approaching lithostatic values after different translations (Fig. A2b). In detail, some minor deformation next to the mobile wall is observed (Fig. A2c) as shown by the displayed strain rate in these areas. As the moving wall proceeds forward, the maximum strain rate typically increases, which is accompanied by expansion of the strain rate distribution along the left boundary of the wedge (Fig. A2c). Similar results are observed by Buiter et al. (2016). None of the experiments produces a shear zone within the wedge interior and simple shear is primarily accommodated by the side friction along the contact between the left wedge boundary and the moving wall. The model results show that Abaqus successfully passes the theoretical test and is able to simulate a compressional Coulomb wedge.

3. Sensitivity tests

One advantage of the numerical technique is that it easily allows parameter values to be varied in order to examine their influence on the solution (Ellis et al., 2004). Here, we carried out some numerical tests to explore the model sensitivity to strain-softening thresholds, material strength, initial wedge thickness and mesh resolution (or cell size).

3.1 Sensitivity to strain softening threshold

Figure A3 shows the resultant deformation after 1000 m of convergence in numerical experiments in which the frictional parameters are changed for comparison. Nominal model is a base case which was chosen as the scenario to analyse in main body of the paper.

In the model shown in Figure A3a, we assume that strain-softening begins at effective strain of 0.5 and ends at effective strain of 1.0 in the nominal case. We then run a suite of models with decreased and increased strain-softening thresholds (Fig. A3b & S3c), the results are qualitatively similar to the nominal case in Fig. A3a despite some difference in structural style and strain partition. A higher strain-softening threshold between strain=1.0 and 2.0 produces narrower shear zones and more diffused deformation at the

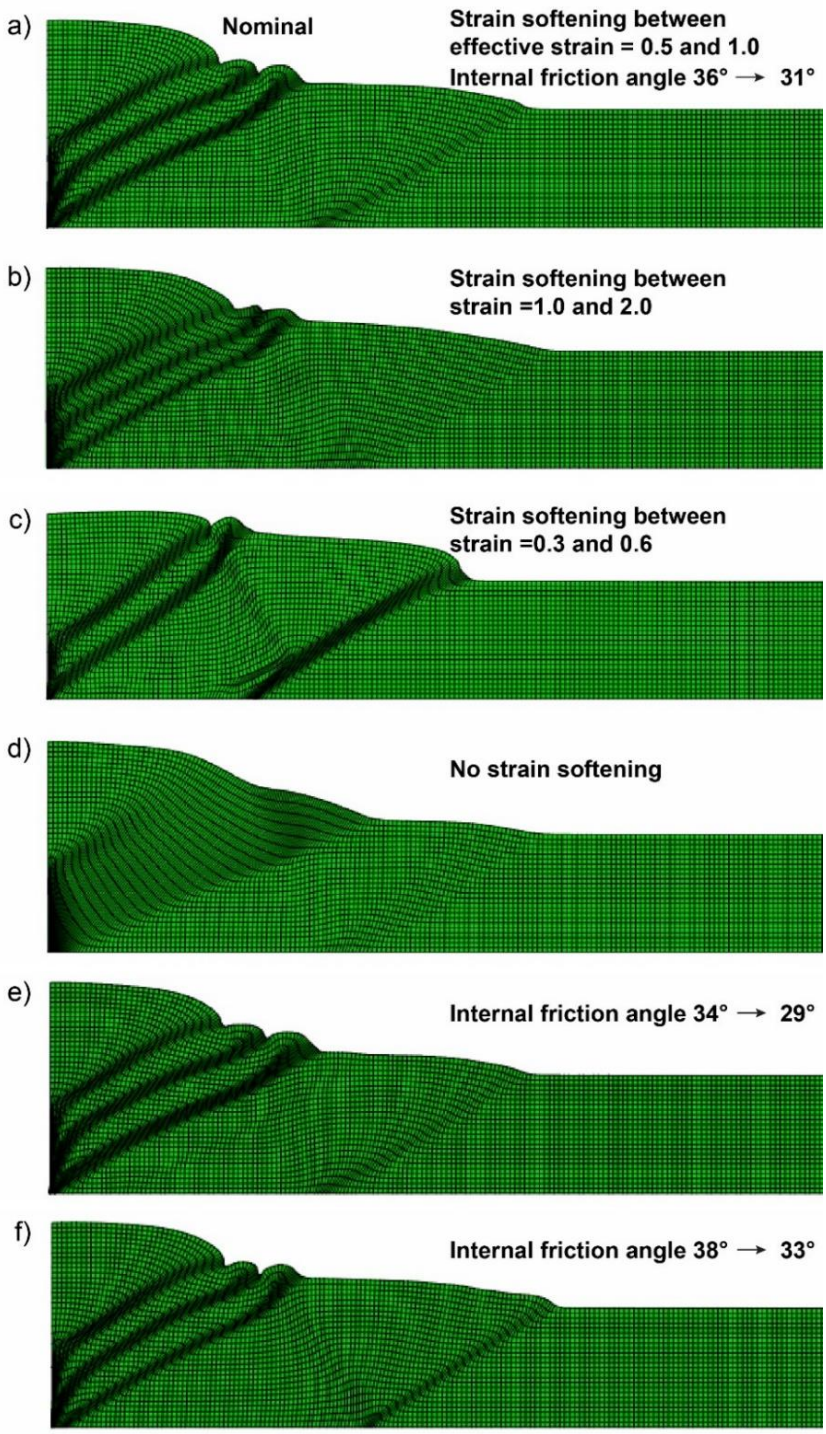

Figure A3 Sensitivity analyses for the numerical frictional experiment. Frames (a)-(f) are shown after 1000m convergence. The "nominal" means this is the base case used in the main set of analysis. The other scenarios represent a suite of tests of model sensitivity to variation in mechanical parameters. (a) Model with strain softening threshold 0.5-1.0 and material strength threshold 36°-31°. (b)Strain softening thresholds at strain = 1.0-2.0. (c)Strain softening thresholds at strain = 0.3-0.6. (d) No strain-softening. (e) Material strength threshold at friction degree 34°-29 °. (e) Material strength threshold at friction degree 38°-33 °.

wedge front (Fig. A3b). For a lower threshold between strain=0.3 and 0.6(Fig. A3c), shear zone width is increased compared with the base case in Figure A3a. The extra softening causes more deformation to be partitioned at the shear zone and the formation of an incipient backward thrust. The model without strain-softening shows extreme diffuse deformation at the first thrust, the mesh is tilted and deformed over a broad region. This is quite unlike the behaviour of the ideal sand in analogues models. This model results indicate that strain softening is not required to develop episodic thrusting and wedge formation, but the thrust style is much irregular (Ellis et al., 2004).

3.2 Sensitivity to internal friction angle

The wedge material of nominal model is defined with peak strength 36° and stable strength 31°. The models with various material strength can produce similar deformation pattern and strain localization compared to the model in Figure A4a. For a lower material strength (34° to 29°), wider shear bands are developed and less strain localizes at the frontal region. For a higher material strength (38°-33°), the model establishes narrower shear zones and more strain localizes at the frontal thrust. It also forms an obvious fold axis which is likely to form a backward thrust with additional convergence. Despite some minor difference of deformation, the overall dynamics are not very different from Figure A4a, indicating than the internal friction angle does not exert a first-order control on the thrust development.

3.3 Sensitivity to cell size

The Figure A4 shows the deformation after 510 m of convergence in numerical experiments. The cell size is 25 m x 25 m at the nominal model, which produces two forward thrusts and an incipient thrust with slight strain localisation (Fig. A4a). The model with finer cell size (15 m X 15 m) produces 3 profound and narrower thrust faults (Fig. A4b). while the model with the coarser mesh (cell size = 35 m X 35 m) produces two forward thrusts with wider shear zones. Due to the wider thrust zone, the deformation is largely accommodated by the two thrusts in coarser mesh model rather than being partitioned into the three narrower thrusts in the finer mesh model. The model results indicate that the mesh resolution plays a key role in determining the width of thrust fault and the number of thrust slices.

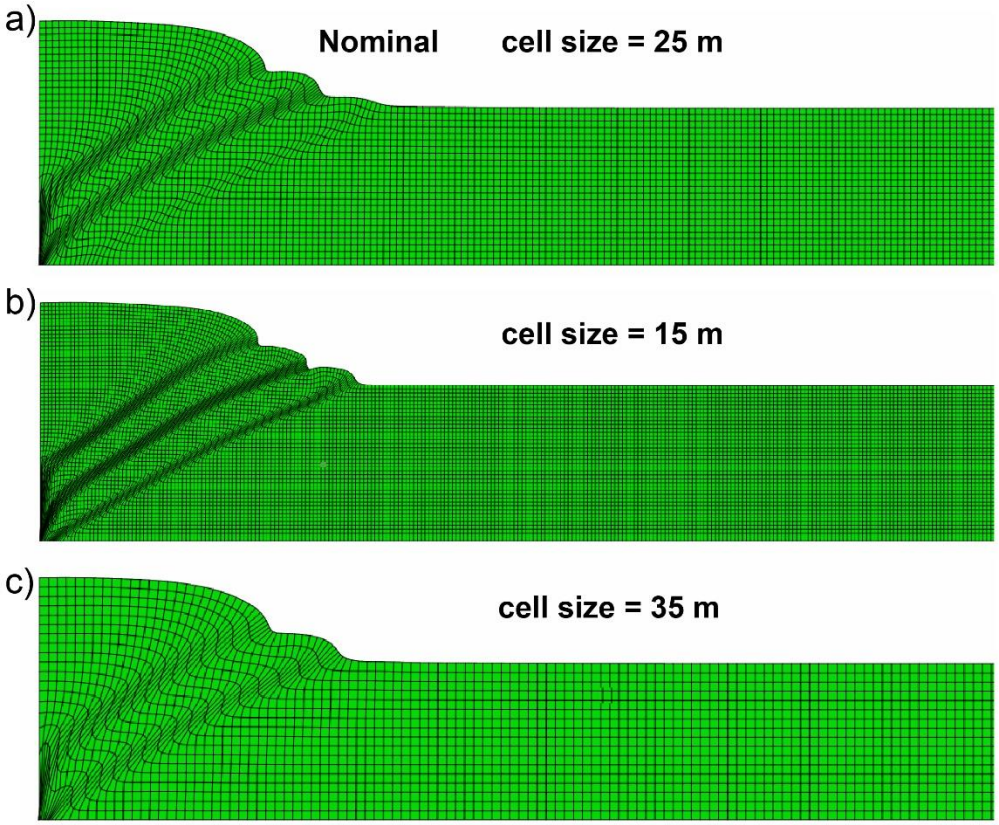

Figure A4 Sensitivity analyses for the numerical frictional experiment. Frames (a)-(f) are shown after 510m convergence. (a) Model with cell size = 25 m. (b) Cell size = 15 m. (c) Cell size = 35 m.

The base case (Nominal) model with cell size 25 m x 25 m gives acceptable simulation and computation run successfully to large displacement. Finer-scale cell size (15 m x 15 m) gives improved fault definition, but computation using this cell size fails after relatively small displacement. Coarser-scale cell size (35 m x 35 m) gives an unacceptable poor definition of the faults.

3.4 Sensitivity to initial model thickness

We run a suit of models with various initial thickness to explore the solution sensitivity to the wedge dimension. The one with 600 m thickness, as a nominal example, produces 3 thrusts next to the mobile wall and some deformation at the frontal region (Fig. A5a). As shown in Figure A5b, an increase in thickness results in wider fault space but not much frontal deformation. In contrast, a decreased thickness leads to narrower fault space and more frontal deformation, which in turn increases the width of the overall thrust belt. The width of thrust zones is comparable to each other, suggesting that thrust zone width is least controlled by wedge thickness. Three thrusts are developed next to the moving wall

in Figure A5a and A5b whereas the thinnest model (Figure A5c) only produces two forward thrusts next to the moving wall, and a thrust further forward and further away from the moving wall and some frontal diffuse deformation, leading to an increase in the width of the entire wedge. This suggests that the thin model tends to propagate forward instead of uplifting because of less basal friction while the thick model tends to build a steeper topographic slope and accommodate more deformation through thrusting by the moving wall. The results indicate that the initial model thickness determines the fault space and influences the resultant wedge width.

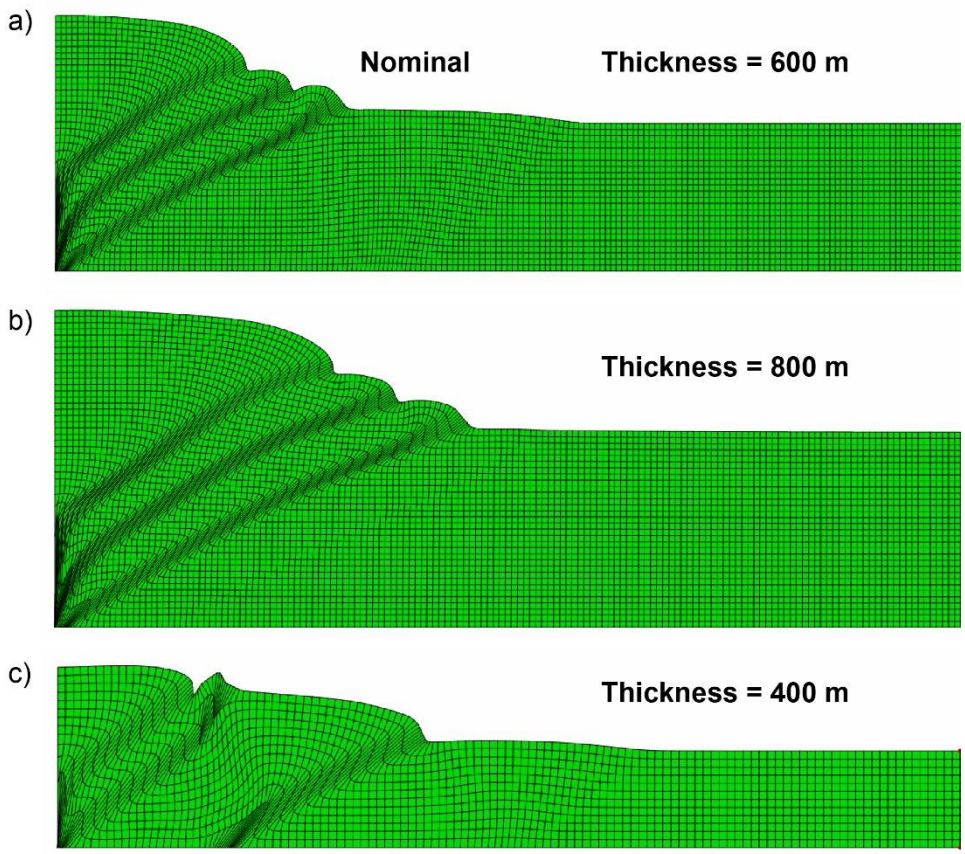

Figure A5 Sensitivity analyses for the numerical frictional experiment. Frames (a)-(c) are shown after 820m convergence. (a) Model with initial thickness = 600 m. (b) Initial thickness = 800 m. (c) Initial thickness = 400 m.

Bibliography

Adam, J., Klaeschen, D., Kukowski, N., and Flueh, E., 2004, Upward delamination of Cascadia Basin sediment infill with landward frontal accretion thrusting caused by rapid glacial age material flux: Tectonics, v. 23, no. 3, p. TC3009, DOI: 10.1029/2002tc001475.

Adam, J., Klinkmüller, M., Schreurs, G., and Wieneke, B., 2013, Quantitative 3D strain analysis in analogue experiments simulating tectonic deformation: Integration of X-ray computed tomography and digital volume correlation techniques: Journal of Structural Geology, v. 55, p. 127-149.

Adam, J., Urai, J. L., Wieneke, B., Oncken, O., Pfeiffer, K., Kukowski, N., Lohrmann, J., Hoth, S., van der Zee, W., and Schmatz, J., 2005, Shear localisation and strain distribution during tectonic faulting - new insights from granular-flow experiments and high-resolution optical image correlation techniques: Journal of Structural Geology, v. 27, no. 2, p. 283-301, DOI: 10.1016/j.jsg.2004.08.008.

Ahmad, M., Mohamad, H., Bischke, R., and Boyer, J., 2004, The Structure and Sequence Stratigraphy of Extensional Basins—A Case Study Offshore Deepwater Sarawak and Sabah, PGCE: Kuala Lumpur, Malaysia p. 18.

Ajakaiye, D. E., and Bally, A. W., 2002, Manual and atlas of structural styles on reflection profiles from the Niger Delta, AAPG Continuing Education Course Notes Series Volume 41, p. 102.

Allmendinger, R. W., and Judge, P., 2013, Stratigraphic uncertainty and errors in shortening from balanced sections in the North American Cordillera: Geological Society of America Bulletin, v. 125, no. 9-10, p. 1569-1579.

Armstrong, F. C., and Oriel, S. S., 1965, Tectonic development of Idaho-Wyoming thrust belt: AAPG Bulletin, v. 49, no. 11, p. 1847-1866.

Arthur, J. R. F., Dunstan, T., Alani, Q., and Assadi, A., 1977, Plastic-deformation and failure in granular media: Geotechnique, v. 27, no. 1, p. 53-74.

Avouac, J. P., Meyer, B., and Tapponnier, P., 1992, On the growth of normal faults and the existence of flats and ramps along the El Asnam active fold and thrust system: Tectonics, v. 11, no. 1, p. 1-11.

Balaguru, A., and Hall, R., Tectonic evolution and sedimentation of Sabah, north Borneo, Malaysia, *in* Proceedings AAPG 2008 International Conference, Cape Town, South Africa, 2008, Search and Discovery Article 30084, p. 15.

Bally, A. W., Gordy, P. L., and Stewart, G. A., 1966, Structure, seismic data, and orogenic evolution of southern Canadian Rocky Mountains.: Canadian Petroleum Geology Bulletin, v. 14, p. 337-381.

Bangs, N. L., Shipley, T. H., Gulick, S. P., Moore, G. F., Kuromoto, S., and Nakamura, Y., 2004, Evolution of the Nankai Trough décollement from the trench into the seismogenic zone: Inferences from three-dimensional seismic reflection imaging: Geology, v. 32, no. 4, p. 273-276.

Barber, D. E., Stockli, D. F., Koshnaw, R. I., Tamar-Agha, M. Y., and Yilmaz, I. O., 2016, Along-strike structural variation and thermokinematic development of the Cenozoic Bitlis-Zagros fold-thrust belt, Turkey and Iraqi Kurdistan, EGU General Assembly, Volume 18: Vienna, Austria.

Barnes, P. M., de Lepinay, B. M., Collot, J. Y., Delteil, J., and Audru, J. C., 1998, Strain partitioning in the transition area between oblique subduction and continental collision, Hikurangi margin, New Zealand: Tectonics, v. 17, no. 4, p. 534-557, DOI: 10.1029/98tc00974.

Barnes, P. M., Lamarche, G., Bialas, J., Henrys, S., Pecher, I., Netzeband, G. L., Greinert, J., Mountjoy, J. J., Pedley, K., and Crutchley, G., 2010, Tectonic and geological framework for gas hydrates and cold seeps on the Hikurangi subduction margin, New Zealand: Marine Geology, v. 272, no. 1, p. 26-48.

Beaumont, C., Fullsack, P., and Hamilton, J., 1992, Erosional control of active compressional orogens, *in* McClay, K. R., ed., Thrust Tectonics: London, Chapman and Hall, p. 1-18.

Berberian, M., 1979, Earthquake faulting and bedding thrust associated with the Tabas-e-Golshan (Iran) earthquake of September 16, 1978: Bulletin of the Seismological Society of America, v. 69, no. 6, p. 1861-1887.

Bergen, K. J., Shaw, J. H., Leon, L. A., Dolan, J. F., Pratt, T. L., Ponti, D. J., Morrow, E., Barrera, W., Rhodes, E. J., and Murari, M. K., 2017, Accelerating slip rates on the Puente Hills blind thrust fault system beneath metropolitan Los Angeles, California, USA: Geology, v. 45, no. 3, p. 227-230.

Bigi, S., Di Paolo, L., Vadacca, L., and Gambardella, G., 2010, Load and unload as interference factors on cyclical behavior and kinematics of Coulomb wedges: Insights from sandbox experiments: Journal of Structural Geology, v. 32, no. 1, p. 28-44, DOI: 10.1016/j.jsg.2009.06.018.

Bilotti, F., and Shaw, J. H., 2005, Deep-water Niger Delta fold and thrust belt modeled as a critical-taper wedge: The influence of elevated basal fluid pressure on structural styles: AAPG Bulletin, v. 89, no. 11, p. 1475-1491, DOI: 10.1306/06130505002.

Bol, A., and Van Hoorn, B., 1980, Structural styles in western Sabah offshore: Bulletin of the Geological Society of Malaysia, no. 12, p. 1-16.

Bombolakis, E. G., 1994, Applicability of critical-wedge theories to foreland belts: Geology, v. 22, no. 6, p. 535-538, DOI: 10.1130/0091-7613(1994)022<0535:aocwtt>2.3.co;2.

Bond, C. E., 2015, Uncertainty in structural interpretation: Lessons to be learnt: Journal of Structural Geology, v. 74, p. 185-200.

Bond, C. E., Lunn, R. J., Shipton, Z. K., and Lunn, A. D., 2012, What makes an expert effective at interpreting seismic images?: Geology, v. 40, no. 1, p. 75-78, DOI: 10.1130/g32375.1.

Bose, S., Mandal, N., Mukhopadhyaly, D. K., and Mishra, P., 2009, An unstable kinematic state of the Himalayan tectonic wedge: Evidence from experimental thrust-spacing patterns: Journal of Structural Geology, v. 31, no. 1, p. 83-91, DOI: 10.1016/j.jsg.2008.10.002.

Boyer, S. E., and Elliott, D., 1982, Thrust systems: AAPG Bulletin, v. 66, no. 9, p. 1196-1230.

Braathen, A., Bergh, S. G., and Maher, J., H. D., 1999, Application of a critical wedge taper model to the Tertiary transpressional fold-thrust belt on Spitsbergen, Svalbard: Geologcial Society of America Bulletin v. 111, no. 8, p. 1468-1685.

Braun, J., and Yamato, P., 2010, Structural evolution of a three-dimensional, finite-width crustal wedge: Tectonophysics, v. 484, no. 1-4, p. 181-192, DOI: 10.1016/j.tecto.2009.08.032.

Broucke, O., Temple, F., Rouby, D., Robin, C., Calassou, S., Nalpas, T., and Guillocheau, F., 2004, The role of deformation processes on the geometry of mud-dominated turbiditic systems, Oligocene and Lower–Middle Miocene of the Lower Congo basin (West African Margin): Marine and Petroleum Geology, v. 21, no. 3, p. 327-348.

Bucher, W. H., 1933, The deformation of the earth's crust, Princeton University Press Princeton.

Buiter, S. J., Schreurs, G., Albertz, M., Gerya, T. V., Kaus, B., Landry, W., le Pourhiet, L., Mishin, Y., Egholm, D. L., and Cooke, M., 2016, Benchmarking numerical models of brittle thrust wedges: Journal of Structural Geology, v. 92, p. 140-177.

Buiter, S. J. H., 2012, A review of brittle compressional wedge models: Tectonophysics, v. 530, p. 1-17, DOI: DOI 10.1016/j.tecto.2011.12.018.

Buiter, S. J. H., Babeyko, A. Y., Ellis, S., Gerya, T. V., Kaus, B. J. P., Kellner, A., Schreurs, G., and Yamada, Y., 2006, The numerical sandbox: Comparison of model results for a shortening and an extension experiment, *in* Buiter, S. J. H., and Schreurs, G., eds., Analogue and Numerical Modelling of Crustal-Scale Processes, Volume 253, p. 29-64.

Bulnes, M., and Poblet, J., 1999, Estimating the detachment depth in cross sections involving detachment folds: Geological Magazine, v. 136, no. 4, p. 395-412, DOI: 10.1017/S0016756899002794.

Burbidge, D. R., and Braun, J., 2002, Numerical models of the evolution of accretionary wedges and fold-and-thrust belts using the distinct-element method: Geophysical Journal International, v. 148, no. 3, p. 542-561, DOI: 10.1046/j.1365-246x.2002.01579.x.

Busk, H. G., 1929, Earth flexures, England, Cambridge University Press.

Butler, R., and Paton, D., 2010, Evaluating lateral compaction in deepwater fold and thrust belts: How much are we missing from “nature’s sandbox”: GSA Today, v. 20, no. 3, p. 4-10.

Butler, R. W., 1985, Thrust tectonics: a personal view: Geological Magazine, v. 122, no. 03, p. 223-232.

Butler, R. W. H., 1987, Thrust sequences: Journal of the Geological Society, v. 144, p. 619-634, DOI: 10.1144/gsjgs.144.4.0619.

Butler, R. W. H., 2013, Area balancing as a test of models for the deep structure of mountain belts, with specific reference to the Alps: Journal of Structural Geology, v. 52, p. 2-16, DOI: 10.1016/j.jsg.2013.03.009.

Butler, R. W. H., and Turner, J. P., 2010, Gravitational collapse at continental margins: products and processes; an introduction: Journal of the Geological Society, v. 167, p. 569-570, DOI: 10.1144/0016-76492010-003.

Byrne, D. E., Wang, W. H., and Davis, D. M., 1993, Mechanical role of backstops in the growth of Fore-arcs Tectonics, v. 12, no. 1, p. 123-144, DOI: 10.1029/92tc00618.

Byrne, T., and Fisher, D., 1987, Episodic growth of the Kodiak convergent margin: Nature, v. 325, p. 338-341, DOI: 10.1038/325338a0.

Carena, S., and Suppe, J., 2002, Three-dimensional imaging of active structures using earthquake aftershocks: the Northridge thrust, California: Journal of Structural Geology, v. 24, no. 4, p. 887-904, DOI: 10.1016/s0191-8141(01)00110-9.

Chamberlin, R. T., 1910, The Appalachian folds of central Pennsylvania: The Journal of Geology, v. 18, no. 3, p. 228-251.

Chapple, W. M., 1978, Mechanics of thin-skinned fold-and-thrust belts: Geological Society of America Bulletin, v. 89, no. 8, p. 1189-1198, DOI: 10.1130/0016-7606(1978)89<1189:motfb>2.0.co;2.

Chen, J., Scharer, K. M., Burbank, D. W., Heermance, R. V., and Wang, C. S., 2005, Quaternary detachment folding of the Mingyaole anticline, southern Tian Shan.: Seismology and Geology, v. 27, no. 4, p. 530-547.

Cobbold, P. R., Mourgues, R., and Boyd, K., 2004, Mechanism of thin-skinned detachment in the Amazon Fan: assessing the importance of fluid overpressure and hydrocarbon generation: Marine and petroleum geology, v. 21, no. 8, p. 1013-1025.

Cook, B. J., Henstock, T. J., McNeill, L. C., and Bull, J. M., 2014, Controls on spatial and temporal evolution of prism faulting and relationships to plate boundary slip offshore north‐central Sumatra: Journal of Geophysical Research: Solid Earth, v. 119, no. 7, p. 5594-5612.

Cooper, M., 2007, Structural style and hydrocarbon prospectivity in fold and thrust belts: a global review: Special Publication-Geological Society of London, v. 272, p. 447-472.

Copley, A., Avouac, J.-P., Hollingsworth, J., and Leprince, S., 2011, The 2001 M-w 7.6 Bhuj earthquake, low fault friction, and the crustal support of plate driving forces in India: Journal of Geophysical Research-Solid Earth, v. 116, p. B08405, DOI: 10.1029/2010jb008137.

Copley, A., Boait, F., Hollingsworth, J., Jackson, J., and McKenzie, D., 2009, Subparallel thrust and normal faulting in Albania and the roles of gravitational potential energy and rheology contrasts in mountain belts: Journal of Geophysical Research-Solid Earth, v. 114, p. B05407, DOI: 10.1029/2008jb005931.

Corredor, F., Shaw, J. H., and Bilotti, F., 2005, Structural styles in the deep-water fold and thrust belts of the Niger Delta: AAPG Bulletin, v. 89, no. 6, p. 753-780, DOI: 10.1306/02170504074.

Cotton, J. T., and Koyi, H. A., 2000, Modeling of thrust fronts above ductile and frictional detachments: Application to structures in the Salt Range and Potwar Plateau, Pakistan: Geological Society of America Bulletin, v. 112, no. 3, p. 351-363, DOI: 10.1130/0016-7606(2000)112<0351:motfad>2.3.co;2.

Coulomb, C. A., 1773, Essai sur une application des regles de maximis & minimis a quelques problemes de statique: relatifs a l'architecture: Academie Royale des Sciences, v. 7, p. 343-382.

Coward, M. P., 1983, Thrust tectonics, thin skinned or thick skinned, and the continuation of thrusts to deep in the crust: Journal of Structural Geology, v. 5, no. 2, p. 113-123, DOI: 10.1016/0191-8141(83)90037-8.

Cowie, P., Attal, M., Tucker, G., Whittaker, A., Naylor, M., Ganas, A., and Roberts, G., 2006, Investigating the surface process response to fault interaction and linkage using a numerical modelling approach: Basin Research, v. 18, no. 3, p. 231-266.

Cowie, P. A., and Roberts, G. P., 2001, Constraining slip rates and spacings for active normal faults: Journal of Structural Geology, v. 23, no. 12, p. 1901-1915.

Cowie, P. A., Roberts, G. P., Bull, J. M., and Visini, F., 2012, Relationships between fault geometry, slip rate variability and earthquake recurrence in extensional settings: Geophysical Journal International, v. 189, no. 1, p. 143-160.

Cruciani, F., Barchi, M., Koyi, H., and Porreca, M., 2017, Kinematic evolution of a regional-scale gravity-driven deepwater fold-and-thrust belt: The Lamu Basin case-history (East Africa): Tectonophysics, v. 712, p. 30-44.

Cruciani, F., and Barchi, M. R., 2016, The Lamu Basin deepwater fold‐and‐thrust belt: An example of a margin‐scale, gravity‐driven thrust belt along the continental passive margin of East Africa: Tectonics, v. 35, no. 3, p. 491-510.

Cruz, L., Malinski, J., Wilson, A., Take, W. A., and Hilley, G., 2010, Erosional control of the kinematics and geometry of fold-and-thrust belts imaged in a physical and numerical sandbox: Journal of Geophysical Research-Solid Earth, v. 115, p. B09404, DOI: 10.1029/2010jb007472.

Cubas, N., Souloumiac, P., and Singh, S. C., 2016, Relationship link between landward vergence in accretionary prisms and tsunami generation: Geology, v. 44, no. 10, p. 787-790.

Cullen, A., 2014, Nature and significance of the West Baram and Tinjar lines, NW Borneo: Marine and Petroleum Geology, v. 51, p. 197-209.

Cullen, A. B., 2010, Transverse segmentation of the Baram-Balabac Basin, NW Borneo: refining the model of Borneo's tectonic evolution: Petroleum Geoscience, v. 16, no. 1, p. 3-29.

D'Amato, D., Pace, B., Di Nicola, L., Stuart, F., Visini, F., Azzaro, R., Branca, S., and Barfod, S., 2016, Holocene slip rate variability along the Pernicana fault system (Mt. Etna, Italy): Evidence from offset lava flows: Geological Society of America Bulletin, v. 129, no. 3/4, p. 304-317.

Dahlen, F. A., 1984, Noncohesive critical coulomb wedges-an exact solution: Journal of Geophysical Research, v. 89, no. NB12, p. 125-133, DOI: 10.1029/JB089iB12p10125.

-, 1990, Critical taper model of fold-and-thrust belts and accretionary wedges: Annual Review of Earth and Planetary Sciences, v. 18, p. 55-99, DOI: 10.1146/annurev.earth.18.1.55.

Dahlen, F. A., Suppe, J., and Davis, D., 1984, Mechanics of fold-and-thrust belts and accretionary wedges-cohesive coulomb theory: Journal of Geophysical Research, v. 89, no. NB12, p. 87-101, DOI: 10.1029/JB089iB12p10087.

Dahlstrom, C., 1969, Balanced cross sections: Canadian Journal of Earth Sciences, v. 6, no. 4, p. 743-757.

Dahlstrom, C. D., 1970, Structural geology in the eastern margin of the Canadian Rocky Mountains: Bulletin of Canadian Petroleum Geology, v. 18, no. 3, p. 332-406.

Dahlstrom, C. D. A., 1990, Geometric Constraints Derived from the Law of Conservation of Volume and Applied to Evolutionary Models for Detachment Folding: Aapg Bulletin-American Association of Petroleum Geologists, v. 74, no. 3, p. 336-344.

Davis, D., Suppe, J., and Dahlen, F. A., 1983, Mechanics of fold-and-thrust belts and accretionary wedges: Journal of Geophysical Research, v. 88, no. B2, p. 1153-1172, DOI: 10.1029/Jb088ib02p01153.

Davis, D. M., and Engelder, T., 1985, The role of salt in fold-and-thrust belts: Tectonophysics, v. 119, no. 1-4, p. 67-88, DOI: 10.1016/0040-1951(85)90033-2.

Davis, E. E., Becker, K., Wang, K. L., Obara, K., Ito, Y., and Kinoshita, M., 2006, A discrete episode of seismic and aseismic deformation of the Nankai trough subduction zone accretionary prism and incoming Philippine Sea plate: Earth and Planetary Science Letters, v. 242, no. 1-2, p. 73-84, DOI: 10.1016/j.epsl.2005.11.054.

Davis, K., Burbank, D. W., Fisher, D., Wallace, S., and Nobes, D., 2005, Thrust-fault growth and segment linkage in the active Ostler fault zone, New Zealand.: Journal of Structural Geology, v. 27, no. 8, p. 1528-1536.

de Vera, J., Granado, P., and McClay, K., 2010, Structural evolution of the Orange Basin gravity-driven system, offshore Namibia: Marine and Petroleum Geology, v. 27, no. 1, p. 223-237, DOI: 10.1016/j.marpetgeo.2009.02.003.

DeCelles, P. G., Gehrels, G. E., Quade, J., Ojha, T. P., Kapp, P. A., and Upreti, B. N., 1998, Neogene foreland basin deposits, erosional unroofing, and the kinematic history of the Himalayan fold-thrust belt, western Nepal: Geological Society of America Bulletin, v. 110, no. 1, p. 2-21, DOI: 10.1130/0016-7606(1998)110<0002:nfbdeu>2.3.co;2.

Del Castello, M., and Cooke, M. L., 2007, Underthrusting-accretion cycle: Work budget as revealed by the boundary element method: Journal of Geophysical Research, v. 112, no. B12, p. B12404, DOI: 10.1029/2007jb004997.

DeMets, C., Gordon, R. G., Argus, D., and Stein, S., 1990, Current plate motions: Geophysical journal international, v. 101, no. 2, p. 425-478.

Deng, H., Koyi, H. A., and Froitzheim, N., 2014, Modeling two sequential coaxial phases of shortening in a foreland thrust belt: Journal of Structural Geology, v. 66, p. 400-415.

Diegel, F. A., Karlo, J., Schuster, D., Shoup, R., and Tauvers, P., 1995, Cenozoic structural evolution and tectono-stratigraphic framework of the northern Gulf Coast continental margin, *in* Jackson, M. P. A., Roberts, D. G., and Snelson, S., eds., Salt tectonics: a global perspective:, Volume 65, AAPG Memoir p. 109-151.

Dixon, J. M., and Liu, S. M., 1992, Centrifuge modeling of the propagation of thrust faults *in* McClay, K. R., ed., Thrust Tectonics: London, Chapman & Hall, p. 53-69.

Dotare, T., Yamada, Y., Adam, J., Hori, T., and Sakaguchi, H., 2016, Initiation of a thrust fault revealed by analog experiments: Tectonophysics, v. 684, p. 148-156.

Doust, H., and Omatsola, E., 1989, Niger delta, Divergent/Passive Margin Basins, Volume 48, AAPG Memoir p. 201-238.

Elliott, D., and Johnson, M., 1980, Structural evolution in the northern part of the Moine thrust belt, NW Scotland: Earth and Environmental Science Transactions of The Royal Society of Edinburgh, v. 71, no. 2, p. 69-96.

Ellis, S., Schreurs, G., and Panien, M., 2004, Comparisons between analogue and numerical models of thrust wedge development: Journal of Structural Geology, v. 26, no. 9, p. 1659-1675, DOI: 10.1016/j.jsg.2004.02.012.

Epard, J. L., and Groshong, R. H., 1993, Excess Area and Depth to Detachment: American Association of Petroleum Geologists Bulletin, v. 77, no. 8, p. 1291-1302.

-, 1995, Kinematic model of detachment folding including limb rotation, fixed hinges and layer-parallel strain: Tectonophysics, v. 247, no. 1-4, p. 85-103, DOI: 10.1016/0040-1951(94)00266-c.

Erslev, E. A., 1991, Trishear fault-propagation folding: Geology, v. 19, no. 6, p. 617-620, DOI: 10.1130/0091-7613(1991)019<0617:tfpf>2.3.co;2.

Evamy, B., Haremboure, J., Kamerling, P., Knaap, W., Molloy, F., and Rowlands, P., 1978, Hydrocarbon habitat of Tertiary Niger delta: AAPG bulletin, v. 62, no. 1, p. 1-39.

Fagereng, A., 2011, Wedge geometry, mechanical strength, and interseismic coupling of the Hukurangi subduction thrust, New Zealand: Tectonophysics, v. 507, p. 26-30.

Faill, R. T., and Nickelsen, R. P., 1999, Appalachian Mountain section of the Ridge and Valley province Geological Survey of Pennsylvania Special Publication, v. 1, no. 269-285.

Fillon, C., Huismans, R., and van der Beek, P., 2012, Syntectonic sedimentation effects on the growth of fold and thrust belts: Geology, v. 41, no. 1, p. 83-86.

Fitz-Diaz, E., Hudleston, P., and Tolson, G., 2011, Comparison of tectonic styles in the Mexican and Canadian Rocky Mountain Fold-Thrust Belt, *in* Poblet, J., and Lisle, R. J., eds., Kinematic Evolution and Structural Styles of Fold-and-Thrust Belts, Volume 349, p. 149-167.

Fitz-Diaz, E., Hudleston, P., Tolson, G., and van der Pluijm, B., 2014, Progressive, episodic deformation in the Mexican Fold–Thrust Belt (central Mexico): evidence from isotopic dating of folds and faults: International Geology Review, v. 56, no. 6, p. 734-755.

Fossen, H., 2010, Structural Geology, England, Cambridge University Press.

Franke, D., Barckhausen, U., Heyde, I., Tingay, M., and Ramli, N., 2008, Seismic images of a collision zone offshore NW Sabah/Borneo: Marine and Petroleum Geology, v. 25, no. 7, p. 606-624, DOI: 10.1016/j.marpetgeo.2007.11.004.

Fuller, C. W., Willett, S. D., and Brandon, M. T., 2006, Formation of forearc basins and their influence on subduction zone earthquakes: Geology, v. 34, no. 2, p. 65-68.

Gee, M. J. R., Uy, H. S., Warren, J., Morley, C. K., and Lambiase, J. J., 2007, The Brunei slide: A giant submarine landslide on the North West Borneo Margin revealed by 3D seismic data: Marine Geology, v. 246, no. 1, p. 9-23, DOI: 10.1016/j.margeo.2007.07.009.

Gerrard, I., and Smith, G., 1982, Post-Paleozoic succession and structure of the southwestern African continental margin, Studies in continental margin geology, Volume 34, American Association of Petroleum Geologists Memoir Tulsa, p. 49-74.

Ghisetti, F. C., Barnes, P. M., Ellis, S., Plaza‐Faverola, A. A., and Barker, D. H., 2016, The last 2 Myr of accretionary wedge construction in the central Hikurangi margin (North Island, New Zealand): Insights from structural modeling: Geochemistry, Geophysics, Geosystems, v. 17, no. 7, p. 2661-2686.

Goguel, J., 1962, Tectonics: San Francisco, Freeman, p. 1-348.

Gonzalez-Mieres, R., and Suppe, J., 2004, Analysis of shortening in an active detachment fold, Nankai Trough–an introduction to “thickness-relief analysis”, Geological Society of America Annual Meeting: Denver.

Gonzalez-Mieres, R., and Suppe, J., 2006, Relief and shortening in detachment folds: Journal of Structural Geology, v. 28, no. 10, p. 1785-1807, DOI: 10.1016/j.jsg.2006.07.001.

Granado, P., De Vera, J., and McClay, K. R., 2009, Tectonostratigraphic evolution of the Orange Basin, SW Africa: Trabajos de geología, v. 29, p. 321-328.

Granado, P., Ferrer, O., Muñoz, J., Thöny, W., and Strauss, P., 2017, Basin inversion in tectonic wedges: Insights from analogue modelling and the Alpine-Carpathian fold-and-thrust belt: Tectonophysics, v. 703, p. 50-68.

Grando, G., and McClay, K., 2004, Structural evolution of the Frampton growth fold system, Atwater Valley-Southern Green Canyon area, deep water Gulf of Mexico: Marine and Petroleum Geology, v. 21, no. 7, p. 889-910, DOI: 10.1016/j.marpetgeo.2003.12.005.

Grando, G., and McClay, K., 2007, Morphotectonics domains and structural styles in the Makran accretionary prism, offshore Iran: Sedimentary Geology, v. 196, no. 1-4, p. 157-179.

Graveleau, F., Malavieille, J., and Dominguez, S., 2012, Experimental modelling of orogenic wedges: A review: Tectonophysics, v. 538, p. 1-66, DOI: 10.1016/j.tecto.2012.01.027.

Groshong, R. H., 2015, Quality control and risk assessment of seismic profiles using area-depth-strain analysis: Interpretation-A Journal of Subsurface Characterization, v. 3, no. 4, p. SAA1-SAA15, DOI: 10.1190/int-2015-0010.1.

Groshong, R. H., Withjack, M. O., Schlische, R. W., and Hidayah, T. N., 2012, Bed length does not remain constant during deformation: Recognition and why it matters: Journal of Structural Geology, v. 41, p. 86-97.

Gulick, S. P. S., Bangs, N. L. B., Shipley, T. H., Nakamura, Y., Moore, G., and Kuramoto, S., 2004, Three-dimensional architecture of the Nankai accretionary prism's imbricate thrust zone off Cape Muroto, Japan: Prism reconstruction via en echelon thrust propagation: Journal of Geophysical Research, v. 109, no. B2, p. B02105, DOI: 10.1029/2003jb002654.

Gunderson, K. L., Anastasio, D. J., Pazzaglia, F. J., and Picotti, V., 2013, Fault slip rate variability on 10 4–10 5 yr timescales for the Salsomaggiore blind thrust fault, Northern Apennines, Italy: Tectonophysics, v. 608, p. 356-365.

Gutscher, M. A., Kukowski, N., Malavieille, J., and Lallemand, S., 1996, Cyclical behavior of thrust wedges: Insights from high basal friction sandbox experiments: Geology, v. 24, no. 2, p. 135-138, DOI: 10.1130/0091-7613(1996)024<0135:cbotwi>2.3.co;2.

-, 1998, Episodic imbricate thrusting and underthrusting: Analog experiments and mechanical analysis applied to the Alaskan accretionary wedge: Journal of Geophysical Research, v. 103, no. B5, p. 10161-10176, DOI: 10.1029/97jb03541.

Haack, R. C., Sundararaman, P., Diedjomahor, J. O., Xiao, H., Gant, N. J., May, E. D., and Kelsch, K., 2000, Niger Delta petroleum systems, Nigeria, *in* Mello, M. R., and Katz, B. J., eds., Petroleum systems of South Atlantic margins, AAPG Memoir 73, p. 213-231.

Hall, R., 1996, Reconstructing Cenozoic SE Asia: Geological Society, London, Special Publications, v. 106, no. 1, p. 153-184.

-, 2013, Contraction and extension in northern Borneo driven by subduction rollback: Journal of Asian Earth Sciences, v. 76, p. 399-411.

Hall, R., and Morley, C. K., 2004, Sundaland basins, *in* Clift, P., Kuhnt, W., Wang, P., and Hayes, D., eds., Continent-Ocean Interactions within East Asian Marginal Seas, Volume 149, p. 55-85.

Hall, R., van Hattum, M. W. A., and Spakman, W., 2008, Impact of India-Asia collision on SE Asia: The record in Borneo: Tectonophysics, v. 451, no. 1-4, p. 366-389, DOI: 10.1016/j.tecto.2007.11.058.

Hamilton, R., and De Vera, J., 2009, Review and global comparison of deepwater fold and thrust belt settings—Implications for their hydrocarbon prospectivity: Shell University Lecture Series.

Hamilton, W. B., 1979, Tectonics of the Indonesian region, US Govt. Print. Off., v. 1078.

Hardy, S., Duncan, C., Masek, J., and Brown, D., 1998, Minimum work, fault activity and the growth of critical wedges in fold and thrust belts: Basin Research, v. 10, no. 3, p. 365-373, DOI: 10.1046/j.1365-2117.1998.00073.x.

Hardy, S., and Ford, M., 1997, Numerical modeling of trishear fault propagation folding: Tectonics, v. 16, no. 5, p. 841-854, DOI: 10.1029/97tc01171.

Hardy, S., Poblet, J., McClay, K., and Waltham, D., 1996, Mathematical modelling of growth strata associated with fault-related fold structures: Geological Society, London, Special Publications, v. 99, no. 1, p. 265-282.

Harms, J. C., Cappel, H. N., and Francis, D. C., 1984, The Makran coast of Pakistan: its stratigraphy and hydrocarbon potential, *in* Haq, B. U., and Milliman, J. D., eds., Marine geology and oceanography of Arabian Sea and coastal Pakistan: New York, Van Nostrand Reinhold, p. 3-26.

Hatcher Jr, R. D., 1972, Developmental model for the southern Appalachians: Geological Society of America Bulletin, v. 83, no. 9, p. 2735-2760.

Hazebroek, H. P., and Tan, D. N., 1993, Tertiary tectonic evolution of the NW Sabah continental margin: Bulletin of the Geological Society of Malaysia, no. 33, p. 195-210.

Hedlund, C. A., 1997, Fault-propagation, ductile strain, and displacement-distance relationships: Journal of structural Geology, v. 19, no. 3-4, p. 249-256.

Hergert, T., and Heidbach, O., 2010, Slip-rate variability and distributed deformation in the Marmara Sea fault system: Nature Geoscience, v. 3, no. 2, p. 132-135.

Hesse, S., Back, S., and Franke, D., 2009, The deep-water fold-and-thrust belt offshore NW Borneo: Gravity-driven versus basement-driven shortening: Geological Society of America Bulletin, v. 121, no. 5-6, p. 939-953, DOI: 10.1130/b26411.1.

Hesse, S., Back, S., and Franke, D., 2010a, Deepwater folding and thrusting offshore NW Borneo, SE Asia: Geological Society, London, Special Publications, v. 348, no. 1, p. 169-185.

Hesse, S., Back, S., and Franke, D., 2010b, The structural evolution of folds in a deepwate fold and thrust belt - a case study from the Sabah continental margin offshore NW Borneo, SE Asia: Marine and Petroleum Geology, v. 27, p. 442-454.

-, 2010c, The structural evolution of folds in a deepwater fold and thrust belt - a case study from the Sabah continental margin offshore NW Borneo, SE Asia: Marine and Petroleum Geology, v. 27, no. 2, p. 442-454, DOI: 10.1016/j.marpetgeo.2009.09.004.

Higgins, S., Clarke, B., Davies, R. J., and Cartwright, J., 2009, Internal geometry and growth history of a thrust-related anticline in a deep water fold belt: Journal of Structural Geology, v. 31, no. 12, p. 1597-1611.

Higgins, S., Davies, R. J., and Clarke, B., 2007, Antithetic fault linkages in a deep water fold and thrust belt: Journal of Structural Geology, v. 29, no. 12, p. 1900-1914.

Hills, D., Moore, G., Bangs, N., and Gulick, S., 2001, Preliminary Results from Integration of 2D PSDM and ODP Leg 196 LWD Velocity Data in the Nankai Accretionary Prism, AGU Fall Meeting San Francisco.

Hinz, K., Fritsch, J., Kempter, E. H. K., Mohammad, A. M., Meyer, J., Mohamed, D., Vosberg, H., Weber, J., and Benavidez, J., 1989, Thrust tectonics along the north-western continental margin of Sabah/Borneo: Geologische Rundschau, v. 78, no. 3, p. 705-730, DOI: 10.1007/bf01829317.

Hinz, K., and Schluter, H. U., 1985, Geology of the Dangerous Grounds, South China Sea, and the Continental Margin off Southwest Palawan: Results of SONNE cruises SO-23 and SO-27: Energy, v. 10, no. 3-4, p. 297-315, DOI: 10.1016/0360-5442(85)90048-9.

Hossack, J. R., 1979, The use of balanced cross-sections in the calculation of orogenic contraction : A review Journal of the Geological Society, London, v. 136, p. 705-711, DOI: 10.1144/gsjgs.136.6.0705.

Hoth, S., Adam, J., Kukowski, N., and Oncken, O., 2006, Influence of erosion on the kinematics of bivergent orogens: Results from scaled sandbox simulations, *in* Willett, S. D., Hovius, N., Brandon, M. T., and Fisher, D. M., eds., Tectonics, Climate, and Landscape Evolution, Volume 398, Geological Society of America Special Paper 398, Penrose Conference Series, p. 201-225.

Hubbard, J., Almeida, R., Foster, A., Sapkota, S. N., Bürgi, P., and Tapponnier, P., 2016, Structural segmentation controlled the 2015 Mw 7.8 Gorkha earthquake rupture in Nepal: Geology, v. 44, no. 8, p. 639-642.

Hubbert, M. K., and Rubey, W. W., 1959, Role of fluid pressure in mechanics of overthrust faulting, I, Mechanics of fluid-filled solids and its application to overthrust faulting: Geological Society of America Bulletin, v. 70, p. 115-166.

Hubert-Ferrari, A., Suppe, J., Gonzalez-Mieres, R., and Wang, X., 2007, Mechanisms of active folding of the landscape (southern Tian Shan, China): Journal of Geophysical Research-Solid Earth, v. 112, p. B03S09, DOI: 10.1029/2006jb004362.

Huerta, A. D., and Harry, D. L., 2012, Wilson cycles, tectonic inheritance, and rifting of the North American Gulf of Mexico continental margin: Geosphere, v. 8, no. 2, p. 374-385.

Hughes, A. N., and Shaw, J. H., 2014, Fault displacement-distance relationships as indicators of contractional fault-related folding styleDisplacement Variations and Folding Styles: AAPG bulletin, v. 98, no. 2, p. 227-251.

-, 2015, Insights into the mechanics of fault-propagation folding styles: Geological Society of America Bulletin, v. 127, no. 11-12, p. 1752-1765.

Hutchison, C. S., 1996, The 'Rajang accretionary prism'and 'Lupar Line'problem of Borneo: Geological Society, London, Special Publications, v. 106, no. 1, p. 247-261.

-, 2004, Marginal basin evolution: the southern South China Sea: Marine and Petroleum Geology, v. 21, no. 9, p. 1129-1148.

Hutchison, C. S., 2005, Geology of North-West Borneo: Amsterdam, Elsevier, p. 1-444.

Hutchison, C. S., and Misra, K. C., 1996, South-East Asian Oil, Gas, Coal and Mineral Deposits. Oxford Monographs on Geology and Geophysics 36: Economic Geology and the Bulletin of the Society of Economic Geologists, v. 91, no. 7, p. 1321.

Ingram, G. M., Chisholm, T. J., Grant, C. J., Hedlund, C. A., Stuart-Smith, P., and Teasdale, J., 2004, Deepwater North West Borneo: Hydrocarbon accumulation in an active fold and thrust belt: Marine and Petroleum Geology, v. 21, no. 7, p. 879-887, DOI: 10.1016/j.marpetgeo.2003.12.007.

Jackson, M. P. A., and Hubec, M. R., 2017, Salt Tectonics: England, Cambridge University Press, p. 1-510.

James, D. M. D., 1984, The geology and hydrocarbon resources of Negara Brunei Darussalam, Brunei Shell Petroleum Company.

Jamison, W. R., 1987, Geometric analysis of fold development in overthrust terranes: Journal of Structural Geology, v. 9, no. 2, p. 207-219, DOI: 10.1016/0191-8141(87)90026-5.

Ji, J., Luo, P., White, P., Jiang, H., Gao, L., and Ding, Z., 2008, Episodic uplift of the Tianshan Mountains since the late Oligocene constrained by magnetostratigraphy of the Jingou River section, in the southern margin of the Junggar Basin, China: Journal of Geophysical Research-Solid Earth, v. 113, p. B05102, DOI: 10.1029/2007jb005064.

Judge, P. A., and Allmendinger, R. W., 2011, Assessing uncertainties in balanced cross sections: Journal of Structural Geology, v. 33, no. 4, p. 458-467.

Karig, D., and Lundberg, N., 1990, Deformation bands from the toe of the Nankai accretionary prism: Journal of Geophysical Research, v. 95, no. B6, p. 9099-9109.

Kaus, B. J. P., 2010, Factors that control the angle of shear bands in geodynamic numerical models of brittle deformation: Tectonophysics, v. 484, no. 1-4, p. 36-47, DOI: 10.1016/j.tecto.2009.08.042.

Khalil, S. M., and McClay, K. R., 2002, Extensional fault-related folding, northwestern Red Sea, Egypt: Journal of Structural Geology, v. 24, no. 4, p. 743-762, DOI: 10.1016/s0191-8141(01)00118-3.

King, R. C., Backe, G., Morley, C. K., Hillis, R. R., and Tingay, M. R. P., 2010a, Balancing deformation in NW Borneo: Quantifying plate-scale vs. gravitational tectonics in a delta and deepwater fold-thrust belt system: Marine and Petroleum Geology, v. 27, no. 1, p. 238-246, DOI: 10.1016/j.marpetgeo.2009.07.008.

King, R. C., Hillis, R. R., Tingay, M. R. P., and Morley, C. K., 2009, Present-day stress and neotectonic provinces of the Baram Delta and deep-water fold- thrust belt: Journal of the Geological Society, London, v. 166, p. 197-200.

-, 2010b, Present-day stress in Brunei, NW Borneo: Superposition of deltaic and active margin tectonics: Basin Research, v. 22, p. 236-247, DOI: 10.1111/j.1365-2117.2009.00407.x.

King, R. C., and Morley, C. K., 2017, Wedge geometry and detachment strength in deepwater fold-thrust belts: Earth-science reviews, v. 165, p. 268-279.

Kley, J., 1996, Transition from basement‐involved to thin‐skinned thrusting in the Cordillera Oriental of southern Bolivia: Tectonics, v. 15, no. 4, p. 763-775.

Kopp, H., and Kukowski, N., 2003, Backstop geometry and accretionary mechanics of the Sunda margin: Tectonics, v. 22, no. 6, p. 1072, DOI: 10.1029/2002tc001420.

Koyi, H., 1995, Mode of internal deformation in sand wedges: Journal of Structural Geology, v. 17, no. 2, p. 293-300, DOI: 10.1016/0191-8141(94)00050-a.

Koyi, H. A., Hessami, K., and Teixell, A., 2000, Epicenter distribution and magnitude of earthquakes in fold-thrust belts: insights from sandbox models: Geophysical Research Letters, v. 27, no. 2, p. 273-276, DOI: 10.1029/1999gl010833.

Koyi, H. A., and Maillot, B., 2007, Tectonic thickening of hanging-wall units over a ramp: Journal of Structural Geology, v. 29, no. 6, p. 924-932, DOI: 10.1016/j.jsg.2007.02.014.

Koyi, H. A., Sans, M., Teixell, A., Cotton, J., and Zeyen, H., 2004, The significance of penetrative strain in the restoration of shortened layers—insights from sand models and the Spanish Pyrenees, *in* McClay, K. R., ed., Thrust tectonics and hydrocarbon systems, Volume 82, AAPG Memoir p. 1-16.

Koyi, H. A., and Vendeville, B. C., 2003, The effect of decollement dip on geometry and kinematics of model accretionary wedges: Journal of Structural Geology, v. 25, no. 9, p. 1445-1450, DOI: 10.1016/s0191-8141(02)00202-x.

Ku, C.-Y., and Hsu, S.-K., 2009, Crustal structure and deformation at the northern Manila Trench between Taiwan and Luzon islands: Tectonophysics, v. 466, no. 3, p. 229-240.

Kudrass, H., Wiedicke, M., Cepek, P., Kreuzer, H., and Müller, P., 1986, Mesozoic and Cainozoic rocks dredged from the South China Sea (Reed Bank area) and Sulu Sea and their significance for plate-tectonic reconstructions: Marine and Petroleum Geology, v. 3, no. 1, p. 19-30.

Lallemand, S., and Le Pichon, X., 1987, Coulomb wedge model applied to the subduction of seamounts in the Japan Trench: Geology, v. 15, p. 1065-1069.

Lathrop, B. A., and Burberry, C. M., 2017, Accommodation of penetrative strain during deformation above a ductile decollement: Lithosphere, v. 9, no. 1, p. 46-57.

Lease, R. O., Burbank, D. W., Hough, B., Wang, Z., and Yuan, D., 2012, Pulsed Miocene range growth in northeastern Tibet: Insights from Xunhua Basin magnetostratigraphy and provenance: Geological Society of America Bulletin, v. 124, no. 5-6, p. 657-677.

Lemiale, V., Muehlhaus, H. B., Moresi, L., and Stafford, J., 2008, Shear banding analysis of plastic models formulated for incompressible viscous flows: Physics of the Earth and Planetary Interiors, v. 171, no. 1-4, p. 177-186, DOI: 10.1016/j.pepi.2008.07.038.

Levell, B. K., 1987, The Nature and Significance of Regional Unconformities in the Hydrocarbon–Bearing Neogene Sequence Offshore West Sabah: Bulletin of the Geological Society of Malaysia, v. 21, p. 55-90.

Lickorish, H., and Ford, M., 1998, Sequential restoration of the external Alpine Digne thrust system, SE France, constrained by kinematic data and synorogenic sediments: Journal of Geological Society, London, v. 134, p. 189-211.

Light, M., Maslanyj, M., Greenwood, R., and Banks, N., 1993, Seismic sequence stratigraphy and tectonics offshore Namibia: Geological Society, London, Special Publications, v. 71, no. 1, p. 163-191.

Lin, A. T., Yao, B., Hsu, S.-K., Liu, C.-S., and Huang, C.-Y., 2009, Tectonic features of the incipient arc-continent collision zone of Taiwan: implications for seismicity: Tectonophysics, v. 479, no. 1, p. 28-42.

Liu, H. Q., McClay, K. R., and Powell, D., 1992, Physical models of thrust wedges, *in* McClay, K. R., ed., Thrust Tectonics: London, Chapman and Hall, p. 71-81.

Lohrmann, J., Kukowski, N., Adam, J., and Oncken, O., 2003, The impact of analogue material properties on the geometry, kinematics, and dynamics of convergent sand wedges: Journal of Structural Geology, v. 25, no. 10, p. 1691-1711, DOI: 10.1016/s0191-8141(03)00005-1.

Lu, R. Q., Xu, X. W., He, D. F., John, S., Liu, B., Wang, F. Y., Tan, X. B., and Li, Y. Q., 2017, Seismotectonics of the 2013 Lushan M-w 6.7 earthquake: Inversion tectonics in the eastern margin of the Tibetan Plateau: Geophysical Research Letters, v. 44, no. 16, p. 8236-8243, DOI: 10.1002/2017gl074296.

Macedo, J., and Marshak, S., 1999, Controls on the geometry of fold-thrust belt salients: Geological Society of America Bulletin, v. 111, no. 12, p. 1808-1822, DOI: 10.1130/0016-7606(1999)111<1808:cotgof>2.3.co;2.

MacKay, M. E., 1995, Structural variation and landward vergence at the toe of the Oregon accretionary prism: Tectonics, v. 14, no. 6, p. 1309-1320.

Mackay, M. E., Moore, G. F., Cochrane, G. R., Moore, J. C., and Kulm, L. D., 1992, Landward vergence and oblique structural trends in the Oregon margin accretionary prism: Implications and effect on fluid flow: Earth and Planetary Science Letters, v. 109, no. 3-4, p. 477-491, DOI: 10.1016/0012-821x(92)90108-8.

Madon, M., Kim, C. L., and Wong, R., 2013, The structure and stratigraphy of deepwater Sarawak, Malaysia: implications for tectonic evolution: Journal of Asian Earth Sciences, v. 76, p. 312-333.

Marques, F. O., and Cobbold, P. R., 2002, Topography as a major factor in the development of arcuate thrust belts: insights from sandbox experiments: Tectonophysics, v. 348, no. 4, p. 247-268, DOI: 10.1016/s0040-1951(02)00077-x.

-, 2006, Effects of topography on the curvature of fold-and-thrust belts during shortening of a 2-layer model of continental lithosphere: Tectonophysics, v. 415, no. 1-4, p. 65-80, DOI: 10.1016/j.tecto.2005.12.001.

Marsden, D., 1992, V 0—K method of depth conversion: The Leading Edge, v. 11, no. 8, p. 53-54.

Masaferro, J. L., Poblet, J., Bulnes, M., Eberli, G. P., Dixon, T. H., and McClay, K., 1999, Palaeogene-Neogene/present day(?) growth folding in the Bahamian foreland of the Cuban fold and thrust belt: Journal of the Geological Society, v. 156, p. 617-631, DOI: 10.1144/gsjgs.156.3.0617.

Masini, M., Bigi, S., Poblet, J., Bulnes, M., Di Cuia, R., and Casabianca, D., 2011, Kinematic evolution and strain simulation, based on cross-section restoration, of the Maiella Mountain: an analogue for oil fields in the Apennines (Italy), *in* Poblet, J., and Lisle, R. J.,

eds., Kinematic Evolution and Structural Styles of Fold-and-Thrust Belts, Volume 349, Geological Society of London Special Publications, p. 25-44.

McClay, K. R., 1992, Glossary of thrust tectonics terms, *in* McClay, K. R., ed., Thrust Tectonics: London, Chapman & Hall, p. 419-433.

McClay, K. R., Whitehouse, P. S., Dooley, T., and Richards, A., 2004, 3D evolution of fold and thrust belts formed by oblique convergence: Marine and Petroleum Geology, v. 21, no. 7, p. 857-877, DOI: 10.1016/j.marpetgeo.2004.03.009.

McClymont, A. F., Villamor, P., and Green, A. G., 2009, Fault displacement accumulation and slip rate variability within the Taupo Rift (New Zealand) based on trench and 3‐D ground‐penetrating radar data: Tectonics, v. 28, p. TC4005, DOI: 10.1029/2008TC002334.

McGilvery, T., and Cook, D. L., 2013, The influence of local gradients on accommodation space and linked depositional elements across a stepped slope profile, offshore Brunei, *in* Roberts, H. H., Rosen, N. C., Fillon, R. H., and Anderson, J. B., eds., Shelf margin deltas and linked down slope petroleum systems: Global significance and future exploration potential, SEPM Society for Sedimentary Geology, p. 387-419.

McGilvery, T. M., and Cook, D. L., 2004, Depositional elements of the slope/basin depositional system offshore Brunei, Proceedings of the Indonesia Petroleum Association Meeting: Jakarta, Indonesia, p. 407-419.

McGroder, M. F., Lease, R. O., and Pearson, D. M., 2015, Along-strike variation in structural styles and hydrocarbon occurrences, Subandean fold-and-thrust belt and inner foreland, Colombia to Argentina: Geological Society of America Memoirs, v. 212, p. 79-113.

McNeill, L. C., and Henstock, T. J., 2014, Forearc structure andmorphology along the SumatraAndaman subduction zone: Tectonics, v. 33, no. 2, p. 112-134, DOI: Doi 10.1002/2012tc003264.

McQuarrie, N., 2004, Crustal scale geometry of the Zagros fold-thrust belt, Iran: Journal of Structural Geology, v. 26, no. 3, p. 519-535, DOI: 10.1016/j.jsg.2003.08.009.

Mello, M. R., Azambuja, N., Mohriak, W., Catto, A., and Françolin, J., 2011, Promising giant new hydrocarbon frontier: the Namibian continental margin: GEOEXPRO, v. 8, no. 6, p. 64-66.

Miller, M. G., 2003, Basement-involved thrust faulting in a thin-skinned fold-and-thrust belt, Death Valley, California, USA: Geology, v. 31, no. 1, p. 31-34.

Mishra, P., and Mukhopadhyay, D. K., 2012, Structural evolution of the frontal fold–thrust belt, NW Himalayas from sequential restoration of balanced cross-sections and its hydrocarbon potential, *in* Bhat, G. M., Craig, J., Thurow, J. W., and Cozzi, A., eds., Geology and Hydrocarbon Potential of Neoproterozoic –Cambrian Basins in Asia, Volume 366, Geological Society, London, Special Publications, p. 201-228.

Mitra, S., 1990, Fault Propagation Folds: Geometry, Kinematic Evolution, and Hydrocarbon Traps: AAPG Bulletin-American Association of Petroleum Geologists, v. 74, no. 6, p. 921-945.

Mitra, S., and Namson, J., 1989, Equal-area balancing: American Journal of Science, v. 289, no. 5, p. 563-599.

Moore, G. F., Shipley, T., Stoffa, P., Karig, D., Taira, A., Kuramoto, S., Tokuyama, H., and Suyehiro, K., 1990, Structure of the Nankai Trough accretionary zone from multichannel seismic reflection data: Journal of Geophysical Research: Solid Earth, v. 95, no. B6, p. 8753-8765.

Moore, G. F., Taira, A., Klaus, A., Becker, L., Boeckel, B., Cragg, B. A., Dean, A., Fergusson, C. L., Henry, P., and Hirano, S., 2001, New insights into deformation and fluid flow processes in

the Nankai Trough accretionary prism: Results of Ocean Drilling Program Leg 190: Geochemistry, Geophysics, Geosystems, v. 2, no. 10, p. 2001GC000166, DOI: 10.129/2001GC000166.

Moore, J. C., and Saffer, D., 2001, Updip limit of the seismogenic zone beneath the accretionary prism of southwest Japan: An effect of diagenetic to low-grade metamorphic processes and increasing effective stress: Geology, v. 29, no. 2, p. 183-186, DOI: 10.1130/0091-7613(2001)029<0183:ulotsz>2.0.co;2.

Moore, J. C., and Silver, E. A., 1987, Continental margin tectonics: Submarine accretionary prisms: Reviews of Geophysics, v. 25, no. 6, p. 1305-1312, DOI: 10.1029/RG025i006p01305.

Mora, A., and Parra, M., 2008, The structural style of footwall shortcuts along the eastern foothills of the Colombian Eastern Cordillera. Differences with other inversion related structures: CT&F-Ciencia, Tecnología y Futuro, v. 3, no. 4, p. 7-21.

Moretti, I., and Callot, J. P., 2012, Area, length and thickness conservation: Dogma or reality?: Journal of Structural Geology, v. 41, p. 64-75.

Morgan, J. K., and Karig, D. E., 1995, Kinematics and a balanced and restored cross-section across the toe of the eastern Nankai accretionary prism: Journal of Structural Geology, v. 17, no. 1, p. 31-45, DOI: 10.1016/0191-8141(94)e0031-s.

Morley, C., 1992, Hydrocarbon generation-a possible cause of elevated pore pressures in the Osen-Roa thrust sheet, Norway: Journal of structural geology, v. 14, no. 6, p. 743-747.

Morley, C., and Guerin, G., 1996, Comparison of gravity‐driven deformation styles and behavior associated with mobile shales and salt: Tectonics, v. 15, no. 6, p. 1154-1170.

Morley, C. K., 1988, Out-of-sequence thrusts: Tectonics, v. 7, no. 3, p. 539-561, DOI: 10.1029/TC007i003p00539.

-, 2002, A tectonic model for the Tertiary evolution of strike-slip faults and rift basins in SE Asia: Tectonophysics, v. 347, no. 4, p. 189-215, DOI: 10.1016/s0040-1951(02)00061-6.

-, 2007a, Development of crestal normal faults associated with deepwater fold growth: Journal of Structural Geology, v. 29, no. 7, p. 1148-1163, DOI: 10.1016/j.jsg.2007.03.016.

-, 2007b, Interaction between critical wedge geometry and sediment supply in a deep water fold belt: Geology, v. 35, no. 2, p. 139-142.

-, 2009a, Geometry of an oblique thrust fault zone in deepwater fold beld from 3D seismic data: Journal of Structural Geology, v. 31, p. 1540-1555.

Morley, C. K., 2009b, Growth of folds in a deep-water setting: Geosphere, v. 5, no. 2, p. 59-89, DOI: 10.1130/ges00186.1.

Morley, C. K., Back, S., Van Rensbergen, P., Crevello, P., and Lambiase, J. J., 2003, Characteristics of repeated, detached, Miocene-Pliocene tectonic inversion events, in a large delta province on an active margin, Brunei Darussalam, Borneo: Journal of Structural Geology, v. 25, no. 7, p. 1147-1169, DOI: 10.1016/s0191-8141(02)00130-x.

Morley, C. K., King, R., Hillis, R., Tingay, M., and Backe, G., 2011, Deepwater fold and thrust belt classification, tectonics, structure and hydrocarbon prospectivity: A review: Earth-Science Reviews, v. 104, no. 1-3, p. 41-91, DOI: 10.1016/j.earscirev.2010.09.010.

Morley, C. K., Tingay, M., Hillis, R., and King, R., 2008, Relationship between structural style, overpressures, and modern stress, Baram Delta Province, northwest Borneo: Journal of Geophysical Research-Solid Earth, v. 113, p. B09410, DOI: 10.1029/2007jb005324.

Morley, C. K., Warren, J., Tingay, M., Boonyasaknanon, P., and Julapour, A., 2014, Comparison of modern fluid distribution, pressure and flow in sediments associated with anticlines growing in deepwater (Brunei) and continental environments (Iran): Marine and petroleum geology, v. 55, p. 230-249.

Mourgues, R., Lacoste, A., and Garibaldi, C., 2014, The Coulomb critical taper theory applied to gravitational instabilities Journal of Geophysical Research:Solid Earth, v. 119, p. 754-765, DOI: 10.1002/2013JB010359.

Mouthereau, F., Lacombe, O., and Meyer, B., 2006, The Zagros folded belt(Fars, Iran): constraints from topography and critical wedge modelling: Geophysical Journal International, v. 165, p. 336-356.

Mueller, K., and Talling, P., 1997, Geomorphic evidence for tear faults accommodating lateral propagation of an active fault-bend fold, Wheeler Ridge, California: Journal of Structural Geology, v. 19, no. 3-4, p. 397-411, DOI: 10.1016/s0191-8141(96)00089-2.

Mulugeta, G., 1988, Modeling the geometry of coulomb thrust wedges: Journal of Structural Geology, v. 10, no. 8, p. 847-859, DOI: 10.1016/0191-8141(88)90099-5.

Mulugeta, G., and Koyi, H., 1987, 3-Dimensionl geometry and kinematics of experimental piggyback thrusting Geology, v. 15, no. 11, p. 1052-1056, DOI: 10.1130/0091-7613(1987)15<1052:tgakoe>2.0.co;2.

-, 1992, Episodic accretion and strain partitioning in a model sand wedge: Tectonophysics, v. 202, no. 2-4, p. 319-333, DOI: 10.1016/0040-1951(92)90117-o.

Nemcok, M., Schamel, S., and Gayer, R., 2009, Thrustbelts: Structural architecture, thermal regimes and petroleum systems: England, Cambridge University Press, p. 1-554.

Nieuwland, D. A., Leutscher, J. H., and Gast, J., 2000, Wedge equilibrium in fold-and-thrust belts: prediction of out-of-sequence thrusting based on sandbox experiments and natural examples: Geologie En Mijnbouw-Netherlands Journal of Geosciences, v. 79, no. 1, p. 81-91.

Nilfouroushan, F., Pysklywec, R., and Cruden, A., 2012, Sensitivity analysis of numerical scaled models of fold-and-thrust belts to granular material cohesion variation and comparison with analog experiments: Tectonophysics, v. 526, p. 196-206, DOI: 10.1016/j.tecto.2011.06.022.

Nilfouroushan, F., Pysklywec, R., Cruden, A., and Koyi, H., 2013, Thermal‐mechanical modeling of salt‐based mountain belts with pre‐existing basement faults: Application to the Zagros fold and thrust belt, southwest Iran: Tectonics, v. 32, no. 5, p. 1212-1226.

Paganoni, M., Cartwright, J., Foschi, M., Shipp, R., and Van Rensbergen, P., 2016, Structure II gas hydrates found below the bottom‐simulating reflector: Geophysical Research Letters, v. 43, no. 11, p. 5696-5706.

Paganoni, M., Cartwright, J. A., Foschi, M., Shipp, C. R., and Van Rensbergen, P., 2018, Relationship between fluid-escape pipes and hydrate distribution in offshore Sabah (NW Borneo): Marine Geology, v. 395, p. 82-103.

Panien, M., Schreurs, G., and Pfiffner, A., 2006, Mechanical behaviour of granular materials used in analogue modelling: insights from grain characterisation, ring-shear tests and analogue experiments: Journal of Structural Geology, v. 28, no. 9, p. 1710-1724, DOI: 10.1016/j.jsg.2006.05.004.

Park, J. O., Tsuru, T., Kodaira, S., Cummins, P. R., and Kaneda, Y., 2002, Splay fault branching along the Nankai subduction zone: Science, v. 297, no. 5584, p. 1157-1160, DOI: 10.1126/science.1074111.

Peach, B. N., Horne, J., Gunn, W., Clough, C. T., Teall, J. J. H., and Hinxman, L. W., 1907, The geological structure of the North-West Highlands of Scotland, Glasgow, HM Stationery Office.

Peel, F. J., 2014, The engines of gravity-driven movement on passive margins: Quantifying the relative contribution of spreading vs. gravity sliding mechanisms: Tectonophysics, v. 633, p. 126-142, DOI: 10.1016/j.tecto.2014.06.023.

Peel, F. J., Travis, C. J., and Hossack, J. R., 1995, Genetic structural provinces and salt tectonics of the Cenozoic offshore US Gulf of Mexico: A preliminary analysis, *in* Jackson, M. P. A., Roberts, D. G., and Snelson, S., eds., Salt Tectonics: A Global Perspective, Volume 65, AAPG MEMOIR, p. 153-175.

Petronas, 1999, The Petroleum geology and resources of Malaysia: Kuala Lumpur, Malaysia Petronas, p. 1-665.

Pfiffner, O. A., 2006, Thick-skinned and thin-skinned styles of continental contraction: Geological Society of America Bulletin, v. 414, p. 153-177.

Platt, J., Leggett, J., Young, J., Raza, H., and Alam, S., 1985, Large-scale sediment underplating in the Makran accretionary prism, southwest Pakistan: Geology, v. 13, no. 7, p. 507-511.

Platt, J. P., 1986, Dynamics of orogenic wedges and the uplift of high pressure metamorphic rocks: Geological Society of America Bulletin, v. 97, no. 9, p. 1037-1053, DOI: 10.1130/0016-7606(1986)97<1037:doowat>2.0.co;2.

Poblet, J., and Lisle, R. J., 2011, Kinematic evolution and structural styles of fold-and-thrust belts: Kinematic Evolution and Structural Styles of Fold-and-Thrust Belts, v. 349, p. 1-24, DOI: 10.1144/sp349.1.

Price, R., 1981, The Cordilleran foreland thrust and fold belt in the southern Canadian Rocky Mountains: Geological Society, London, Special Publications, v. 9, no. 1, p. 427-448.

Price, R., and Mountjoy, E., 1970, Geologic structure of the Canadian Rocky Mountains between Bow and Athabasca Rivers—a progress report: Geological Association of Canada Special Paper, v. 6, p. 7-25.

Ramsay, J. G., and Huber, M. I., 1987, The techniques of modern structural geology, Volume 2: San Diego, Academic press, p. 1-307.

Ranero, C. R., and von Huene, R., 2000, Subduction erosion along the Middle America convergent margin: Nature, v. 404, no. 6779, p. 748.

Rangin, C., Bellon, H., Benard, F., Letouzey, J., Muller, C., and Sanudin, T., 1990, Neogene arc-continent collision in Sabah, northern Borneo (Malaysia): Tectonophysics, v. 183, no. 1-4, p. 305-319.

Rice-Oxley, E. D., 1991, Palaeoenvironments of the Lower Miocene to Pliocene sediments in offshore NW Sabah area: Bulletin of the Geological Society of Malaysia, v. 28, p. 165-194.

Rich, J. L., 1934, Mechanics of low-angle overthrust faulting as illustrated by Cumberland thrust block, Virginia, Kentucky, and Tennessee: AAPG Bulletin, v. 18, no. 12, p. 1584-1596.

Roberts, G. P., Cowie, P., Papanikolaou, I., and Michetti, A. M., 2004, Fault scaling relationships, deformation rates and seismic hazards: an example from the Lazio–Abruzzo Apennines, central Italy: Journal of Structural Geology, v. 26, no. 2, p. 377-398.

Rodgers, J., 1949, Evolution of thought on structure of middle and southern Appalachians: American Association of Petroleum Geologists Bulletin, v. 33, p. 1643-1654.

Rodgers, J., 1963, Mechanics of Appalachian foreland folding in Pennsylvania and West Virginia: AAPG Bulletin, v. 47, no. 8, p. 1527-1536.

Roscoe, K. H., 1970, Influence of strains in soil mechanics Geotechnique, v. 20, no. 2, p. 129-170.

Rowan, M. G., Peel, F. J., and Vendeville, B. C., 2004, Gravity-driven Fold Belts on passive margins, *in* McClay, K. R., ed., Thrust tectonics and hydrocarbon systems, AAPG Memoir 82, p. 157-182.

Rowan, M. G., Trudgill, B. D., and Fiduk, J. C., 2000, Deep-water, salt-cored foldbelts: Lessons from the Mississippi Fan and Perdido foldbelts, northern Gulf of Mexico: Atlantic Rifts and Continental Margins, v. 115, p. 173-191.

Ruh, J. B., 2013, Dynamic evolution of thin-skinned fold-and-thrust belts: field study, magnetostratigraphy and numerical modelling applied to the Zagros and Makran mountains (Iran) [PhD: ETH Zurich, 1-236 p.

Ruh, J. B., Gerya, T., and Burg, J. P., 2013, High‐resolution 3D numerical modeling of thrust wedges: Influence of décollement strength on transfer zones: Geochemistry, Geophysics, Geosystems, v. 14, no. 4, p. 1131-1155.

Ruh, J. B., Kaus, B. J. P., and Burg, J.-P., 2012, Numerical investigation of deformation mechanics in fold-and-thrust belts: Influence of rheology of single and multiple decollements: Tectonics, v. 31, p. TC3005, DOI: 10.1029/2011tc003047.

Sandal, S. T., 1996, The geology and hydrocarbon resources of Negara Brunei Darussalam (1996 revision): Syabas Bandar Seri Begawan, Brunei Darussalam, Brunei Shell Petroleum Company/Brunei Museum p. 1-243.

Sans, M., Vergés, J., Gomis, E., Parés, J., Schiattarella, M., Travé, A., Calvet, F., Santanach, P., and Doulcet, A., 2003, Layer parallel shortening in salt-detached folds: constraint on cross-section restoration: Tectonophysics, v. 372, no. 1, p. 85-104.

Sapin, F., Hermawan, I., Pubellier, M., Vigny, C., and Ringenbach, J. C., 2013, The recent convergence on the NW Borneo Wedge-a crustal-scale gravity gliding evidenced from GPS: Geophysical Journal International, v. 193, no. 2, p. 549-556.

Sapin, F., Pubellier, M., Lahfid, A., Janots, D., Aubourg, C., and Ringenbach, J. C., 2011, Onshore record of the subduction of a crustal salient: example of the NW Borneo Wedge: Terra Nova, v. 23, no. 4, p. 232-240.

Scarselli, N., McClay, K., and Elders, C., 2016, Seismic geomorphology of Cretaceous megaslides offshore Namibia (Orange Basin): insights into segmentation and degradation of gravity-driven linked systems: Marine and Petroleum Geology, v. 75, p. 151-180.

Schlische, R. W., Groshong, R. H., Withjack, M. O., and Hidayah, T. N., 2014, Quantifying the geometry, displacements, and subresolution deformation in thrust-ramp anticlines with growth and erosion: From models to seismic-reflection profile: Journal of Structural Geology, v. 69, p. 304-319.

Schlüter, H., HINz, K., and Block, M., 1996, Tectono-stratigraphic terranes and detachment faulting of the South China Sea and Sulu Sea: Marine Geology, v. 130, no. 1-2, p. 39-78.

Schori, M., Mosar, J., and Schreurs, G., 2015, Multiple detachments during thin-skinned deformation of the Swiss Central Jura: a kinematic model across the Chasseral: Swiss journal of geosciences, v. 108, no. 2-3, p. 327-343.

Schreurs, G., Buiter, S. J., Boutelier, J., Burberry, C., Callot, J.-P., Cavozzi, C., Cerca, M., Chen, J.-H., Cristallini, E., and Cruden, A. R., 2016, Benchmarking analogue models of brittle thrust wedges: Journal of Structural Geology, v. 92, p. 116-139.

Schreurs, G., Buiter, S. J. H., Boutelier, D., Corti, G., Costa, E., Cruden, A. R., Daniel, J.-M., Hoth, S., Koyi, H. A., Kukowski, N., Lohrmann, J., Ravaglia, A., Schlische, R. W., Withjack, M. O., Yamada, Y., Cavozzi, C., Del Ventisette, C., Brady, J. A. E., Hoffmann-Rothe, A., Mengus, J.-M., Montanari, D., and Nilforoushan, F., 2006, Analogue benchmarks of shortening and extension experiments, *in* Buiter, S. J. H., and Schreurs, G., eds., Analogue and Numerical Modelling of Crustal-Scale Processes, Volume 253, p. 1-27.

Selzer, C., Buiter, S. J. H., and Pfiffner, O. A., 2007, Sensitivity of shear zones in orogenic wedges to surface processes and strain softening: Tectonophysics, v. 437, no. 1-4, p. 51-70, DOI: 10.1016/j.tecto.2007.02.020.

-, 2008, Numerical modeling of frontal and basal accretion at collisional margins: Tectonics, v. 27, no. 3, p. TC3001, DOI: 10.1029/2007tc002169.

Şengör, A. C., and Bozkurt, E., 2013, Layer-parallel shortening and related structures in zones undergoing active regional horizontal extension: International Journal of Earth Sciences, v. 102, no. 1, p. 101-119.

Séranne, M., and Anka, Z., 2005, South Atlantic continental margins of Africa: a comparison of the tectonic vs climate interplay on the evolution of equatorial west Africa and SW Africa margins: Journal of African Earth Sciences, v. 43, no. 1-3, p. 283-300.

Shaw, J. H., Connors, C. D., and Suppe, J., 2005, Seismic interpretation of contractional fault-related folds: An AAPG seismic atlas, Volume 53, American Association of Petroleum Geologists, p. 1-157.

Shaw, J. H., Novoa, E., and Connors, C. D., 2004, Structural controls on growth stratigraphy in contractional fault-related folds, *in* McClay, K. R., ed., Thrust tectonics and hydrocarbon systems, Volume 82, AAPG Memoir p. 407-419.

Sherkati, S., Letouzey, J., and de Lamotte, D. F., 2006, Central Zagros fold-thrust belt (Iran): New insights from seismic data, field observation, and sandbox modeling: Tectonics, v. 25, no. 4, p. TC4007, DOI: 10.1029/2004tc001766.

Shipley, T. H., McIntosh, K. D., Silver, E. A., and Stoffa, P. L., 1992, Three‐dimensional seismic imaging of the Costa Rica accretionary prism: Structural diversity in a small volume of the lower slope: Journal of Geophysical Research: Solid Earth, v. 97, no. B4, p. 4439-4459.

Simons, W. J. F., Socquet, A., Vigny, C., Ambrosius, B. A. C., Abu, S. H., Promthong, C., Subarya, C., Sarsito, D. A., Matheussen, S., Morgan, P., and Spakman, W., 2007, A decade of GPS in Southeast Asia: Resolving Sundaland motion and boundaries: Journal of Geophysical Research-Solid Earth, v. 112, p. B06420, DOI: 10.1029/2005jb003868.

Simpson, G., 2011, Mechanics of non-critical fold-thrust belts based on finite element models: Tectonophysics, v. 499, no. 1-4, p. 142-155, DOI: 10.1016/j.tecto.2011.01.004.

Simpson, G. D. H., 2006, Modelling interactions between fold-thrust belt deformation, foreland flexure and surface mass transport: Basin Research, v. 18, no. 2, p. 125-143, DOI: 10.1111/j.1365-2117.2006.00287.x.

-, 2009, Mechanical modelling of folding versus faulting in brittle-ductile wedges: Journal of Structural Geology, v. 31, no. 4, p. 369-381, DOI: 10.1016/j.jsg.2009.01.011.

-, 2010a, Formation of accretionary prisms influenced by sediment subduction and supplied by sediments from adjacent continents: Geology, v. 38, no. 2, p. 131-134, DOI: 10.1130/g30461.1.

-, 2010b, Influence of the mechanical behaviour of brittle-ductile fold-thrust belts on the development of foreland basins: Basin Research, v. 22, no. 2, p. 139-156, DOI: 10.1111/j.1365-2117.2009.00406.x.

Smit, J. H. W., Brun, J. P., and Sokoutis, D., 2003, Deformation of brittle-ductile thrust wedges in experiments and nature: Journal of Geophysical Research-Solid Earth, v. 108, no. B10, p. 2480, DOI: 10.1029/2002jb002190.

Smith, G., McNeill, L., Henstock, T. J., and Bull, J., 2012, The structure and fault activity of the Makran accretionary prism: Journal of Geophysical Research-Solid Earth, v. 117, p. B07407, DOI: 10.1029/2012jb009312.

Smith, G. L., McNeill, L. C., Wang, K., He, J., and Henstock, T. J., 2013, Thermal structure and megathrust seismogenic potential of the Makran subduction zone: Geophysical Research Letters, v. 40, no. 8, p. 1528-1533, DOI: 10.1002/grl.50374.

Socquet, A., Simons, W., Vigny, C., McCaffrey, R., Subarya, C., Sarsito, D., Ambrosius, B., and Spakman, W., 2006a, Microblock rotations and fault coupling in SE Asia triple junction (Sulawesi, Indonesia) from GPS and earthquake slip vector data: Journal of Geophysical Research: Solid Earth, v. 111, p. B08409, DOI: 10.1029/2005JB003963.

Socquet, A., Vigny, C., Chamot‐Rooke, N., Simons, W., Rangin, C., and Ambrosius, B., 2006b, India and Sunda plates motion and deformation along their boundary in Myanmar determined by GPS: Journal of Geophysical Research: Solid Earth, v. 111, p. B05406, DOI: 10.1029/2005JB003877.

Soliva, R., Benedicto, A., and Maerten, L., 2006, Spacing and linkage of confined normal faults: importance of mechanical thickness: Journal of Geophysical Research: Solid Earth, v. 111, p. B01402, DOI: 10.1029/2004JB003507.

Steuer, S., Franke, D., Meresse, F., Savva, D., Pubellier, M., and Auxietre, J.-L., 2014, Oligocene–Miocene carbonates and their role for constraining the rifting and collision history of the Dangerous Grounds, South China Sea: Marine and Petroleum Geology, v. 58, p. 644-657.

Stockmal, G. S., Beaumont, C., Nguyen, M., Lee, B.,, 2007, Mechanics of thin-skinned fold and-thrust belts: insights from numerical models.: Geological Society of America Bulletin, v. Whence the Mountains? Inquiries into the Evolution of Orogenic Systems: A Volume in Honor of Raymond A. Price, no. 433, p. 63-98.

Storti, F., and McClay, K., 1995a, Influence of syntectonic sedimentation on thrust wedges in analog models: Geology, v. 23, no. 11, p. 999-1002, DOI: 10.1130/0091-7613(1995)023<0999:iossot>2.3.co;2.

-, 1995b, Influence of syntectonic sedimentation on thrust wedges in analogue models: Geology, v. 23, no. 11, p. 999-1002, DOI: 10.1130/0091-7613(1995)023<0999:iossot>2.3.co;2.

Strayer, L. M., Hudleston, P. J., and Lorig, L. J., 2001, A numerical model of deformation and fluid-flow in an evolving thrust wedge: Tectonophysics, v. 335, no. 1-2, p. 121-145, DOI: 10.1016/s0040-1951(01)00052-x.

Sun, C., Jia, D., Yin, H., Chen, Z., Li, Z., Shen, L., Wei, D., Li, Y., Yan, B., and Wang, M., 2016, Sandbox modeling of evolving thrust wedges with different preexisting topographic relief: Implications for the Longmen Shan thrust belt, eastern Tibet: Journal of Geophysical Research: Solid Earth, v. 121, p. 4591-4614.

Suppe, J., 1983, Geometry and kinematics of fault-bend folding: American Journal of Science, v. 283, no. 7, p. 684-721.

Suppe, J., 2007, Absolute fault and crustal strength from wedge tapers: Geology, v. 35, no. 12, p. 1127-1130, DOI: 10.1130/g24053a.1.

-, 2014, Fluid overpressures and strength of the sedimentary upper crust: Journal of Structural Geology, v. 69, p. 481-492.

Suppe, J., Chou, G. T., and Hook, S. C., 1992, Rates of folding and faulting determined from growth strata, *in* McClay, K. R., ed., Thrust Tectonics, Springer, Dordrecht, p. 105-121.

Suppe, J., Connors, C. D., and Zhang, Y., 2004, Shear fault-bend folding, *in* McClay, K. R., ed., Thrust tectonics and hydrocarbon systems, Volume 82, AAPG Memoir p. 303-323.

Suppe, J., and Medwedeff, D. A., 1990, Geometry and kinematics of fault-propagation folding: Eclogae Geologicae Helvetiae, v. 83, no. 3, p. 409-454.

Tan, D. N., and Lamy, J., 1990, Tectonic evolution of the NW Sabah continental margin since the Late Eocene: Bulletin of the Geological Society of Malaysia, v. 27, p. 241-260.

Tate, R., 2001, The geology of Borneo Island: map: Geological Society of Malaysia.

Tingay, M. R. P., Hillis, R. R., Morley, C. K., King, R. C., Swarbrick, R. E., and Damit, A. R., 2009, Present-day stress and neotectonics of Brunei: Implications for petroleum exploration and production: AAPG Bulletin, v. 93, no. 1, p. 75-100, DOI: 10.1306/08080808031.

Tingay, M. R. P., Hillis, R. R., Morley, C. K., Swarbrick, R. E., and Drake, S. J., 2005, Present-day stress orientation in Brunei: a snapshot of 'prograding tectonics' in a Tertiary delta: Journal of the Geological Society, v. 162, p. 39-49, DOI: 10.1144/0016-764904-017.

Tingay, M. R. P., Hillis, R. R., Morley, C. K., Swarbrick, R. E., and Okpere, E. C., 2003, Variation in vertical stress in the Baram Basin, Brunei: tectonic and geomechanical implications: Marine and Petroleum Geology, v. 20, no. 10, p. 1201-1212, DOI: 10.1016/j.marpetgeo.2003.10.003.

Tongkul, F., 1991, Tectonic evolution of Sabah, Malaysia: Journal of Southeast Asian Earth Sciences, v. 6, no. 3-4, p. 395-405.

Tongkul, F., 1994, The geology of Northern Sabah, Malaysia: its relationship to the opening of the South China Sea Basin Tectonophysics, v. 235, no. 1-2, p. 131-147, DOI: 10.1016/0040-1951(94)90021-3.

Totake, Y., Butler, R. W. H., Bond, C. E., and Aziz, A., 2018, Analyzing structural variations along strike in a deep-water thrust belt: Journal of Structural Geology, v. 108, p. 213-229, DOI: 10.1016/j.jsg.2017.06.007.

Trudgill, B. D., Fiduk, J. C., Weimer, P., Rowan, M. G., Gale, P. E., Korn, B. E., Phair, R. L., Gafford, W. T., Dischinger, J. B., Roberts, G. R., and Henage, L. F., 1995, The geological evolution of the deep water Perdido Foldbelt, Alaminos Canyon, northwestern deep Gulf of Mexico. : Gulf Coast Association of Geological Societies Transactions, v. 45, p. 573-579.

Trudgill, B. D., Rowan, M. G., Fiduk, J. C., Weimer, P., Gale, P. E., Korn, B. E., Phair, R. L., Gafford, W. T., Roberts, G. R., and Dobbs, S. W., 1999, The perdido fold belt, northwestern deep gulf of mexico, part 1: Structural geometry, evolution and regional implications1: AAPG bulletin, v. 83, no. 1, p. 88-113.

Trümpy, R., 1960, Paleotectonic evolution of the Central and Western Alps: Geological Society of America Bulletin, v. 71, no. 6, p. 843-907.

Tsuji, T., Matsuoka, T., Yamada, Y., Nakamura, Y., Ashi, J., Tokuyama, H., Kuramoto, S. i., and Bangs, N. L., 2005, Initiation of plate boundary slip in the Nankai Trough off the Muroto peninsula, southwest Japan: Geophysical Research Letters, v. 32, no. 12, p. L12306, DOI: 10.1029/2004GL021861.

Tuitt, A., King, R., Hergert, T., Tingay, M., and Hillis, R., 2012, Modelling of sediment wedge movement along low-angle detachments using ABAQUS™: Geological Society, London, Special Publications, v. 367, no. 1, p. 171-183.

Underhill, J. R., and Paterson, S., 1998, Genesis of tectonic inversion structures: seismic evidence for the development of key structures along the Purbeck–Isle of Wight Disturbance: Journal of the Geological Society, v. 155, no. 6, p. 975-992.

Van Rensbergen, P., and Morley, C. K., 2003, Re-evaluation of mobile shale occurrences on seismic sections of the Champion and Baram deltas, offshore Brunei, *in* VanRensbergen, P., Hillis, R. R., Maltman, A. J., and Morley, C. K., eds., Subsurface Sediment Mobilization, Volume 216, p. 395-409.

Vernant, P., Nilforoushan, F., Hatzfeld, D., Abbassi, M., Vigny, C., Masson, F., Nankali, H., Martinod, J., Ashtiani, A., and Bayer, R., 2004, Present-day crustal deformation and plate kinematics in the Middle East constrained by GPS measurements in Iran and northern Oman: Geophysical Journal International, v. 157, no. 1, p. 381-398.

von Hagke, C., Oncken, O., and Evseev, S., 2014, Critical taper analysis reveals lithological control of variations in detachment strength: An analysis of the Alpine basal detachment (Swiss

Alps): Geochemistry Geophysics Geosystems, v. 15, no. 1, p. 176-191, DOI: 10.1002/2013gc005018.

von Huene, R., and Scholl, D. W., 1991, Observations at convergent margins concerning sediment subduction, subduction erosion, and the growth of continental crust: Reviews of Geophysics, v. 29, no. 3, p. 279-316, DOI: 10.1029/91rg00969.

Wallace, L. M., Reyners, M., Cochran, U., Bannister, S., Barnes, P. M., Berryman, K., Downes, G., Eberhart‐Phillips, D., Fagereng, A., and Ellis, S., 2009, Characterizing the seismogenic zone of a major plate boundary subduction thrust: Hikurangi Margin, New Zealand: Geochemistry, Geophysics, Geosystems, v. 10, no. 10, p. Q10006.

Wang, C., Chen, H., Cheng, X., and Li, K., 2013, Evaluating the role of syn-thrusting sedimentation and interaction with frictional detachment in the structural evolution of the SW Tarim basin, NW China : Insights from analogue modeling Tectonophysics, v. 608, p. 642-652.

Wang, K., and Hu, Y., 2006, Accretionary prisms in subduction earthquake cycles: The theory of dynamic Coulomb wedge: Journal of Geophysical Research-Solid Earth, v. 111, p. B06410, DOI: 10.1029/2005jb004094.

Wang, W., Yin, H., Jia, D., Wu, Z., Wu, C., and Zhou, P., 2018, Calculating detachment depth and dip angle in sedimentary wedges using the area-depth graph: Journal of Structural Geology, v. 107, p. 1-11.

Wang, W. H., and Davis, D. M., 1996, Sandbox model simulation of forearc evolution and noncritical wedges: Journal of Geophysical Research, v. 101, no. B5, p. 11329-11339, DOI: 10.1029/96jb00101.

Weimer, P., and Buffler, R. T., 1992, Structural Geology and Evolution of the Mississippi Fan Fold Belt, Deep Gulf of Mexico (1): AAPG Bulletin, v. 76, no. 2, p. 225-251.

Westbrook, G. K., Ladd, J. W., Buhl, P., Bangs, N., and Tiley, G. J., 1988, Cross section of an accretionary wedge: Barbados Ridge complex: Geology, v. 16, no. 7, p. 631-635, DOI: 10.1130/0091-7613(1988)016<0631:csoaaw>2.3.co;2.

Westbrook, G. K., Smith, M. J., Peacock, J. H., and Poulter, M. J., 1982, Extensive underthrusting of undeformed sediment beneath the accretionary complex of the Lesser Antilles subduction zone: Nature, v. 300, no. 5893, p. 625-628, DOI: 10.1038/300625a0.

White, R. S., 1982, Deformation of the Makran accretionary sediment prism in the Gulf of Oman (north-west Indian Ocean): Geological Society, London, Special Publications, v. 10, no. 1, p. 357-372.

White, R. S., and Louden, K. E., 1982, The Makran Continental Margin: Structure of a Thickly Sedimented Convergent Plate Boundary: Convergent Margins: Field Investigations of Margin Structure and Stratigraphy, *in* Watkins, J. S., and Drake, C. L., eds., Studies in Continental Margin Geology: Tulsa, OK, USA, American Association of Petroleum Geologists Memoir, p. 499-518.

Wickens, H. d. V., and McLachlan, I., 1990, The stratigraphy and sedimentology of the reservoir interval of the Kudu 9A-2 and 9A-3 boreholes: Communications of the Geological Survey of Namibia, v. 6, p. 9-22.

Wilkerson, M. S., and Dicken, C. L., 2001, Quick-look techniques for evaluating twodimensional cross sections in detached contractional settings: AAPG Bulletin, v. 85, p. 1759-1770.

Willett, S., Beaumont, C., and Fullsack, P., 1993, Mechanical model for the tectonics of doubly vergent compressional orogens: Geology, v. 21, no. 4, p. 371-374, DOI: 10.1130/0091-7613(1993)021<0371:mmftto>2.3.co;2.

Willett, S. D., 1992, Dynamic and kinematic growth and change of a coulomb wedge, *in* McClay, K. R., ed., Thrust Tectonics, p. 19-31.

William, A. G., Lambiase, J. J., Back, S., and Jamiran, M. K., 2003, Sedimentology of the Jalan Salaiman and Bukit Melinsung outcrops, western Sabah: is the West Crocker Formation an analogue for Neogene turbidites offshore?: Bulletin of the Geological Society of Malaysia, v. 47, p. 63-75.

Wiltschko, D. V., and Groshong, R. H., 2012, The Chamberlin 1910 balanced section: Context, contribution, and critical reassessment: Journal of Structural Geology, v. 41, p. 7-23.

Woodward, N. B., 1987, Geological applicability of critical-wedge thrust-belt models: Geological Society of America Bulletin, v. 99, no. 6, p. 827-832, DOI: 10.1130/0016-7606(1987)99<827:gaoctm>2.0.co;2.

Woodward, N. B., Boyer, S. E., and Suppe, J., 1990, Balanced Geological Cross‐Sections: Balanced Geological Cross-Sections: An Essential Technique in Geological Research and Exploration, p. 1-126.

Wu, J. E., McClay, K., and Frankowicz, E., 2015, Niger Delta gravity-driven deformation above the relict Chain and Charcot oceanic fracture zones, Gulf of Guinea: Insights from analogue models: Marine and Petroleum Geology, v. 65, p. 43-62, DOI: 10.1016/j.marpetgeo.2015.03.008.

Wu, J. E., and McClay, K. R., 2011, Two-dimensional analog modelling of fold and thrust belts: dynamic interactions with syncontractional sedimentation and erosion AAPG Bulletin, v. 94, p. 301-333.

Wu, S., Bally, A. W., and Cramez, C., 1990, Allochthonous salt, structure and stratigraphy of the north-eastern Gulf of Mexico. Part II: Structure: Marine and Petroleum Geology, v. 7, no. 4, p. 334-370.

Xu, S., Ye, Q., Li, S., Somerville, I., Feng, H., Tang, Z., Shu, D., and Bi, H., 2016, Sequential patterns in Cenozoic marginal basins of the Northwest Pacific: Geological Journal, v. 51, p. 387-415.

Yamada, Y., Baba, K., and Matsuoka, T., 2006, Analogue and numerical modelling of accretionary prisms with a decollement in sediments, *in* Buiter, S. J. H., and Schreurs, G., eds., Analogue and Numerical Modelling of Crustal-Scale Processes, Volume 253, p. 169-183.

Yamato, P., Kaus, B. J. P., Mouthereau, F., and Castelltort, S., 2011, Dynamic constraints on the crustal-scale rheology of the Zagros fold belt, Iran: Geology, v. 39, no. 9, p. 815-818, DOI: 10.1130/g32136.1.

Yan, P., and Liu, H., 2004, Tectonic-stratigraphic division and blind fold structures in Nansha Waters, South China Sea: Journal of Asian Earth Sciences, v. 24, no. 3, p. 337-348.

Yang, X., Peel, F. J., Sanderson, D. J., and McNeill, L. C., 2017, Episodic growth of fold-thrust belts: Insights from Finite Element Modelling: Journal of Structural Geology, v. 102, p. 113-129.

Yin, A., Dubey, C., Kelty, T., Gehrels, G., Chou, C., Grove, M., and Lovera, O., 2006, Structural evolution of the Arunachal Himalaya and implications for asymmetric development of the Himalayan orogen: Current Science, p. 195-206.

Yin, A., and Kelty, T. K., 1991, Structural Evolution of the Lewis Plate in Glacier-National-Park, Montana - Implications for Regional Tectonic Development: Geological Society of America Bulletin, v. 103, no. 8, p. 1073-1089.

Zalan, P., Shaw, J., Connors, C., and Suppe, J., 2005, End members of gravitational fold and thrust belts (GFTBs) in the deep waters of Brazil: An AAPG Seismic Atlas: AAPG Studies in Geology, v. 53, p. 147-156.

Zhao, W. L., Davis, D. M., Dahlen, F. A., and Suppe, J., 1986, Orign of convex accretionary wedges-evidence from Barbados: Journal of Geophysical Research-Solid Earth and Planets, v. 91, no. B10, p. 10246-10258, DOI: 10.1029/JB091iB10p10246.

Zhou, J., Zhang, B., and Xu, Q., 2016, Effects of lateral friction on the structural evolution of fold-and-thrust belts: Insights from sandbox experiments with implications for the origin of landward-vergent thrust wedges in Cascadia: Geological Society of America Bulletin, v. 128, no. 3-4, p. 669-683.

Zienkiewicz, O. C., and Taylor, R. L., 1991, The finite element method, New York, McGraw-Hill.